Università degli Studi di Pavia   Istituto Universitario di Studi Superiori

An Innovative Superelastic System for Base Isolation

A Thesis Submitted in Partial Fulfilment of the Requirements
for the Degree of Doctor of Philosophy in

EARTHQUAKE ENGINEERING

by

Gabriele Attanasi

August, 2009

This page intentionally left blank.

Università degli Studi di Pavia

Istituto Universitario di Studi Superiori

European School for Advanced Studies in Reduction of Seismic Risk

ROSE School

An Innovative Superelastic System for Base Isolation

A Thesis Submitted in Partial Fulfilment of the Requirements
for the Degree of Doctor of Philosophy in

EARTHQUAKE ENGINEERING

by

Gabriele Attanasi

Supervisors:
Prof. Ferdinando Auricchio - Università degli Studi di Pavia
Prof. Gregory L. Fenves - University of Texas at Austin

August, 2009

This page intentionally left blank.

ABSTRACT

The objective of the present work is to propose a new seismic isolation device based on superelastic material components manufactured using shape memory alloys. Seismic isolation is one of the most effective options for passive protection of structure. Shape memory alloys (SMAs) are characterized by unique mechanical properties due to a solid-solid transformation between phases of the alloy.

An isolation bearing system based on a SMA superelastic effect is intended to provide a nonlinear flag-shaped lateral displacement-shear force hysteresis, characterized by an yielding force which limits the induced seismic force, additional damping, and recentering properties to reduce or eliminate the eventual cumulative damage.

The innovative device configuration is proposed and its mechanical components are defined. The concept is based on two separate systems, one to transmit the vertical load and another to laterally restrain the isolated content. Experimental tests on the superelastic restraining system components are performed to characterized their response and to validate the numerical model.

The structural response of the innovative device is then investigated considering different building properties and compared with traditional isolation systems. Results show that proposed superelastic isolation device is characterized by an attractive response from the earthquake engineering point of view because of its capability in reaching the isolated structure design goals, i.e. modification of the structural response, ability to undergo large displacement demand without lost of strength, energy dissipation, and recentering after the seismic event.

A simplified procedure for isolation device components dimensioning has been studied to get a superelastic responding isolator characterized by the wanted design force capacity and displacement capability. Design provisions for superelastic base isolated structures following a direct displacement based approach are also proposed and applied in a structural design example.

This page intentionally left blank.

ACKNOWLEDGEMENTS

This page intentionally left blank.

CONTENTS

This page intentionally left blank.

LIST OF TABLES

This page intentionally left blank.

LIST OF FIGURES

This page intentionally left blank.

1. Preface and Outline

A large proportion of the population in the world lives in seismic hazard regions and are at risk from earthquakes of varying severity and frequency of occurrence. Every year earthquakes cause significant loss of life and damage to properties.

Traditionally, progress in design and assessment methods of civil structures comes after major earthquakes, whenever the need of improving the safety level of engineering structures became evident. The importance of continuous and extensive research is recognized as the most important factor to provide new methods to reduce the most severe earthquake effects.

In this context, seismic isolation is a technology which mitigates the earthquake effects on buildings and on their potentially vulnerable contents. The concept of protecting a structure from the damaging effects of an earthquake by introducing a support isolating the building from the shaking ground is quite old, but research continues for seeking more effective, economical, and reliable seismic isolation systems.

In the last years, major developments have occurred on advanced material properties. The term *advanced* in the civil structural context refers to a capability to increase the structural performance, safety, building design life time, and serviceability with respect to traditional materials. A key aspect to move towards the improved structural technology is the development of advanced materials and its integration in innovative structural systems to provide improved performance.

An example of smart materials is Shape Memory Alloys (*SMA*), which has unique properties, including the shape memory effect and the superelastic effect. These properties, which have led to numerous applications in the biomedical and aerospace industries, have also been evaluated for applications in the area of seismic resistant design and retrofitting.

In the present work the focus is on the possibility of integrating the SMA application in seismic isolation technology. The motivation of the investigation is to exploit this possibility with a critical point of view, trying to identify a suitable device configuration and evaluating its main properties and implications in isolation-superstructure system global response.

Conceptually, the dissertation is composed by different parts, following the rational development of the investigation.

A theoretical investigation is performed to characterize numerically the response of isolation systems made of innovative materials. Results show some interesting properties in the innovative device with respect the current state of art.

For this reason, a real isolation device is designed, taking advantages of innovative properties of shape memory alloys. The goal is to investigate the possibility of proposing a real device configuration able to improve the structural response during the seismic events with respect to the actual isolation bearings.

The designed device has not been fully manufactured yet. Nevertheless, the behavior of the restraining system device component is verified through experimental tests. The numerical model which the previous design is based on is validated and the results are consistent with the experimental results.

The proposed innovative device response is investigated checking the numerical response of different base isolated structures. Being the response positive, the structural design procedure using innovative isolation system is formalized and a design example is provided.

The complete outline of the dissertation is summarized below.

- Chapter 2 provides some basics on seismic isolation. The fundamental concepts are reported together with the isolated structure basic dynamics. The actual most common isolation bearings are also described in this chapter.

- Chapter 3 introduces the shape memory alloys. The most significative physical characteristics and mechanical properties of this class of alloys are reported underlining the most important features interesting from the seismic engineering perspective. Principles and examples of SMA design in earthquake engineering are reported, together with a literary review of the most SMA significative applications in energy dissipation and base isolation contexts.

- Chapter 4 contains the feasibility assessment of superelastic bearing system for seismic isolation. In this chapter, the existence of an idealized superelastic isolation bearing is assumed, characterized by a given flag-shaped lateral displacement-shear force hysteresis. A response comparison with an actual isolation bearing is performed. In particular, the hysteretic damping approach and the direct computation of the response through time history analyses are proposed. Parametric investigation is presented to identify the variables which have significant effect on the flag-shaped hysteresis device response.

- Chapter 5 reports the theoretical, numerical and experimental investigation on the real superelastic lateral restraining system on which the innovative device is based. The basics of its theoretical mechanical behavior are presented and a numerical model is used to determine its global response. Experimental tests are

then performed on different device configurations. The test results turn out to be very attractive for the design and the numerical model is validated.

- Chapter 6 proposes the real superelastic device configuration. Its main components are characterized separately, and their previous most significative applications in literature are reported. The global response of the innovative device is numerically investigated and a comparison with existing device configurations is carried out. An approximate design procedure for the innovative device is then presented. The aim is to provide a design tool to get an optimized geometrical configuration as a function of the needed design displacement capacity and strength.

- Chapter 7 presents the investigation on the innovative system response compared with an actual bearing response considering single degree of freedom systems. Two innovative superelastic device configurations are proposed, characterized by the same lateral restraining system but with different bearing device properties.

- Chapter 8 reports the constant ductility spectra for flag-shaped hysteresis systems. The constant ductility spectra concept and applications are presented and the analyses are performed for the two innovative isolation system configurations.

- Chapter 9 compares the innovative isolation system response with respect to an actual isolation bearing investigating the effects in a stiff superstructure building modeled as a multi degree of freedom system. Two cases are considered, one in which the superstructure is supposed to respond elastically and another in which it is supposed to experience damaging.

- Chapter 10 compares the innovative isolation system response with respect to an actual isolation bearing by investigating the effects in a flexible superstructure building modeled as a multi degree of freedom system. Again two cases are considered, one in which the superstructure is supposed to respond elastically and another in which it is supposed to experience damaging.

- Chapter 11 proposed a direct displacement base design procedure for superelastic isolation device structures. The general procedure for base isolated structures is recalled and particular provisions are presented for the flag-shaped superelastic bearing system design. Finally, a design example is performed and its response is numerically checked.

- Chapter 12 reports the main conclusions of the investigation.

This page intentionally left blank.

2. Basics on Seismic Isolation

2.1 INTRODUCTION

This chapter introduces the fundamentals of seismic isolation. In Section 2.2, the main concepts are described and the advantages in using this method are evaluated. The isolated system dynamic behavior is reported in Section 2.3. The most common seismic isolation bearing device configurations are then described in Section 2.4.

2.2 FUNDAMENTAL CONCEPTS

Seismic isolation is a technique for reducing the seismic risks in different types of structures, like buildings and bridges. The goal in using seismic isolation is to modify the global response and improve the structural performance. This section summarizes some of the most important. An extensive description of the topic can be found in Skinner *et al.* [1993], Naeim and Kelly [1999] and Priestley *et al.* [2007].

2.2.1 Response Regularization

Isolation is a design method to regularize the response and to modify the relative effective stiffness and strength in the structure. The isolation system affects the global structural behavior because it is an additional element providing stiffness in series with respect to the superstructure with its stiffness. The isolation layer is more flexible than the rest of the structure, hence it absorbs a large part of the displacement demand. If the isolators are designed in a correct way, providing enough displacement capacity, we can take advantage of this in the protection of the superstructure. Since the displacement demand of the superstructure is small, we can assure its elastic response. Moreover, if nonlinear isolation system devices are used, the maximum base shear transmitted to the superstructure is limited and capacity design can be performed. In this way all the nonlinear and dissipating phenomena will occur at the isolation level, and brittle failure mode will be avoided.

2.2.2 Period Shift

A change in global structure stiffness shifts the fundamental period of vibration. Since the isolation layer is more flexible than the superstructure, the fundamental period of

the isolated structure is increased with respect to the one in the non isolated condition, inferring to either the displacement or the acceleration demand. Thus, the isolation system affects strongly the properties of the first mode of vibration. In an isolated structure the fundamental mode is very different from all the other modes and it is even more important than in the not isolated case. The vertical profile of the horizontal displacements is approximately rectangular, with equal motions for all the masses. Furthermore, fundamental mode is characterized by a large participating mass, almost equal to the total mass. Therefore the isolation system determines the first period and damping of an isolated structure, and these, in their turn, control the structural seismic response.
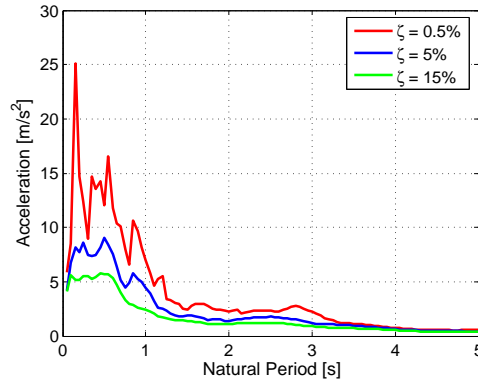
Figure 2.1. Displacement response spectra for different damping factor values experiencing the El Centro (1940) ground motion (see Chopra [2006])
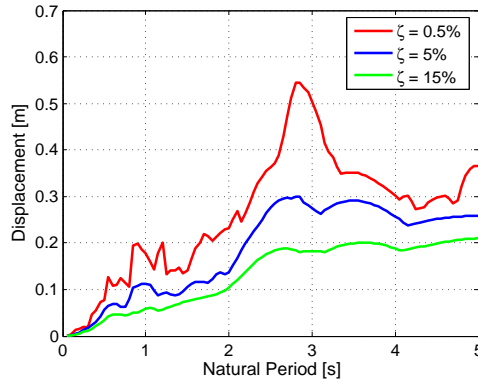
Figure 2.2. Acceleration response spectra for different damping factor values experiencing the El Centro (1940) ground motion (see Chopra [2006])

Displacement and acceleration response spectra are shown respectively in Figure 2.1 and

in Figure 2.2. Maximum accelerations are at the greatest when the first vibrational period of the structure is in the short period range. On the contrary, displacement demand is high for long periods. Furthermore, damping is effective in reducing both acceleration and displacement ordinate.

Seismic isolation induces the elongation of fundamental mode period and this is a primary reason for the effectiveness of the method. It leads to a reduction in the inertia load acting on the structure and to an increase in the demand of displacements, which anyway is carried out mostly by the isolators. Higher modes producing deformations in the structure are usually not excited by the ground motion.

2.2.3 Energy Dissipation

The presence of isolation system increases the global energy dissipation capacity of the structure. This helps to reduce the displacement demand as shown in Figure 2.1. Usually we refer to the assumption according to which different structural elements contribute to the overall energy dissipation as a function of their displacements. Hence if the structural displacement demand is all localized in the isolation system and the superstructure is rigid, the isolation devices determines the energy dissipation; otherwise, if superstructure deforms, the energy is dissipated according to the isolation and to the structure dissipation contributions.

2.3 BASE ISOLATED STRUCTURE DYNAMICS

The linear theory of seismic isolation has been described in detail in Naeim and Kelly [1999] and it is summarized here. This section presents the two mass isolated structural model as shown in Figure 2.3. The mass m_s represents the superstructure and the mass
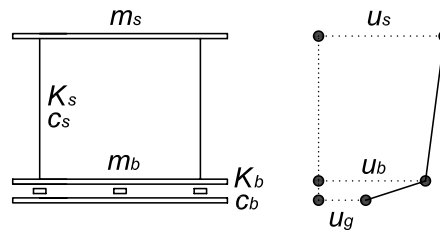
Figure 2.3. Isolated system dynamic model and parameters

m_b is the mass of the storey levels above the isolation system. The superstructure stiffness and damping are k_s and c_s and the stiffness and damping of the isolation system are k_b and c_b respectively. Absolute displacements of the two masses are u_s and u_b while u_g is the ground displacement.

For simplicity, the relative displacements are assumed as independent variables, being:

$$v_b = u_b - u_g$$
$$v_s = u_s - u_b$$

(2.1)

The definition in Equation (2.1) is particularly feasible because the relative degrees of freedom are represented respectively as the isolation system displacement v_b and the superstructure drift v_s.

The equation of motion of the system is given by:

$$M\ddot{v} + C\dot{v} + Kv = = Mr\ddot{u}_g$$

(2.2)

in which M, C, and K are respectively the mass, the damping and the stiffness matrices of the two-degree of freedom system characterized by the displacement vector v. The previous Equation (2.2) can be rewritten explicitly in terms of the quantities in Equation (2.1) as:

$$\begin{bmatrix} m_s + m_b & m_s \\ m_s & m_s \end{bmatrix} \begin{Bmatrix} \ddot{v}_b \\ \ddot{v}_s \end{Bmatrix} + \begin{bmatrix} c_b & 0 \\ 0 & c_s \end{bmatrix} \begin{Bmatrix} \dot{v}_b \\ \dot{v}_s \end{Bmatrix} + \begin{bmatrix} k_b & 0 \\ 0 & k_s \end{bmatrix} \begin{Bmatrix} v_b \\ v_s \end{Bmatrix} =$$
$$= \begin{bmatrix} m_s + m_b & m_s \\ m_s & m_s \end{bmatrix} \begin{Bmatrix} 1 \\ 0 \end{Bmatrix} \ddot{u}_g$$

(2.3)

defining the mass ratio γ as:

$$\gamma = \frac{m_s}{m_s + m_b}$$

(2.4)

the natural frequencies ω_b and ω_s are given by:

$$\omega_b^2 = \frac{k_b}{m_s + m_b} \qquad \omega_s^2 = \frac{k_s}{m_s}$$

(2.5)

and it is assumed that the following relation is valid:

$$\epsilon = \frac{\omega_b^2}{\omega_s^2} = O\left(10^{-2}\right)$$

(2.6)

damping factors ξ_b and ξ_s are defined by:

$$2\omega_b \xi_b = \frac{c_b}{m_s + m_b} \qquad 2\omega_s \xi_s = \frac{c_s}{m_s}$$

(2.7)

the system dynamic relations from Equation (2.3) therefore become:

$$\gamma \ddot{v}_s + \ddot{v}_b + 2\omega_b \xi_b \dot{v}_b + \omega_b^2 v_b = -\ddot{u}_g$$
$$\ddot{v}_s + \ddot{v}_b + 2\omega_s \xi_s \dot{v}_s + \omega_s^2 v_s = -\ddot{u}_g$$

(2.8)

as ω_1 and ω_2 are the natural frequencies of the two structural modes as expressed in (2.5), they can be also computed as:

$$\omega_1^2 = \frac{1}{2(1-\gamma)} \left\{ \omega_b^2 + \omega_s^2 - \sqrt{\left(\omega_b^2 - \omega_s^2\right)^2 + 4\gamma \omega_b^2 \omega_s^2} \right\}$$
$$\omega_2^2 = \frac{1}{2(1-\gamma)} \left\{ \omega_b^2 + \omega_s^2 + \sqrt{\left(\omega_b^2 - \omega_s^2\right)^2 + 4\gamma \omega_b^2 \omega_s^2} \right\} \tag{2.9}$$

and to first order in ϵ are given by:

$$\omega_1^2 = \omega_b^2 (1 - \gamma \epsilon)$$
$$\omega_2^2 = \frac{\omega_s^2}{1-\gamma} (1 + \gamma \epsilon) \tag{2.10}$$

while the mode shapes normalized in the isolation system displacement component are:

$$\phi^{(1)} = \left\{ \begin{array}{c} 1 \\ \epsilon \end{array} \right\} \qquad \phi^{(2)} = \left\{ \begin{array}{c} 1 \\ -\frac{1}{\gamma}[1 - (1-\gamma)\epsilon] \end{array} \right\} \tag{2.11}$$

analysis leads to express modal masses as:

$$M_1 = \left(m_s + m_b\right)(1 + 2\gamma \epsilon) \qquad M_2 = \left(m_s + m_b\right) \frac{(1-\gamma)[1 - 2(1-\gamma)\epsilon]}{\gamma} \tag{2.12}$$

and participation factors can be expressed as:

$$\Gamma_1 = 1 - \gamma \epsilon \qquad \Gamma_2 = \gamma \epsilon \tag{2.13}$$

Equation (2.13) reveals the basic concept which an isolation system relies upon: the participation factor of the second mode, responsible for the structural deformation, is of the order of magnitude of ϵ and if the two frequencies are well separated, as assumed in Equation (2.6), it may be very small.

Since the participation factor of the second mode is very small, it is also almost orthogonal to the earthquake input: this means that, in any case, the input energy associated to the second mode structural frequency will not be inferred to the structure. Basically, the isolation system works by deflecting energy through its orthogonality property rather than by absorbing it.

Nevertheless, energy absorption is another component of the isolation system. Modal damping ratios depend on the superstructural and on the isolator damping coefficients. When they can be treated separately, and the energy dissipation can be described just by

linear viscous damping, the following simple relationships are found:

$$\xi_1 = \xi_b \left(1 - \frac{3}{2}\gamma\epsilon\right) \qquad \xi_2 = \frac{\xi_s + \gamma\xi_b\sqrt{\epsilon}}{\sqrt{1-\gamma}}\left(1 - \frac{\gamma\epsilon}{2}\right) \qquad (2.14)$$

which demonstrates that if the ϵ is small enough the damping coefficient of the fundamental mode is the damping coefficient of the isolation system.

2.4   TRADITIONAL BEARING DEVICES

The present section presents a summary of the most common seismic isolation bearing devices. Bearings are designed to transmit the vertical load and to dissipate energy through friction, viscous damping or hysteretic damping. Usually they are also intended to reduce or control the horizontal force and displacement demand.

2.4.1   Low and High Damping Laminated Rubber Bearings

In laminated rubber bearings, steel plates are inserted in a vulcanized piece of rubber to confine the rubber laterally and reduce its tendency to bulge, as shown in Figure 2.4. Hence, shims increase the vertical stiffness and improve stability under horizontal forces. This type of bearing shows a substantially linear response and the rubber

Figure 2.4. Laminated rubber bearing structure [from Dolce *et al.* [2007a]]

properties controls essentially the dissipation. Low dissipation rubber provides a linear force-displacement relation, as shown in Figure 2.5, while high dissipation rubber gives a more dissipative response as shown in Figure 2.6. The fundamental property of this type of bearing is the dependance between the vertical load capacity, period of vibration and displacement capacity.

Maximum displacement capacity of this class of bearings is limited by either the plan or height dimensions: typical design capacities for medium seismicity areas range in the order of 200mm with ultimate capacities up to 300mm (as reported in Priestley *et al.* [2007]). The
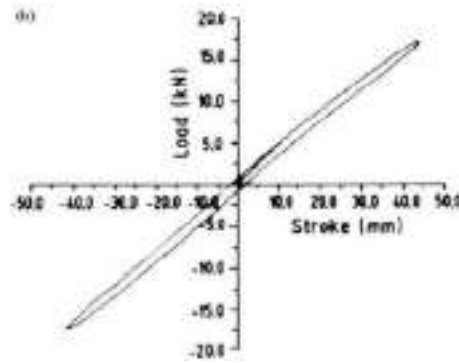
Figure 2.5. Laminated low damping rubber bearing (LDRB) force-displacement relation [from Jain and Thakkar [2005]]
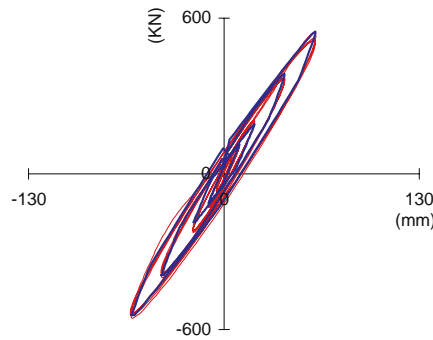
Figure 2.6. Laminated high damping rubber bearing (HDRB) force-displacement relation [from Dolce et al. [2007a]]

viscous damping is of the order of 5% for normal rubber and in the order of 15%-20% for high dissipating rubber (Priestley et al. [2007]). Given the constitutive force displacement relation being quasi-elastic, the devices are usually characterized by recentering capacity and almost constant stiffness. The failure is usually related to instability due to large displacements, either in the form of Euler instability or as roll-out instability (as noticed in Priestley et al. [2007]).

2.4.2   Lead Rubber Bearings

Lead rubber bearings (*LRB*) are low damping laminated rubber devices with a lead plug inserted in the core, as shown in Figure 2.7. The aim of the lead addition is to increase both the stiffness at the relatively low horizontal force levels and the energy dissipation capacity. The resulting horizontal force-displacement relation curve is shown in Figure 2.8. It can
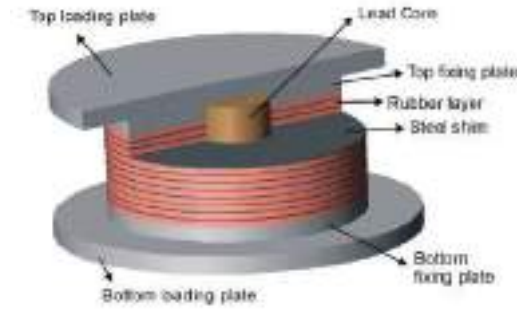
Figure 2.7. Lead rubber bearing device sectioned to show the lead core and the steel shims

be interpreted as a combination of the linear response of the rubber bearing and of the elasto-perfectly plastic response of a confined lead plug. Hence we can describe it using an elastoplastic model with hardening, as shown in Figure 2.8. Maximum displacement is still
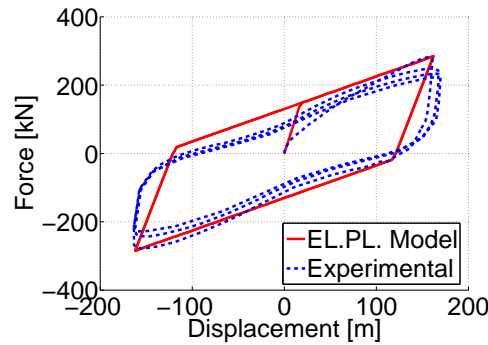
Figure 2.8. Lead rubber bearing (LRB) force-displacement relation: experimental test results [courtesy of *AGOM International srl*] and elastoplastic model (from Attanasi *et al.* [2009b])

governed either by the allowable shear strain in the rubber or by the global stability of the device under vertical load. Post-yielding stiffness corresponds to the mere rubber stiffness and the unloading branch of the force-displacement curve is approximately parallel to the initial stiffness branch up to yielding of the lead plug in the opposite direction. Referring to typical geometries and proportions between lead plug and rubber, the yield force is in the range of one half of the ultimate force and the post-yield stiffness in the range of one tenth of the initial stiffness (as reported also in Priestley *et al.* [2007]). Displacement capacity, response at failure, sensitivity to vertical input are similar to those described for the rubber bearings.

From Figure 2.8 it is also evident that the device has significative hysteretic dissipation. Recentering capacity of lead rubber bearings depends on the ratio between post-yield and initial stiffness and on the ratio between ultimate and yield strength. A larger tendency to recentering is shown if the hardening is high, but residual displacements depend mainly on the loading history and they usually are not negligible (Priestley *et al.* [2007]).

2.4.3 Friction Pendulum Devices

The friction pendulum system (*FPS*) is conceptually based on the properties of pendulum motion, as reported in Christopoulos and Filiatrault [2006] and Priestley *et al.* [2007]. The structure is supported on an articulated teflon-coated load element sliding on the
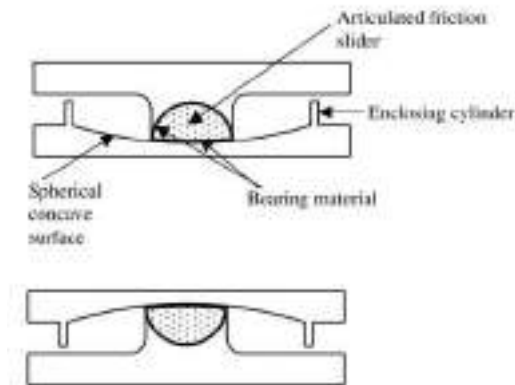
Figure 2.9. Double configuration friction pendulum system (FPS) device cross sections [from Ates *et al.* [2005]]

inside of a spherical surface as shown in Figure 2.9, hence any horizontal displacement is implying a vertical uplift of the supported weight. If friction force is neglected, the system
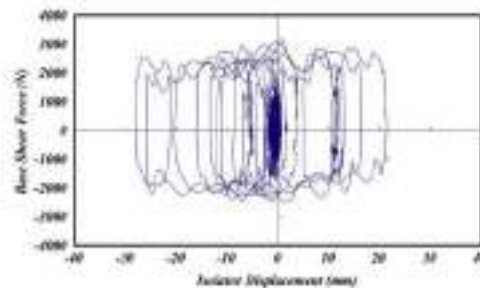
Figure 2.10. Force-displacement FPS result from experimental dynamic tests [from Tsai *et al.* [2008]]

equation of motion is similar to that of a pendulum with equal mass and length given by the radius of curvature of the spherical surface. The expected force-displacement relation is rigid for horizontal loads lower than the resisting friction force and proportional to the ratio between the seismic weight and the radius of curvature for larger loads. An example of FPS force-displacement relation is reported in Figure 2.10.

Theoretically, the device does not have a displacement limit, but for the physical size of the bearing related to the possibility of manufacturing the devices. It exhibits favorable self centering properties based on the effect of the weight (see Priestley *et al.* [2007]).

3. Shape Memory Alloys and their Potentials and Applications in Seismic Engineering

3.1 INTRODUCTION

Shape memory alloys (*SMAs*) are a remarkable class of metals that can offer high strength, large energy dissipation through hysteretic behavior, extraordinary strain capacity (up to 8%) with full shape recovery to zero residual strain, and a high resistance to corrosion and fatigue (see Wilson and Wesolowsky [2005]). Aspects that are all desirable from an earthquake engineering perspective.

Their various physical characteristics result from solid-solid transformation between austenite and martensite phases of the alloy that may be induced by stress or temperature. The most commercially successful SMA is a binary alloy of nickel and titanium (NiTi). Although SMAs are relatively expensive compared to most other materials used in seismic engineering, in certain forms their capacity for high energy loss per unit volume means that comparatively a small quantity can be made to be especially effective.

The shape memory effect was first discovered in 1932 (Olander [1932]), but there was relatively little interest in it until the effect was discovered in equiatomic nickel-titanium (NiTi, often called *Nitinol*, see Jackson *et al.* [1972]). The shape memory effect is now known to occur in a number of alloys, for example, copper, aluminum, and zinc. Binary Nitinol alloys and some of the copper-based tertiary alloys have received most of the commercial attention because of their capability to recover substantial amounts of strain and to generate significant force upon change of shape. Copper is attractive as an alloy element because it is less expensive than Nitinol, although no references to its use in seismic applications could be found in the literature. For many uses, Nitinol is the favored material because of its superior strength, high resistance to corrosion and fatigue, and large useable strain range properties that are also favorable for seismic applications (Song *et al.* [2006]). Nitinol alloys are available as single and stranded wires, ribbons, strips, tubing, and bars. Early commercial applications of Nitinol (i.e., hydraulic line couplings) made use of its thermal shape memory behavior. Now, however, the emphasis has shifted to take advantage of the superelastic behavior (i.e., common applications include use in eyeglass frames, sporting goods, cell phone antennas, and dental and medical applications), and some applications make use of both effects (Wilson and Wesolowsky [2005]). In the present work, SMAs are referred to as Nitinol SMAs.

In this chapter, Section 3.2 carries out an overview of the SMA physical properties. Features that make this material suitable for seismic applications are reported in Section 3.3 and its mechanical properties in Section 3.4. In Section 3.5 the design principles for SMA device are reported as proposed by previous investigations. Finally, some of the most relevant seismic applications of SMAs are summarized in Section 3.6.

3.2   PHYSICAL CHARACTERISTICS OF SHAPE MEMORY ALLOYS

NiTi is composed of essentially equal atomic percentages of nickel and titanium ($\sim$ 55% Ni by weight). Other elements trace amounts and thermo-mechanical processing may be used to provide special physical properties (see Wilson and Wesolowsky [2005]).

The physical behavior of SMAs is a function of stress, strain, and temperature (T), and it is controlled by both chemical composition and thermo-mechanical processing. The shape memory and superelastic effects mentioned earlier occur as a result of solid-solid transformations between austenite (A) and martensite (M). These are two material phases having the same chemical composition but different crystallographic structures.

At low temperatures, the alloy is in a martensite phase. This is described as a *twinned* state, which means that one side of a microscopic material plane is a mirror image of the position of the atoms on the other side (as shown in Figure 3.3). As temperature is increased, it will transform first to a state where both martensite and austenite coexist, and finally to a fully austenite phase. Figure 3.1 shows the phase transformation cycle in the absence of applied stress and as a function of temperature. The reversible solid-solid
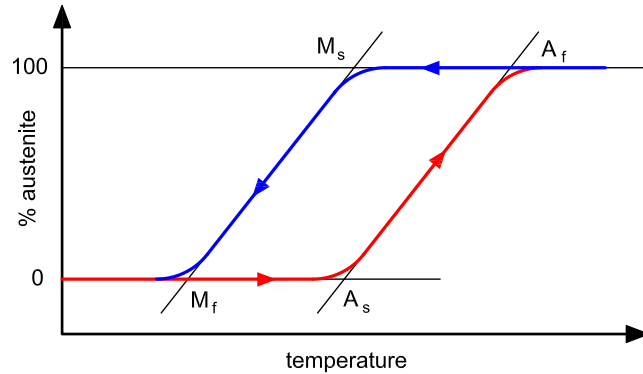
Figure 3.1. **Variation in austenite phase fraction as a function of temperature. This shows the phase transformation cycle without applied stress (see Wilson and Wesolowsky [2005])**

phase transformations, at zero load, are marked by four transition temperatures, reported in Figure 3.1. Upon heating from a fully martensitic phase, A_s is the temperature at the start of the $M \rightarrow A$ phase transformation and A_f is the temperature at the finish of this transformation in which the material is in a fully austenite phase. Upon cooling from a

fully austenite phase, M_s is the temperature at the start of the $A \to M$ transformation and M_f is the martensite finish temperature when the material is in a fully martensite phase. Thus, the transformations $M \to A$ and $A \to M$ do not take place at the same temperature, which gives rise to the hysteresis shown in Figure 3.1, and $M_f < (M_s \sim A_s) < A_f$. To determine these temperatures, calorimetry can be used.

The microstructure can be controlled by thermo-mechanical treatment during the alloy production. At low temperatures (*M-phase*) the material tends to be soft and ductile, and at high temperatures (*A-phase*) it is stiff and strong. When under stress, the behavior of a SMA depends upon the temperature of the material (T) in relation to the various thermal transformation regions shown Figure 3.1. The stress-strain characteristics within three temperature ranges have been recognized in Graesser and Cozzarelli [1991] and are shown in Figure 3.2.

(a) $T < A_s$ (b) $T > A_f$ (c) $T \gg A_f$
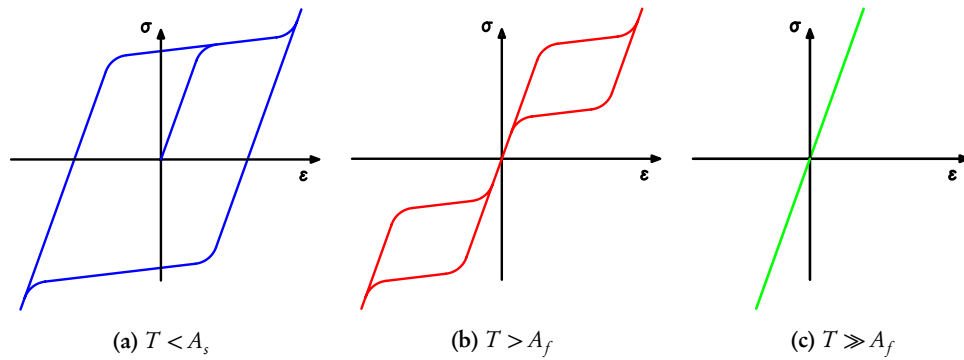
Figure 3.2. **Schematic stress (σ) strain (ε) curves of SMAs at different temperatures (see** Graesser and Cozzarelli **[**1991**])**

If the material is loaded and then unloaded when $T < A_s$ (Figure 3.2a, material is in the martensitic state) the stress strain relation is about elastoplastic and residual strains are recorded. This is accomplished through a transformation from twinned martensite to a de-twinned form. A conceptual picture of this is shown in Figure 3.3 and the process has been identified in Ocel *et al.* [2004]. Subsequently, if the material is heated above A_f then cooled, the residual strain will disappear as the atoms re-orientate themselves, and the material will return its original shape. This is the *shape memory effect*, (SME).

If the material is stressed at a temperature slightly above A_f (Figure 3.2b, material is in austenitic state) through a cycle ranging from zero to the maximum stress and then back to zero, the following six regions can be identified (Wilson and Wesolowsky [2005]):

- elastic response of austenite material at low strains ($\varepsilon < 1\%$);

- stress-induced transformation $A \to M$ with a long and almost constant stress plateau (at intermediate $1\% < \varepsilon < 6\%$ to large strains $\varepsilon > 8\%$);
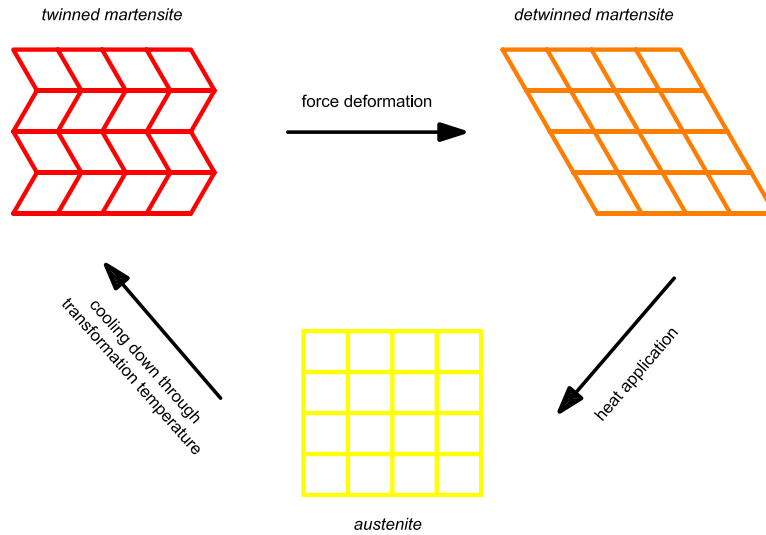
Figure 3.3. Schematic of thermo-elastic martensite austenite phase transformation (see Ocel *et al.* [2004])

- elastic behavior in the stress-induced martensite phase at large strains ($\varepsilon > 8\%$);

- elastic recovery of strain as the stress is removed;

- spontaneous recovery of strain along a lower and almost constant stress path due to $M \rightarrow A$ transformation;

- elastic recovery in austenite phase.

This remarkable behavior, characterized by large nonlinear elastic strains with little additional increase in stress, is called *superelasticity* (*SE*), or *pseudoelasticity* (*PSE*). The length of the superelastic plateau is limited by crystallographic changes. The reverse transformation occurs because stress-induced martensite phase is unstable at high temperatures and once the applied stress is removed, the existing stress in the material acts to drive the reverse transformation during unloading. If the applied stress is increased, eventually the elastic limit of the stress-induced martensite phase will be exceeded and plastic strain will be induced. This can provide additional energy dissipation. Continued application of stress will eventually result in fracture of the SMA at strains that may be as high as 70% (Wilson and Wesolowsky [2005]). Cyclic loading of the material through the superelastic range produces large hysteresis loops, energy dissipation, and zero residual displacement. On the other hand, although cyclically loaded martensite ($T < A_s$) also produces hysteresis loops, there is a residual displacement after the load is removed. In both cases (shape memory and superelasticity) partial or full shape recovery is driven by phase transformation, and both are the same phenomenon. The only difference is the way

in which the transformation is induced i.e thermally in the first case and mechanically upon unloading in the second case.

In the thermal region $A_s < T < A_f$, the material will exhibit partial superelasticity. If the $T \gg A_f$ then martensite cannot be stress-induced, the superelastic effect will not be achieved, and the austenite will deform initially as a linear elastic material and eventually as a plastic material, as shown in Figure 3.2c.
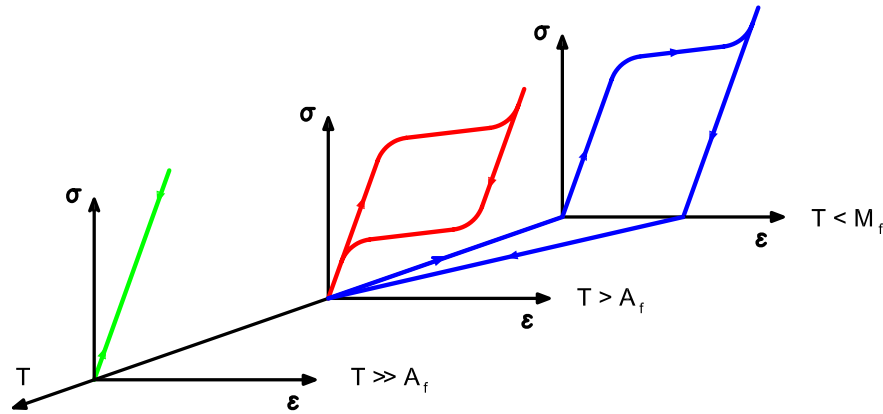
Figure 3.4. **Thermo-mechanical uniaxial response of a SMA material (temperature scale increases towards the left, see DesRoches *et al.* [2004])**

Figure 3.4, after DesRoches *et al.* [2004], provides a useful summary of SMA stress as a function of strain and temperature showing the shape memory hysteresis effect in martensite at low material temperature, superelastic effect due to austenite-martensite phase transformations at intermediate temperature, and elastic/plastic behavior of austenite at high temperature. This figure is actually a composite plot of the stress-strain curves from Figure 3.2, including the temperature effects. The shape memory effect is shown by the lines in the horizontal strain-temperature plane, with the arrows showing heating above temperature A_f then cooling to remove residual strain.

3.3 FEATURES OF SHAPE MEMORY ALLOYS FOR SEISMIC APPLICATIONS

As reported in Wilson and Wesolowsky [2005], SMAs possess features making them excellent potential candidates for use in seismic engineering applications.

The variable modulus of elasticity in superelastic behavior ($T > A_f$) can be used to provide force and displacement control in three regimes. At low strains ($\varepsilon < 1\%$) the elastic modulus of the austenite phase can be used to limit strains under service load conditions. Although the SMA modulus of elasticity is only about 40 to 50% of that of steel, the stiffness of a SMA device can be specified by the physical dimensions of the element in the

same manner as the stiffness characteristics of a LRB is specified by the dimensions of the rubber bearing and the lead core. At intermediate strains ($1\% < \varepsilon < 6\%$) in the superelastic plateau) the reduced modulus can be used to limit the force transmitted to the structure while it undergoes rather large displacements. At large strains ($\varepsilon > 6\%$) the increased modulus in the stress-induced martensite phase can be used to control displacements under severe earthquake loadings.

Upon unloading the lower stress path of the reverse transformation results in hysteretic energy dissipation. The superelastic behavior also means that austenite elements can be used to provide full self-centering (zero residual strain upon unloading). When $T < M_f$, martensite material can be used to provide a high energy dissipation capability because of the full hysteresis loops, although there will be a residual strain upon unloading. When $T > A_f$, superelastic behavior results in lower damping because of the narrower loops. A combination of both martensite and austenite elements can be used to achieve both large energy dissipation and self-centering (see Dolce *et al.* [2000]).

Nitinol is highly resistant to corrosion. It also has an excellent fatigue resistance even though it has extraordinary ductility because deformation at large strains is facilitated by internal material friction during crystallographic reorientation as the phase transformation proceeds, rather than by conventional plastic deformation (dislocation slip) such as occurs in steel. As mentioned earlier, the mechanical behavior of Nitinol is very sensitive to the chemical composition and the thermomechanical treatment applied during preparation of the alloy. The superelasticity effect is sensitive to the ambient temperature of the material as reported in Dolce and Cardone [2001b]. For use in seismic applications the temperature T of the material must be such that $T > A_f$. Furthermore, the temperature range from A_f to the maximum temperature at which superelasticity occurs should be as wide as possible and centered near the average ambient service temperature of the SMA device.

3.4 Mechanical Properties of Shape Memory Alloys

In this section, the work of a number of authors to investigate the mechanical properties of Nitinol is summarized. In this context, the presentation focuses mainly on those aspects relevant to seismic engineering applications. Important contributions to provide informations on Nitinol specimen testing and on device design of for earthquake engineering applications are reported in particular in Dolce *et al.* [2000], Dolce *et al.* [2001], Dolce and Cardone [2001a], and Dolce and Cardone [2001b].

3.4.1 SMAs in Tension and Compression

The most common form of Nitinol material for seismic uses is either thin wires or bars in tension (see Wilson and Wesolowsky [2005]). wires may be wrapped repeatedly around posts in a device to increase the amount of material without increasing the overall size of

the device. Clark *et al.* [1995] examined a device with multiple loops of Nitinol wrapped around two cylindrical posts. The device was subjected to increasing cyclic (tension only) loads up to a strain of 8% at a rate of 50% per minute. Results showed that for increasing strain both the loading and unloading transformation yield stresses decrease (i.e., the loops shift downwards). The thickness of the hysteresis loop, however, remained constant across all tests.

This behavior was confirmed by Piedboeuf *et al.* [1998], who showed that after 200 cycles, the behavior had not noticeably deteriorated, as reported in Figure 3.5, although several initial cycles are needed to stabilize the superelastic effect. DesRoches *et al.* [2004] also
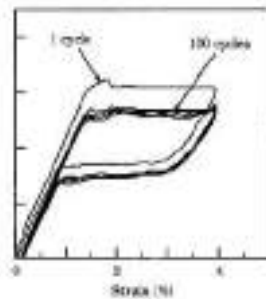
Figure 3.5. Stress-strain curve for multiple cycles of Nitinol wire showing eventual stabilization of superelastic hysteresis loops at stress levels lower than initial cycle (from Piedboeuf *et al.* [1998], stress scale not reported)

noted this behavior for both Nitinol wires and bars.

Krumme *et al.* [1995] tested superelastic Nitinol wires at strains up to 10% and achieved energy dissipation up to 17.2MN-m/m³ which is the energy dissipation normalized with respect to volume of Nitinol wire. The authors clearly pointed out the influence of the arrangement of the SMA elements on the energy dissipation characteristics of the device. Using pre-tensioned wires an almost rectangular hysteresis loop was obtained; without the pretensioning the hysteresis behavior was flag-shaped. Specially tailored hysteretic shapes, such as step-like behavior, were achieved using various kinematic mechanisms for engaging the Nitinol material.

Plietsch and Ehrlich [1997] tested thin, round, tapered Nitinol bars. They discovered that, in the superelastic state, the largest transformation strain in tension was roughly twice that in compression, while the corresponding stress in tension was only half that in compression. This asymmetry of tension/compression behavior was also noted for martensite specimens, but not for austenite specimens. The behavior of the three cases is shown in Figure 3.6. The authors concluded that the asymmetric behavior was caused by the selective formation of different stress-induced crystallographic states during tension and compression loading where, for a given strain, the volume fraction of martensite in the specimen is different under tension and compression. Similar behavior has also been

(a) austenite   (b) pseudoelastic   (c) martensite
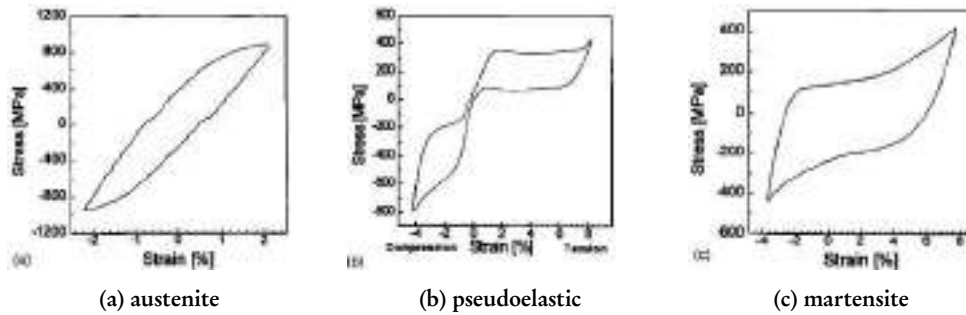
Figure 3.6. Tension-compression hysteresis for Nitinol (from Plietsch and Ehrlich [1997])

observed by Graesser and Cozzarelli [1991] and Liu *et al.* [1998].

Wilde *et al.* [1998] subjected thin, round, tapered, Nitinol bars to cyclic loads of increasing strain at a frequency of 0.001Hz (basically, statically applied loads). Similar differences in the compression/tension behavior were observed where the maximum stress in compression was almost twice that in tension.

Liu *et al.* [1999] tested a thin, round, fully martensitic Nitinol bar using cyclic loading at increasing strains. Once again, the maximum force attained in compression was approximately twice that attained in tension. At maximum strain values, the material appeared to undergo a cyclic hardening, while at zero strain it appeared to undergo a cyclic softening process. The martensitic composition of this bar produces the full hysteresis loop around the origin. This study further examined the effects of strain rate on the hysteretic properties of the martensitic bar. It was found that as the frequency of loading increased, the area of the hysteretic loops decreased slightly, but it was concluded that it had negligible effects on the damping capacity of the material. It was also observed that the temperature of the bar increased significantly with higher strain rates. The authors point out that there has been very little research in the area of exploring the cyclic properties of SMAs in their martensitic state.

Dolce and Cardone [2001b] have conducted extensive tension tests on superelastic austenitic Nitinol wires, focusing on the sensitivity of mechanical behavior to temperature, loading frequency, strain amplitude, and repeated cyclic loading. Figure 3.7 shows hysteresis results changing the loading frequency for slightly pretensioned (0.5%) wires. For the same case, secant stiffness, energy loss, and equivalent damping are reported in Figure 3.8. The energy loss per cycle is a function of the area enclosed by the hysteresis loop (see Chopra [2006]). The energy loss per unit weight of the SMA material is used as a measure of the effectiveness of energy dissipation (i.e., for use in comparing the effectiveness of various stress modes to optimize use of the SMA material). From Figure 3.7 it is obvious that the hysteretic behavior depends upon the frequency of loading and the strain amplitude. It is clear that there is a distinct difference in behavior between

(a) 0.02Hz   (b) 0.2Hz   (c) 2.0Hz
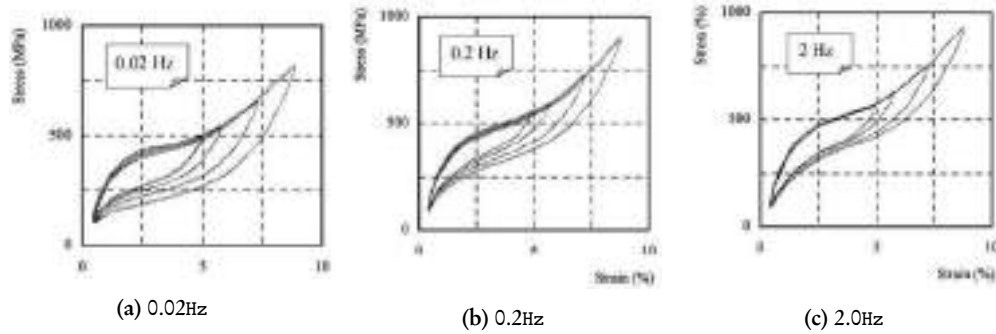
Figure 3.7. Cyclic tensile tests on pre-tensioned superelastic wires: hysteresis as a function of the loading frequency (from Dolce and Cardone [2001b])

the pseudostatic loading at 0.02Hz and the dynamic loading at the two higher frequencies. At higher rates of cyclic loading the hysteresis loops narrow (dissipated energy decreases) and translate upwards (secant stiffness increases), resulting in lower energy dissipation and equivalent damping, and higher peak stresses at all strain levels. Similar results have been reported by Krumme *et al.* [1995], Clark *et al.* [1995], Piedboeuf *et al.* [1998], Dolce *et al.* [2000], and DesRoches *et al.* [2004]. These effects are due to self-heating of the specimen because loading into the superelastic range is an exothermic process.

For all loading frequencies, as the strain amplitude is increased there is a downward migration of the unloading branch of the loop (although the loading branch is unaffected). While this provides increased energy dissipation at higher strains, the equivalent damping decreases because of the increase in displacement. Figure 3.8 shows that in the 0.24Hz frequency range, where most seismic applications occur, the cyclic behavior of austenite wires is basically insensitive to strain rate. Secant stiffness, energy loss, and equivalent damping are all essentially constant over this frequency range, with an equivalent damping in the rather narrow range of $5 - 7\%$. The mechanical behavior of previously cycled Nitinol is distinctly different from that of an uncycled specimen, as the hysteretic behavior of the material has been shown to stabilize with an increasing number of cycles. The most apparent change during the initial cyclic loading was a narrowing of the hysteresis loops, accompanied by a slight downward shift of the loading branch of the loops. Reductions in the energy dissipation and equivalent damping, and slight increases in residual displacements were observed during the first 10 cycles or so, but substantially less change occurred during subsequent cycling as the material stabilized. This emphasizes the importance of precycling SMA wires in order to establish stable hysteresis behavior.

Figure 3.9 shows the effect of strain amplitude for a pseudostatic loading at a rate of 0.01Hz at $30°C$ on austenite wire that was stabilized by precycling for 20 cycles at 6% strain. The energy loss increases more than linearly with increasing strain amplitudes because of the downward migration of the unloading portion of the hysteresis loops. The

(a) secant stiffness

(b) dissipated energy

(c) equivalent damping
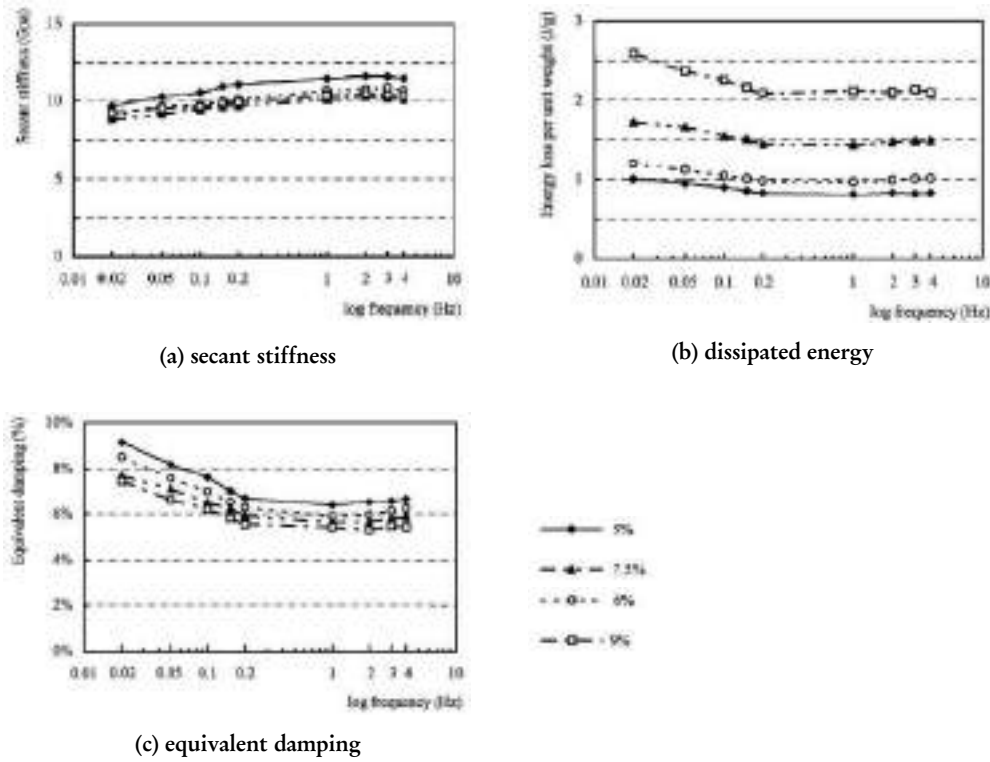
Figure 3.8. Cyclic tensile tests on pre-tensioned superelastic wires: mechanical behaviour as a function of strain amplitude (see legend) and frequency of loading (from Dolce and Cardone [2001b])

equivalent damping increases at low to moderate strain amplitudes but levels off at high strains because of the increase in secant stiffness as the SMA transforms from the austenite superelastic phase to the stiffer martensite phase. Figure 3.10a shows stress-strain curves after stabilization at various ambient temperatures for austenite wires in tension when $A_f = -5°C$. This gives superelastic temperatures that would be suitable for most seismic applications. For the $-10°C$ test, the residual strain ($\sim 1\%$) is due to the presence of some martensite at the end of the unloading (see Wilson and Wesolowsky [2005]). If the temperature of the specimen rises above $-5°C$, this residual strain will disappear as the remaining martensite is automatically transformed into austenite. As the temperature of the material increases above A_f, the shape and internal area of the superelastic loops remain consistent but there is a noticeable upward shift of the loop. Similar results were observed in Duerig et al. [1990], Clark et al. [1995], Piedboeuf et al. [1998], and Wolons et al. [1998]. This means that the stresses relevant to the start and finish of the transformations increase as shown in Figure 3.10b. In this case there is a linear increase in these stresses of about 6MPa/°C, although it is reported that this range can be rather

(a) hysteresis   (b) dissipation
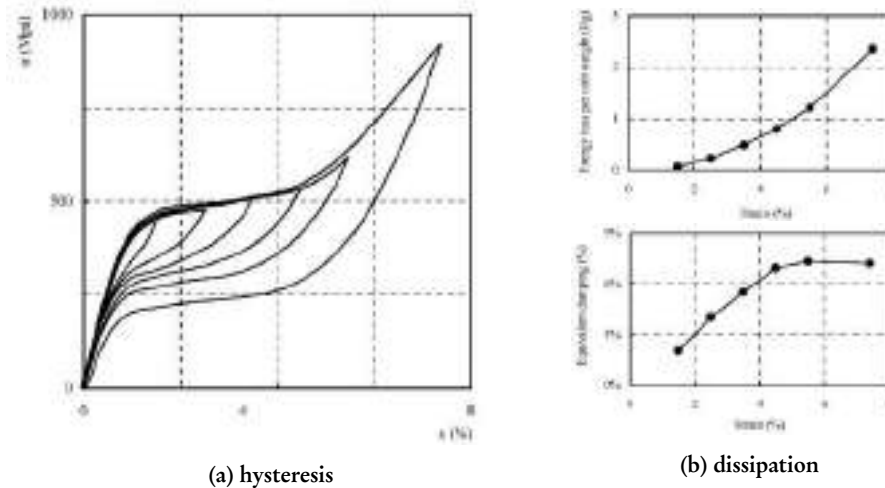
Figure 3.9. Cyclic loading and unloading tensile tests on austenite superelastic wire: influence of strain amplitude (from Dolce and Cardone [2001b])

wide, from ~ 3 to ~ 20MPa/$^\circ C$ (see Dolce and Cardone [2001b]). The transformation temperatures can be determined from the intersection of their respective lines with the horizontal axis in Figure 3.10b. The lines in stress-temperature plot in Figure 3.10b are boundaries of phase changes in the SMA material under uniaxial tension. Figure 3.10c shows that the energy dissipation is nearly constant across the temperature range. However, because the secant stiffness increases linearly with increasing temperature there is a consequent linear decrease in equivalent damping in Figure 3.10d from 13% to 8% as the temperature rises from $-10^\circ C$ to $40^\circ C$. This behavior becomes important in seismic applications if a SMA device is subjected to a wide range of ambient temperatures (Wilson and Wesolowsky [2005]).

3.4.2   SMAs in Torsion

Dolce and Cardone [2001a] performed a series of sinusoidal torsional tests on hexagonal, round, and U-shaped bars (both austenite and martensite), ranging from 6.7mm to 30mm in diameter. The tests were conducted at 0.01, 0.1, 0.5, and 1.0Hz for up to 1650 cycles of loading and with tangential strains up to 24% (a twist of 22°). The mechanical behavior of the bars was found to be independent of the frequency of loading in the case of martensite, and slightly dependent on it for the austenite bars. An important finding was that the equivalent damping capacity of the martensite bars was approximately three times higher than that of austenite bars (17% vs. 5%), although the austenite bars offered the advantage of low residual displacements (10% of maximum displacement) upon unloading. Cyclic behavior of the bars was demonstrated to be highly repeatable

(a) stress strain curves at different temperatures   (b) transformation stresses

(c) energy dissipation   (d) equivalent damping
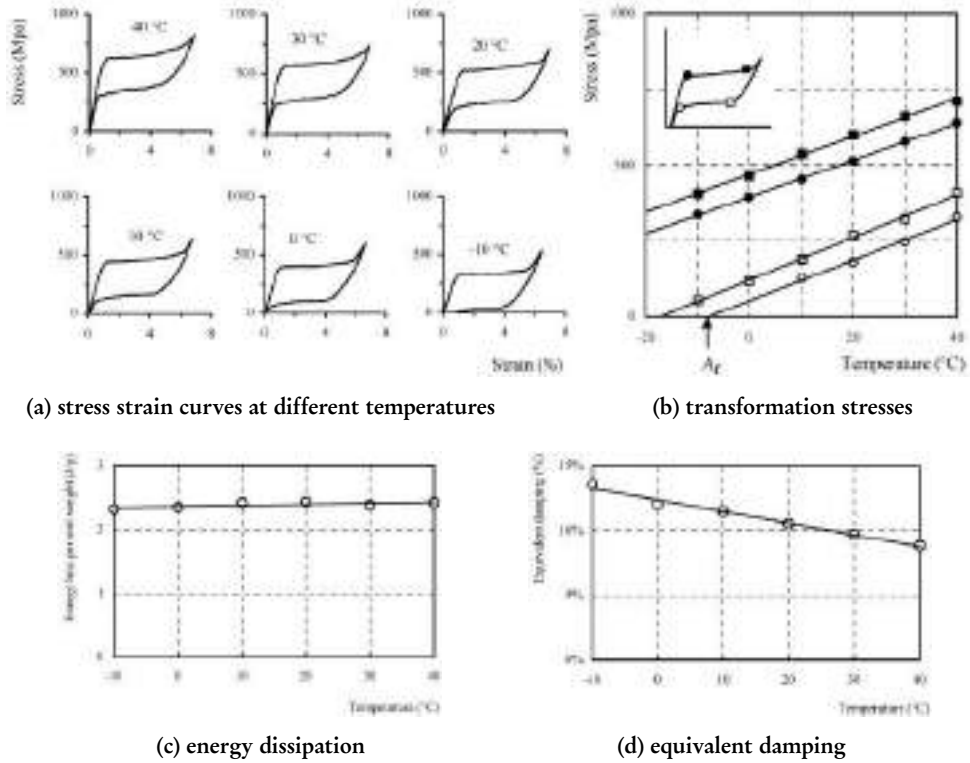
Figure 3.10. Austenite wire in tension: results as a function of temperature (from Dolce and Cardone [2001b])

after a few initial cycles of stabilization. The fatigue resistance of both types of bars was found to be more than adequate for even multiple seismic events. Finite element simulations showed that the distribution of strain-hardening in the most highly strained parts of the bars favored an increase in strain in the parts that were initially less strained. This clearly indicates that under torsional loading the entire volume of the material does not undergo an $A \rightarrow M$ transformation all at once; rather, there is a propagation of the formation of martensite through the specimen, driven by the distribution of torsional and strain-hardening-induced stresses. While it was concluded that SMA bars subjected to torsion show great potential as components in seismic resistant devices, Dolce *et al.* [2000] comment that torsional devices require quite a large mechanism to transform linear displacement into rotation, and large lengths to adequately clamp the bars; issues that do not affect tension and bending devices to the same extent. For this reason, torsional devices may not be as practical to implement as devices that use other modes of deformation.

3.5 PRINCIPLES AND EXAMPLES OF SHAPE MEMORY ALLOY DEVICE DESIGN

As recognized in Wilson and Wesolowsky [2005], there have been relatively few attempts to design seismic response modification devices that incorporate SMAs into their components. The SMA device design is characterized by relative complexity involved in producing SMAs, hence most current implementation schemes use the material in its simplest forms, i.e. wires or bars, often directly attached between structural components. There have been, however, few attempts to create a *device* that uses SMAs as a component therein. The one designed by Dolce et al. [2000] is similar to that devised by Krumme et al. [1995] and is further explained in the present section.

Dolce et al. [2000] have designed and tested reduced and full scale prototype Nitinol-based devices; braces for frame structures, and sliding isolation devices for buildings and bridges. Their full-scale brace was designed for a maximum force of 200kN and 20mm displacement; the sliding isolation system was designed for up to 600kN force and 180mm displacement.

Mechanical details of the designed device will be described in the following sections. In this context, the main interest is to focus the design philosophy as presented in Dolce et al. [2000]. Idealized depictions of the stress-strain behavior of two SMA element groups and

(a) recentering group   (b) dissipating group   (c) complete device
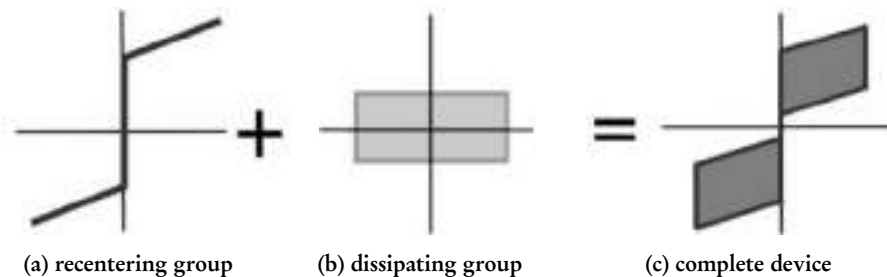
Figure 3.11. **Idealized behaviour of the two functional groups of SMA elements (from Dolce et al. [2000])**

of their possible global response are shown in Figure 3.11. They consist of:

1. a self-centering group of single-acting pre-tensioned superelastic austenitic wires (on their own these have relatively low energy dissipation);

2. an energy dissipating group of either martensitic bars in bending, or double-acting pre-tensioned superelastic austenitic wires.

The point is that in Dolce et al. [2000] two functional groups of SMA material are proposed and they are designed to be working in parallel to optimize the structural goals. An appealing feature of using these two functional groups is the possibility to obtain a wide variety of cyclic behavior with the same device simply by varying the arrangement of the SMA components.

The behavior of a device with only the re-centering elements is shown in Figure 3.11a, with zero displacement at the end of the loading. The ordinate from which the yielding branch starts in Figure 3.11a is the pre-tensioning force; the force available to re-center the structural system. This might typically be selected as the force corresponding to about 4% strain, a value that is in about the mid-range of the superelastic strain region for Nitinol. The slope of the yielding branch is controlled by the stiffness of the wires. As this device uses only single-acting pre-tensioned austenitic wire, the hysteresis loops are narrow, and the damping is rather low, at about $4 - 6\%$, independent of cyclic strain amplitude and pretension force.

Figure 3.11b shows behavior of a device with only the energy-dissipating elements. Large energy dissipation is possible with this device, but this is accompanied by large residual displacement at the end of loading. The size of the hysteresis loop is controlled by the number of elements in the dissipating group. Dolce *et al.* [2000] found that a configuration of this device with double-acting pre-tensioned austenite wires had an equivalent damping that ranged from about 15% at 1% strain to about 40% at 9% strain.

This remarkable increase over the damping in device of group 1 has been achieved solely by using the pre-tensioned austenite wires in a double-acting manner. Furthermore, the device exhibited a softening effect that provided an upper limit to force as strains were increased, a feature that can control the force imparted to structural elements. Another configuration of device of group 2, using martensite bars in bending, produced an equivalent damping that decreased from about 20% at small strains to about 10% at large strains. This device exhibited a hardening effect that can be used to control displacements. The above two functional groups can be combined to create a hybrid device, shown in Figure 3.11c, that produces double flag-shaped hysteresis loops providing both enhanced energy dissipation and re-centering capabilities. The two functional groups must be calibrated to optimize the performance of the device. For example, to provide complete re-centering, the pre-tensioning force of group 1 elements must be greater than the force in the dissipating group at zero displacement. A device in which both groups are pre-tensioned superelastic austenitic wires was found to have the superior performance, with equivalent damping ranging from about 10% at low strains to about 18% at total strain of about 9%. For a device with martensitic bars, the equivalent damping was about half of these values. In addition, the high initial stiffness for small displacements means that the device will not be sensitive to wind or other service loads. Testing repeated on this device after 20 days produced essentially identical hysteresis loops to the original tests, indicating that relaxation of the pre-tensioned wires was virtually nonexistent.

3.6 Seismic Applications of Shape Memory Alloys

Nitinol was not seriously considered for seismic applications until the end of the 1980s, when the first articles began to appear exploring its cyclic properties. Currently, applications of SMAs in seismic engineering have been generally at the theoretical and

laboratory study level, paving the way for their implementation in real structures (Wilson and Wesolowsky [2005]). Within this context, selected current applications of SMAs for bridges and buildings are described. No attempt was made to present a comprehensive or exhaustive list of the extensive literature pertaining the Nitinol applications in civil engineering. The presentation here focuses on those applications considered more relevant to provide a general idea of the state-of-the art in the SMA device utilization.

Two different categories are considered inhere, even if the distinction is not always straightforward. Some examples of SMA applications to control vibrations and dissipate energy in fixed base structures are reported in Section 3.6.1. The most relevant examples of structural isolation systems using SMA either for energy dissipation or recentering effect are then summarized in Section 3.6.2.

3.6.1   SMAs in Additional Damping Systems

Clark *et al.* [1995] and Higashino *et al.* [1996] presented a study of analytical results of using a SMA device for control of a multistory building. Devices, consisting of multiple loops of SMA wire, were incorporated into eccentric bracing at each level, as shown Figure 3.12. The model was subjected to a Northridge ground motion record scaled to 0.2g, 0.4g,
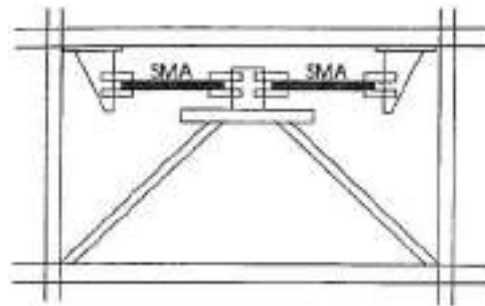
Figure 3.12. Schematic of a bay modeled with two isolation devices composed of multiple loops of Nitinol wire wrapped around two posts (from Higashino *et al.* [1996])

and 0.6g (like other studies, the SMA devices were modeled using bilinear elastoplastic behavior). It was found that interstory drift decreased by almost 50% for each of the three levels of input, while the first-floor interstory drift was reduced even further. The energy absorbed by the frame was reduced to about 15% compared to the frame without the devices. The one noted drawback was the increase in acceleration, as high as 200% in some stories, attributed to an increase in initial stiffness due to the austenite phase of the hysteretic behavior. Although initially all of the SMA devices were designed to be identical, it was discovered that the most effective control strategy was to use devices on the first floor having twice the yield stress of those on the other floors. Using this strategy, the devices on the first five floors were effective in dissipating energy through hysteretic

behavior, but there was almost no energy dissipation at the top floor, even for the 0.6g ground motion.

DesRoches and Liu [1999] tried SMAs as hinge restrainers between frames from a multiple frame bridge. Each frame was modeled as a single-degree-of-freedom system; pounding of the frames was also taken into account. A uniaxial trilinear tension model of a wire Nitinol device was used to connect the two frames. The behavior of the frames was compared to behavior exhibited by traditional bilinear devices. It was found that SMA devices provided considerable displacement reductions compared to the same structures that were non-restrained or restrained using more traditional means, while providing similar maximum forces transmitted between frames.
Subsequently, DesRoches and Andrawes [2002] and DesRoches and Delemont [2002] investigated the use of SMA restrainer bars to reduce excessive movement at abutments and intermediate deck joints. Full-scale tests of SMA bars were used to establish force-displacement characteristics, which were then used to model the SMA restrainers using finite element program. The SMA bars were found to be effective in reducing the relative displacement at the piers and abutments, including for near-field ground motions. Considering the same restraining system configurations and their potentials in seismic response, in Andrawes and DesRoches [2007] the effect of variability in SMA hysteretic properties was explored. The results showed that in general SMAs are relatively stable in their effectiveness despite slightly variations in hysteretic properties.

Tirelli and Mascelloni [2000] describe shake-table tests on replications of historical unreinforced masonry walls retrofitted with SMA cross-bracing tendons attached to the face of the wall. The unreinforced wall collapsed during testing, whereas the retrofitted wall sustained only minor damage, even at a peak ground acceleration 60% larger than that used for the unreinforced wall.

One of the few actual implementations of an SMA device in a full scale seismic retrofit is described by Forni *et al.* [1996a], Forni *et al.* [1996b], Castellano *et al.* [2001], and Indirli *et al.* [2001] who report on the retrofit of a bell tower in Italy. The 18.5m tower was built in 1302, and substantially modified in the 1800s, mostly by adding masonry infills and increasing its height. The masonry was unreinforced and of poor quality, making it especially vulnerable to earthquake damage. In October 1996 the tower was seriously damaged by a $M_L = 4.8$ earthquake. The repair of the tower consisted of both conventional and innovative measures. The conventional retrofit included repairing and replacing masonry and floor slabs. An innovative retrofit scheme, shown in Figure 3.13, was adopted to increase the flexural stability of the tower. A full tower-height prestressing steel bar was installed in each inside corner of the tower (thus sparing the outside masonry any modification), anchored to the foundation and the roof. A superelastic SMA device was installed at the third-floor level in each bar. Each device consisted of 60 1mm diameter Nitinol wires 300mm long. The wires were post-tensioned to 20kN into the superelastic region, resulting in a controlled constant compressive force being applied to the masonry
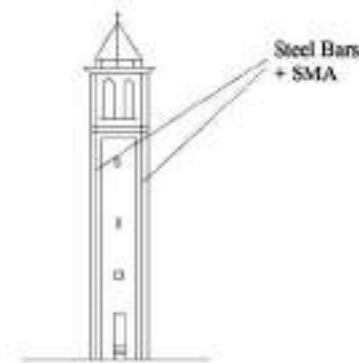
Figure 3.13. San Giorgio bell tower retrofit using four pretensioned steel tie bars and superelastic SMA devices in the inside corners of the San Giorgio bell tower, anchored to the foundation and the roof (from Indirli *et al.* [2001])

that prevented tensile stresses from developing during an earthquake. This concept was verified using a finite element model of the tower and a record from the 1996 earthquake. In this case the finite element model considered the behavior of the SMA devices using a simple elastoplastic stress-strain model. Through use of this model the post-tensioning was optimized so that the maximum horizontal displacement at the top of the tower would be limited to about 12mm. Pre- and post-retrofit vibration tests indicated that the tower had been stiffened and mode shape behavior changed by the retrofit, including elimination of a torsional mode that was responsible for some of the damage. The retrofit was completed in September 1999. In June 2000 a similar magnitude earthquake ($M_L = 4.5$) occurred at the same epicenter but the tower was not damaged. Although this is the best documented verification of the seismic performance of a full-scale installation of SMA devices to date, it is not clear whether the SMA devices contributed to the improved performance of the tower or whether the use of prestressing rods alone would have provided similar performance. Unfortunately, the study authors do not address this aspect.

Castellano *et al.* [2001] report on the validation and application of techniques for the restoration of cultural heritage buildings. This program focuses on masonry buildings retrofitted with SMA devices, one of which was the San Giorgio bell tower. In addition to the method described for the tower, the installation of steel bars and dampers within columns and floor slabs is also presented. The retrofit schemes were modeled with finite elements and verified with shake table testing of scale models. Similar surveys have been completed by Mazzolani and Mandara [2002].

Leon *et al.* [2001] report on a steel beam-column connection that was augmented by Nitinol tendons, as shown in Figure 3.14. Full-scale beam-column connections were tested with and without the tendon devices. The initial set of tests was halted because the shear tab weld fractured on each end. Since the tendons were designed to act in the
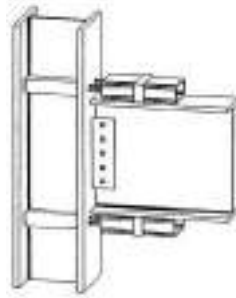
Figure 3.14. Steel beam-column connection using shape memory alloy tendons (from Leon *et al.* [2001])

shape memory mode (purely martensitic behavior), the tendons were heated upon the end of cycling to restore the connection to its original configuration. After repairing and reinforcing the shear welds, the specimens were retested. The tendons showed that at repeated 4% cyclic strains, the hysteretic loops were nearly identical, leading to the conclusion that the SMA connection was able to undergo repeated large deformation without strength degradation. Further, the hysteretic loops of the second set of test were nearly identical to those of the first set, indicating that the tendons were able to recover their properties following heating to restore their original shape.

Corbi [2003] proposed using the SMA tendon associated low level part of a multi-story shear frame. The numerical simulation showed that the SMA tendon isolation device decisively improves the dynamic response capacity of the structures either in terms of response reduction or re-centering capacity.

In the work by Han *et al.* [2003] eight damper devices made of the SMA wires and steel wires were diagonally installed in a two-story steel frame structure. Both experimental analysis and numerical verification were conducted to demonstrate the effectiveness of the SMA dampers on vibration reduction. Experimental comparisons of the frame responses with and without dampers showed that the vibration of the controlled frame decayed very much faster than that of the uncontrolled frame. The simulation has demonstrated that the largest displacement of the controlled frame is only 15% of that of the uncontrolled case.

The combined steel SMA type braces were also adopted by Tamai and Kitagawa [2002] in their seismic resistance devices as shown in Figure 3.15. The authors also proposed an exposed type column base with SMA anchorage for seismic resistance. The SMA anchorages are made of Nitinol SMA rods and steel bars. The results obtained from the pulsating tension loading tests and numerical simulation of the SMA rods, have shown that the SMA wires were very effective in dissipating energy and reducing the building vibration under severe seismic ground motion. In Tamai *et al.* [2003], they reported the pulsating tension loading tests on the exposed-type column base with SMA anchorages. It
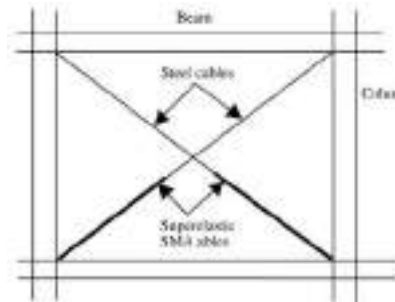
Figure 3.15. Schematic of the SMA braces for frame structures proposed in Tamai and Kitagawa [2002] **(from** Song *et al.* [2006])

was observed that, contrary to the accumulated residual strain of ordinary anchorages, the SMA anchorages can recover their original shape after cyclic loadings and therefore their resisting performance remains the same to prevent plastic deformation and damage in the structural columns.

Auricchio *et al.* [2006a] assessed the seismic performance of a three- and a six-storey steel frame equipped with different bracing configurations. The bracing systems consist of traditional buckling-restrained steel braces and superelastic Nitinol braces. The new bracing system was proved to be effective in reducing earthquake induced vibrations. In this context, an investigation on the numerical and experimental damping properties of Nitinol was performed and it is reported in Auricchio *et al.* [2006b].

In McCormick *et al.* [2006] superelastic Nitinol shape wires and bars were studied to determine their damping and recentering capability for applications in the structural control of buildings subjected to earthquake loadings. It was shown that large diameters bars perform as well as wire specimens used in non civil engineering applications.

Torra *et al.* [2007] presented additional damping applications based on SMA technology on small residential buildings. The authors proposed an optimization design methodology for the dampers and analyzed the performances through numerical investigation. The simulation proved that the SMA dampers are capable of reducing the maximum oscillation amplitude induced by particular ground motion by a factor 2 and that they dissipate 50% of the energy transmitted to the structure.

Ma and Cho [2008] presented a new SMA-based damper. It is shown in Figure 3.16 and it mainly consisting of pre-tensioned superelastic SMA wires and two precompressed springs, which function as energy dissipation and re-centring group, respectively (as proposed in Dolce *et al.* [2000]). The pre-tensioned SMA wires and roller system offered the damper an enhanced stroke and high-energy dissipation capacity, while the precompressed springs supplied the damper with an expected restoring force. With maintaining the precompression imposed on the springs equal to the initial reaction force gap for two groups of SMA wire looped at a minor move of middle anchor, the damper

Figure 3.16. Schematic diagram of the SMA damper sectional view (figure reprinted from Ma and Cho [2008])

showed both good energy dissipation capacity and full re-centring capability. The results demonstrated that the equivalent damping ratio of 12%, stoke of 30mm and full re-centring capability can be achieved in a 1m long SMA damper.

3.6.2   SMAs in Seismic Isolation

Krumme *et al.* [1995] examined the performance of a sliding SMA device, in which resistance to sliding was achieved by opposing pairs of Nitinol tension elements. The

Figure 3.17. Sliding isolation system proposed by Krumme *et al.* [1995] (from Wilson and Wesolowsky [2005])

device, illustrated in Figure 3.17, was designed with a force capacity of 53.4kN, stroke of 75mm, mass of 13.6kg, and plan dimensions of 250 and 1000mm. The performance of this device was examined for use in analytical studies on a 1970s era non-ductile concrete frame building retrofit. The stress-strain behavior was modeled using finite elements and the structural performance was examined under both non-isolated and isolated conditions. Although the details of the study are sparse, the results for the non-isolated building demonstrated that severe structural damage was likely to occur from a moderate or severe earthquake, as evidenced by the soft story in the first floor and large rotational demands on the first-story columns. The isolated case showed marked improvement with interstory drifts and column rotational demands being reduced to acceptable levels.
The device in Figure 3.17 is also similar in concept to one proposed by Sweeney and Hayes [1995], which was modeled for application in the retrofit of 1950s-era non-ductile concrete frame building.

   Inaudi and Kelly [1994] reported on experimental tests of a tuned mass damper (TMD) connected to the floor of a multistory structure through SMAs. The TMD consisted of a

mass sliding on a frictionless bearing oriented along the longitudinal horizontal axis of the floor slab. Nitinol wire loops were mounted transversely to the axis of the sliding mass, providing both damping and restoring forces for the TMD. The ends of the SMA wires were pin connected to both the frame and the mass, in order to eliminate bending in the wires. Various initial tension forces and yield tensions were considered. All configurations provided displacement reductions in the system, and it was concluded that the most significant improvement in displacement control was obtained when the prestress tension was set to tune the apparent frequency of the TMD to the first natural frequency of the isolated structure.

Bondonet and Filiatrault [1996] conducted an analytic study using a two degree of freedom lumped mass model of a bridge pier/superstructure system with a single SMA device installed between the pier and the superstructure. The pier was modeled using a conventional linear spring and damper system. The Graesser and Cozzarelli [1991] approach was used to model the superelastic behavior. The model was subjected to earthquake ground motion records characteristic of the seismic design level for Vancouver (peak ground acceleration 0.21g) and the deck-level accelerations for a fixed and isolated deck were compared. Several variations of device parameters were examined, providing a large range of acceleration and displacement behavior. It was found that deck-level accelerations could be reduced by up to 90% by the SMA device, and the self-centering characteristics resulted in negligible residual displacements. As the SMA yield force was increased, both the maximum and residual displacements between the deck and the pier decreased, particularly for short isolated periods, and the maximum acceleration of the deck increased substantially. Increasing the effective isolation period increased both the maximum and residual displacements between deck and pier, and reduced the deck accelerations. Increasing stiffness in the superelastic region decreased displacements and increased accelerations. The design of a SMA based isolation bearing was proposed by the same authors in Bondonet and Filiatrault [1997].

Wilde et al. [2000] performed a study similar to that of Bondonet and Filiatrault [1996], where a pier was modeled with an isolated mass representing the deck. Two cases were considered: the first one considering a rubber bearing and a SMA device, and the second one having a laminated lead-rubber bearing (LRB) with a displacement restrainer. The SMA was modeled with identical behavior for both tension and compression. The bridge was subjected to two versions of a Kobe ground motion (PGA scaled to 0.4g and 0.6g), and to sinusoidal excitation to represent the effects of wind and traffic loadings. The relative displacement reductions for the harmonic load resulted considerable, while they were less pronounced for the earthquake loading. The force transmitted to the pier was generally higher for the SMA system. During the transitions from the superelastic to the martensite phases of the SMA system at high strains, the bridge deck experienced considerably higher accelerations (peak values $\sim$ 200% higher). These were not seen for the LRB system.

Dolce *et al.* [2000] present a study on testing and application of two full-scale isolation
SMA prototype devices, shown in Figure 3.18, that have full re-centering and some energy
dissipation capabilities, as well as high resistance to large strain cycle fatigue. The devices
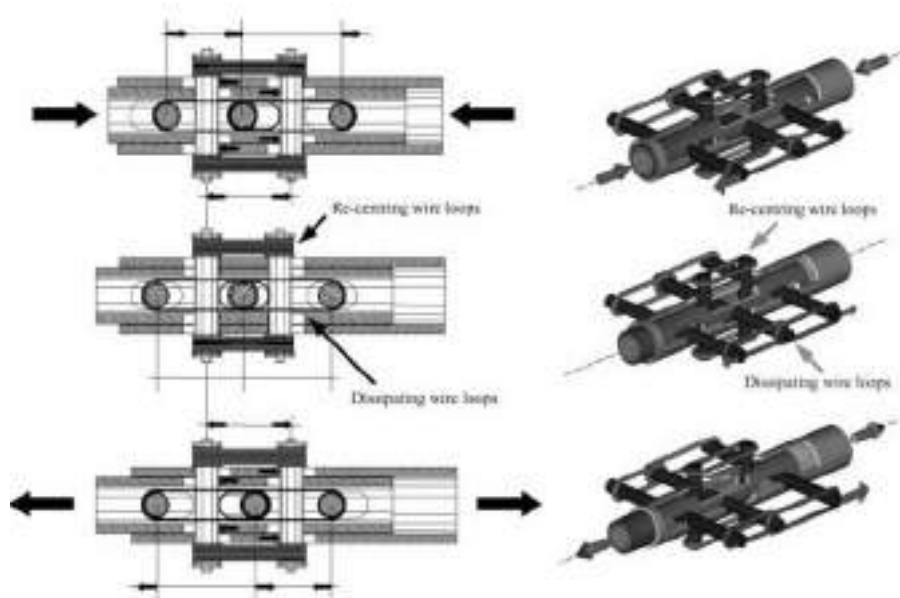
**Figure 3.18. Functional scheme of SMA device including both re-centering and dissipating groups of
shape memory alloy wires (from Dolce *et al.* [2000])**

have two separate groups of SMA wires, one intended to re-center the device, and the
other to dissipate energy, as discussed earlier in Section 3.5 and reported in Figure 3.11.
The applicability of these devices was demonstrated on a small building in Italy, where
a variation of the device was employed that was intended to produce only re-centering
behavior. The three-story concrete frame building was equipped with re-centering SMA
devices, as well as steel-Teflon sliding bearings. The top of the building was displaced
140mm, then suddenly released. After only two oscillations, the building regained its
original position, with no residual displacement.
A full suitability of the devices and a great potential of SMAs in the passive seismic control
of civil structures resulted from the study. From Dolce *et al.* [2000], SMA resulted to
be characterized by great versatility, i.e. the possibility to obtain a wide range of cyclic
behaviors, from fully re-centering to highly dissipating, by simply varying the number
and/or the characteristics of the SMA components, thus allowing to calibrate the shape
of the loops according to any particular individual need. By properly calibrating the
number of SMA elements and their pre-stress level, a double flag shaped hysteresis loops
was obtained, taking advantage of:

- self-centering capability, with also the possibility to provide a supplemental re-centering force to bring back the structural system at its initial configuration when the earthquake is over, even in presence of parasite non conservative forces external to the devices, such as friction of bearing or plastic forces of structural elements;

- high stiffness for small displacements, to avoid the structure to be moved by wind or small tremors;

- good energy dissipation capability, to reduce accelerations and displacements caused by an earthquake;

- further important properties common to all types of devices based on Nitinol shape memory alloys like fatigue resistance, long-term reliability, high durability, no aging degradation, substantial independence from oscillation frequency in the range of interest for seismic applications, rather limited sensitivity to temperature compatible with the typical applications of civil engineering.

Re-centering seismic isolation devices gained the best mechanical characteristics of both quasi elastic devices (e.g. rubber isolators) and elasto-plastic devices (e.g. steel hysteretic dampers). On the one hand, they recovered the initial position of the structure, with a good control of displacements, on the other hand, they put a threshold to the force transmitted to the superstructure, thus well controlling forces. The full possibility of designing the mechanical behavior, thanks to the modularity of the two groups of elements governing the two aspects (re-centering and energy dissipation), permitted to calibrate the desired features and for the specific needs.

Bruno and Valente [2002] presented a numerical investigation where SMAs were implemented in isolator devices and in bracing. The results were compared to those of non-isolated structures, as well as ones that were braced with steel members and isolated with rubber bearings. Structural and nonstructural damage was lower for the isolation schemes using SMAs than for all other situations.

Khan *et al.* [2004] analytically studied the effects of *vertical* SMA springs to isolate a single-degree-of-freedom system from a ground excitation simulated by a shake table. The idea of using SMA spring to control vibration was proposed originally by Liang and Rogers [1997], even if for general application without any reference to seismic design. In Khan *et al.* [2004] was shown that the vibration isolation depended on the relative displacement of SMA springs, because small displacements did not trigger the stress-induced martensitic transformation. Moreover, the SMA springs achieved the best isolation effect only when the system vibrated at a frequency near its resonance frequency and under higher loading levels. Figure 3.19 shows the experimental setup for the SMA spring isolation system developed by Lagoudas *et al.* [2004], on which the experiments were conducted by the same research group. It was shown that the significant impact of
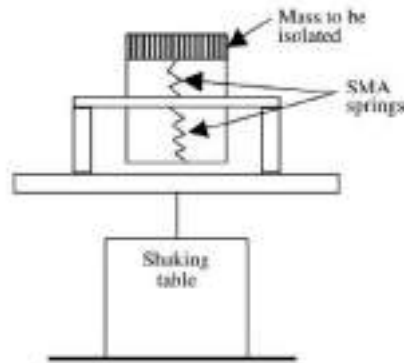
Figure 3.19. Schematic of the SMA spring isolation device as suggested in Khan *et al.* [2004] and Lagoudas *et al.* [2004] (from Song *et al.* [2006])

SMA springs on the dynamic response of the vibration system lied on two aspects: greatly altering the system resonance frequency and resonance amplitude.

Choi *et al.* [2006] proposed a new concept of an isolation device in which shape memory alloy wires were incorporated in an elastomeric bearing, as reported in Figure 3.20. A three-span continuous steel bridge was used for seismic analyses to compare the
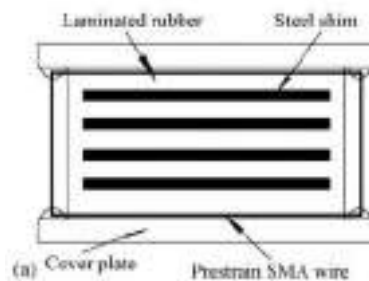
Figure 3.20. Schematic of the SMA rubber isolation device (from Choi *et al.* [2006])

performance of lead-rubber and the proposed bearings. The proposed bearings turned out to limit the deck relative displacement effectively with strong ground motions and recover the original undeformed shape.

Dolce *et al.* [2007b] and Cardone *et al.* [2003], presented the results from an extensive program of shaking table tests on innovative (SMA based) and traditional isolation systems. The SMA isolation device was composed by a flat sliding bearing and lateral Nitinol restrainer. The basic idea was described in Cardone *et al.* [2003] and further developments were presented also in Dolce *et al.* [2007a] after Dolce *et al.* [2005]. In Figure 3.21

the schematic of the bearing isolation system is reported. The conclusion of the shake
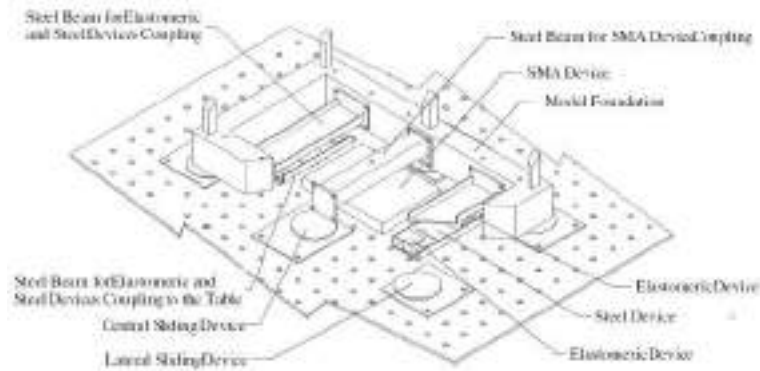
Figure 3.21. Sliding bearing SMA isolation system (figure reprinted from Cardone *et al.* [2003])

table tests, referring in particular to the latest investigation, was that different isolation systems or different characteristics of the same type of isolation system lead to different performances of the isolated structure. There is no optimal system and no isolated period which can minimize, at the same time, base displacement, base shear (i.e. interstorey drifts) and floor accelerations. In particular re centering SMA based devices were characterized by displacements and base shear maximum demands compatible with the design ones. However, high floor accelerations were recorded, especially at low seismic intensities.
In the same investigation framework, Cardone *et al.* [2009] proposed simplified methods for the design of bridges equipped with strongly nonlinear isolation systems considering also the Nitinol device.

Casciati *et al.* [2007] and Casciati and Hamdaoui [2008] proposed a new base isolation device consists of two disks, one vertical cylinder with an upper enlargement sustained by three horizontal cantilevers, and at least three inclined shape memory alloy (SMA) bars, as shown in Figure 3.22. The SMA bars were intended to limit the relative motion between the base and the superstructure, to dissipate energy by their super-elastic constitutive law and to guarantee the re-centring of the device. To verify the expected performance, a prototype was built and tested under sinusoidal waves of displacement of increasing frequency with different amplitudes. Results showed a highly dissipative but non recentering force displacement behavior.

Different papers (see Liu *et al.* [2008a], Liu *et al.* [2008b], and Liu *et al.* [2008c]) described the results of an investigation campaign on a new type of SMA wire-laminated rubber combined bearings. They were produced by fixing SMA wire diagonally around conventional laminated rubber bearings, basically following the same principle with respect to the design presented by Choi *et al.* [2006]. Through shake table tests, analysis was made on effects of isolation system on energy dissipation, equivalent horizontal
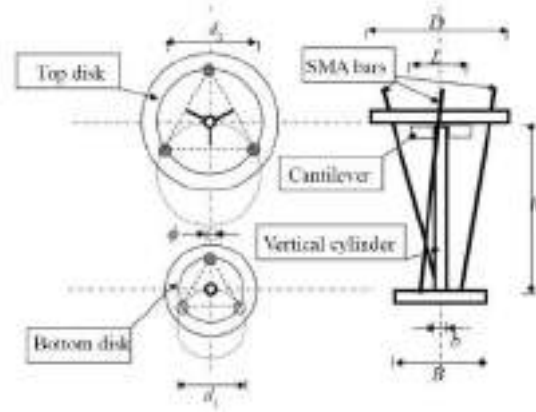
Figure 3.22. Schematic of the SMA isolation device (from Casciati *et al.* [2007])

stiffness, maximum restoring force, and equivalent damping ratio. The authors recognized favorable conditions for the seismic response of the proposed device.

A hybrid base isolation system that is composed of linear elastomeric bearings, friction-pendulum bearings, shape memory alloy wires, and magneto-rheological dampers was proposed for the mitigation of seismic motions in Shook *et al.* [2008]. Results showed that the proposed superelastic semi-active base isolation system can reduce base drifts by 18% and maintain favorable superstructure response.

4. Feasibility Assessment of Superelastic Bearing System for Seismic Isolation

4.1 INTRODUCTION

The objective of this chapter is to investigate the feasibility of a new seismic isolation device conception based on the superelastic effect given by shape memory alloys. In this context, the term *shape memory alloys device* refers to a bearing systems characterized by a non-linear horizontal force-displacement relation which can be described by a *flag-shape* hysteresis. An isolation bearing system based on a SMA superelastic effect is intended to provide the nonlinear properties of yielding devices, limiting the induced seismic force and providing additional damping characteristics, together with recentering properties to reduce or eliminate the cumulative damage. Nevertheless, flag-shape hysteresis is characterized by much less energy dissipation with respect to other isolation technologies, therefore its effectiveness has to be investigated.

Thus, in the preset chapter the dynamic response of a proposed innovative SMA isolation devices is compared with equivalent traditional bearing (lead rubber bearing, *LRB*) response. Dynamic time history analyses are used to evaluate its effectiveness in reaching the structural design goals, and to compare it with traditional isolation devices.

Regarding the chapter structure, in Section 4.2 and Section 4.3 the actual lead rubber bearing proposed as a reference parameter and the innovative superelastic device are respectively introduced. Section 4.4 contains the device comparison as a function of their theoretical hysteresis dissipation. Time history analysis procedure and results are then reported: Section 4.5 describes the modeling issues and the analysis procedure, Section 4.6 contains results from rigid superstructure analysis, and Section 4.7 presents results from flexible superstructure analysis. Parametric investigation on the effectiveness of flag-shaped model in affecting the time history results is then reported in Section 4.8. Finally, main conclusions are listed in Section 4.9.

4.2 REFERENCE LEAD RUBBER ISOLATION DEVICE

To define the main features, underline the drawbacks, and eventually be able to examine the advantages of an isolation system characterized by a flag-shaped lateral force-lateral displacement relation, a response comparison is performed with respect to an *equivalent*

Table 4.1. Nominal design properties of reference lead rubber bearing diameter 500mm (courtesy of *AGOM International srl*)

LRB 500 (elastoplastic model)		
yielding shear	V_y	**147 kN**
design shear	V_d	**262 kN**
yielding displacement	u_y	**17.5 mm**
design displacement	u_d	**162 mm**
initial stiffness	k	**8.4 kN/mm**
second stiffness	rk	**0.8 kN/mm**
secant stiffness	k_e	**1.62 kN/mm**
seismic vertical load	W	**1653 kN**

lead-rubber bearing system. Obviously superelastic device is characterized by a different force-displacement relation with respect to traditional isolation bearings, but the models have the same yielding and design forces, and the same yielding and design displacements. The concept of equivalence therefore involves that the two different nonlinear hystereses are characterized by the same initial and second stiffness and the same yielding force and strength. Hence, effective periods are the same too and from a direct-displacement based design point of view the only difference between the traditional bearing and the actual isolation device is the hysteretic energy dissipation (see Priestley *et al.* [2007]).
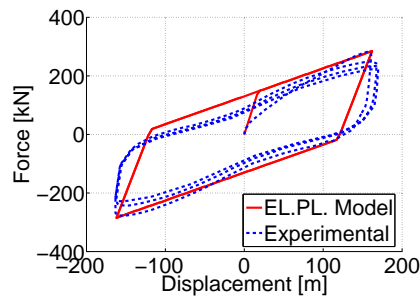
Figure 4.1. Isolator LRB 500 force-displacement relations experimental and modeling comparison (from Attanasi *et al.* [2009b], experimental data and model parameters have been provided by *AGOM International srl*)

The isolator we consider as a reference is an actual lead rubber bearing, which has been fully characterized experimentally. It is produced by *AGOM International srl* and the manufacturer provides parameters for the design in terms of elastoplastic hysteresis, as listed in Table 4.1. The force-displacement relation of the model and the comparison with experimental test results is shown in Figure 4.1. Elastoplastic model is clearly an

approximation of the real behavior of the isolator. In particular, the comparison with the experimental results shows that the elastoplastic model does not estimate the initial stiffness nor the degradation very well. However, for the representation of the general characteristics of the devices, the adopted model is acceptable, being exact in terms of secant stiffness at the design displacement and giving a good estimation of the hysteretic energy dissipated and of residual displacements. The lead core contribution provides a large and highly dissipating hysteresis, characterized by an equivalent hysteretic damping equal to 28% according to the hysteresis area based approach (see Chopra [2006]). The isolator device is compatible with a seismic demand represented by Eurocode 8 (*EC8*, see CEN [2004]) type 1 spectra relative to a $PGA = 0.25$g and a soil type C.

4.3 SUPERELASTIC ISOLATION DEVICE

The assumed superelastic isolation device shear force lateral displacement relation is reported in Figure 4.2. The key parameters characterizing the nonlinear behavior of the
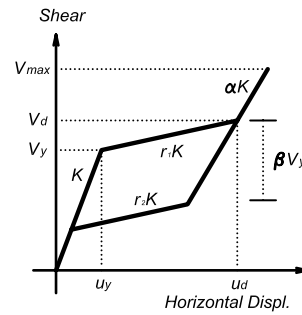
Figure 4.2. SMA superelastic isolation device force-displacement relation

device are:

- K: initial lateral stiffness for the system, relative to the first shape memory alloy stiffness contribution and, eventually, to the other stiffness sources;

- V_y: lateral force corresponding to the reaching of the device linear limit; it can be interpreted as the shear that produces the initial transformation in the shape memory alloys;

- u_y: lateral displacement corresponding to reaching of the linear limit of the force-displacement relation for the device;

- V_d: lateral force corresponding to reaching of the end of plateau limit; it can be interpreted as the shear at the end of transformation in the shape memory alloys;

- u_d: lateral displacement corresponding to reaching of the end of plateau limit;

- $r_1 K$: lateral stiffness for the system after reaching the shape memory alloy elastic limit loading, taking also in account, eventually, the other stiffness sources; r_1 is the fraction of the loading second stiffness respect the first one;

- αK: lateral stiffness for the system after reaching the shape memory alloy second elastic limit at the end of the phase transformation; α is the fraction of the unloading second stiffness respect to the initial one;

- $r_2 K$: lateral stiffness for the system after reaching the shape memory alloy elastic limit unloading, taking also in account, eventually, the other stiffness sources; r_2 is the fraction of the unloading second stiffness respect to the initial one;

- βV_y: the lateral force difference between the level of force at which the first transformation (when it is loaded) occurs and the level of force at which the second transformation (when it is unloaded) occurs; β is the fraction of the V_y lateral force;

- V_{max}: the maximum lateral force which the device can stand without breaking.

The device we consider behaves in the same way if subjected both to positive and to negative shear, which implies the force-displacement relation is symmetric wit respect to the origin.

Even if the shear force-lateral displacement relation is similar to superelastic behavior described in Section 3.4.1, thus in theory it could be easily provided by a Nitinol device working in tension and compression, no real design has been performed in this part of the work. We just assume to be able to design and manufacture a SMA bearing based on the superelastic effect for the horizontal force-displacement relation. At this first stage, since the feasibility of the conception is still being investigated, the device has been defined just in terms of the hysteretic relationship, without evaluating the technology able to provide that hysteresis.

Hence, the superelastic isolation device is characterized by the hysteresis in Figure 4.2 assuming for the shear and displacement (and hence stiffness) parameters the same values reported in Table 4.1. Moreover, the superelastic device has the same stiffness for loading and unloading in the flag-shape plateau, thus $r_1 = r_2 = r$, and $\alpha = 1$, which means the final stiffness is the same as the initial one. A large ductility capability in the flag-plateau is assumed, so that the final hardening occurs far away from the displacement range considered in the design. Finally, the *dissipation* capability of the flag-shape hysteresis is represented by the β parameter, which is a measure of the ratio of dissipation, and several dissipation values have been considered in the investigation.

4.4   EQUIVALENT DAMPING APPROACH REDUCTION FACTOR EVALUATION

For the design purpose, according to Direct Displacement Based Design (*DDBD*) approach by Priestley *et al.* [2007], the structure is modeled with an equivalent single degree of

freedom system (*SDOF*). This is characterized by an equivalent mass (m_e) lumped at an equivalent height (h_e), as shown in Figure 4.3.

The procedure is based on the assumption that a nonlinear system can be represented
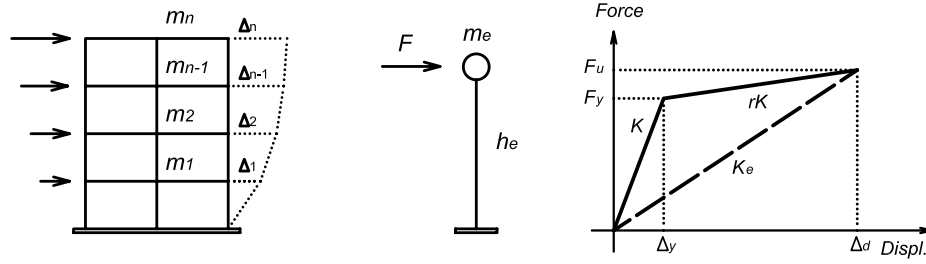
Figure 4.3. MDOF structure – equivalent SDOF and effective stiffness concept for a bilinear force displacement relation envelope

by an *equivalent* linear system having a stiffness k_e equal to the secant stiffness to the design displacement of the original system, plus an additional damping component, the hysteretic damping, which contributes with the viscous damping to define the *equivalent damping* ξ_e. The equivalence concept is shown in Figure 4.4, which reproduces the original and the equivalent models for an elasto-plastic hysteresis system. The equivalent damping

(a) nonlinear system   (b) equivalent system
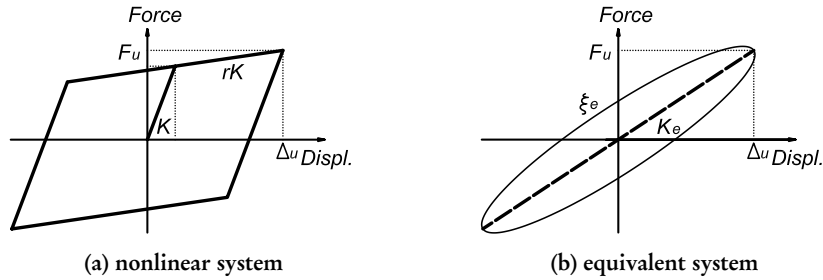
Figure 4.4. Equivalent system concept: an original nonlinear system is modeled through a linear system plus an additional damping amount

component ξ_e is a measure of the energy dissipated by the structure per cycle and depends on the area of the hysteresis loop together with the elastic viscous damping. Hence, it is a function of the hysteresis relation shape and of the ductility demand.

The equivalent linear system approach was originally proposed in Jacobsen [1930] and Jacobsen [1960]. Plenty of investigations have been performed on the topic for its importance in design modeling. Between the most important contributions the work by Rosenblueth and Herrera [1964], Jennings [1968], and Shibata and Sozen [1976] can

be mentioned as first attempts for its practical application. An exhaustive overview on the state of art for the equivalent system modeling and recent provisions for its application to DDBD are then proposed in Grant *et al.* [2005] and Dwairi *et al.* [2007].

In the present investigation, damping modeling and estimation is a key point to evaluate the design and the response of the ideal superelastic isolation system and comparison with actual LRB. Moreover, we consider two systems with the same secant stiffness, because the design displacement and shear are the same, and initial and second stiffness are also the same, thus the most important difference is given by the equivalent damping ratio. The two force-displacement relations are shown in Figure 4.5.

(a) lead rubber bearing   (b) superelastic system
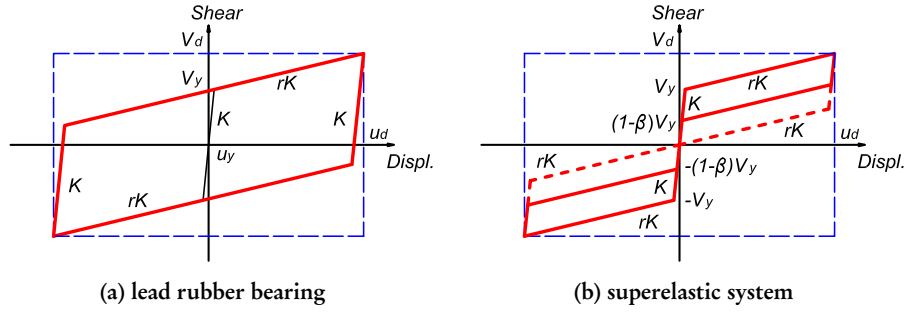
Figure 4.5. Theoretical hysteretic comparison between elastoplastic (LRB) and flag-shape (SMA) devices (for the flag-shaped model the limit case for $\beta = 1$ is reported in dotted line)

Following a hysteretic area based approach referring to the two models, LRB and SMA device, an estimation of the equivalent viscous damping of the system is given by (see Chopra [2006]):

$$\xi_{hyst} = \frac{2}{\pi} \frac{A_1}{A_2} \tag{4.1}$$

in which A_1 is the area of the hysteresis skeleton curve and A_2 is the area of the rectangle enveloping the hysteresis relation, as represented in Figure 4.5. The damping coefficient for the two hysteresis relations is a function of the displacement ductility μ, as follows.

- elastoplastic model (see Grant *et al.* [2005]):

$$\xi_{hystEP} = \frac{2}{\pi} \frac{(\mu-1)(1-r)}{\mu(1+r\mu-r)} \tag{4.2}$$

- flag-shape model (see Attanasi *et al.* [2009b]):

$$\xi_{hystFS} = \frac{1}{\pi} \frac{\beta(\mu-1)(1-r)}{\mu(1+r\mu-r)} \tag{4.3}$$

From the comparison between Equation (4.2) and Equation (4.3), the ratio of the two expressions is a function of β if all the other parameters are kept constant. For $\beta = 1$, which is the case of the dotted line hysteresis in Figure 4.5, Equation (4.3) gives a damping ratio which is one half of the value given by Equation (4.2). This is shown in Figure 4.6a,

(a) hysteretic damping
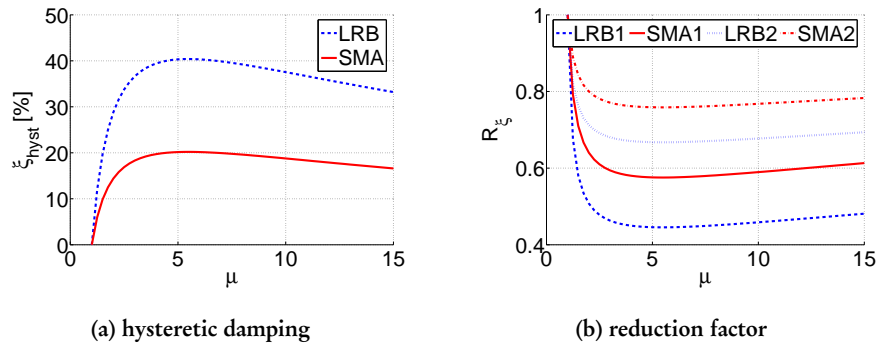
(b) reduction factor

Figure 4.6. Hysteretic damping ratio comparison and equivalent damping reduction factor comparison [the far field values are named (1) while near field are named (2) in the legend] for elastoplastic and flag-shape model considering $r = 5\%$ and $\beta = 1$

in which for a constant r value and considering $\beta = 1$, the hysteretic damping component is plotted according to the Equation (4.2) and Equation (4.3) as a function of displacement ductility. Using the equivalent damping to estimate a reduction coefficient for the design spectra function of the seismic source distance with respect to the design site (following the approach proposed in Priestley *et al.* [2007]), the reduction factors R_ξ are computed and plotted in Figure 4.6b (see Attanasi *et al.* [2009a]). Examining the comparison between a flag-shape model and an elastoplastic model equivalent damping estimation, SMA device results in a smaller energy dissipation with respect to LRB. Hence, if the equivalent damping concept is exact, the flag shaped constitutive relation would significantly reduce the advantages of isolation.

The approach described in this section leads to the conclusion that an isolation device based on a SMA technology and flag-shape hysteresis is always supposed to be less favorable in terms of displacement and force demand with respect to a similar system based on elastoplastic hysteresis. This is because the damping reduction factor is much lower for SMA flag-shape force displacement relation with respect to LRB elastoplastic hysteresis. Even if the SMA devices were characterized by the largest dissipation parameter β, their reduction factor would be one half of the LRB one. For a more reasonable value of $\beta = 0.5$ the SMA reduction factor would be one fourth on the LRB one.

Some researches have been performed looking at the problem of estimating the peak response considering the viscous damping computation together with the secant stiffness

and several conclusions were that this estimation approach is not very accurate (see Christopoulos *et al.* [2002], Priestley and Grant [2005], and Grant *et al.* [2005]). For these reasons, the approximate computation of the equivalent damping reduction factor may not be sufficient to conclude that a superelastic device is not a suitable solution for base isolation applications.

4.5   Seismic Response Evaluation of Isolation Devices

To investigate the response of a shape memory alloy isolator device in more depth and to compare it with the response of an equivalent classical lead rubber bearing, a series of time history analyses are performed. Direct computation of the response and evaluation of envelopes is the best way also to evaluate the accuracy of the equivalent damping reduction factor approach for a large ductility flag-shaped force displacement relation.

4.5.1   Numerical Models for the Isolators

The displacement based design procedure models the structure considering an equivalent linear system characterized by the secant stiffness. If we assume that the design has been performed correctly and all the nonlinear phenomena take place in the isolation level, we focus on its contribution to the overall structural response (Priestley *et al.* [2007]).
To model the isolation device a first option is to use a linear elastic stiffness to the design point, while a more detailed model is to use the real nonlinear hysteresis of the device. In this study case, both the actual LRB elastoplastic and the SMA flag-shaped models are characterized by the same secant stiffness, because of the assumptions of Section 4.2 and Section 4.3.
The response in terms of shear and displacement demands of the nonlinear systems is supposed to be smaller than the one of the equivalent linear secant system because of the contribution of the hysteretic dissipation. In concept the hysteretic damping contribution should be representative of this dissipation and the ratio between the linear and the nonlinear system demands is supposed to be estimated considering the reduction factor R_ξ. To evaluate this assumption, time history analyses considering three models for the isolator devices are performed:

- elasto-plastic model (Figure 4.7a). The elastoplastic model is representative of the actual lead rubber bearing device.

- flag-shape model (Figure 4.7b). The flag-shape model reproduces the shear-horizontal displacement relation of the shape memory alloy device. We target a device that performs like the real LRB system in the sense of equivalent shear and displacement capacity and initial and second stiffness.

- linear elastic model (Figure 4.7c). Given the design displacement u_d and the design shear V_d, which are the same for the previous models, we carry out the analysis of

the equivalent linear system, considering a secant stiffness.

(a) LRB system   (b) SMA system   (c) ELAS system
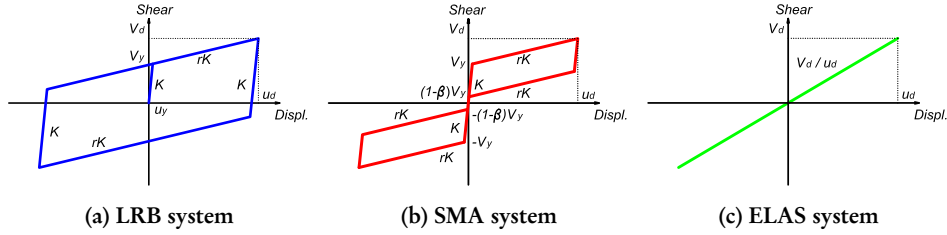
Figure 4.7. Base shear horizontal displacement models for the isolation device response comparison

Regarding the elastic damping component in the nonlinear elements, a constant damping proportional to the initial stiffness is used to have the same energy dissipation in the three models if the velocity histories are the same.

$$c = 2\xi_{SEC}\sqrt{k_e\,\frac{W}{g}} = 2\xi_{NL}\sqrt{k\,\frac{W}{g}} \quad \Rightarrow \quad \xi_{NL} = \xi_{SEC}\sqrt{\frac{k_e}{k}} \tag{4.4}$$

Given that the damping ratio of the linear elastic system is assumed to be $\xi_{SEC} = 5\%$, according to Equation (4.4), to guarantee a constant damping c, the coefficient results $\xi_{NL} = 2.2\%$. This last is used for the elastoplastic and flag-shape models given that the initial stiffness k is the same.

This simplified approach is not based on a damping coefficient which changes with the tangent stiffness, as recently suggested in Petrini *et al.* [2008] and which it is supposed to be a more consistent approach. Nevertheless, result differences are small and this approach has been adopted because evaluating the hysteretic dissipation through a constant elastic damping seems more rational.

4.5.2   Evaluation of Different Flag-Shape Dissipation Capability Ratios

The flag-shape hysteresis that can be obtained by the SMA superelastic effect (as shown is Figure 4.2) usually does not show a dissipation coefficient as large as the largest one ($\beta \simeq 1$). The superelastic hysteresis is characterized by a maximum dissipation parameter of the order of $\beta \simeq 0.7$, and this is a function of the material, so the value can be smaller. Even if an high dissipation flag shaped hysteresis is supposed to be preferable, we want to investigate different dissipation coefficient responses, eventually closer to actual shape memory alloys superelastic effect parameters.

For this purpose, more analyses were performed to evaluate the system response if the β factor is smaller, including zero hysteretic dissipation as a limiting case (see also Priestley and Tao [1993]). Six cases are considered, $\beta = 0.95$, $\beta = 0.75$, $\beta = 0.55$, $\beta = 0.35$, $\beta = 0.15$, and $\beta = 0.0$ (nonlinear elastic behavior), as shown in Figure 4.8.
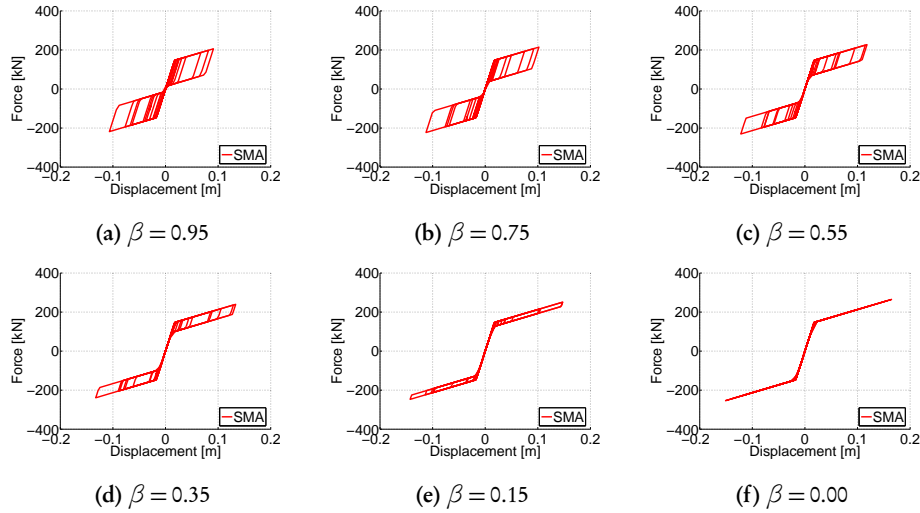
Figure 4.8. Flag-shape hysteresis considering different dissipation parameters used in the analyses (from THA g.m. #3)

4.5.3   Time History Analysis Ground Motion Set

Several ground motions are used in the analyses in order to consider the variability of the seismic input. The basic case is the original design spectra for the LRB isolator, which is the EC8 type 1 $PGA = 0.25\,g$ soil C, as reported in Section 4.2.

Given that the effective period of the reference system is about 2 seconds, the corner period at 2 seconds prescribed by the EC8 is not suitable for the investigation. Hence, remaining consistent with the EC8 expressions for the spectra computation, the corner period of the design spectra has been extended up to 4 seconds (see Attanasi *et al.* [2009b]). A first set is composed by seven artificial generated ground motions compatible with the design spectra. Those spectra were created from random seeds using a research oriented program (Carr [2001]), considering as a input the design spectra. In addition, recorded but scaled ground motions for seven near fault ground motions were selected from the database SAC [1997]. The aim is to evaluate the effects in the hysteretic response of ground motions with velocity pulses. Elastic displacement spectra for the artificial and natural ground motions are shown in Figure 4.9 and the pseudo-acceleration spectra are in Figure 4.10. Additional informations on the ground motion properties used in the present chapter investigation may be found in Attanasi [2008].

(a) artificial

(b) natural
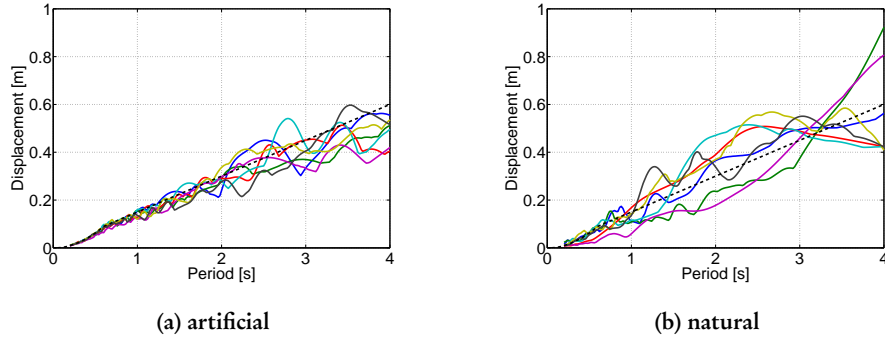
Figure 4.9. Displacement elastic 5% damping spectra for compatible artificial and near fault ground motions compared with design spectra

(a) artificial

(b) natural
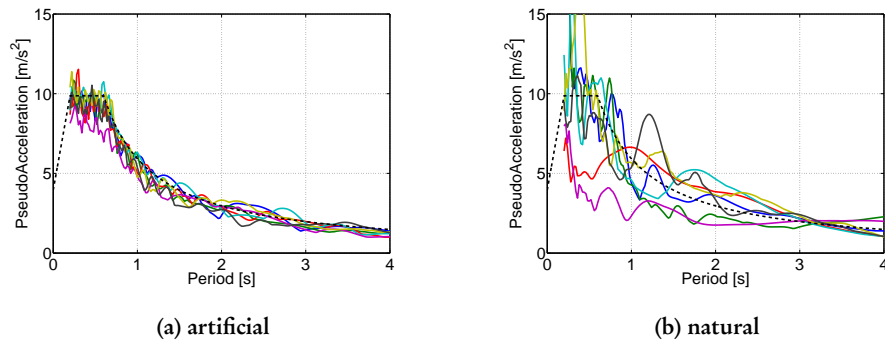
Figure 4.10. Pseudo acceleration elastic 5% damping spectra for compatible artificial and near fault ground motions compared with design spectra

4.6 RIGID SUPERSTRUCTURE TIME HISTORY ANALYSES RESULTS

The design and analysis of an isolated structure can be performed assuming that the superstructure is rigid and therefore the base shear - lateral displacement of the structure is given by the shear displacement relation of the isolation system. This means that all the displacement occurs only at the isolation level, as reported in model in Figure 4.11.
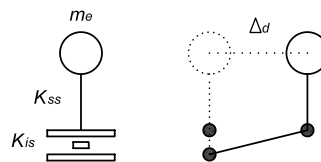
Figure 4.11. Base isolated rigid structure equivalent displacement profile

To assess the effects of isolation, the envelopes of displacement and force in the nonlinear system are normalized with respect to the corresponding maximum demands in the linear secant system. Results are reported respectively in Figure 4.12 and Figure 4.13, being these ratios the reduction factors between the linear and nonlinear system due to hysteretic dissipation. The mean values for all the hysteresis considered are then shown in Figure 4.14. The input energy is expected to change from an isolation system to another too, therefore the mean value of the input and absorbed energy together with the percentage of input energy dissipated is shown in Figure 4.16.

(a) $\beta = (0.95, 0.75,$ and $0.55)$ (b) $\beta = (0.35, 0.15,$ and $0.00)$
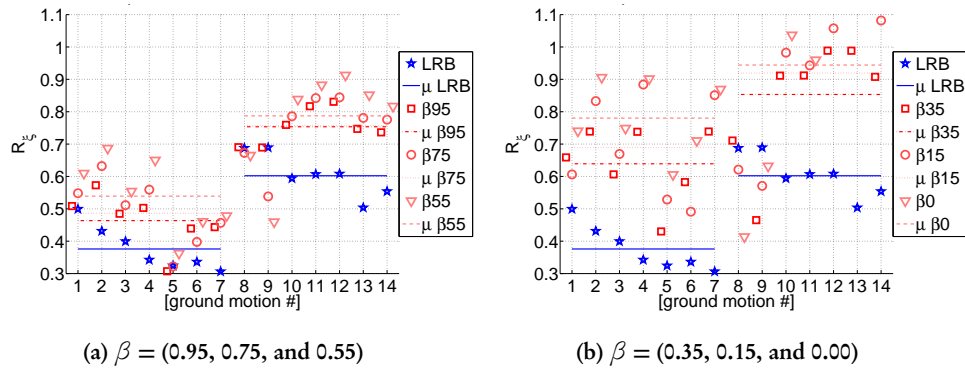
Figure 4.12. Displacement demand values for elastoplastic and different flag-shaped dissipation parameters normalized with respect to linear elastic system response for artificial (1:7) and for near fault (8:14) ground motions

(a) $\beta = (0.95, 0.75,$ and $0.55)$ (b) $\beta = (0.35, 0.15,$ and $0.00)$
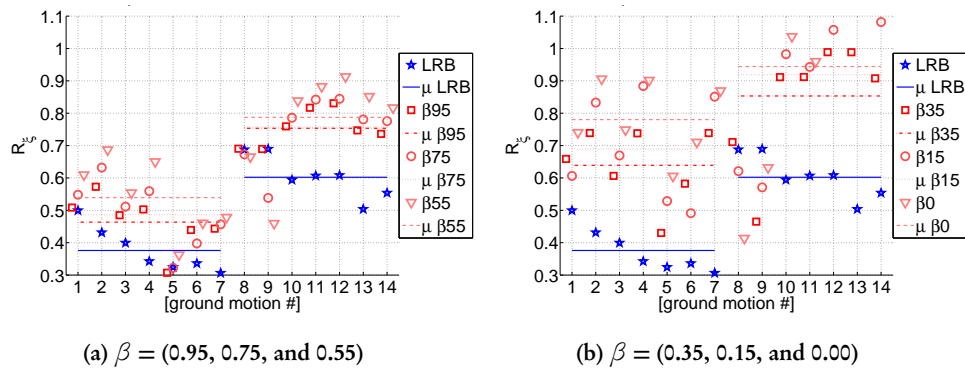
Figure 4.13. Shear force demand values for elastoplastic and different flag-shaped dissipation parameters normalized with respect to linear elastic system response for artificial (1:7) and for near fault (8:14) ground motions

(a) displacement   (b) shear force
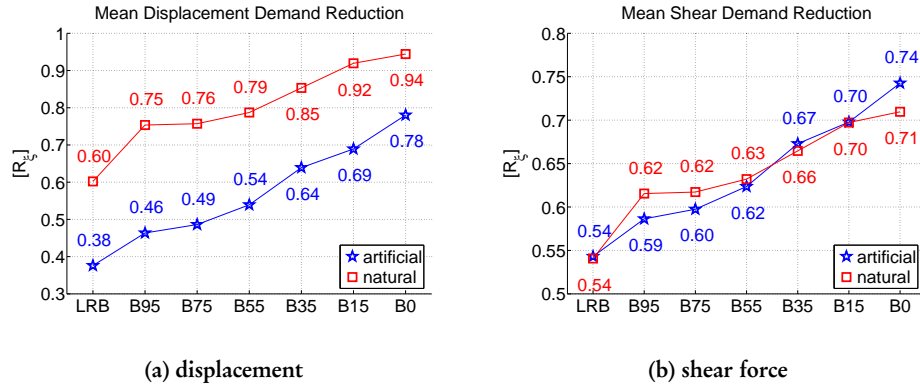
Figure 4.14. Displacement and shear mean reduction factors over the 14 ground motions for the considered hysteresis, listed in the horizontal axis

The most important conclusion is that differences between the lead rubber bearing elastoplastic model and shape memory alloy flag-shape model are small when compared with the linear elastic displacement and force demand, especially for the medium high flag-shape model dissipation case. Even changing significantly the dissipation factor for a very narrow flag-shape hysteresis does not change the demand quantities as much as would be expected by an area based approach reduction factor computation.

Considering the shear demand comparison in Figure 4.14b, it is clear that similarities appear to be more important than differences. In terms of displacement demand in Figure 4.14a, differences of large dissipation capability flag-shape model and elastoplastic model are not large, even if the strong reduction of dissipation increases the system demand, producing in some near fault events a displacement even larger than the one from linear elastic system.

(a) displacement comparison   (b) LRB residuals (artificial g.m.s)   (c) LRB residuals(natural g.m.s)
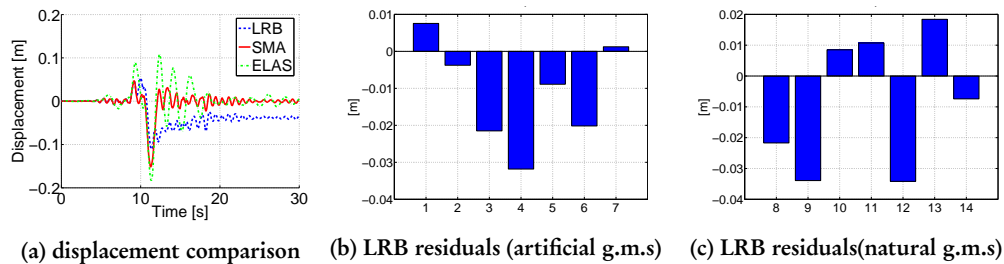
Figure 4.15. Displacement-time response from an analysis of the three systems and LRB model residual displacements in artificial and near-fault ground motions

Another critical issue for isolation bearings concerns the residual displacements. These

are very undesirable in an isolation system device since they lead to the needing of re-centering of the system after the seismic event. Of course the problem strongly affects an elastoplastic model, especially with a pulse-like near fault seismic input. A major advantage of a SMA is the re-centering capability. An example of displacement time history comparison is reported in Figure 4.15a. Figure 4.15b and Figure 4.15c show that lead rubber bearing system is characterized by residuals in all the ground motions.

Finally, considering the energy absorbed, the elastoplastic model has about the 80% of the input energy dissipated through the hysteretic relation; in the flag-shape model the percentage is around the 70% for the large medium dissipation capabilities. As a

(a) mean input and absorbed   (b) absorbed over input
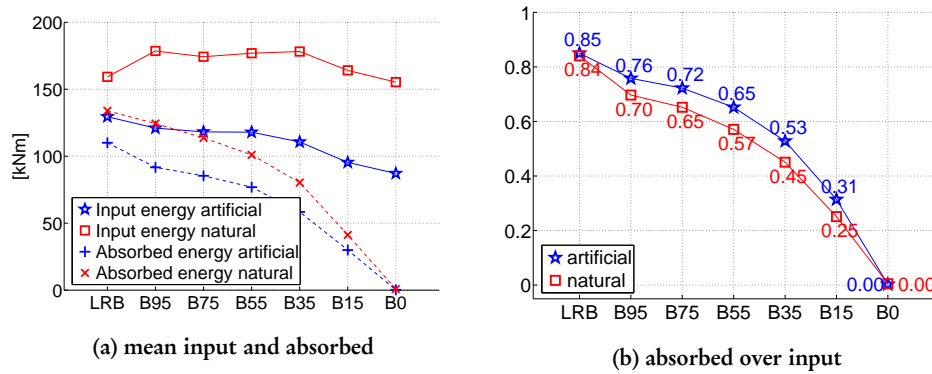
Figure 4.16. Mean energy balance results showing the amount of input energy absorbed by the systems (4.16a) and ratio between the total input energy and the absorbed one (4.16b) for all the considered hysteresis, listed in the horizontal axis

general conclusion, the response of an idealized SDOF isolation system based on flag-shape hysteresis considering different dissipations is quite good and comparable to the lead rubber bearing response for a dissipation value in the range $\beta = 50\%$.

4.7   FLEXIBLE SUPERSTRUCTURE TIME HISTORY ANALYSIS RESULTS

We also perform time history analysis comparisons considering flexible superstructure to investigate the isolation system effectiveness, as shown in Figure 4.17. The global design displacement is the sum of the isolation system displacement and of the superstructure displacement:

$$\Delta_{d,sys} = \Delta_{d,is} + \Delta_{d,ss} \tag{4.5}$$

Since the superstructure response is supposed to be elastic, displacements of the structural members are not critical. Hence $\Delta_{d,is} > \Delta_{d,ss}$. To have a superstructure deformation contribution significative, we look for a structure in which the ratio between the isolated fundamental period and the not isolated one is quite small, in the order of two.
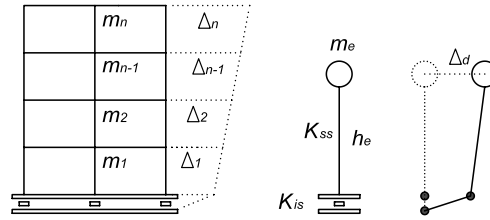
Figure 4.17. Base isolated flexible structure equivalent displacement profile and SDOF parameters

4.7.1   Analyzed Structure

We consider a simplified design procedure for a base isolated building to get a structural configuration compatible with the original isolator characteristics. The response of the five bay, three story plane frame shown in Figure 4.18 is investigated. The isolation system
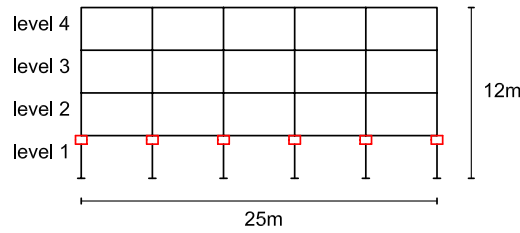
Figure 4.18. Geometric outline of the frame system we are considering for the flexible superstructure approach

is located at the first level, so the first floor is fixed with the foundations and the first slab is rigid and isolated from the first level of columns and foundations. The design philosophy is to isolate the upper stories, which are supposed to resist the seismic event elastically and to design the first storey to resist to the maximum load without plastic damage, assuming rigid foundations. There are two column sections, one for the first story and a second for the upper floors. The beam section is constant in all the levels and it is small to provide the required flexibility to the superstructure. The geometric properties are summarized in Table 4.2. The isolation system is modeled as a spring element, like in the previous SDOF system analysis. The mass is lumped at the beam-column connections, computed based on the tributary areas of the floors.

The non-isolated structure has a fundamental mode of vibration period of 1.07s, and a summary of the non-isolated building modal is reported in Table 4.3. Modeling the isolation system with an equivalent linear secant stiffness using parameters in Table 4.1, the resulting modal properties are reported in Table 4.4. The fundamental period elongation from the non-isolated to the isolated case is about the 100%, so the superstructure flexibility is supposed to be significant and has to be taken into account, as

Table 4.2. Frame model geometric properties

Test Frame Properties					
Materials			1st level Columns		
Conc. Elastic Mod.	E	25000 MPa	Depth	d_{1c}	0.80 m
Conc. Poisson Mod.	v	0.4	Width	w_{1c}	0.80 m
Beams			upper level Columns		
Depth	d_b	0.40 m	Depth	d_{uc}	0.40 m
Width	w_b	0.25 m	Width	w_{uc}	0.30 m

Table 4.3. Modal properties from fixed structure analysis

Not Isolated Modal Frame Properties		
Mode Number	Vibration Period	Participating Mass
1	1.07s	69%
2	0.33s	10%
3	0.18s	3%
4	0.09s	16%

Table 4.4. Modal properties from isolated structure analysis

Isolated Modal Frame Properties		
Mode Number	Vibration Period	Participating Mass
1	2.14s	98.3%
2	0.58s	1.6%

suggested in Priestley *et al.* [2007]. Before conducting the time history analyses, the system force-deformation behavior is investigated through a pushover analysis. The applied load pattern is constant with the height of the building to represent the isolated structure first mode of vibration. The system capacity curve, governed by the isolation properties, is the same for both the lead rubber and the shape memory alloy isolation bearings. The base shear and the first level displacement relationship account for the behavior of the isolation system alone. Comparing the base shear with the roof level displacement curve, we investigate the flexibility of the superstructure. The results of pushover analysis and comparison are shown in Figure 4.19.
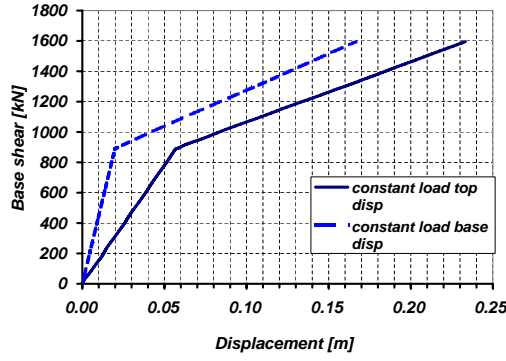
Figure 4.19. Capacity curve from pushover analysis of the structure; an uniform lateral load has been considered and two displacement control points have been taken into account, one at the top of the first level and one at the roof level of the superstructure

4.7.2 System Modeling Issues

The time history analyses uses the same ground motions we used previously and the same force-displacement relations for the isolators. An important issue in this context is the global structural damping evaluation. We want to take into account explicitly in the equation of motion only the viscous component of the isolation devices. The model in this case is more complex with respect to the SDOF because of the isolation system and superstructure contributions. The superstructure is assumed to have a 5% equivalent viscous damping in all vibration modes.

To compare the results, we want to take into account the same damping contribution in all the isolated structural models referring to the system secant stiffness to the design displacement. Given the initial stiffness of the nonlinear models, a 5% ratio of the secant stiffness is equivalent to 2.2% based on the initial stiffness of the isolation device. The isolator damping ratio to be combined with the super structure damping, which is done using a weighted sum of the flexibility sources in the structural first mode, leads to:

$$\xi_{e,sys} = \frac{\xi_{e,is}\Delta_{d,is} + \xi_{e,ss}\Delta_{d,ss}}{\Delta_{d,is} + \Delta_{d,ss}} = \frac{\xi_{e,is}D_{max\ base} + \xi_{e,ss}D_{max\ ss}}{D_{max\ top}} =$$
$$= \frac{2.2 \cdot 0.167 + 5 \cdot 0.066}{0.233} = 3 \tag{4.6}$$

in which $\Delta_{d,is}$ and $\Delta_{d,ss}$ are respectively the design displacement of the isolation system and of the superstructure. They are approximated as $D_{max\ base}$ and $D_{max\ ss}$, which are the contribution of the total displacement given by the isolation system and by the superstructure computed from the pushover analysis at the design total displacement. The damping ratios $\xi_{e,is}$ and $\xi_{e,ss}$ are respectively the damping coefficient of the isolation

system and of the superstructure. According Equation 4.6, system viscous damping for the first mode is the 3% of the critical one, still computed using the initial stiffness. Hence we perform analyses of lead rubber bearing frame isolated system and of shape memory alloys device frame isolated system considering the value $\xi_{e,sys} = 3\%$ in the fundamental mode.

4.7.3 Evaluation of Results considering different SMA Dissipation Capabilities

To investigate response of flexible superstructure system, the response is reported in term of floor shear, floor displacement and acceleration demand.

(a) level #1

(b) level #2

(c) level #3

(d) level #4
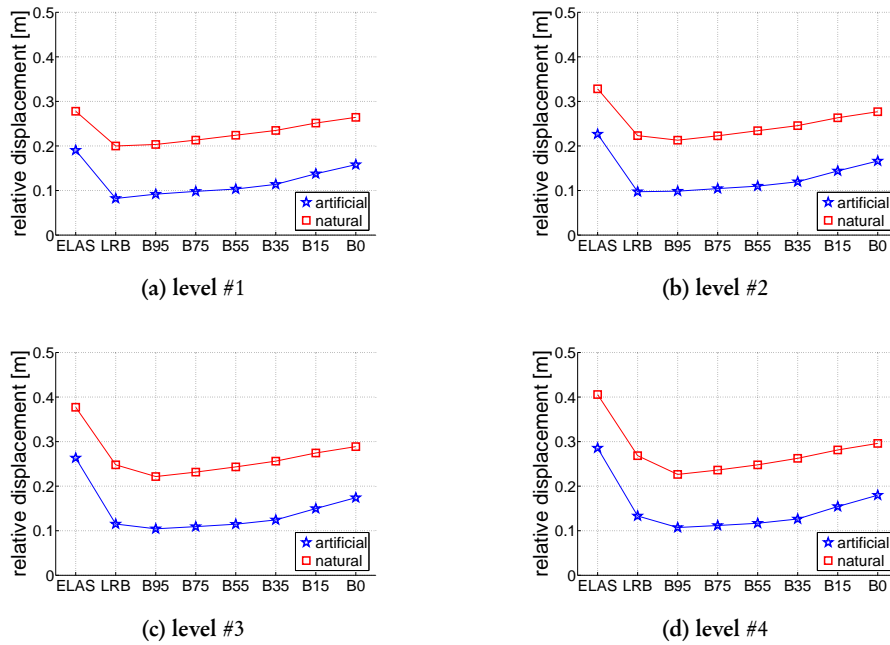
Figure 4.20. Maximum relative displacement demand mean values from artificial and near fault ground motions at different levels

- Displacements.
  The first comparison concerns displacements at different floor levels as shown in Figure 4.20. The test results confirm that the displacement demand is larger in equivalent secant stiffness linear elastic system than in nonlinear hysteresis models. The nonlinear system energy dissipation is larger for artificial ground motion, but it is still important also for near fault events. The displacement reduction factor increases with the increase of the floor level number. Concerning the elastoplastic and flag-shape model comparison, responses are not very different for the higher

range of SMA dissipation parameters. Large dissipating flag shaped hysteresis models performs better than the less dissipating ones, but if the flag-shape dissipation factor β is at least about $\beta \simeq 50\%$, the maximum displacement demand in flag-shape model is similar to the one of lead rubber bearing isolation device.

- Accelerations.

  Seismic isolation reduces the acceleration at the floor levels compared the non-isolated structure. The nonlinear hysteresis models produces larger mean accelerations than the linear elastic secant stiffness model. However, the flag shape models for a range of $\beta > 50\%$ is more favorable in terms of floor acceleration than elastoplastic model at every level, as shown in Figure 4.21.

(a) level #1

(b) level #2

(c) level #3

(d) level #4
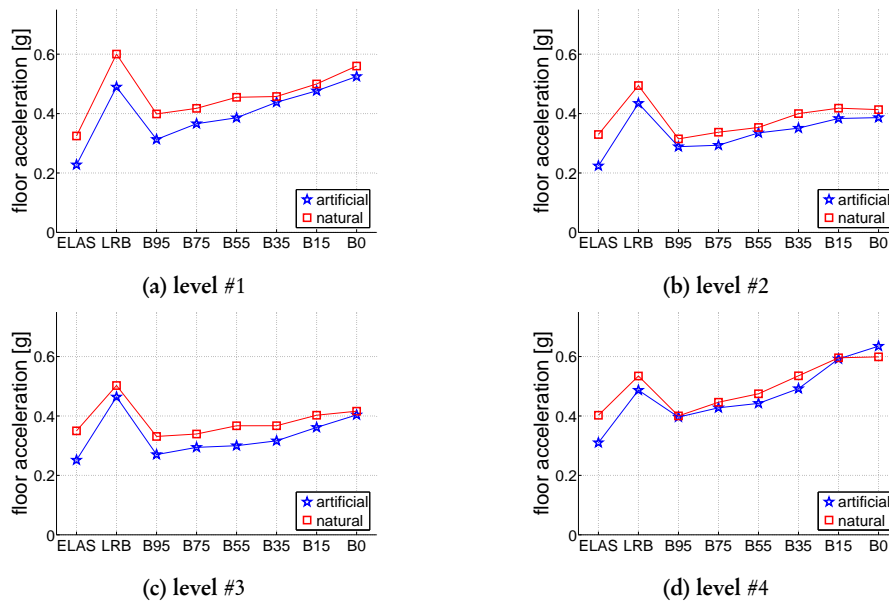
Figure 4.21. Maximum total acceleration demand mean values from artificial and near fault ground motions at different levels

- Shear forces.

  The mean values of story shear force are not very different considering the linear, the elastoplastic and the flag-shape models, as shown in Figure 4.22. While the linear model response values are characterized by a decrease of story shear demand with increasing elevation in the building, in the nonlinear cases variation along building elevation is less important. The differences between flag-shape and elastoplastic

model are quite small and also the differences in decreasing the SMA dissipation are small. Flag-shape hysteresis perform well for a large range of β values, at least larger than $\beta = 50\%$, for which the floor shear is very similar or smaller than in the case of the elasto-plastic model.

(a) level #1   (b) level #2

(c) level #3   (d) level #4
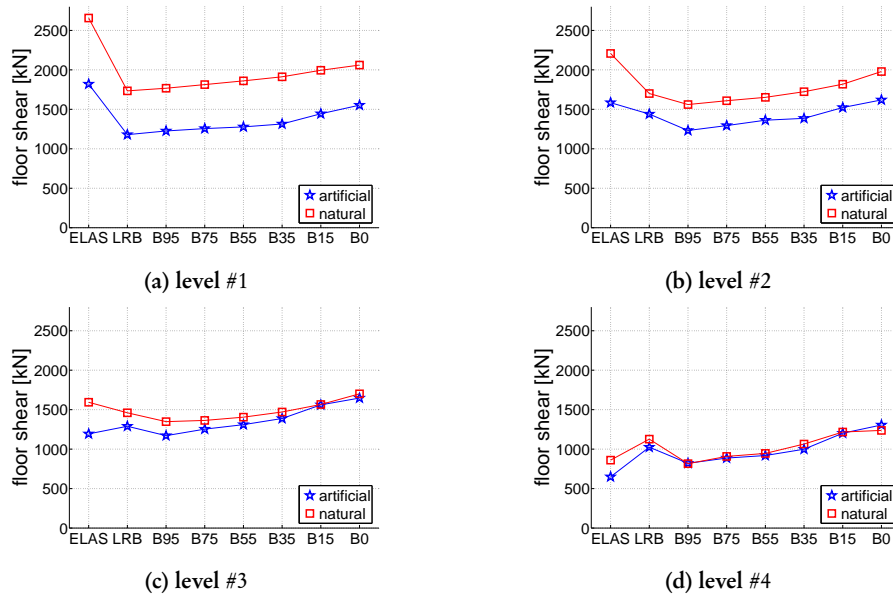
Figure 4.22. Maximum shear demand mean values from artificial and near fault ground motions at different levels

4.8   RESPONSE SENSITIVITY ANALYSIS ON THE SUPERELASTIC HYSTERESIS

The investigation performed in Section 4.6 and Section 4.7 was based on a fixed flag-shaped superelastic device hysteresis, which is shown in Figure 4.7b. This is characterized by the same initial stiffness k and the same hardening r with respect to the actual LRB system, as reported in Table 4.1. Hence the hysteresis backbone curve is the same between SMA and LRB systems. This was used to get an estimation of the real computed reduction factor as a function of the flag-shape dissipation capability and to debunk the concept of largely more severe force and displacement demand due to the less dissipating hysteresis being all the remaining variables constant.

As noted in Andrawes and DesRoches [2007] anyway, hysteretic properties of SMAs are known to be highly sensitive to factors such as the alloy chemical composition, the manufacturing processing of the alloy, and the loading strain rate. Moreover it is very

unlikely to get an initial stiffness and a hardening factor in the superelastic device constant with respect to the LRB system.

Therefore, this part is focused on exploring the effect of variability in superelastic hysteretic properties on their effectiveness as potential seismic isolation bearings. A sensitivity analysis was conducted using a simplified SDOF model.

4.8.1 Analysis Models

The superelastic hysteretic shape was assumed to be defined using three parameters, which are:

- initial stiffness (k), considering the value array:
  [2000, 2500, 3000, 3500, 4000, 4500, 5000]kN/m

- hardening coefficient ($r = r_1 = r_2$), considering the value array:
  [0.05, 0.10, 0.15, 0.20, 0.25, 0.30]

- dissipation capability (β), considering the value array:
  [0.15, 0.25, 0.35, 0.45, 0.55, 0.65, 0.75, 0.85, 0.95]

and are shown in Figure 4.2. They were chosen as a reasonable value range for SMA restrainer devices. The design shear force and design displacement (V_d and u_d respectively, still referring to Figure 4.2) are kept constant and equal to the design value for LRB system as reported in Table 4.1. Hence also the secant stiffness (k_e, see Table 4.1) is constant. Figure 4.23 provides an idea of the performed parametric investigation: the design level is kept fixed and first and second stiffness are changed in a compatible manner.

Considering the same approach presented in Section 4.5.1, the different superelastic hysteresis response were compared with respect to the LRB model (see Figure 4.7a) and the linear secant to the design displacement model (see Figure 4.7c). The same seismic weight with respect to previous time history analyses was considered and it is reported in Table 4.1. The considered ground motion set is the same one reported in Section 4.5.3.

4.8.2 Analysis Results

The analysis results are catalogued through the dissipation parameter in the present section. Since the dissipation influence in the results has been already investigated in Section 4.6 and Section 4.7, only the data for $\beta = 0.35$, $\beta = 0.55$, $\beta = 0.75$, and $\beta = 0.95$ are reported in the present part. Their evaluation is anyway enough to identify the response trend, which agrees with the missing results.

For the highest dissipation capability of the flag-shaped model ($\beta = 0.95$), the displacement and shear force envelopes are reported respectively in Figure 4.24a and Figure 4.24b. The superelastic hysteresis mean values over the entire ground motion set of the maximum demands are reported as a curved surface function of the initial stiffness value

(a) high k, high r

(b) high k, low r

(c) low k, high r

(d) low k, low r
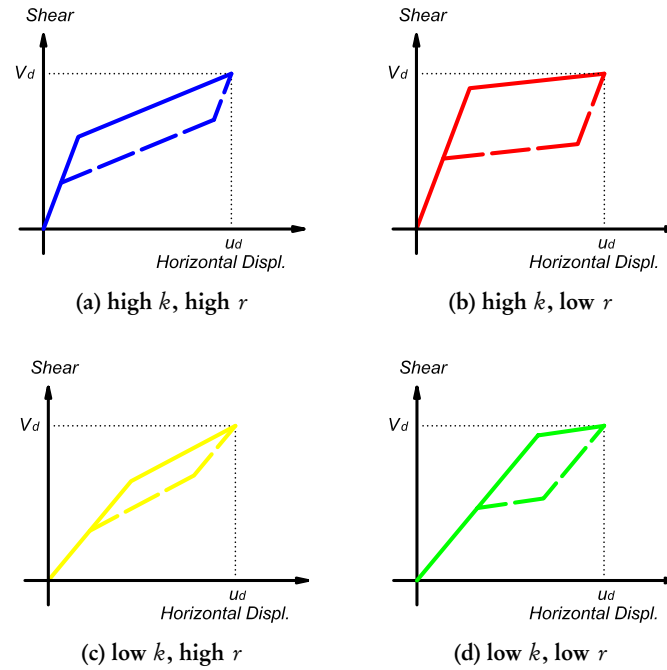
Figure 4.23. Parametric investigation hysteresis example for $\beta = 0.5$

k and of the hardening coefficient r. The corresponding results for secant linear and elastoplastic relation are identified by constant planes in the same plots.

Normalizing the results in Figure 4.24 by the demand in the linear elastic system, the displacement and shear reduction values are reported in Figure 4.25a and Figure 4.25b respectively. Being tri-dimensional plots quite difficult to be identified, results have been reported in Figure 4.26 as well, in which easier two-dimensional plots are proposed. Each plot is referred to a given initial stiffness and the variable in the horizontal axis is the hardening coefficient.
For the other dissipation values only the two-dimensional plot set has been reported. Results from $\beta = 0.75$ are shown in Figure 4.27, from $\beta = 0.55$ in Figure 4.28, and from $\beta = 0.35$ in Figure 4.29.

As a general comment on the results of the investigation in the present section, the following points can be reported.
The initial stiffness is likely to be obviously the most important parameter to limit the maximum displacement, because being all the other parameters constant, decreasing the initial slope the displacement demand increases. Anyway, regarding high initial stiffness, a low second slope produces small displacement demand, while an high second slope system is characterized by large displacement envelopes. The reason for this phenomenon is in
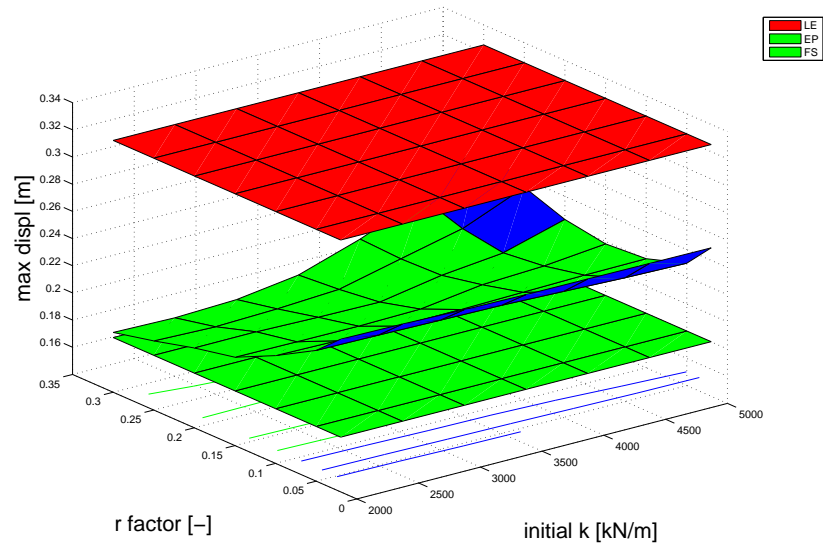
(a) displacement envelopes
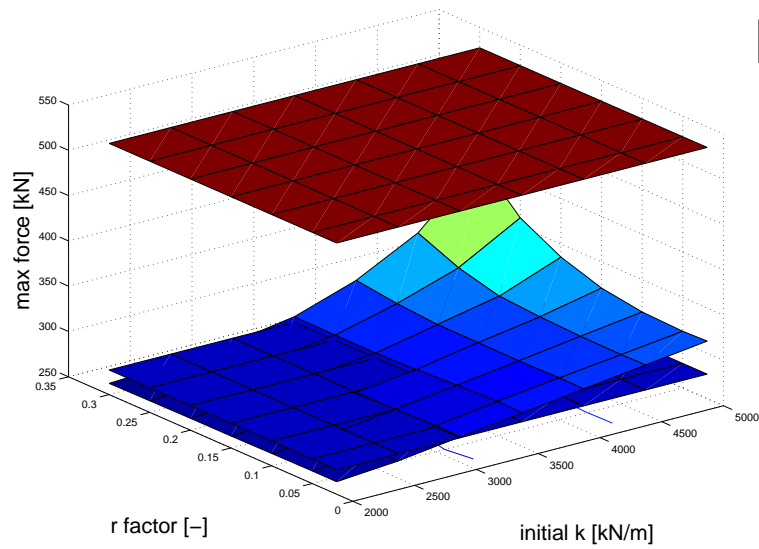
(b) force envelopes

Figure 4.24. Displacement and shear force demand envelopes for $\beta = 0.95$
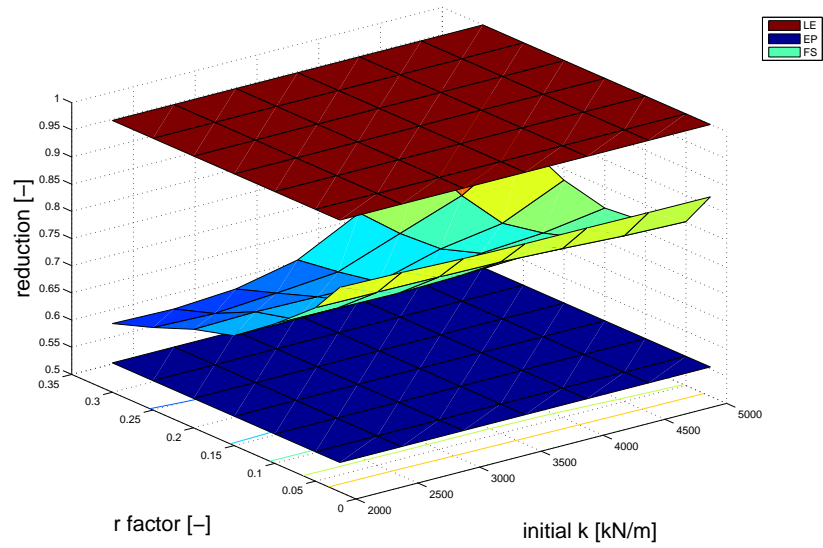
(a) displacement reduction
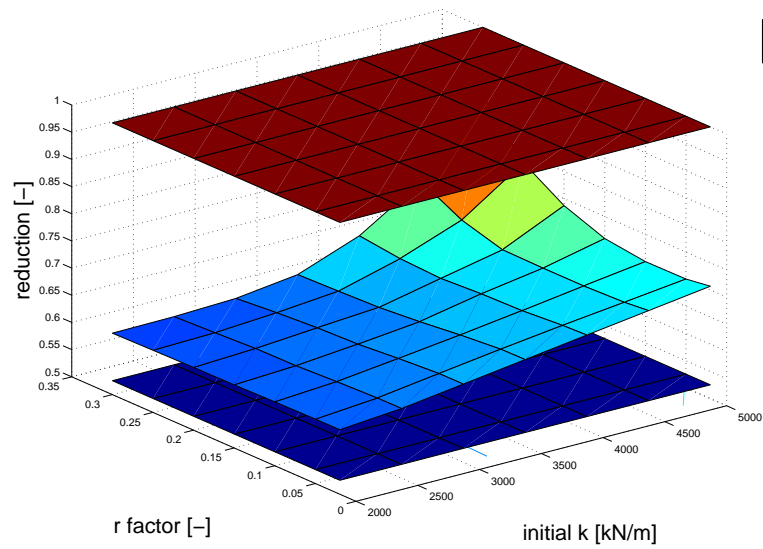
(b) force reduction

Figure 4.25. Displacement and shear force demand reduction for $\beta = 0.95$

the fact that, given the high initial stiffness, a low hardening coefficient causes a relatively high yielding force, as reported in Figure 4.23b. In this case the response stays mainly in the linear range. If the hardening coefficient is high, the system configuration is the one shown in Figure 4.23a, with a low yielding force and expected large nonlinear response, causing larger displacements.

On the other side, if the initial stiffness is low, the displacement demand is quite insensitive from the second stiffness factor, being the results similar for both low and high hardening. This is due to the fact that given the low stiffness the response is mainly linear when the yielding force is larger (case in Figure 4.23d) and even when the linear elastic limit is lower for larger hardening factor (as in Figure 4.23c), differences between linear and nonlinear range are not very important in terms of displacement demands because stiffness is about the same.

Consequently, the shear force demand in the system results characterized by a larger demand as the hardening factor is increased being the remaining parameters constant. Nevertheless the increase as a function of the second stiffness is parabolic for initial high stiffness while it is linear and less important for low initial stiffness.

The different dissipation capability of the flag-shaped hysteresis affects the system response but not as critically as expected. Differences in the response between $\beta = 0.95$ and $\beta = 0.75$ are negligible, differences between $\beta = 0.95$ and $\beta = 0.55$ are very small. Influence of dissipation capability in affecting the response is anyway larger for displacement than for force envelopes.

4.9 CONCLUSIONS

An investigation about the feasibility of shape memory alloy technology application to seismic isolation devices has been performed. The responses data evaluation from time history analyses was considered the most suitable method to study the problem. We have compared behavior of a model representing a conventional lead rubber bearing device with the behavior of a hypothetical shape memory alloy device and an equivalent linear elastic model. Even if the hystereses are different, they were characterized by the same secant stiffness and strength.

The reduction factor of displacements and forces based on the hysteresis area estimation would indicate that the flag-shape hysteresis produces larger seismic demand compared with the elastoplastic model. On the contrary, time history analyses demonstrate that differences are present, but they are not as large as indicated using the hysteretic area based approach. Considering both the single degree of freedom and the multiple degree of freedom analyses, displacement and force demand of a shape memory alloy device is close to a lead rubber bearing system demand and the energy dissipation is almost the same, regardless the big differences in hysteretic area. Analogous results are found considering an energy approach, because the absorbed energy from the time history analyses is similar between elastoplastic and flag-shape models. We verified that

these conclusions are valid not only for the more dissipating flag-shaped model, but also for smaller dissipation flag-shape hysteresis provided that the beta parameter is at least of the order of $\beta \simeq 50\%$. In practice this mean that even if the dissipation parameter is keep in a level characteristic of the non-prestressed shape memory alloy, results are still quite good. Shape memory alloy based technology system has zero residual displacement. This is an important advantage for damage mitigation in structural seismic design if compared with the lead rubber bearing systems with elastoplastic model.

A sensitivity analysis on SDOF system was conducted to examine the effect of variability of fundamental hysteresis parameters on the effectiveness of SMA isolation bearing. The outcomes of the studies show that the initial slope and the second slope of the SMAs hysteresis have important effects on the structural response envelopes. An high initial stiffness and a low second stiffness would be the combination more favorable.

Given the previous results, the conclusion of the present chapter is that the SMA application in seismic isolation is possible and can lead to several advantages. A SMA device used as a lateral restrain element for a bearing system would provide re-centering properties together with good energy dissipation capability.
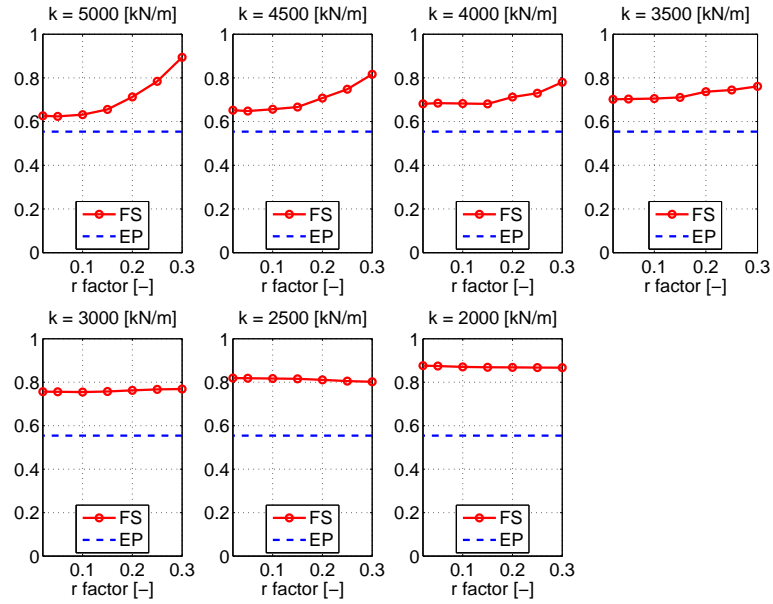
(a) displacement reduction
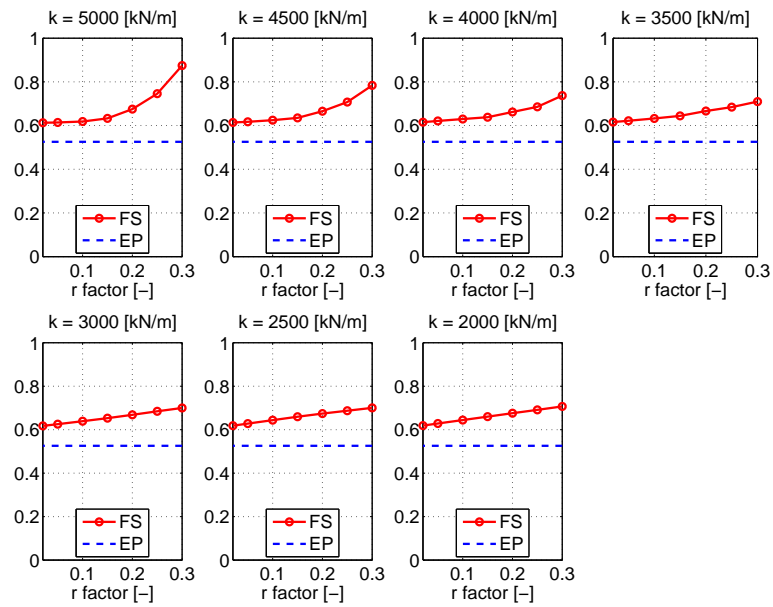
(b) force reduction

Figure 4.26. Displacement and Shear force demand reduction for $\beta = 0.95$
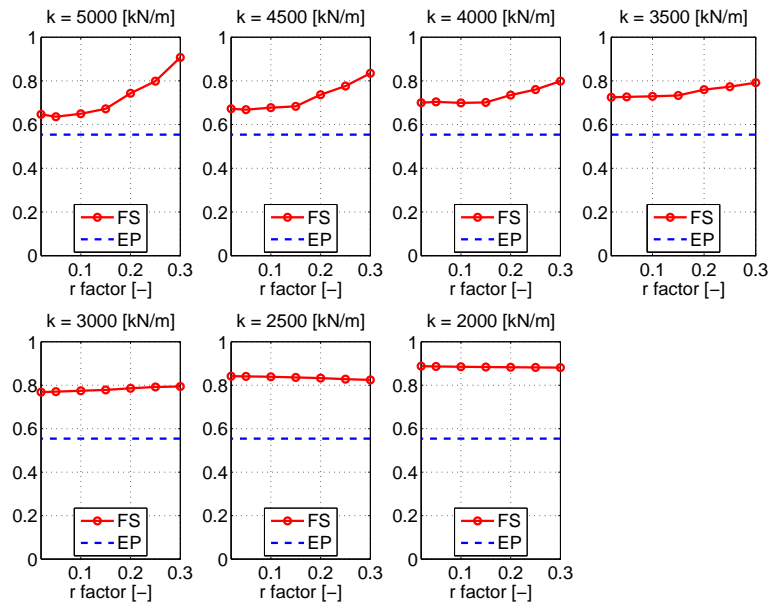
(a) displacement reduction
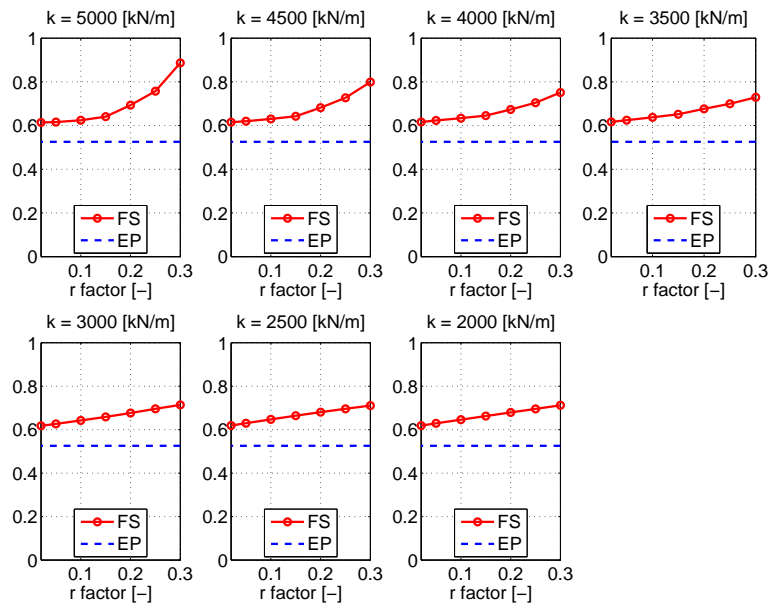
(b) force reduction

Figure 4.27. Displacement and Shear force demand reduction for $\beta = 0.75$
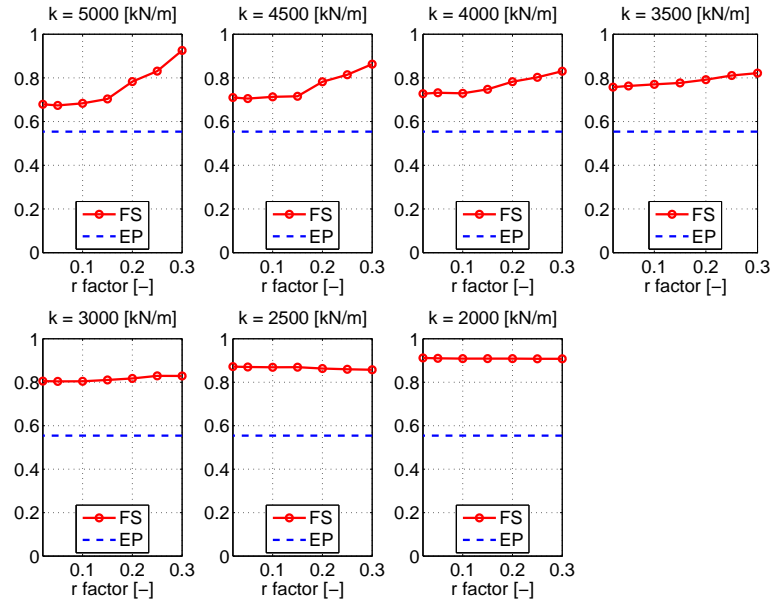
(a) displacement reduction
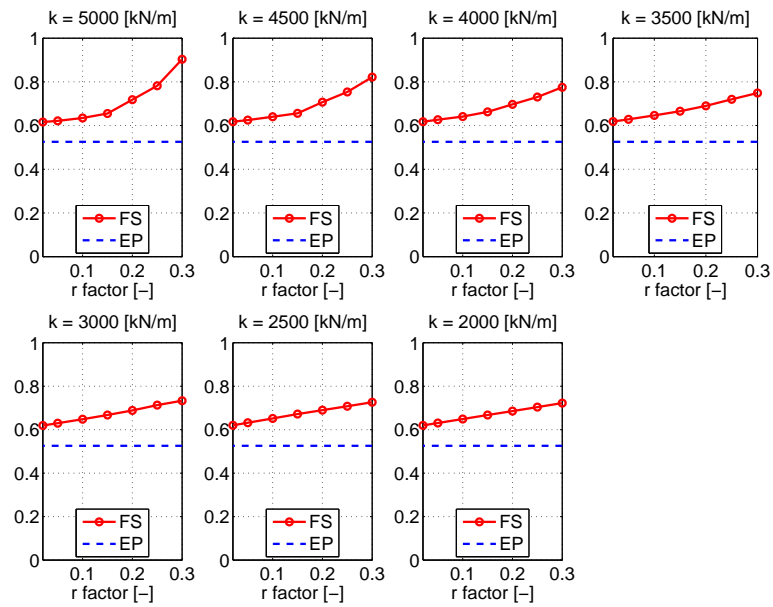
(b) force reduction

Figure 4.28. Displacement and Shear force demand reduction for $\beta = 0.55$
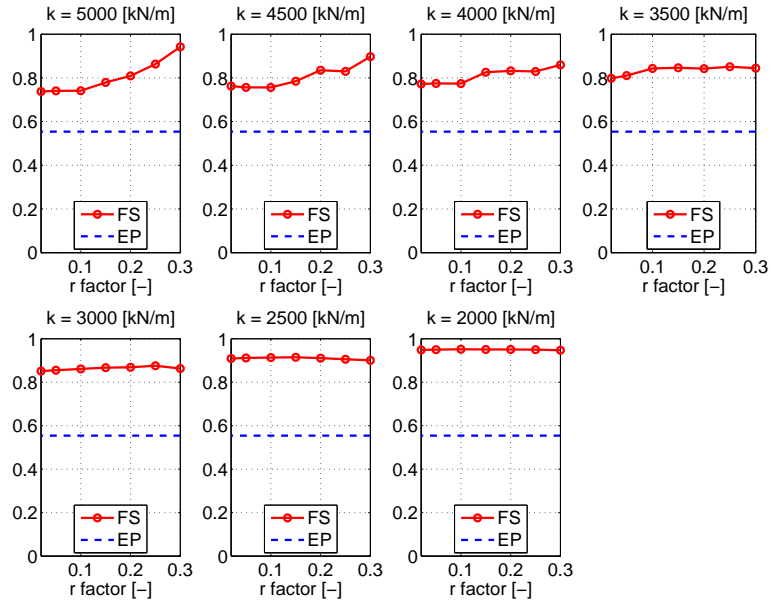
(a) displacement reduction
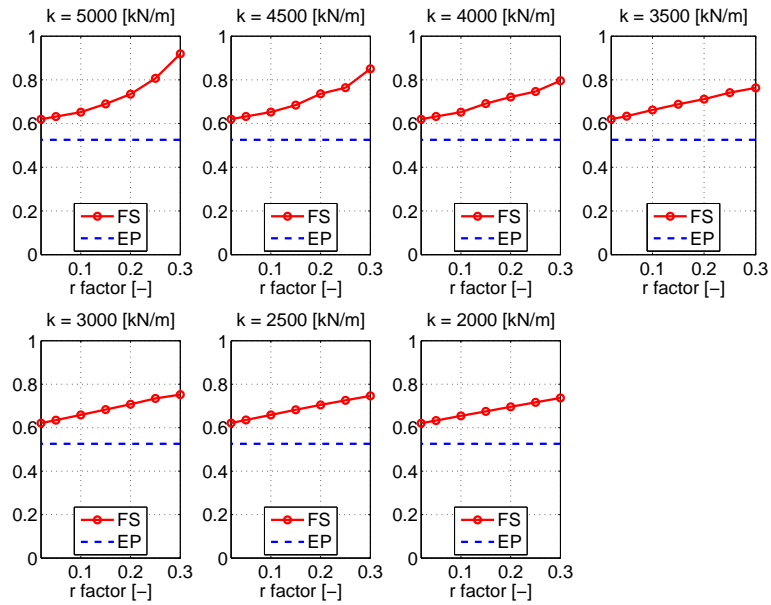
(b) force reduction

Figure 4.29. Displacement and Shear force demand reduction for $\beta = 0.35$

5. Theoretical Numerical and Experimental Investigation on Coil Spring System

5.1 INTRODUCTION

Following a classical definition given in spring design manuals, for example the one contained in Wahl [1963], a mechanical spring may be defined as *an elastic body whose primary function is to deflect, distort or absorb energy under load and which recovers its original shape when released after being distorted*. This definition underlines the fact that springs have been historically designed to accommodate displacements, to provide energy dissipation, restraining, and re-centering force.

In the present work, the spring configuration is proposed as a restrainer device solution. We refer to helical spring, which is the most widely used type of spring and is made of bar stock or wire coiled into a helical form, the load being applied along the helix axis. It works in compression or tension when the helix is respectively compressed or extended. The choice of coil spring is due to its capability in sustaining large displacement with acceptable material deformations, without loss of strength and being possible to fit the device into limited available space. Moreover, the idea is to use superelastic material (SMA) springs. This is to take advantage of the interesting properties of this innovative material, as described in Chapter 3.

A possible application of this kind of device in civil engineering is in the context of seismic isolation. The superelastic spring could be used to provide lateral restraining effect constituting the basic component of the superelastic isolation system. Anyway, it may be a suitable solution for all the implementations in which it is important to provide a restoring force even after the restrainer linear limit is exceeded.

Actually, conventional springs are characterized by design deflection values and stresses which are not beyond the elastic limit, so the large majority of springs is designed considering a linear elastic load-deflection response. On the contrary, the goal of the present chapter is to evaluate the response of superelastic springs and exploiting the material superelastic behavior. This means to consider devices designed to work in a nonlinear geometric and material response range, i.e. taking advantage of the nonlinearity but without renouncing to the recentering and restraining properties.

Three different levels of analysis are proposed to describe the spring behavior:

- a theoretical level, considering the traditional approach based on elastic and plastic

analysis of spring mechanical devices;

- a finite element level, in which the device response has been predicted considering a numerical model suitable to describe its properties;

- an experimental level, in which the real device response has been experimentally tested.

This complex and multi-structured approach provides a good global view of the problem. Conceptually, the verification process can be described as follows.

The theoretical analyses give a good initial idea of the main device mechanical properties, even if under particular and restrictive conditions, the most important of which is usually the small displacement assumption. The finite element analysis is then performed for both linear elastic and superelastic material, showing good agreement under the assumption on which the preliminary analysis is valid, and providing more informations on the overall behavior of the device. The numerical analysis at this stage is referred to full scale spring device class which can be suitable for base isolation application. Theoretical and finite element analysis together with their result comparisons are described in Section 5.2.

Then, experimental tests are performed on different geometry and reduced size specimens with respect to the previous investigated spring class. For the tested devices and conditions, the numerical model is checked and validated. Description of the experimental campaign and comparison with finite element results are discussed in Section 5.3.

The main findings and conclusions are described in Section 5.4.

5.2 BASICS ON SPRING MECHANICS AND NUMERICAL RESPONSE EVALUATION

In this section some of the most important spring system properties are investigated. An overview on the basic mechanics is presented for the linear spring system in Section 5.2.1 together with the finite element linear elastic analysis results in Section 5.2.2. Then, some issues on nonlinear material spring behavior are reported in Section 5.2.3 and examples of superelastic material finite element analysis results are presented in Section 5.2.4.

5.2.1 Linear Elastic Material Coil Spring Mechanics

Coil springs are loaded usually in the direction of their axis either in tension or in compression, as shown in Figure 5.1. If this condition is verified and we consider a load P, in a generic point of the spring having coil radius R, the internal actions are (see Figure 5.2):

- axial force: $N = P sin\alpha$

- shear force: $V = P cos\alpha$
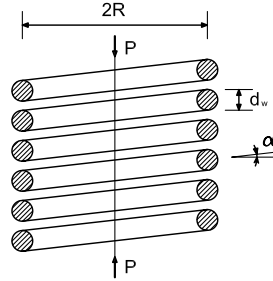
Figure 5.1. Helical spring under compressive load

- bending moment: $M_f = RP \sin\alpha$
- torque: $M_t = RP \cos\alpha$
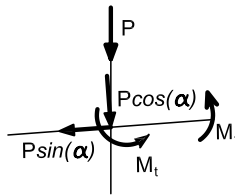
Figure 5.2. Internal actions along helical spring axis

Internal actions are function of the pitch angle α which is usually small, so bending moment and axial load are negligible. Shear induced stresses are negligible as well. Hence for the equilibrium computation the most important contribution is the one given by torque.

(a) Axial stiffness

Evaluating the *external work* and the *internal work* associated to the torque, we obtain:

$$\frac{1}{2}P\Delta = \frac{1}{2}\int_{l_w} M_t \, d\varphi \tag{5.1}$$

in which Δ is the displacement of the spring in the direction of the coil axis, φ is the rotation of the spring wire around its axis, and l_w is the total length of the coil wire. Considering the shear modulus of the material G and the polar inertia moment of the wire section J_p, Equation (5.1) can be written as:

$$\frac{1}{2}P\Delta = \frac{1}{2}\int_{l_w} M_t \, d\varphi = \frac{1}{2}\int_{l_w} M_t \frac{M_t \, d l_w}{G J_p} \tag{5.2}$$

Expressing the torque M_t as a function of the external load P, assuming the coil and wire properties constant along all the spring length and being d_w the wire section circular diameter, Equation (5.2) can be expressed as:

$$\frac{1}{2}P\Delta = \frac{1}{2}\int_{l_w} \frac{P^2 R^2 dl_w}{GJ_p}cos^2\alpha = \frac{1}{2}\frac{P^2 R^2}{GJ_p}cos^2\alpha \int_{l_w} dl_w \tag{5.3}$$

hence, the deflection in the load direction is given by:

$$\Delta = \frac{PR^2}{GJ_p}cos^2\alpha \int_{l_w} dl_w = \frac{32R^2}{G\pi d_w^4}l_w cos^2\alpha\, P \tag{5.4}$$

recalling that the length l_w is the length of the wire of the spring measured along the wire axis, it can be computed as:

$$l_w = \frac{2\pi R}{cos\alpha}n_c \tag{5.5}$$

being n_c the number of the spring coils. Therefore, the stiffness of the spring is given by the expression:

$$k_{spr} = \frac{P}{\Delta} = \frac{G\, d_w^4}{64\, R^3\, n_c}cos\alpha \cong \frac{G\, d_w^4}{64\, R^3\, n_c} \tag{5.6}$$

The result presented in Equation (5.6) is defined in the present work as the spring *theoretical stiffness*. It turns out that the spring theoretical stiffness is related to material properties and to geometry, being in particular proportional to the diameter of the wire (to the fourth power) and inversely proportional to the coil radius (to the third power) and to the number of coils.

(b) Internal stresses

Recalling that we are assuming to be always in the material elastic range, the non trivial internal stress components are given by the torque and the shear stresses. Both for the case of tension and compression load, these components are more demanding in the internal side of the wire, because they sum up as shown in Figure 5.3. The maximum shear stress demand is then given by:

$$\tau_{max} = \tau_{Mt} + \tau_V = \frac{16R}{\pi d_w^3}P + \frac{4}{3}\frac{4}{\pi d_w^2}P = \frac{16R}{\pi d_w^3}P\left(1 + \frac{1}{3}\frac{d_w}{R}\right) \tag{5.7}$$

Equation (5.7) has been obtained considering the classical expression to compute the torque tangential stress in a straight bar. The presence of a wire curvature would induce a non linear stress distribution along the wire diameter (as shown in Figure 5.4), which are however neglected for simplicity in Equation (5.7) and in the following derivations. A
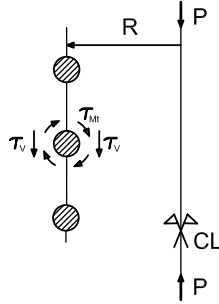
Figure 5.3. Internal stress in the helical spring wire section due to torque and shear under compressive load
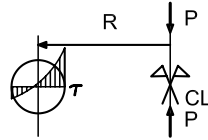
Figure 5.4. Elastic shearing stress distribution across transverse diameter of helical spring of small coil radius and large wire diameter

more extended discussion of the problem is presented in Wahl [1963]. Equation (5.7) also shows that the shear force contribution in terms of tangent stress demand is relevant if the wire diameter d_w is large and the coil radius R is small, otherwise it can be neglected.

(c)   *Large deflection effect*

A key aspect that has to be taken into account in the evaluation of the spring stiffness and of the internal stress computation is the issue of large deflection in the modification of the spring geometry. This effect becomes relevant when the pitch angle is relatively large and the deflection per turn more than one half of the coil height, as demonstrated in Wahl [1963].

As shown in Figure 5.5, when a compressive spring deflects from the initial position to a new one, being Δ the axial displacement, the coil radius changes, increasing from R_0 to R, and the pitch angle decreases, going from α_0 to α. Since the spring deflection is proportional to the cube of coil radius, it follows that the spring becomes more flexible as it is compressed. Regarding the stress, its torque component decreases linearly with the coil radius while its shear component remains constant with the coil radius. Of course the opposite effect occurs in tension springs.

We assume to consider fixed ends and this implies that the number of coils n_c is constant. Being the total wire length l_w constant, due to Equation (5.5) the ratio between the $cos\alpha$ and the coil radius R is constant as well. Given the previous assumptions, using the

(a) initial configuration   (b) final configuration
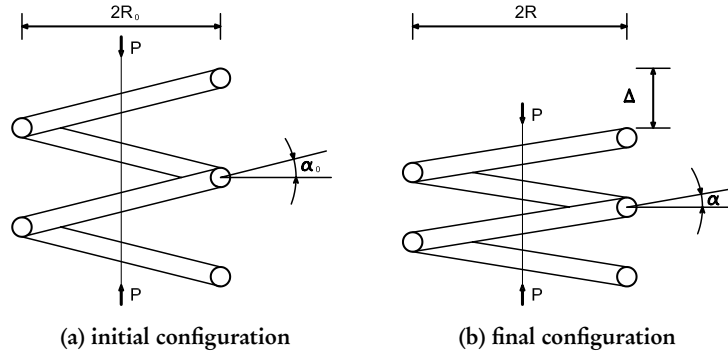
Figure 5.5. Open-coiled helical spring with large deflection

Equation (5.6), it is possible to compute the stiffness of the spring for each deformed configuration, corresponding to a generic coil radius R. In particular, the relation between
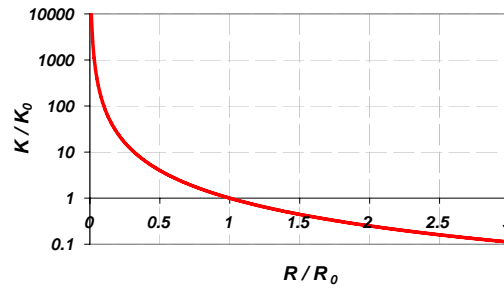
Figure 5.6. Stiffness ratio (actual over initial) as a function of coil radius ratio (actual over initial)

the initial stiffness $k_0 = k_{spr}(R_0)$ and the actual stiffness $k = k_{spr}(R)$ as a function of the initial and actual radius, respectively R_0 and R, is shown in Figure 5.6.

In an open-coiled helical spring subjected to an axial tension giving a large deflection, it can be important to evaluate the tendency for its coils to unwind. In fact one end of the coil tends to rotate with respect to the other about the spring axis. In this situation the boundary conditions turn out to be very important. If the rotation can take place freely i.e. without restraint, a reduction of the number of coils usually occurs. Otherwise, if the ends are prevented from rotation, end moments acting on the coil axis are induced to prevent this rotation.

(d) Buckling or instability of compression springs

If compression springs are slender, instability may occur with a consequent spring sidewise fly-out. Two types of buckling or instability of helical compression springs can occur

fixed end   *guided end*

fixed end   *fixed end*

(a) double-fixed-end
case

(b) fixed-guided-end case
(or double-hinged-end)
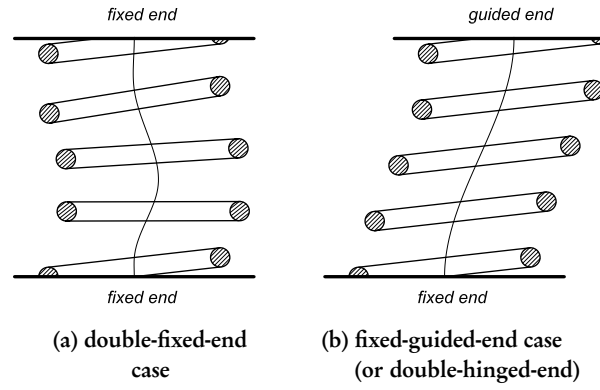
Figure 5.7. Buckling of springs with fixed or guided ends

in practice depending on the end constrained conditions as shown in Figure 5.7a. The theoretical analysis of buckling of helical compression springs contained in Haringx [1949] shows that the critical deflection at which instability occurs depends on the slenderness of the spring, which can be evaluated considering the coil radius R, the wire diameter d_w, the pitch angle α, the number of coils n_c, and the spring end fastening method.

(e)   Lateral stiffness

Theoretical analyses of laterally loaded springs, which is shown in Figure 5.8, are reported in Wahl [1963] and Crede [1951]. They provide an approximate expression to evaluate the lateral stiffness of the spring which can be at the same time loaded in the direction of its axis and in the direction perpendicular to its axis. If k_y is the stiffness of the spring
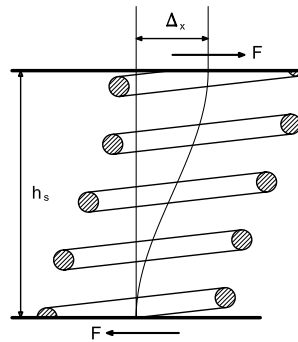
Figure 5.8. Lateral loaded spring (one end fixed, the other guided)

along its vertical axis direction, the ratio between k_y and the lateral stiffness k_x can be

estimated through some charts like the one shown in Figure 5.9, in which h_s is the total spring height, Δ_x is the transversal displacement, as shown in Figure 5.8, and $D = 2R$ is the coil diameter.
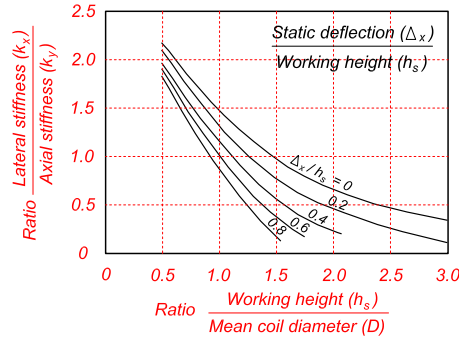
Figure 5.9. Ratio of lateral to axial stiffness for helical compression springs (data from Wahl [1963] and after Crede [1951])

5.2.2   Finite Element Analysis on Elastic Material Coil Spring Model

Finite element (*FE*) analysis is a valid option to check the stiffness expression for an elastic spring in the small-deflection range and to understand the real mechanics of the device subjected to large-displacements. Hence, the spring behavior in tension and compression has been checked using the FE program ABAQUS [2003] and the results have been compared with some of the previously discussed analytical solutions.

The considered spring is characterized by a geometry configuration which can be suitable for civil engineering applications as lateral restrainer. The coil radius is $R = 50$mm and wire section is circular, with diameter $d_w = 30$mm. The height of the spring axis is $h_s = 200$mm and the height of one single coil is $s = 108$mm. The number of coils is $n_c = 1.85$. The geometry is described using 36 straight beam elements for each spring coil. The mesh is shown in Figure 5.10 and it is evident that the adopted number of elements is sufficient to reproduce the coil curvature. The most important geometrical non dimensional quantities are reported next:

- wire diameter versus initial coil radius:

$$\eta_1 = \frac{d_w}{R} = 0.60 \tag{5.8}$$

- wire diameter versus initial coil height:

$$\eta_2 = \frac{d_w}{s} = 0.28 \tag{5.9}$$

(a) fixed-hinged case   (b) fixed-fixed case
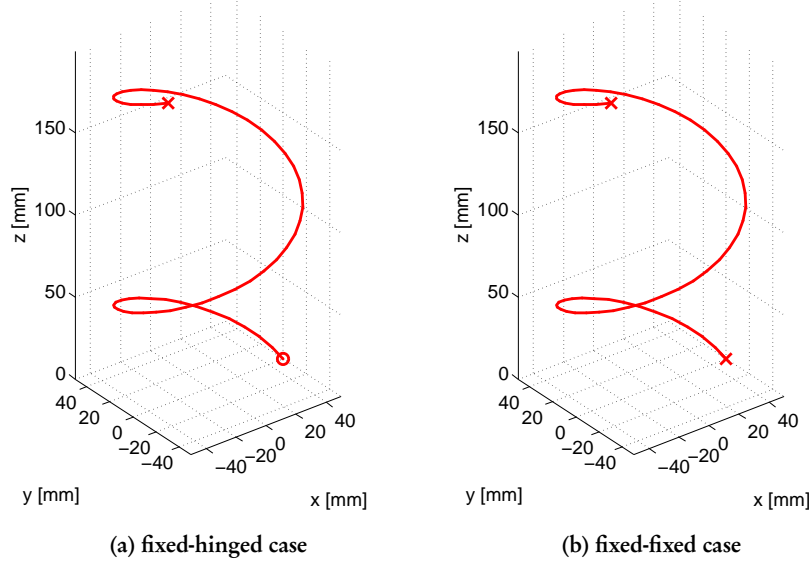
Figure 5.10. Spring mesh for FE elastic material test

- initial coil radius versus initial coil height:

$$\eta_3 = \frac{R}{s} = 0.46 \tag{5.10}$$

The material is assumed to be *elastic* with Young modulus $E = 45\text{GPa}$ and Poisson ratio $v = 0.33$, hence with a shear elastic modulus $G = 16917\text{MPa}$. Based on Equation (5.6), the theoretical stiffness of the spring is $k_{spr} = 923\text{N/mm}$.

The numerical test consists of a displacement control test in which one end of the spring is displaced in the direction of its axis (looking at Figure 5.10, this is the z axis). The displacement is applied at a final node which is clamped and restrained to rotate (*fixed node*). We are interested in evaluating the device response considering two different boundary conditions of the other extremity:

- hinged end case: this is the case in which the node is free to rotate around the x and y axis (as shown in Figure 5.10a);

- fixed end case: in this case the node is restrained to rotate (as shown in Figure 5.10b).

Accordingly, we consider a *fixed-hinged* condition and a *fixed-fixed* condition.

The spring is subjected to a 100% elongation, i.e. the maximum displacement at which the spring has been subjected is 200mm and it has been reached with 3 cycles of amplitude 100mm, 150mm, and 200mm.

The test is performed assuming the material to behave elastically even if internal stresses exceed common material strengths. The reason is that the purpose of the test is to investigate the theoretical spring load-deflection relation and to define a particular range for which the stiffness computation expression is valid. From the internal stress distribution evaluation, it is clear anyway that as soon as the spring deflection becomes relevant, the hypothesis of uniform stress is unrealistic and the large-displaced device is characterized by high stress concentration regions. This is particularly important in the fixed-fixed case, for which stresses at clamped ends are very large.

(a)   Fixed-hinged condition

Results of tension-compression test on the fixed-hinged spring together with the theoretical stiffness of the spring based on Equation (5.6) are shown in Figure 5.11a, in which the convention positive-tension, negative-compression is adopted.
 The FE test provides proofs for the following conclusions:

- the stiffness computed using Equation (5.6) is a good approximation for the initial stiffness of the spring but it is valid only for not too large displacements, both in tension and in compression;

- as the elongation in tension increases, the stiffness increases more than proportionally: this is due to the reduction of the coil radius associated to spring deformation as already described in Figure 5.6;

- in compression the buckling of the spring causes a decrease of the load capacity getting a very low stiffness.

(b)   Fixed-fixed condition

Results of the tension-compression test for the fixed-fixed condition are shown in Figure 5.11b, assuming a positive-tension negative-compression convention. The comparison summary and conclusions are:

- the stiffness is increased with respect to the fixed-hinged case and the maximum load in tension for the same displacement is about 30% higher;

- being the spring more restrained, no severe buckling is observed compared with the fixed-hinged case, in which the stability issue has been demonstrated to be very important; hence in compression the load-deflection shows a maximum acting load significantly larger than in the previous case.
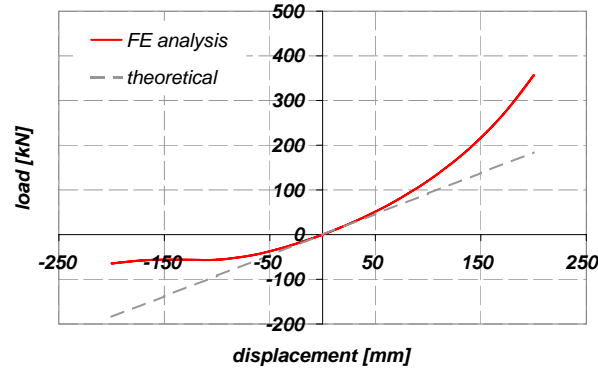
(a) fixed-hinged case
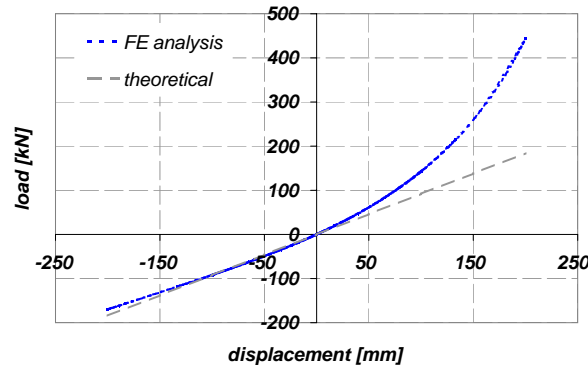
(b) fixed-fixed case

Figure 5.11. Elastic spring FE tension-compression test results and theoretical spring stiffness k_{spr} comparison (positive-tension, negative-compression convention adopted)

5.2.3 Nonlinear Inelastic Material Coil Spring Mechanics

The linear elastic hypothesis as assumed in Section 5.2.1 is only a particular case in mechanical behavior. Hence, some issues on the nonlinear spring mechanics are presented here. More informations are presented in literature, in particular in Wahl [1963].

In typical alloys the relation between the tangent stress τ and the angular deformation γ is nonlinear and an approximation of it is the elasto-plastic one shown in Figure 5.12. The initial elastic limit has been defined considering γ_{pl}, τ_{pl} and their ratio G, which is the conventional shear modulus of elasticity.
Integrating the stresses in the wire section it is possible to get the relation between the rotation of the wire around its axis θ and the torque in the wire $M_t(\theta)$. This characterized by a linear elastic range, bounded by M_{pl} and θ_{pl}, followed by a nonlinear range, as
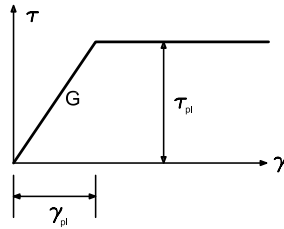
Figure 5.12. Nonlinear stress-strain monotonic relation (idealized elasto-plastic)

qualitatively described in Figure 5.13. Hence, stress nonlinearity and its distribution
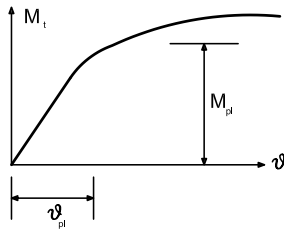
Figure 5.13. Nonlinear torque-rotation relation

in the section, which produces also the section torque moment-rotation nonlinearity, together with the actions on a deflected wire being large displaced, make the problem quite more complex than presented here. Classical strength check are not applicable under the previous hypothesis and the theoretical stiffness is valid only until the shear modulus remains constant. Moreover, due to imperfections or to localizations of stresses for instability or lateral load condition issues, the plasticization does not occur at the same time along all the spring.

Obviously, to neglect the nonlinearity of material can lead to severe errors in the design. On the other side, the designer has the chance to take advantage of the nonlinearity for its design purpose. In particular, like all the yielding phenomena, it can produce favorable conditions to limit the maximum acting force in the spring.

5.2.4 Finite Element Analysis on Superelastic Material Coil Spring Model

We now want to investigate springs made of shape memory alloys. Due to the highly nonlinear response of SMA, the numerical validation process is a compulsory step in the pre-design of such a device. For this reason, numerical analyses have been performed using the finite element *FE* program ABAQUS [2003].

(a)   Material model properties

We assume the spring to be made of a superelastic shape memory alloy characterized by a flag-shaped stress-strain relation model related to material transformation process. This is reported in Figure 5.14. In loading it shows an initial elastic response followed
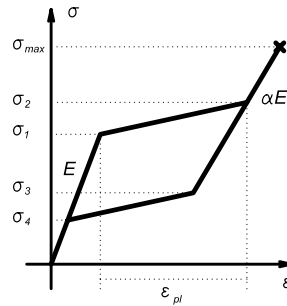
Figure 5.14. Superelastic flag-shaped stress-strain model

by a softening due to the material transformation and then by a hardening when the transformation finishes. During the unloading process, the branch is initially almost linear; when the reverse transformation occurs a softening is shown until the initial loading branch is reached again and followed in opposite direction.

The material properties used in the analysis are compatible with actual manufactured high dissipation superelastic shape memory alloys and they are summarized in Table 5.1. It

Table 5.1. Superelastic SMA material properties (flag-shaped model as defined in Figure 5.14) used in the FE modeling

SMA material properties (flag-shaped model)		
1st transf. stress	σ_1	600 MPa
2nd transf. stress	σ_2	800 MPa
3rd transf. stress	σ_3	300 MPa
4th transf. stress	σ_4	100 MPa
rupture stress	σ_{max}	1200 MPa
plateau strain	ϵ_{pl}	5 %
initial Young modulus	E	45 GPa
final Young modulus	αE	15 GPa
Poisson ratio	ν	0.33

has been assumed in all the numerical tests involving SMA that the temperature is not affecting the material response. A numerical characterization of the material is shown in

Figure 5.15 in which the results from a tension test considering three cycles of loading and unloading at different amplitudes are reported. The analyses are performed without considering the device failure when the rupture stress is reached in the material. All the numerical test are concluded neglecting the maximum stress distribution and the eventual failure is checked during the analysis postprocessing. Hence the stresses maxima have to
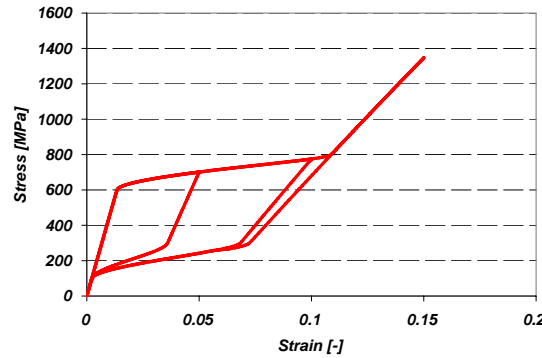
Figure 5.15. SMA constitutive relation from FE analysis

be checked after each analysis to be sure the material capacity is not exceeded.

(b)   Spring mesh properties

The geometry of the spring is the one already described in Section 5.2.2 and reproduced in Figure 5.10. As reported before, the reason for the choice of such a type of spring geometry is given by its suitability in acting as a restrainer for actual isolator device force and displacement levels. This is because according a predesign considering a reasonable material yielding and maximum stress and maximum strain, this spring configuration is able to carry the needed shear and to undergo the design displacement without rupture.

The spring coil radius is $R = 50$mm, the spring axis height is $h_s = 200$mm, the height of one single coil is 108mm, the number of coils is $n_c = 1.85$, and the wire diameter is $d_w = 30$mm. It is modeled through 36 beam elements for each spring coil. Two sets of boundary conditions have been considered for the test, one in which the coil spring ends are fixed-fixed and another in which they are fixed-hinged, as shown respectively in Figure 5.10a and in Figure 5.10b. Based on Equation (5.6), the theoretical stiffness of the spring is $k_{spr} = 923$N/mm.

(c)   Test procedure

The numerical test consists of a displacement control test in which one end of the spring is displaced in the z direction (with reference to Figure 5.10) while the other is kept fixed.

The maximum displacement at which the spring has been subjected is 200mm and it has been reached with 3 cycles of amplitude 100mm, 150mm, and 200mm as shown in Figure 5.16.
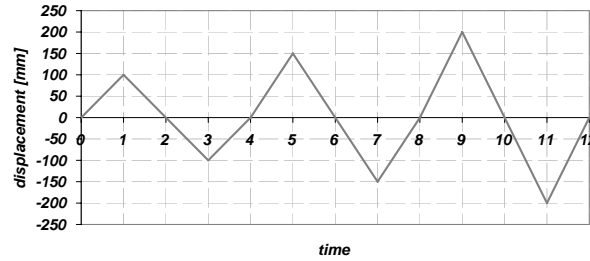
Figure 5.16. Applied displacement history at the spring end in the numerical test

(d)   Fixed-hinged condition

In Figure 5.17 two snapshots of the deformed mesh during the test are shown using a color-map which provides informations on the stress concentration in the elements. The hinged node (the left end one) is free to rotate and in this area the coil is quite flexible, undergoing large deformations and experiencing low stresses. Stress history in term of equivalent *von Mises* stresses in two illustrative nodes is also shown in Figure 5.18. Figure 5.17a reproduces the maximum spring deformation in tension, in which the spring is elongated of 100% of the original length of its axis. Stresses are quite uniform in the central region of the spring, being the equivalent von Mises stress about $\sigma_{vM} = 900\mathrm{MPa}$ in this area. The peak stress in tension occurs in correspondence of one of the central nodes of the spring and the history of stress in this node in shown in Figure 5.18a. For the maximum positive displacement the stress plateau limit is exceeded, but based on material properties reported in Table 5.1, the alloy is not supposed to reach the rupture point.

Figure 5.17b reproduces the spring deformed in compression. In this case the maximum stress occurs in the nodes which are about at one quarter of the spring length, close to the hinged node which rotates to make the compression possible and it increases the torque in the wire in that region. Checking the stress history in a node in this area, as shown in Figure 5.18b, maximum stresses occurs when the spring is in compression but the rupture limit is not exceeded.

The resulting force-displacement relation of the spring is shown in Figure 5.19. The use of superelastic material produces an hysteresis characterized by a flag-shaped relation which is significantly affected by spring large deflection effects. The tensile behavior is characterized by the geometrical effect associated with radius reduction. This is responsible for the significative hardening after the material yielding, even if the material

(a) spring in tension

(b) spring in compression
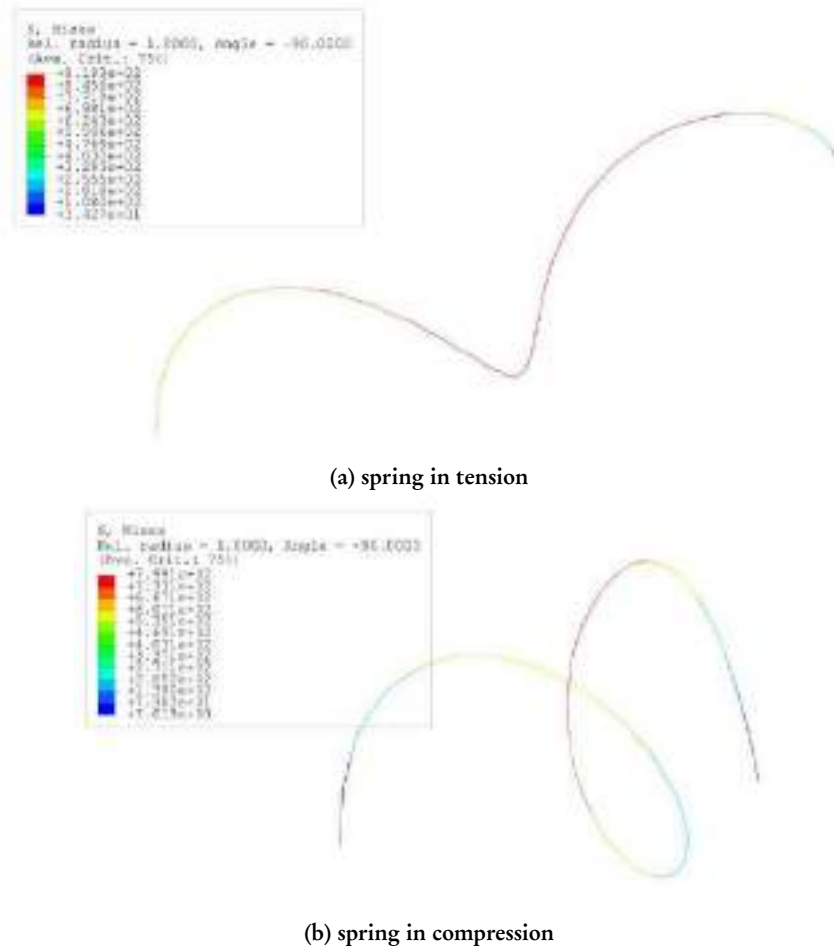
Figure 5.17. Superelastic fixed-hinged spring deformed mesh in tension-compression test

plateau is almost flat, as shown in Figure 5.15. At the largest displacement the effect of second hardening in stress-strain relation already noticed in Figure 5.18a occurs, providing response characterized by a very high local stiffness.

Compression response is strongly affected by spring buckling. As the elastic analysis cases have shown previously, instability produces a reduction in the maximum force that can be developed and a final hardening is given just by the second hardening in the material response.

The test result also shows that the theoretical stiffness computed for the spring from expression in Equation (5.6), following the approach described in Section 5.2.1, is very close to the initial stiffness of the superelastic spring. As already noticed in the elastic case, the range for which the approximation is acceptable is anyway different in tension and in
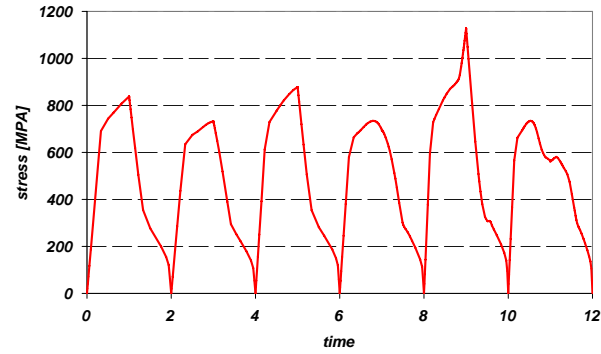
(a) maximum stresses node in tension
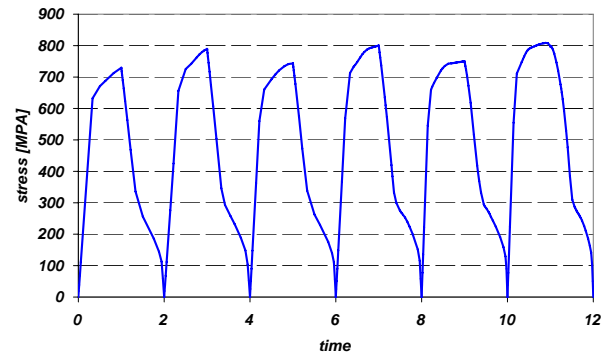
(b) maximum stresses node in compression

Figure 5.18. Superelastic fixed-hinged spring stresses in tension-compression test

compression.

(e)   *Fixed-fixed condition*

In the fixed-fixed condition the end node rotations are not permitted. The same axial displacement history shown in Figure 5.16 is used.

The deformed model of the fixed-fixed condition is shown under tension in Figure 5.20a and under compression in Figure 5.20b. Again the mesh color-map shows the equivalent von Mises stresses in the elements. The main effect of the fixed node is the development of high stresses in the region close to the clamping, especially in the tension condition. The maximum stress demand occurs in the center of the spring during both tension and compression. Looking at the equivalent von Mises stress history in two illustrative nodes of the mesh, as reported in Figure 5.21, the maximum stress developed in the spring results to be larger than the one in the fixed-hinged case. In some nodes the theoretical rupture limit is exceeded. This occurs due to high tension stress demand, as shown in Figure
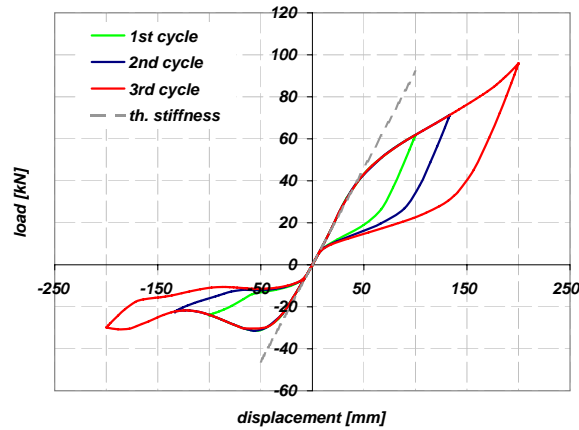
Figure 5.19. Superelastic fixed-hinged spring tension-compression test results and theoretical spring stiffness comparison (positive-tension, negative-compression convention adopted)

5.21a. Second hardening material limit is exceeded in nodes developing high stress in compression, as shown in Figure 5.21b.

The resulting force-displacement relation is reported in Figure 5.22. Again, the superelastic material affects the response in terms of global force-displacement providing a flag-shaped relation, like in the fixed-hinged case.
The hysteresis comparison between the two different boundary condition tests is reported in Figure 5.23. First of all, the effectiveness of the restrain conditions in reducing the vulnerability to buckle is reported. In fact, in compression the response is more regular, the relation has a stable flag with a flat plateau, and the maximum compression force is higher with respect to the previous case. Regarding the stiffness, it is larger in this case both in tension and in compression, and the theoretical stiffness value is exceeded in the initial linear range too. Finally and consequently, maximum force demand is higher.

Considering advantages and problem of fixed versus hinged node configuration, even if the response of the fixed-fixed spring is more stable and produces better behavior in compression, the increase in stresses makes more difficult to reach larger displacements given the same spring configuration and avoiding its rupture. On the other side, manufacturing a fixed-hinged spring is supposed to be more complex than a fixed-fixed one.

5.3 SUPERELASTIC COIL SPRING EXPERIMENTAL TESTS

Experimental tests have been performed on superelastic material coil springs produced by *SAES Getters*, an Italian shape memory alloy manufacturer, during March and April 2009. The objective of the experimental campaign is to check the response of spring devices and

(a) spring in tension
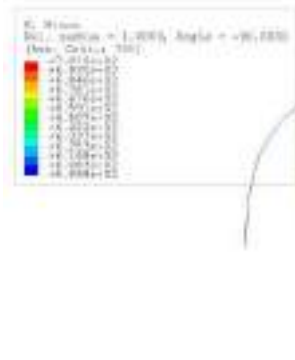
(b) spring in compression

Figure 5.20. Superelastic fixed-fixed spring deformed mesh in tension-compression test

to compare it with the results provided by FE analysis to validate the numerical analysis procedure. If it is verified that the numerical model is able to predict the response of the force-displacement behavior of the devices, the FE investigation can be used as a powerful tool to characterize the nonlinear spring behavior.

The tested specimens are described in Section 5.3.1, while the experimental set up in Section 5.3.2. Test results are then presented in Section 5.3.3 and the experimental data analysis for the material characterization in Section 5.3.4. Finally the numerical and experimental testing result comparison is carried out in Section 5.3.5.
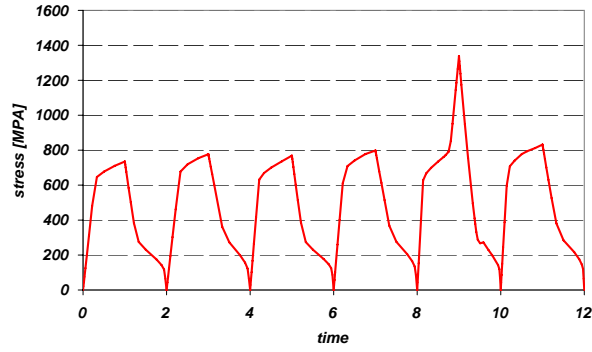
(a) maximum stresses node in tension
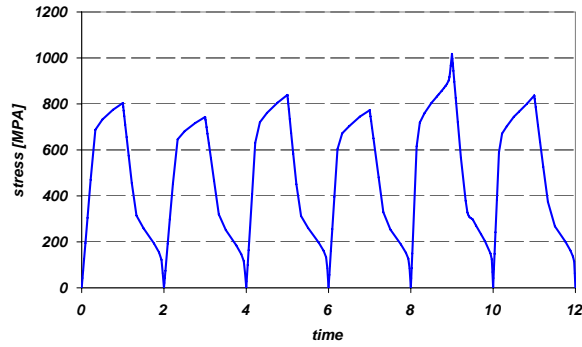
(b) maximum stresses node in compression

Figure 5.21. Superelastic fixed-fixed spring stresses in tension-compression test

5.3.1   Experimental Specimens Geometry

Specimens used in the tests are characterized by a reduced geometry and different material properties with respect to the configurations investigated in the previous sections of the present chapter, thus far from the type of device which could be used for seismic isolation restrain purpose. The coil is made of a 1mm diameter superelastic shape memory alloy wire. It has been winded on a circular bar of 5mm radius. Hence $d_w = 1$mm and $R = 3$mm. The coil height is about $s = 7.5$mm. Three main non-dimensional ratios are considered for the spring geometrical characterization:

- wire diameter - initial coil radius:

$$\eta_1 = \frac{d_w}{R} = 0.33 \qquad (5.11)$$
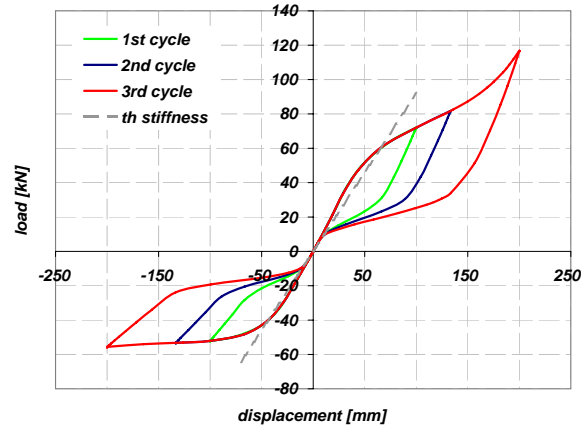
Figure 5.22. Superelastic fixed-fixed spring tension-compression test results and theoretical spring stiffness comparison (positive-tension, negative-compression convention adopted)
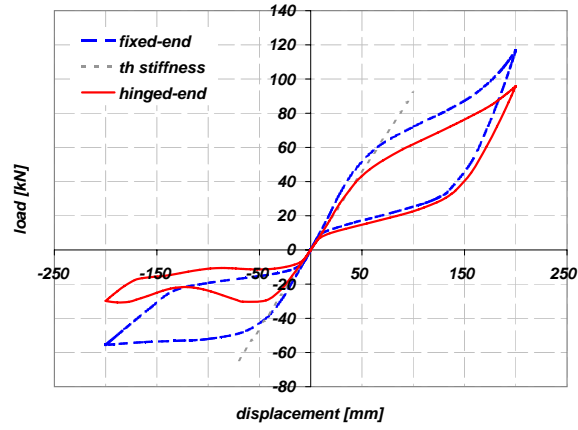
Figure 5.23. Superelastic spring test FE results comparison

- wire diameter - initial coil height:

$$\eta_2 = \frac{d_w}{s} = 0.13 \qquad (5.12)$$

- initial coil radius - initial coil height:

$$\eta_3 = \frac{R}{s} = 0.40 \qquad (5.13)$$

The comparison of the geometrical ratios between the specimen configuration and the spring as considered in Section 5.2.2 shows that the η_3 is about the same (Equation (5.10) vs Equation (5.13)), while η_1 and η_2 in this case are about one half of the previous (Equation (5.8) vs Equation (5.11) and Equation (5.9) vs Equation (5.12) respectively).

Even if in reduced dimensions, the tested specimens are characterized by geometrical ratios not far from an hypothetical device used as a lateral restrain. Three specimen configurations have been manufactured and are shown in Figure 5.24, respectively with 3 coils (S1A, in Figure 5.24a), 4 coils (S2A, in Figure 5.24b), and 5 coils (S3A, in Figure 5.24c).

(a) S1A

(b) S2A

(c) S3A

Figure 5.24. Tested superelastic spring specimens

5.3.2 Experimental Set-Up

All the tests have been performed at SAES Getters laboratories, in Lainate, Milano, Italy.

(a) Test Machine

For the uniaxial test in tension and in compression, the *Sun 500* universal testing machine produced by *Galdabini spa* was used. The Sun 500 test system is characterized by two column rigid system with 5kN maximum capacity ensuring high static and semi-dynamic

resistance and moveable crossheads. The dimensions and technical specifications are summarized in Table 5.2 and a picture of the testing machine during the experiments is shown in Figure 5.25. The control hardware unit consists of digital electronics with

(a) overall view

(b) detail of the clamping pliers

Figure 5.25. Testing machine, Galdabini Sun 500

SDM technology and 32-bit microprocessor and control is based on closed-loop test with dedicated units measuring load, stroke and deformation.

Table 5.2. Dimensions and technical specification for test machine Galdabini Sun 500

Galdabini Sun 500	
total height	$1685mm$
width	$730mm$
depth	$650mm$
load frame capacity	$5kN$
load reading resolution	$1/200000\ s^{-1}$
stroke reading resolution	$1\mu m$
minimum speed at maximum load	$0.0005mm/min$
maximum speed at maximum load	$500mm/min$
controlled total stroke	$1000\ mm$
maximum distance between connecting adapters	$1000\ mm$
maximum distance between columns	$350\ mm$

(b)   Clamping System

The clamping system solution has been an issue in the experimental tests campaign. Due to the particular material and to the dimension of the coil wire it has not been possible to weld the spring dead coil to a particular clamping system. The used solution is shown in Figure 5.26. It consists of an allen screw whose head diameter is the same as the winding

(a) first view   (b) second view

Figure 5.26. Spring clamping system solution

bar diameter. The coils fit around it and the dead coil is fastened using a bold and a little steel plate inserted in the screw as well. The screw has then been fastened at the clamping plier of the testing machine.

5.3.3   Results of Experimental Testing

The different protocols and results of tension-compression axial tests on the springs are described in the present section. In general, from the results it turned out that the clamping system influenced the tests. This is due to the contact between the coil wire and the head of the allen screw.

In tension, being the allen screw head of the same diameter of the internal coil diameter when the spring is not loaded, it prevents the reduction of diameter of the coil providing more stiffness and reducing the expected displacement for the same level of force. In compression the influence is even more important because it limits significantly the maximum displacement capability of the spring before reaching the contact between the elements. Moreover, the reduction of the free length of the spring due to the clamping system is particularly important especially for the shortest specimen. This aspect increases the buckling load in the member with respect to theoretical not restrained condition.

Nevertheless, results turned out to be very interesting, regardless of the few problems related to the boundary conditions.

(a)   Specimen S1

The specimen S1 is the 3 coils spring, the total axis length is about $h_{sS1} = 22.87\text{mm}$ (as shown in Figure 5.24a). Two displacement controlled tests have been performed on the spring, considering the following displacement histories:

- test #1: ± 0mm, $+4$mm, -4mm, $+8$mm, -8mm, $+12$mm, -12mm, ± 0mm

- test #2: ± 0mm, $+15$mm, -10mm, $+20$mm, -10mm, $+25$mm, -10mm, $+30$mm

Maximum displacement in compression Δ_{cS1} and in tension Δ_{tS1} over the spring axis length ratios are respectively:

$$\frac{\Delta_{cS1}}{h_{sS1}} = 52\% \qquad \frac{\Delta_{tS1}}{h_{sS1}} = 131\% \tag{5.14}$$

Limitation in compression displacement is due to boundary condition geometry compatibility. The test velocity was constant and equal to 4mm/min. Two snapshots of the deformed spring during the test are shown in Figure 5.27. Results of the performed

(a) maximum compression (-15mm)   (b) maximum tension ($+30$mm)

Figure 5.27. Specimen S1 experimental test pictures

tests are shown in Figure 5.28.

Data report a quite stable global superelastic response of the axially loaded spring. Some irregularities in the response curve is shown in correspondence of large positive displacements. It is due to the contact phenomena between the coil wire and the clamping system. After the test, the specimen has been checked and measured. The spring wire resulted undamaged and the initial geometry was perfectly recovered.
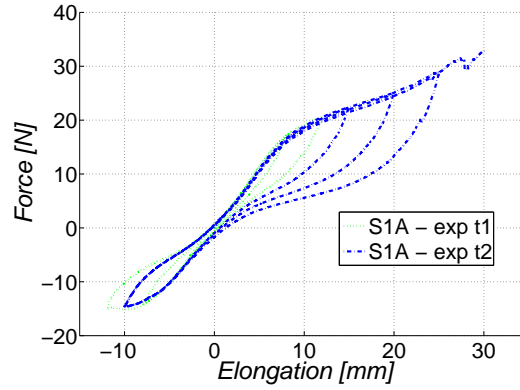
Figure 5.28. Specimen S1 experimental test results

(b)   Specimen S2

The specimen S2 is the 4 coils spring, the total axis length is about $h_{sS2} = 27.61\text{mm}$ (as shown in Figure 5.24b). Two displacement controlled tests have been performed on the spring, considering the following displacement histories:

- test #1: $\pm 0\text{mm}$, $+10\text{mm}$, -10mm, $+15\text{mm}$, -15mm, $+20\text{mm}$, -20mm, $\pm 0\text{mm}$

- test #2: $\pm 0\text{mm}$, $+25\text{mm}$, -10mm, $+30\text{mm}$, -10mm, $+35\text{mm}$, -10mm, $+40\text{mm}$, $\pm 0\text{mm}$

Maximum displacement in compression Δ_{cS2} and in tension Δ_{tS2} over the spring axis length ratios are respectively:

$$\frac{\Delta_{cS2}}{h_{sS2}} = 72\% \qquad \frac{\Delta_{tS2}}{h_{sS2}} = 145\% \tag{5.15}$$

Limitation in compression displacement is due to boundary condition geometry compatibility. The test velocity was constant and equal to 4mm/min. Two snapshots of the deformed spring during the test is shown in Figure 5.29. Results of the performed tests are shown in Figure 5.30.

During the maximum compression displacement, contact between the coil wire and the clamping system was reached as shown in Figure 5.29a and this led to maximum compression force peak. Beside this, the spring system is characterized by a very good and stable flag-shaped response. Again the specimen shows a perfect superelastic behavior. After the test, the spring wire resulted undamage and the initial geometry was perfectly recovered.

(a) maximum compression (−20mm) (b) maximum tension (+40mm)

Figure 5.29. Specimen S2 experimental test pictures
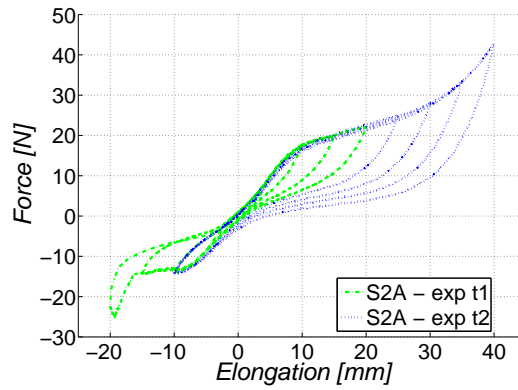
Figure 5.30. Specimen S2 experimental test results

(c) *Specimen S3*

The specimen S3 is the 5 coils spring, the total axis length is about $h_{sS3} = 35.07$mm (as shown in Figure 5.24c). A displacement controlled tests have been performed on the spring, considering the following displacement history:

- test #1: ±0mm, +10mm, −10mm, +20mm, −10mm, +40mm, −15mm, ±0mm

Maximum displacement in compression Δ_{cS3} and in tension Δ_{tS3} over the spring axis length ratios are respectively:

$$\frac{\Delta_{cS3}}{h_{sS3}} = 43\% \qquad \frac{\Delta_{tS3}}{h_{sS3}} = 114\% \qquad (5.16)$$

(a) maximum compression (−15mm)   (b) maximum tension (+40mm)

Figure 5.31. specimen S3 experimental test pictures.
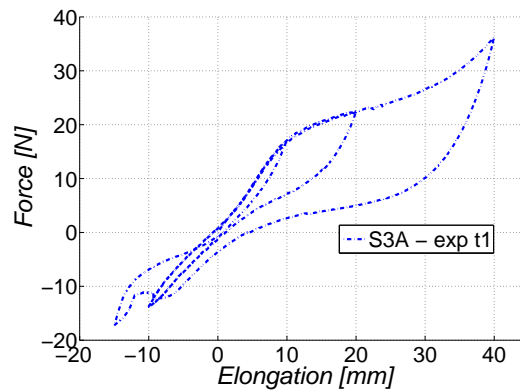
Figure 5.32. specimen S3 experimental test results.

Limitation in compression displacement is due to boundary condition geometry compatibility. The test velocity was constant and equal to 4mm/min. Two snapshots of the deformed spring during the test is shown in Figure 5.31. Results of the performed tests are shown in Figure 5.32. The spring system is characterized by a very good and stable flag-shaped response and the specimen shows a perfect superelastic behavior, without residual deformations of damages.

(d)   Conclusions on Experimental Test Results

The coil spring system response has been investigated in experimental tests. Results show a very good superelastic behavior with almost negligible residual displacements even after displacements in tension of the same order of magnitude of the initial spring

axis length. No damage was registered in any specimen. Response turned out to be not symmetric between tension and compression due to buckling instability and impossibility of reaching the same force levels in compression as in tension. Test results proved anyway that given a particular spring geometry, the yielding elongations and the elongation at which hardening after the plateau occurs are not independent variables. To avoid second hardening, a maximum elongation of the order of 4 or 5 times the yielding displacement (i.e. maximum displacement ductility) has not to be exceeded.

5.3.4   Experimental Data Analysis and Material Characterization

To manufacture the spring, the original wire is subjected to thermo-mechanical treatments which alter the original properties. Hence it is not possible to perform tests on the original wire to detect the material properties. For this reason, the experimental results relative to specimen *S1A* are used to compute material properties through a trial and error fitting process. Accordingly, several numerical analyses were performed considering the given geometry, changing between different material properties until the model has been able to describe in a suitable way this single test results. Then, the final parameters have been used to predict the results of specimens *S2A* and *S3A*. Since they have been found independently from these results, this is a correct validation process. The final values are reported in this section.

Referring to the model shown in Figure 5.33 and defined in ABAQUS [2003], the material parameters are reported in Table 5.3. The corresponding material, considering
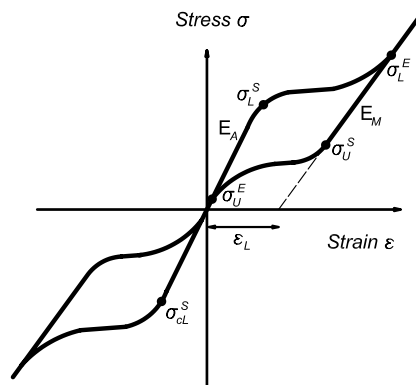
Figure 5.33. SMA superelastic uni-axial stress-strain

a simple uniaxial tension test using a FE analysis program ABAQUS [2003], shows the behavior reported in Figure 5.34. No temperature dependence has been considered in the material properties.

Table 5.3. SMA superelastic uni-axial stress-strain parameters

SMA superelastic ($d_w = 1mm$)					
$E_A\ [MPa]$	32000	$\sigma_L^S\ [MPa]$	350	$\sigma_U^E\ [MPa]$	10
$E_M\ [MPa]$	12000	$\sigma_L^E\ [MPa]$	375	$\sigma_{cL}^S\ [MPa]$	350
$\nu_A = \nu_M$	0.33	$\sigma_U^S\ [MPa]$	200	$\epsilon^L\ [-]$	0.07
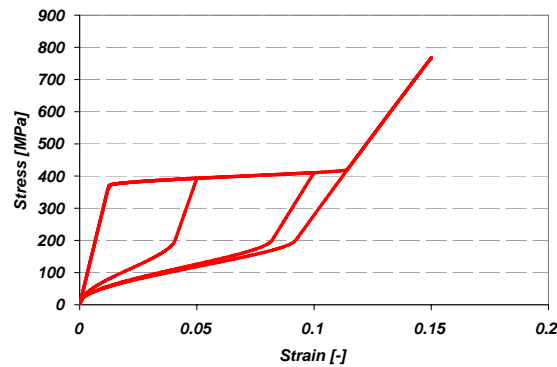
Figure 5.34. SMA constitutive relation for the considered specimen

5.3.5 Numerical and Experimental Testing Result Comparison

Numerical analyses have been performed to reproduce the response of the same specimens tested in the experimental campaign. The philosophy followed in the modeling is to use a model as simple as possible. For this reason, the spring has been modeled using two-nodes simple beam elements reproducing the wire axis geometry. Since the elements are straight, each single coil has been approximated using 36 elements. The circular section has been assigned and the superelastic material properties are the ones described in Section 5.3.4. Regarding the boundary conditions, even if the clamping system is quite complex to be described, end nodes are modeled as fixed.

(a)   Specimen S1

Comparison between experimental and numerical test result for specimen S1 is shown in Figure 5.35. The numerical model describes very well the experimental test results. Of course it does not reproduce the clamping system contact effect on the coil wire, but beside this, the experimental response is very well modeled.
In tension, the initial elastic stiffness, the loading cycles and the unloading cycles resulting from the FE analysis are very close to the experimental data. In compression the FE
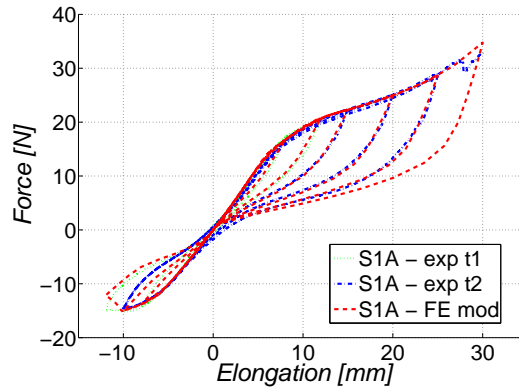
Figure 5.35. Specimen S1 experimental and numerical test result comparison

analysis underestimates the unloading stiffness. Moreover it predicts a buckling which is not occurring in the experiments. Probably this is due to the fact that the model does not take into account the clamping system effectiveness in reducing the free length of the spring and in conditioning the displacement capability of the coil wire.

(b)   Specimen S2

Comparison between experiments and numerical test result for specimen S2 is shown in Figure 5.36. Regarding the response of specimen S2, the FE model is still quite good in
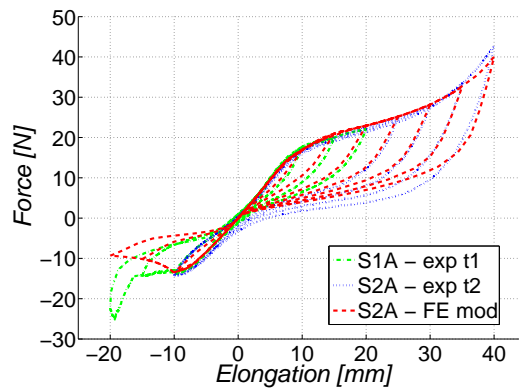
Figure 5.36. Specimen S2 experimental and numerical test result comparison

predicting the experimental data.

In compression, numerical results overestimate the buckling, while they do not consider the contact problem due to the clamping system. Of course this is due to the incapacity

of the simple model used to describe this phenomenon. In tension response, the comparison between experiments and numerics shows that for low-displacement cycles the unloading stiffness is a bit underestimated, as well as the maximum force and the residual displacement at the end of each large-displacement cycle. Anyway, due to the fact that differences are very small, numerical result reproduces very well the specimen force-displacement behavior.

(c)   Specimen S3

Comparison between experimental and numerical test result for specimen S3 is shown in Figure 5.37. Again, the FE model can be considered quite good in predicting the
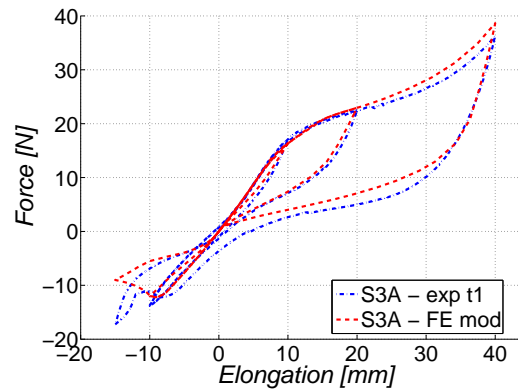
Figure 5.37. Specimen S3 experimental and numerical test result comparison

experimental response. The instability in compression is not captured perfectly, the maximum force is slightly overestimated, and the residuals are slightly underestimated. Nevertheless elastic limit and after yielding behavior are well described both in tension and in compression.

(d)   Conclusions on Experimental and Numerical Test Result Comparison

A very simple model has been used to predict the response of superelastic coil springs tested and results are very good. There are some differences between the real response and the FE model results, but they can be considered negligible and the numerical analysis is able to predict all the main experimental data in terms of force-displacement relation. The most important discrepancies between numerical and experimental results is the spring behavior in compression. Probably these are ascribed to the fixed end boundary condition which has been assumed for the numerical model of the spring. Nevertheless, due to its simplicity, the finite element model proposed in the present work can be used to perform

fast analyses and it is an important tool for pre-design springs which are supposed to reach a design maximum force and a design displacement.

5.4   Conclusions on Nonlinear Superelastic Coil Spring System Properties

In the present chapter, investigation on the mechanical properties of a coil spring system has been performed. Coil spring is a classical device used in mechanics and characterized by well defined theoretical design principles. Anyway, springs have been used almost only in their elastic range. On the contrary, here the superelastic response has been investigated too, from the basic concepts of plasticization of the wire section to the complex numerical response of superelastic material coil springs validated by experimental data. Main concerns were the geometrical and material nonlinearity effects.

Hence a theoretical, numerical, and experimental campaign has been performed. The main findings are listed next.

- The coil spring system turns out to be a very flexible device. The design is controlled by different almost independent parameters like the *coil radius*, the *wire diameter*, and the *pitch angle* both for the linear properties, in particular in the definition of the *initial stiffness*, and for the nonlinear ones, like in the definition of the *linear elastic limit*.
  This leads to the fact that in theory, given a needed initial stiffness and a plastic limit, it is always possible to find a particular spring configuration which is able to provide the needed properties.

- The possibility of defining as a free parameter the *number of coils* allows to design springs able to reach any displacement capability responding in the linear or in the nonlinear range.
  Obviously increasing the spring displacement capability only changing the number of coils affects the initial stiffness of the spring. On the contrary the yielding limit is not affected because it is almost independent from the length of the spring. Anyway the chance of modifying the number of coils can be used together with the other design parameters to reach the final needed configuration.
  If the coil spring is designed to behave in the plastic range, the number of coils can be designed to reach the needed displacement capability without exceeding the rupture material strain. In particular, the pitch and the coil radius can be designed for a total elongation which can exceed the 100% with respect to the initial coil height without reaching the rupture. Nevertheless it has to be taken into account that in a inelastic spring the maximum displacement ductility, evaluated as the rupture strain displacement over yielding displacement in the coil axis direction, is limited. For usual configurations its maximum is about 4 or 5.

- In Dolce and Cardone [2001a], it was concluded that SMA material subjected to torsion shows great potentials as component in seismic resistant devices but this behavior is quite difficult to reproduce. The spring device, which is mainly working in torsion, leads to a more rational utilization of the material and at the same time is a quite simple configuration to be manufactured.
Moreover, an ideal optimization of the material would lead to use a pipe section instead of circular section. This would not affect significantly the technical properties of the device, in particular the force and displacement capacity, because in the spring torsionally responding most of the contribution is given by exterior material layers. On the other side eventual advantages have to be compared in the material saving and in the device manufacturing increasing complexity.

- The boundary conditions affects quite significantly the spring response. Of course the response is more stable for the spring end being fixed but this configuration produces higher stress concentrations close to the bounds. The hinged-fixed case is affected by relevant compression buckling but internal stresses are lower than the previous case for the same displacements.

- Both experimental and numerical responses of superelastic material coil spring consist of a flag-shaped force-displacement relation. Hence the superelastic spring is a recentering-theoretical zero residual displacement device.

- The spring linear limit can be easily identified and it is due to both material yielding but also large-displacement geometrical issues. For the initial range the linear approximation provides good results and the approximate expressions are reliable for initial stiffness computation. Very simple finite element model is able to reproduce the general experimental spring behavior with enough precision for the engineering purpose.

Based on the previous, coil spring system could be designed to be used as lateral restrainer made of superelastic material. It provides a stable flag-shaped force-displacement response and large displacement capability with limited overall dimensions.
An important advantage of this device configurations is the large freedom in design. Regardless the conditions to be satisfied for the restrain device application, the availability of many free parameters leads to a simple design to meet the given requirements.

Hence the superelastic manufactured spring seems suitable to be used as a lateral restrainer for base isolation devices. Anyway, theoretically the superelastic spring field of application is very large. All the applications for which a superelastic recentering effect and a relatively large displacement capability is attractive can take advantage of this device configuration. The preliminary device design can be accomplished using the proposed FE model which from this investigation turned out to be able to describe the superelastic spring behavior, as the modeling-experimental result matching suggests.

6. Innovative Superelastic Isolation Device

6.1 INTRODUCTION

In this chapter, the conception of an innovative base isolation device is presented. The aim of the design process is to get a configuration providing good isolation and recentering properties. The idea is to use superelastic material devices as lateral restraining system components. This is to make profit of the shape memory alloy material properties, which have been already introduced in Chapter 3, and of the SMA device hysteretic response, which has been investigated in Chapter 4.

In general, an optimal device should be able to:

- transmit the vertical load both in the seismic and in the most demanding non-seismic condition;

- provide a suitable lateral stiffness under the seismic design condition conditioning the structural effective period;

- limit the base shear transmittable to the superstructure;

- accommodate most of the displacement demand of the isolated structure without loss of strength;

- reduce the residual displacements at the end of the design seismic event through some lateral recentering restrainer devices;

- supply a relevant initial stiffness and strength to ensure the isolation system rigidity under service loads, like wind;

- permit easily to replace any components.

To meet the previous requirements, the new system conception is based on two different contributions:

1. a device intended to carry and transmit the vertical load, and

2. a device working horizontally as a lateral restrainer.

Hence the idea is to decouple lateral and vertical load transmission elements in the system to optimize the design of the both of them.

The solution we propose consists of a *flat sliding bearing* and a superelastic material lateral restrainer manufactured using Nitinol *helical spring* components.

The horizontal slider is supposed to *carry the vertical load* and to *provide lateral displacement capability* to the structure. Being its design based on a particular friction coefficient which can be either almost negligible or relevant, it also provide *high initial stiffness*, *yielding shear*, and some *energy dissipation*. An idea of the properties and of the behavior of the lateral slider device is proposed in Section 6.2.

Superelastic spring system is then demanded to act as a recentering lateral restrainer system. The choice of the spring shape and of its horizontal orientation in the direction of the motion, is due to the need of undergoing large deformations together with limitation of the maximum material stress and reduction of the device dimensions. As resulting from the numerical and experimental investigations on superelastic springs reported in Chapter 5, such a lateral restrainer system is characterized by *large displacement capability without loss of strength* due to high deformability of the springs, *limitation of the maximum transmittable shear* due to the nonlinearity of the constitutive relation of the material, and theoretical *recentering* action given by the superelastic behavior of the springs. The global spring system response considering different suitable configurations and computed through numerical analyses is described in Section 6.3. In the same section, a simplified design procedure for spring systems is proposed. The motivation is to provide a pre-design tool to propose a suitable spring configuration as a function of the design displacement capability and design shear force.

Section 6.4 presents then a practical example of superelastic isolation bearing device design equivalent to an actual isolation device. The technical properties of its final configuration are showed as well, together with comparison with other SMA isolation configuration proposals.

Finally, in Section 6.5 the main conclusions on the device design are reported.

6.2   FLAT SLIDER DEVICE

A flat slider device is a bearing transmitting the vertical load in a structure consisting of a steel interface in contact with a polymer material interface. The most common type of sliding bearing is characterized by the use of steel and teflon, or polytetrafluoroethylene (*PTFE*), interfaces. An example of this bearing device is shown in Figure 6.1.

Flat slider devices have been traditionally used to accommodate thermal movements and effects of pre-stressing, creep and shrinkage in bridge or long structure. More recently, they have been proposed as a part of seismic isolation systems (see Kelly [1986]). In the present work we consider this last application possibility.

Several investigations have been performed to identify slider behavior in seismic conditions. An overview on some of the most interesting contributions is reported in

(a) lateral view   (b) plan view
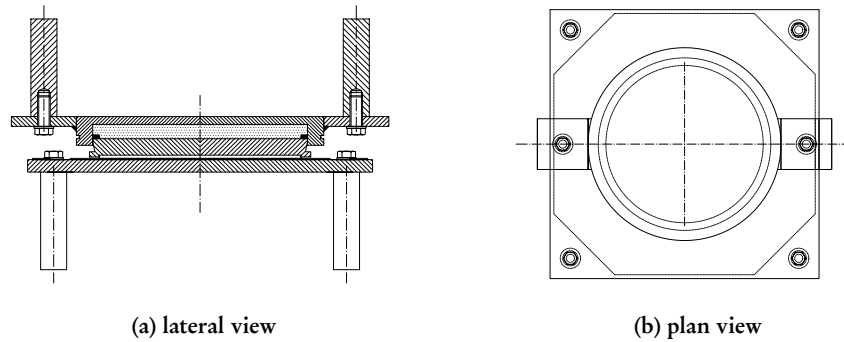
Figure 6.1. Flat slider device (courtesy of *AGOM International srl*)

Section 6.2.1.

Basics on a very simplified model used to describe the frictional response and the device design principles followed in the present work are then reported in Section 6.2.2.

6.2.1 Previous Investigations on Flat Sliders for Seismic Applications

Some of the most interesting contributions on the evaluation of flat slider system properties in seismic base isolation applications are reported in the present section. Even if the most common application of slider elements in seismic isolation is relative to friction pendulum system (see Section 2.4.3), in the present summary the focus is only on flat devices.

In Mokha *et al.* [1990] the frictional properties of sheet type teflon steel interfaces in relation to their application in sliding bearings for base-isolated building and bridge structures were investigated. Through experimental tests conducted on teflon-steel interfaces, the effect of sliding velocity, sliding acceleration, bearing pressure, type of teflon, and surface finish on the frictional characteristics of sliding bearings have been identified. It was found that sliding acceleration has insignificant effects on the recorded values of frictional force. On the contrary, the authors recognized that sliding velocity and bearing pressure can have important effects. Differences between breakaway (or static) coefficient of friction and sliding (or kinetic) coefficient of friction were studied as well. The main conclusion on the slider application was that there are two important advantages in sliding isolation systems with restoring force. First, the function of carrying the vertical load and the function of providing horizontal stiffness at the isolation interface are separated. This results in a more stable system that eliminates the need for a fail-safe mechanism. Second, sliding systems with weak restoring force are insensitive to variations in the frequency content of ground excitation and tend to limit the intensity of the force imparted to the superstructure. This insensitivity to the frequency content of excitation is the most important advantage of sliding isolation systems (as also recognized later in Dolce

et al. [2005]). In Constantinou *et al.* [1990] the same authors presented a mathematical model suitable to describe the teflon sliding bearing behavior.

Proposals of isolation systems based on sliding bearings together with other lateral restraining elements were presented in Constantinou *et al.* [1991] and Bondonet and Filiatrault [1997], being in this last one proposed the possibility of using a superelastic material device, as already reported in Section 3.6.2.

An actively controllable friction sliding isolation bearing was proposed in Nagarajaiah *et al.* [1993] focusing on the importance of providing a variable friction force to improve the structural seismic response.

Makris and Chang [2000] assessed the efficiency of various dissipative mechanisms to protect structures from pulse-type and near-source ground motions in conjunction with base isolation. Dissipation forces of the plastic (friction) type resulted very efficient in reducing displacement demands although occasionally they were responsible for substantial permanent displacements. It was found that the benefits by hysteretic dissipation are nearly indifferent to the level of the yield displacement of the hysteretic mechanism and that they depend primarily on the level of the plastic (friction) force. The study concluded that a combination of relatively low friction and viscous forces is attractive since base displacements are substantially reduced without appreciably increasing base shears and superstructure accelerations.

Jangid [2000] proposed an expression to optimize the friction force considering a multi degree of freedom system base isolated using sliding elements. The optimization was anyway targeted only to reduce the floor acceleration demand.

In Higashino *et al.* [2003] the fundamental characteristics and durability of a low friction sliding bearing were studied performing experimental tests and all the results indicated that the device shows stable characteristics and good duration properties for being used in seismic isolation.

Dolce *et al.* [2005] is probably the most important contribution on sliding device for seismic isolation applications. This is based on a comprehensive program of experimental tests on steel-teflon interfaces in order to fully investigate the effects of sliding velocity, contact pressure, air temperature, number of cycles and state of lubrication, on the mechanical behavior of steel-teflon sliders. Friction loops as a function of different loading history are reported in Figure 6.2. Based on the experimental outcomes, the following conclusions were drawn:

- the coefficient of friction increases rapidly with velocity, up to a certain velocity value, beyond which it remains almost constant, as shown in Figure 6.4; being such value lower than earthquake induced maximum velocities, the design value of the frictional force in seismic applications can be assumed to be independent from frequency of loading and displacement amplitude;

- the sliding friction coefficient of steel-teflon interfaces reduces while increasing pressure; moreover it increases while increasing velocity and while decreasing air

(a) triangular displacement history   (b) sinusoidal displacement history
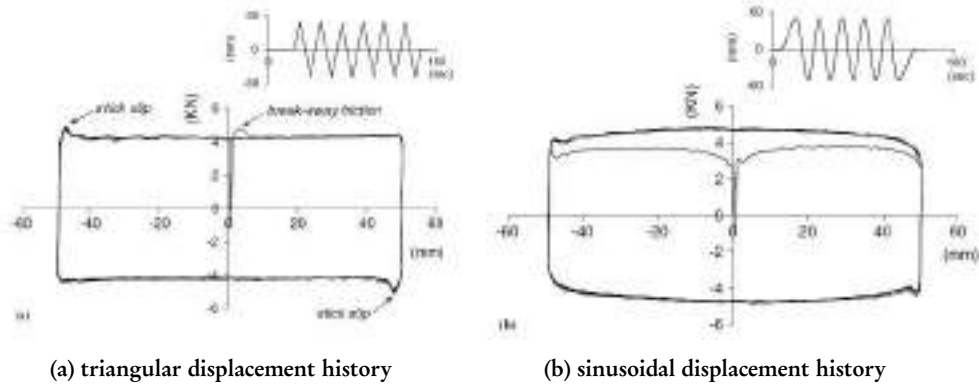
Figure 6.2. Typical frictional force displacement at low peak velocities (from Dolce *et al.* [2005])

(a) triangular displacement history   (b) sinusoidal displacement history
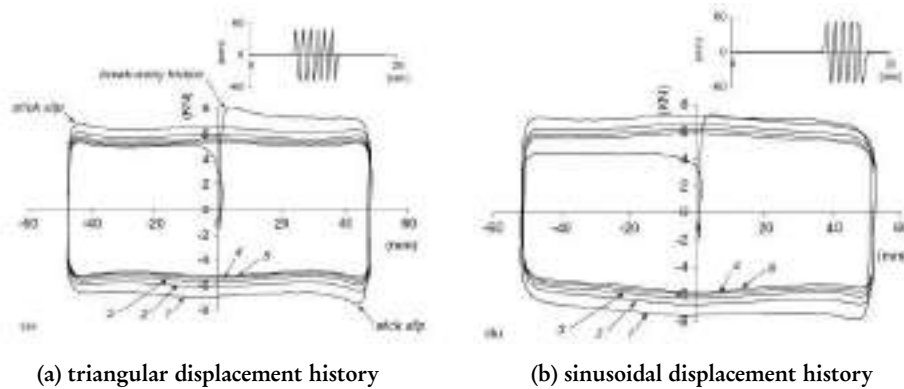
Figure 6.3. Typical frictional force displacement at high peak velocities (from Dolce *et al.* [2005])

temperature (see again Figure 6.4);

- the coefficient of friction tends to decrease during continuous loading cycles at high velocities (see Figure 6.3), due to self-heating of the sliding interfaces: the phenomenon is anyway exhausted in a few cycles, due to the attainment of a new thermal equilibrium with the ambient;

- lubrication considerably reduces the frictional resistance of steel-teflon sliding interfaces and, as a consequence, the wear of teflon.

Several isolation systems based on sliding bearings were implemented and tested by the same research group. The most important results are reported in Cardone *et al.* [2003] (the proposed device configuration has been reported in Figure 3.21), Dolce *et al.* [2007a], and Dolce *et al.* [2007b].

(a) low temperature   (b) high temperature
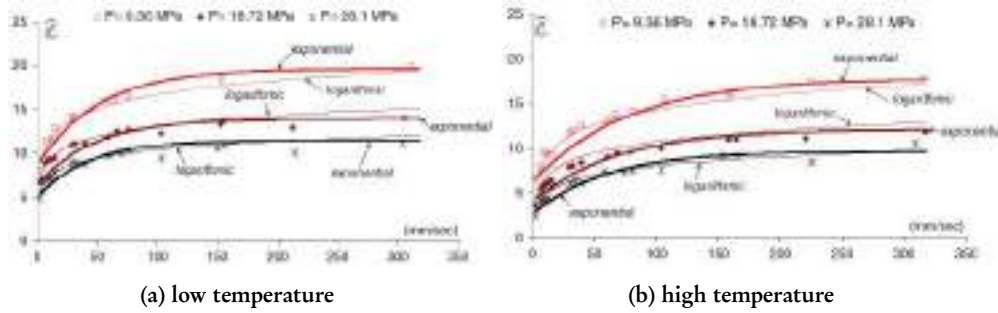
Figure 6.4. Variation of the friction coefficient with sliding velocity, air temperature and bearing pressure (from Dolce *et al.* [2005])

6.2.2   Flat Slider Device Design Principles

In general, a sliding system is able to limit the transmittable force to a predefined level function of the coefficient of friction which is almost independent from the intensity and the spectral content of the earthquake. Important drawbacks in seismic isolation applications are anyway the large dispersion in the peak displacements and the occurrence of residual displacements. A detailed description of advantages and disadvantages of flat sliding bearing systems in seismic isolation has been presented in Dolce *et al.* [2005].

In this work context, sliding bearings are intended to carry the vertical structural load supporting the weight of the superstructure and the force induced by the overturning moment. Furthermore, the eventuality of providing additional energy absorbing capacity is also considered, because of its favorable effects on structural response and energy dissipation (as noticed in Makris and Chang [2000]). To avoid the main disadvantages about the displacement control already mentioned, they are designed to work in parallel with lateral restoring and recentering elements.

The simplest model to describe the friction is the Coulomb friction law (see Dolce *et al.* [2005]), according which the friction force F_f can be defined as a function of the normal force F_n as:

$$F_f \le \mu F_n \tag{6.1}$$

For surfaces at rest relative to each other, $\mu = \mu_s$ in which μ_s is the coefficient of static friction, usually larger than its kinetic counterpart. The Coulomb friction may take any value from zero up to F_f, and the direction of the frictional force against a surface is opposite to the motion that surface would experience in the absence of friction. Thus, in the static case, the frictional force is exactly what it must be in order to prevent motion between the surfaces. The Coulomb approximation provides a threshold value for this force, above which motion would occur.

For surfaces in relative motion, $\mu = \mu_k$, where μ_k is the coefficient of kinetic friction. The Coulomb friction is equal to F_f, and the frictional force on each surface is exerted in

the direction opposite to its motion relative to the other surface.

Typical frictional force-displacement loops recorded during experimental tests are shown in Figure 6.2 and Figure 6.3. From these plot, it is possible to identify the breakaway friction, which is the maximum frictional force developed at the beginning of the cycle, function of the static friction coefficient, and the stick-slip, occurring at the motion reversal.

As resulting from data in Figure 6.2 and Figure 6.3, a first order approximation to describe the friction model can be a *rigid-plastic model* in which the yielding force is computed considering the Coulomb relation. Due to the possibility of lubrification of the sliding surface, almost zero-friction coefficient device can be designed as well as already reported in Dolce *et al.* [2005].

In this investigation the flat slider bearing systems are designed to be able to carry the vertical load and to provide a design lateral force. Simple rigid-plastic behavior is then considered as a function of the lateral displacement of the device, neglecting the dependence of the response from other quantities.

Anyway, two possible conditions are considered in our design configurations:

- an high friction coefficient device, which is supposed to provide some energy dissipation,

- a very low friction device, in which the friction coefficient is negligible, not affecting the system base shear response.

For the two of them the geometry is the same, again the one shown in Figure 6.1, and it is assumed that differences are only given by different sliding interface materials or lubrification.

To describe their response elastoplastic model is used. The yielding displacement is estimated of the order of few millimeters, to get a force-displacement relation very close to rigid-plastic model. The yielding force, computed as a function of the friction coefficient (about zero in the second type) and the vertical load, is a design variable.

Obviously, the slider system design can be performed also considering several devices with different friction coefficient, in order to get the requested friction force in the global structure regardless its total mass. Overturning moment induced axial force variation is also taken into account in the design, as suggested in Priestley *et al.* [2007].

6.3 COIL SPRING LATERAL RESTRAINER

In Chapter 5, the possibility of using a single coil spring system as a lateral restrainer has been investigated. The main conclusions were that coil spring systems can be designed to be used as lateral restrainers made of superelastic material. They provide stable flag-shaped force-displacement response, large displacement capability with limited overall dimensions, and are characterized by large freedom in design to get the wanted

displacement capability and strength. Obviously, the force-displacement relation needed for a base isolation restraining system is impossible to be obtained using only one spring. Anyway, if springs are used, the design of complex spring system configuration based on several elements can be adopted and verified. The aim of the design process is to get a spring configuration characterized by a stable and symmetrical response, regardless the direction of the seismic motion in plan. The spring system response has been checked using a numerical model which has been validated with experimental test results (as reported in Chapter 5).

An overview of the seismic applications in which the spring system has been proposed in previous works is reported in Section 6.3.1. The response of a system composed by two spring acting in parallel is presented in Section 6.3.2. The response of a system composed by eight springs in radial position is then reported in Section 6.3.3. A simplified procedure for nonlinear spring system preliminary design is described in Section 6.3.4.

6.3.1   Previous Investigations on Coil Spring System for Dissipation and Restraining

The coil spring is a mechanical device class which has been widely used since the beginning of mechanical engineering. On overview of the classical application is provided in Wahl [1963]. In this section, the goal is to present a limited number of relevant works in which the spring has been proposed for innovative applications and which are somehow close to the idea of using superelastic spring as a lateral restrainers in base isolation applications.

From our point of view the most interesting contribution is the investigation presented in Constantinou *et al.* [1991] on *sliding bearing and helical steel spring* isolation system. The idea to decouple the vertical load transmission from the shear resisting system is
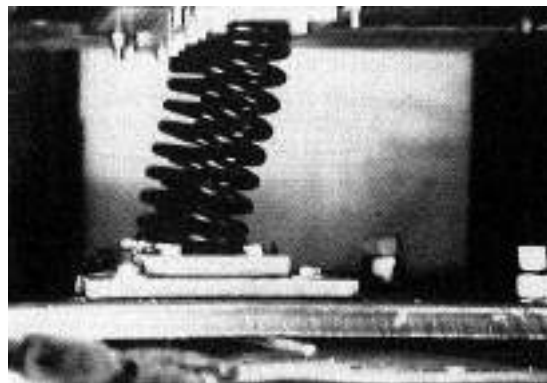
Figure 6.5. Helical steel spring unit under deformation (from Constantinou *et al.* [1991])

interesting and has been re-proposed in the present work. Anyway, the helical spring was applied in the vertical direction, hence it was deforming laterally, not axially, being

(a) friction only   (b) spring + friction
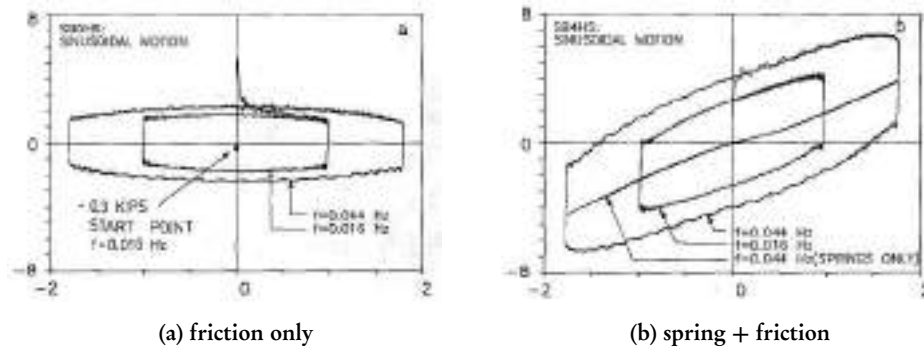
Figure 6.6. Force displacement loops of isolation system (from Constantinou *et al.* [1991])

not very efficient. This is reported in Figure 6.5, reprinted from the original paper. The device has been experimentally tested and the resulting hysteresis of the friction system is shown in Figure 6.6a. The total response, taking into account the spring contribution is shown in Figure 6.6b. It turns out that the steel spring is responding completely elastically and the displacement is so small that the geometrical nonlinearity, which it is expected to significantly affect the response for large displacements, is in this case negligible.

The idea of using lateral spring restrainers for isolation bearing was proposed in Bondonet and Filiatrault [1997]. In this case the chrome-vanadium springs were set with their axis along the direction of the bearing motion. The possibility of using SMA in the same work was considered but only as a theoretic assumption.

Liang and Rogers [1997] described the design of *SMA springs* for applications in vibration control. Recognizing that a spring made of SMA could be changing its mechanical stiffness as a function of the deformation, it could provide recovery stress (SME), or it could be designed reaching high damping capability, the authors were suggesting SMA spring application in active vibration control (see Figure 6.7). In Liang and Rogers [1997] a
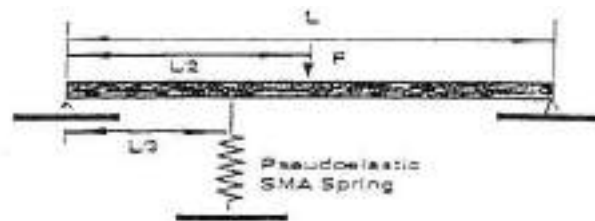
Figure 6.7. Schematic of vibration filter using a SMA spring (from Liang and Rogers [1997])

new spring design approach to take into account the nonlinear material response was also proposed, even if it does not seem straightforward in its application.

Ma and Cho [2008] presented the theoretical design of a new SMA based damper mainly consisting of of pre-tensioned superelastic SMA wires and two precompressed springs. The schematic of the device is shown in Figure 3.16. In this design conception *steel springs* are used as recentering elements while the dissipation is demanded to SMA wires.

6.3.2   Response of two Springs in Parallel

The first step in the present work is the investigation on the response of a system composed by two springs in parallel. We mean to have two springs, both of them connected with the point which has to be restrained and which is moved during the test, but being one in compression and the other in tension at the same time. The system configuration scheme is shown in Figure 6.8. Hence, even if the two springs are set in series, their effect on the restrained mass is the effect of two spring in parallel, that is the reason for the configuration name.
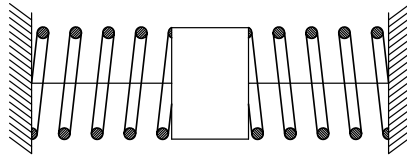
Figure 6.8. Schematic of the double spring system

(a)   Spring Geometrical Properties

A coil spring geometry is assumed: the coil radius is $R = 50$mm, the height of the spring axis is $h_s = 200$mm, the height of one single coil is 108mm, the number of coils is $n_c = 1.85$, and the wire section is circular, with diameter $d_w = 30$mm. Two boundary conditions are checked, the fixed-fixed one and the fixed-hinged one, as previously defined in Section 5.2.4. The same mesh geometry showing the different boundary condition cases are shown respectively in Figure 6.9a and in Figure 6.9b.

(b)   Material model properties

A superelastic shape memory alloy is assumed to be used for the spring manufacture, characterized by a flag-shaped stress-strain relation model, like the one shown in Figure 5.14. The material properties used in the analysis are compatible with actual manufactured high dissipation superelastic shape memory alloys (*SMA*) and are summarized in Table 6.1. It has been assumed in all the numerical tests involving SMA that the temperature does not affect the response of the material, which responds always accordingly to the same stress-strain relation.

(a) fixed-hinged case

(b) fixed-fixed case
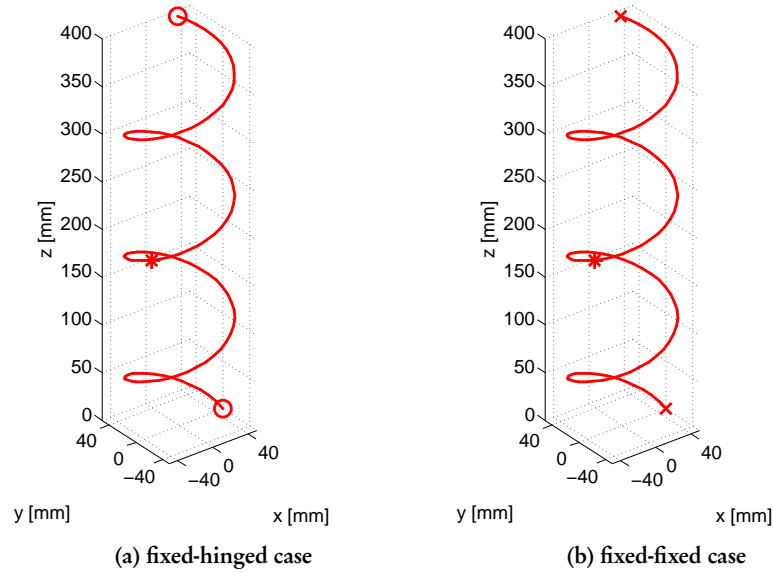
Figure 6.9. Spring mesh geometry for FE double spring test (point at which the displacement history is applied is identified with the star)

Table 6.1. Superelastic SMA material properties (flag-shaped model as defined in Figure 5.14) used in the FE modeling

SMA material properties (flag-shaped model)		
1st transf. stress	σ_1	600 MPa
2nd transf. stress	σ_2	800 MPa
3rd transf. stress	σ_3	300 MPa
4th transf. stress	σ_4	100 MPa
rupture stress	σ_{max}	1200 MPa
plateau strain	ε_{pl}	5 %
initial Young modulus	E	45 GPa
final Young modulus	αE	15 GPa
Poisson ratio	ν	0.33

(c)   Numerical Test Results

Results are shown in Figure 6.10 for the fixed-hinged analysis and in Figure 6.11 for the fixed-fixed case. Of course resulting force-displacement relations are given by the sum of the tensile and compressive spring contributions. The comparison of the maximum

amplitude cycles is shown in Figure 6.12.

Differences in boundary conditions plays a key role in the definition of the spring
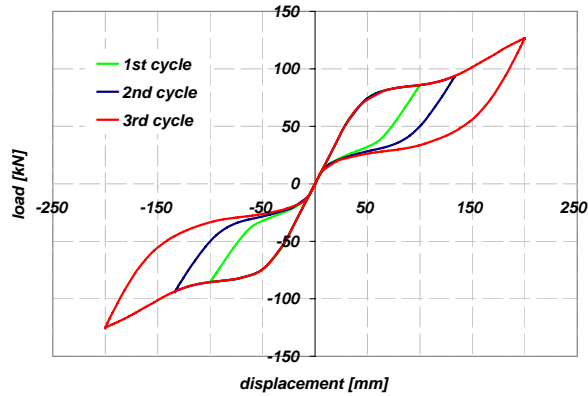
Figure 6.10. Superelastic double fixed-hinged spring tension-compression test results (positive-tension, negative-compression convention adopted)
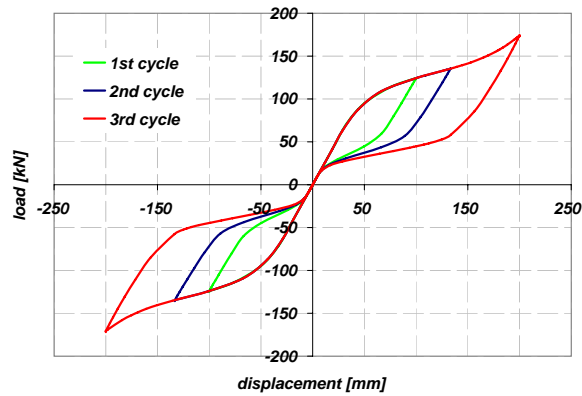
Figure 6.11. Superelastic fixed-fixed spring tension-compression test results (positive-tension, negative-compression convention adopted)

yielding limit and in the second stiffness of the device. Figure 6.12 clearly shows that the yielding shear capacity of the fixed-fixed system is almost 40% higher than the fixed-hinged one. On the other side, during the unload, the two systems provide a similar curve for the load as a function of the decreasing displacement. Regarding the system stiffness after yielding, the fixed-hinged second stiffness is very low, due to the buckling of the spring in
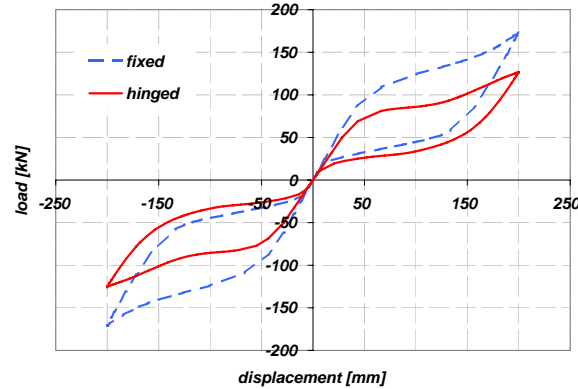
Figure 6.12. Superelastic double spring test FE results comparison

compression, while in the fixed-fixed case the second stiffness is a not negligible percentage of the initial one. Concerning the stress distribution in the SMA coil wire, the maximum demand is higher in the fixed-fixed case with respect to the fixed-hinged case.

(d)   Double Spring Configuration Conclusions

Considering the double spring configuration, the system response is very good. The compressive and tensile component summed together provide a final hysteresis regular and smooth, because the large deflection local problems which affect the compressive buckling and the tensile hardening compensate themselves. Theoretically, superelastic material constitutive law is working properly both in tension and in compression. Nonetheless, the use of two elements, one in tension and the other in compression at the same time, for sure is an advantage in favorite the recentering of the systems after buckling.

The two boundary conditions are characterized by different displacement capability before reaching the rupture stress and different yielding and maximum force. From the performed analysis the flat plateau given by the fixed-hinged solution can be an attractive property for a lateral restrain which is intended to work in the non-linear range limiting also the transmittable force.

6.3.3   Response of Eight Springs in Radial Position

The double spring configuration shown in Figure 6.8 and checked in Section 6.3.2 works properly if it is supposed to act as a restrainer in the direction of the two springs. On the contrary, its response is not suitable if the direction of the motion can be completely arbitrary. Basically this last one is the case of the earthquake input motion which is
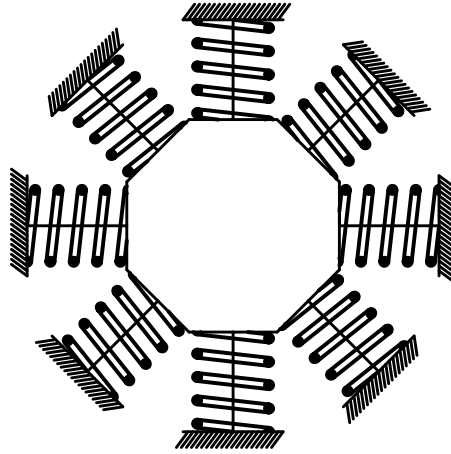
Figure 6.13. Schematic of eight spring system

totally unknown, also with respect to the direction. Hence, for seismic applications, a first requirement for a restrainer is to provide the same shear force-lateral response in any direction.

Considering a system based on coil spring, the multiple direction restraining ability can be provided designing a system made up of several springs located all around the device which is to be restrained. Theoretically, three spring devices at $2/3\pi \mathtt{rad}$ angle are enough for this purpose. On the other side, a radial system like this is perfectly symmetric only if the number of restraining springs is infinite. For this reason in the present work we consider the possibility of using eight springs in radial position, as shown in Figure 6.13, assuming that the response is constant regardless the direction of motion.

Moreover, the use of eight springs instead of just two is not a simply way of providing symmetrical response in plan but the complex system produces a response different with respect to the double spring configuration due to the non-negligible contribution of the other six elements. Assuming that no torsion occurs in the device and that the displacement occurs along two spring axis direction, for each displacement history one spring is compressed, two are lateral displaced and compressed, one is in tension, two are laterally displaced and in tension, and the other two, whose axis is perpendicular to the displacement direction, contributes only with their lateral stiffness and strength.

Due to the complexity of the framework, a numerical investigation has been performed using a FE method.

(a)   *Spring Geometrical and Material Properties*

The same material properties and spring dimensions described in Section 6.3.2 are used considering the eight springs in radial position as described in the mesh geometry reported

in Figure 6.14. In this complex configuration still the boundary conditions of the springs are very important and again two possibilities are investigated, a fixed-hinged condition, as shown in Figure 6.14a, and a fixed-fixed one, as shown in Figure 6.14b.

(a) fixed-hinged case   (b) fixed-fixed case
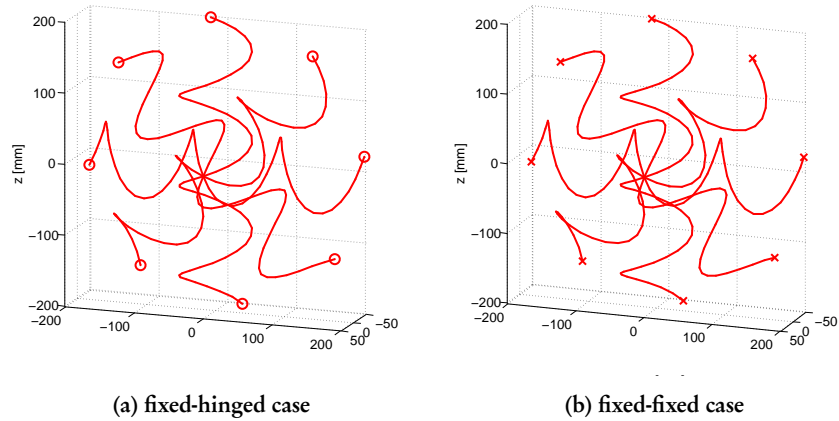
Figure 6.14. Spring mesh geometry for FE eight radial spring test

(b)   Numerical Test Results

Results of fixed-hinged condition are show in Figure 6.15 while those of the fixed-fixed condition in Figure 6.16. The force-displacement relation is a flag-shaped hysteresis stable
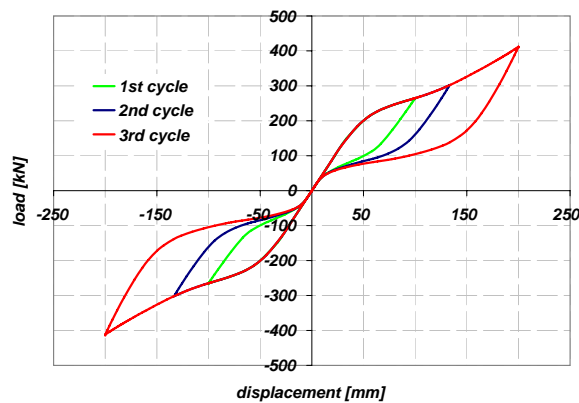
Figure 6.15. Superelastic fixed-hinged radial spring tension-compression test results (positive-tension, negative-compression convention adopted)
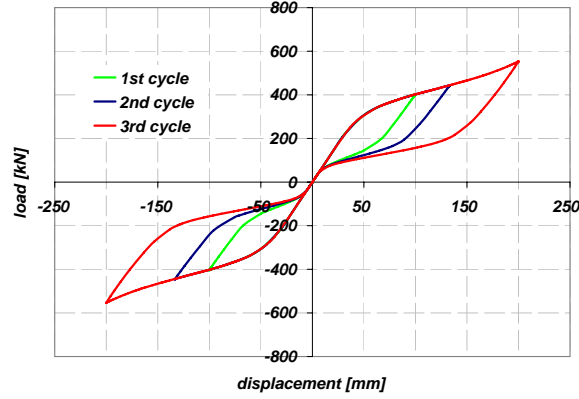
Figure 6.16. Superelastic fixed-fixed radial spring tension-compression test results (positive-tension, negative-compression convention adopted)

and smooth. In Figure 6.17 the comparison of the maximum displacement cycle response is presented for the two boundary conditions. The fixed-fixed system is much stiffer before yielding and presents an higher stiffness hardening after. Hence the yielding force is much larger in the fixed-fixed case with respect to the fixed-hinged one. At yielding, force in the fixed-fixed configuration is almost 60% higher than in the fixed-hinged. Difference increases in the first part of the plateau. Then, at maximum displacement, due to the material final hardening, difference is lower.

Figure 6.17 also reports the eight radial spring (system in Figure 6.13) response together with the double spring configuration (system in Figure 6.8) response for the fixed-hinged case. It is appreciable the difference in the maximum yielding force. Based on the numerical test performed, the ratio between the two spring fixed-hinged system yielding force and the eight spring fixed-hinged radial configuration system is:

$$c_{2h \to 8h} = \frac{P_{y8Xh}}{P_{y2Xh}} \simeq 2.75 \tag{6.2}$$

and the ratio between the two springs fixed-hinged system yielding force and the eight springs fixed-fixed radial configuration system is about:

$$c_{2h \to 8f} = \frac{P_{y8Xf}}{P_{y2Xh}} \simeq 4.50 \tag{6.3}$$

Coefficients in Equation (6.2) and Equation (6.3) can be used to estimate the shear capacity of the eight radial spring configuration (system in Figure 6.13) with respect to the two
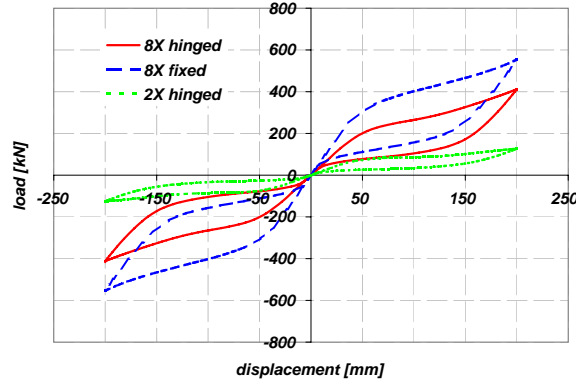
Figure 6.17. Two-parallel fixed-hinged spring system response compared with fixed-hinged and fixed-fixed eight-radial spring system

axially loaded spring configuration (system in Figure 6.8). Based on results in Figure 6.17, the elastic limit displacement is about the same for the two-springs and the eight-springs systems. This is reasonable since the yielding point is mainly controlled by the axially loaded springs. Effect of the laterally loaded springs in lateral shear capacity is also appreciable in the higher second hardening stiffness. As a final remark, the maximum displacement ductility in the fixed-fixed case is expected to be lower than the fixed-hinged one because higher material stresses (which can lead to device rupture) are reached in the fixed-fixed system for lower displacements.

(c) Considerations and Numerical test Results on Pipe Wire Section Spring

For the sake of completeness, response of the pipe-section spring has been checked. The motivation in using a pipe section device is to optimize the material without any relevant reduction of the technical capability of the spring. Figure 6.18 compares the results obtained considering a pipe section with the results of the same system considering a circular section. Obviously the same spring configuration is evaluated (eight radial springs) with the same boundary conditions (fixed-hinged). The circular wire section has diameter $d_w = 30$mm and the circular pipe section has external diameter $d_w = 30$mm and internal diameter $d_p = 20$mm. Differences in the response are very small, almost negligible. Just the maximum shear is a bit lower but still the change is not critical.

Hence we can conclude that the use of pipe section instead of circular section has to be evaluated based merely on cost estimations because differences in the response are not important. Anyway, to be able to carry also the shear, it is suggested that the internal pipe diameter (i.e. the diameter of the internal hole) should not to be larger than two thirds of
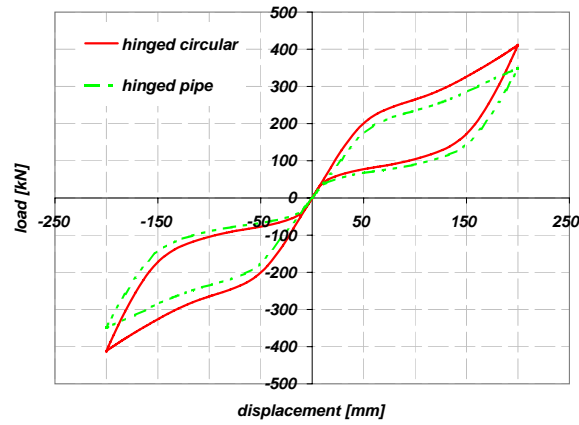
Figure 6.18. Circular - pipe section spring result comparison (eight spring radial fixed-hinged
       configuration)

the total external diameter, as reported in Equation (6.4).

$$d_p \leq \frac{2}{3} d_w \qquad (6.4)$$

(d)   Radial Spring Configuration Conclusions

As a general conclusion, the use of several superelastic springs to reach a symmetrical
plain restraining response provides a force-displacement relation very interesting.   It
has been verified through numerical analyses that the system gives a non-linear relation
which limits the maximum transmissible force and dissipate energy, and it avoids residual
displacements.

6.3.4   Simplified Procedure for Nonlinear Spring Systems Pre-Design

In the previous sections, coil spring system numerical behavior has been investigated.
Results show that coil spring system could be used as a lateral restrainer because of
its nonlinear and recentering force-displacement relation. Moreover coil spring systems
properties depend on several geometrical parameters which, in the limit of the usual
material properties, provide a large configuration freedom to meet the design requirements
in terms of displacement capability, initial stiffness, and yielding force.
Nonetheless, the real design of a device to accomplish a particular design condition is not
trivial, at least at the beginning of the process. The same freedom in determining the
several geometrical parameters is also a further difficulty in the final design definition.

For this reason, a simplified procedure for pre-design of inelastic spring systems is provided in this section. Of course this procedure turns out to give a spring configuration which has to be checked and can be improved, but it is intended as an useful starting point to optimize the design process.

(a)   Basic Assumptions

It is assumed that the spring system has to provide a wanted force at yielding P_y being characterized by enough displacement capability to reach the design displacement Δ without significant loss of strength.
The objective is the design of a system based on two springs. The springs have the same properties, work in parallel, and are at the same time one in tension and the other in compression, as described in Section 6.3.2. Concerning the boundary conditions, this base procedure has been calibrated for the fixed-hinged condition. Extensions will be presented either for other spring configuration and different boundary conditions.
First of all basic spring material properties knowledge is needed. We assume that

- Young's modulus E and

- tensile yielding stress σ_y

of the superelastic wire is known, maybe after a material characterization campaign. Through the previous we can estimate the shear modulus G and the yielding shear stress τ_y respectively as:

- the elastic shear modulus G is computed based on the initial elastic modulus E:

$$G = 0.4E \tag{6.5}$$

which corresponds to apply the basic elastic theory for alloy con considering a Poisson ratio $\nu = 0.25$.

- the shear yielding stress is derived from the tensile yielding stress σ_y considering the simplified relation:

$$\tau_y = 0.65\sigma_y \tag{6.6}$$

which provides a reliable mean value considering two spring in asymmetric condition, one in tension and the other in compression, fixed-hinged and assumed to be carrying only the shear component.

Finally the spring wire section is assumed to be circular or pipe shape, having a given polar inertia modulus J_p.

(b)   Yielding Force

The first parameter we want to take into account in the design is the yielding force of the spring system, being the yielding given both by material properties and geometrical properties. The yielding shear in the superelastic wire, which corresponds to axial force transmitted by the spring, is estimated as:

$$P_y = 2\frac{\tau_y \pi d_w^3}{16R} \tag{6.7}$$

in which d_w is the diameter of the wire and R the coil radius. Therefore, the Equation (6.7) leads to the definition of trial wire diameter d_w and trial coil radius R to satisfy the force requirement. Figure 6.23 shows the theoretical yielding force as a function of the previous parameters. Entering the plot from the y axis with the needed yielding force it is possible to get a feasible combination of d_w and R.

(c)   Initial Spring Stiffness and Design Ductility

Starting from the theoretical spring stiffness k_{spr}, the secant stiffness given by the tensile and compressive springs can be estimated as:

$$k_{2Xspr} = 2c_k k_{spr} \tag{6.8}$$

in which k_{spr} is defined by Equation (6.9):

$$k_{spr} = \frac{G\, d_w^4}{64\, R^3\, n_c} \tag{6.9}$$

being n_c the number of coils.

c_k is a factor taking into account the fact that when the system apparently yields the secant stiffness is smaller than the theoretical one because of the buckling of the spring in compression. In the case of fixed-hinged spring, it is suggested $c_k = 0.75$. It is assumed to have defined previously d_w and R, the free variables are the wire section (circular or pipe) and the total spring wire length.

   The design displacement Δ of the spring is a given parameter. From the yielding force P_y and the initial stiffness of the system k_{2Xspr} the yielding displacement Δ_y can be estimated:

$$\Delta_y = \frac{P_y}{k_{2Xspr}} \tag{6.10}$$

and the system displacement ductility is given as:

$$\mu_\Delta = \frac{\Delta}{\Delta_y} \tag{6.11}$$

From numerical tests the maximum spring displacement ductility μ_Δ is about 4 and 5. Therefore the stiffness design has to be performed considering also the ductility limit, concerning the fact that making the system stiffer the maximum displacement capability is affected as well. Referring to Figure 6.24 and Figure 6.25 it is possible to get as a function of the required ductility and stiffness (on the y axis respectively in Figure 6.24 and Figure 6.25) the total wire length l_w and the internal diameter of the pipe d_p (for $d_p = 0.5 d_w$ the section is circular, not pipe).

(d)   Pitch Angle

The following step is to determine the pitch angle in the spring coil α. After having fixed the spring wire diameter and section, the coil radius and the total wire length, the pitch angle can be computed being based on the number of coils n_c and the spring axis length h_s. Entering Figure 6.26 and Figure 6.27 from the y axis respectively with the spring axis length or with the coil number, it is possible to compute the pitch angle either for the previous assumed total wire length and for different length, in case of adjustments.

(e)   Procedure Summary

From the problem a design yielding force P_y and a design displacement Δ are given. Other conditions can be given by the geometrical limits either of the material or of the available space destined to the restrainer element.
A feasible spring system restrained is wanted. The procedure consists of the following steps:

- using Figure 6.23 from P_y, trial values for d and R are found;

- given the previous, using Figure 6.24 and Figure 6.25 the total wire length l_w is estimated based on consideration on the design displacement ductility μ_Δ and on the initial stiffness k_{2Xspr};

- given the previous, the pitch angle α is obtained using Figure 6.26 and Figure 6.27 in order to make the spring satisfying the requirement of axial length or coil number.

(f)   Procedure Validation

Few examples of the presented procedure were performed to validate the methodology. Three examples are presented here.

- Design example #1:

  required yielding force: $P_y = 140 \text{kN}$
  required design displacement: $\Delta = 300 \text{mm}$

design ductility: $\mu_{Delta} = 4 \Rightarrow \Delta_y = 75$mm

resulting wire: diameter $d_w = 40$mm, circular section $d_p = 20$mm
resulting coil radius: $R = 70$mm
resulting wire length: $l_w = 750$mm
resulting pitch angle: $\alpha = 28$
resulting number of coils: $n_c = 1.50$
resulting spring axis length: 398.78mm
resulting yielding force: $P_y = 140.02$kN
resulting initial stiffness: $k_{spr} = 1846$kN/m
resulting ductility demand: $\mu_\Delta = 5.27$

The resulting spring behavior has been checked using FE analysis. The force-displacement relation compared with design nonlinear curve is shown in Figure 6.19.
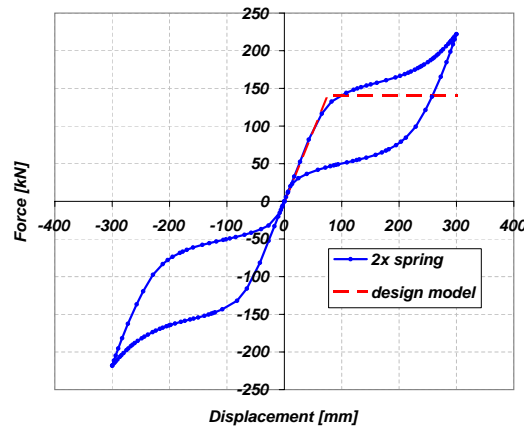
Figure 6.19. Spring design example #1 FE results and comparison

- Design example #2:

  required yielding force: $P_y = 45$kN
  required design displacement: $\Delta = 100$mm
  design ductility: $\mu_{Delta} = 3 \Rightarrow \Delta_y = 33.33$mm

  resulting wire: diameter $d_w = 25$mm, circular section $d_p = 12.5$mm
  resulting coil radius: $R = 50$mm
  resulting wire length: $l_w = 300$mm

resulting pitch angle: $\alpha = 18$
resulting number of coils: $n_c = 0.91$
resulting spring axis length: 97.47mm
resulting yielding force: $P_y = 47.86$kN
resulting initial stiffness: $k_{spr} = 1381$kN/m
resulting ductility demand: $\mu_\Delta = 3.84$

The resulting spring behavior has been checked using FE analysis. The force-displacement relation compared with design nonlinear curve is shown in Figure 6.20.
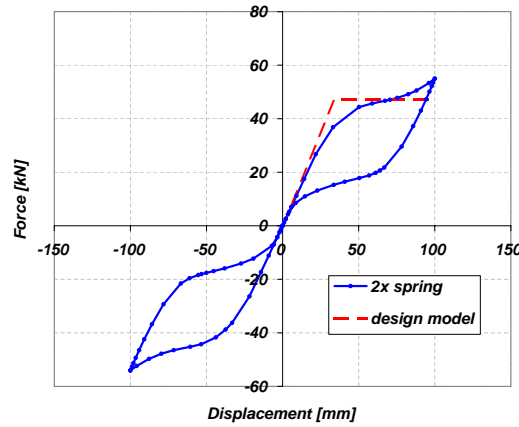
Figure 6.20. Spring design example #2 FE results and comparison

- Design example #3:

  required yielding force: $P_y = 300$kN
  required design displacement: $\Delta = 500$mm
  design ductility: $\mu_{Delta} = 3.2 \Rightarrow \Delta_y = 156.25$mm

  resulting wire: diameter $d_w = 60$mm, circular section $d_p = 30$mm
  resulting coil radius: $R = 110$mm
  resulting wire length: $l_w = 1500$mm
  resulting pitch angle: $\alpha = 25$
  resulting number of coils: $n_c = 1.967$
  resulting spring axis length: 699.46mm
  resulting yielding force: $P_y = 300.73$kN

resulting initial stiffness: $k_{spr} = 1893\text{kN/m}$
resulting ductility demand: $\mu_\Delta = 4.196$

The resulting spring behavior has been checked using FE analysis. The force-displacement relation compared with design nonlinear curve is shown in Figure 6.21.
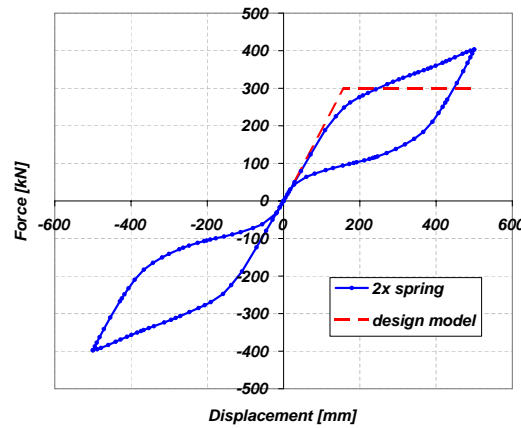
Figure 6.21. Spring design example #3 FE results and comparison

(g)   *Conclusions on the Simplified Procedure*

The simplified procedure is an useful tool to pre-design a spring system based on the required yielding force, design displacement and maximum ductility. Results are a good starting point for a more refined design but of course the output of the simplified procedure is perfectible through some iterations.

Nonetheless the procedure is applicable directly only to two-spring-in-parallel, fixed-hinged configurations. An approximated procedure to extend the results to more interesting configurations, like the eight spring radial one, is needed. This can be given by the comparison between the response of the different systems. Figure 6.17 shows the response of the two-parallel fixed-hinged spring system compared with the eight-radial spring system both in fixed-hinged and fixed-fixed cases, as resulting from numerical analyses. Given that the response is symmetrical, the plot of only the positive quadrant is then reproduced in Figure 6.22. We can assume that the ratio between the yielding force in the radial spring configuration and in the two-spring configuration can be estimated using the ratios defined in Equation (6.2) and Equation (6.3). Therefore to pre-determine the size of springs for radial configuration with eight fixed-hinged system we can get a trial first design applying the procedure considering as a design yielding force in the spring
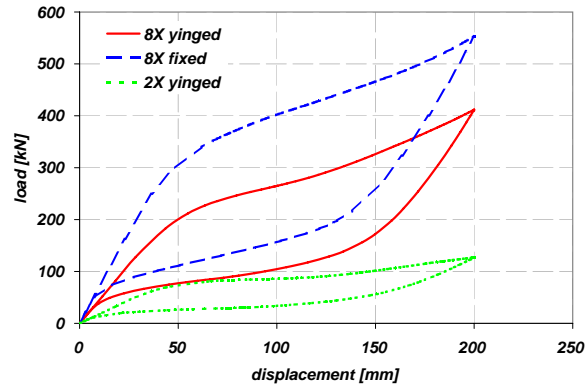
Figure 6.22. two-parallel fixed-hinged spring system response compared with fixed-hinged and fixed-fixed end eight-radial spring system (only positive quadrant).

the design base shear divided by $c_{2h \to 8h}$, while if we want to use a radial configuration with eight fixed-fixed springs we need to divide the design base shear by $c_{2h \to 8f}$. The same coefficients provide an acceptable approximation even if used to determine the proportion the ratio between two and eight spring configuration in the case of pipe section.
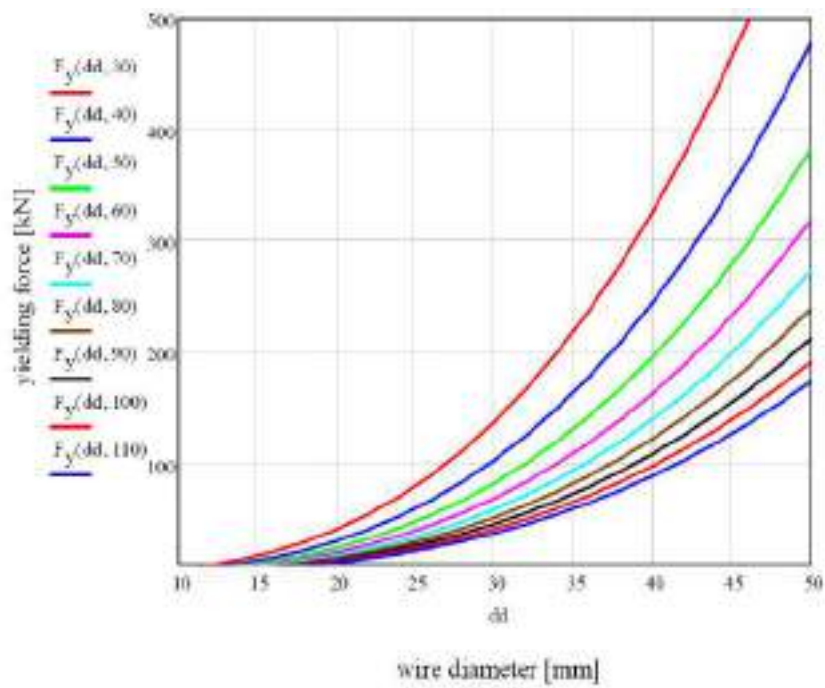
Figure 6.23. Yielding force in the spring function of wire diameter and coil radius: the wire diameter is on _x_ axis, while different color lines correspond to different coil radius
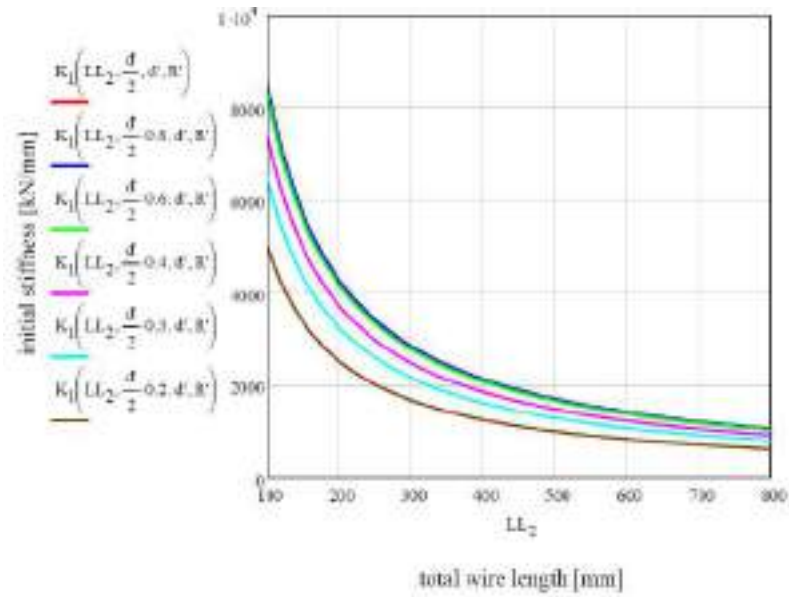
Figure 6.24. Initial stiffness in the spring function of wire diameter and coil radius: the total wire length is on x axis, while different color lines correspond to different section pipe internal radius
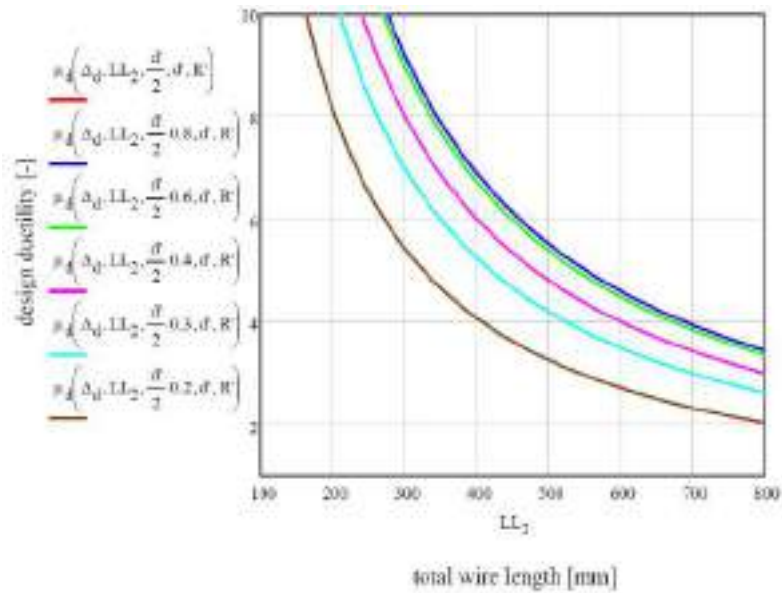
Figure 6.25. Design ductility in the spring function of wire diameter and coil radius: the total wire length is on x axis, while different color lines correspond to different section pipe internal radius
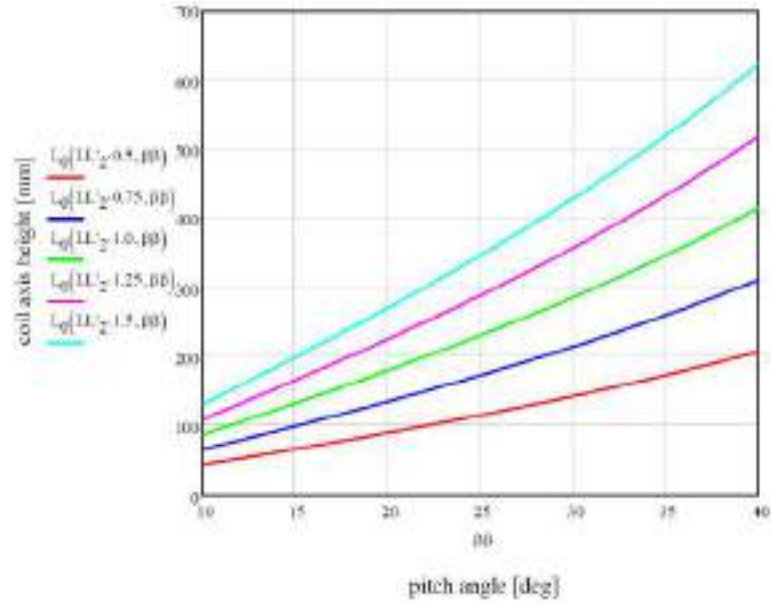
Figure 6.26. Spring axis length function of total wire length and pitch angle: the pitch angle is on x axis, while different color lines correspond to different wire length
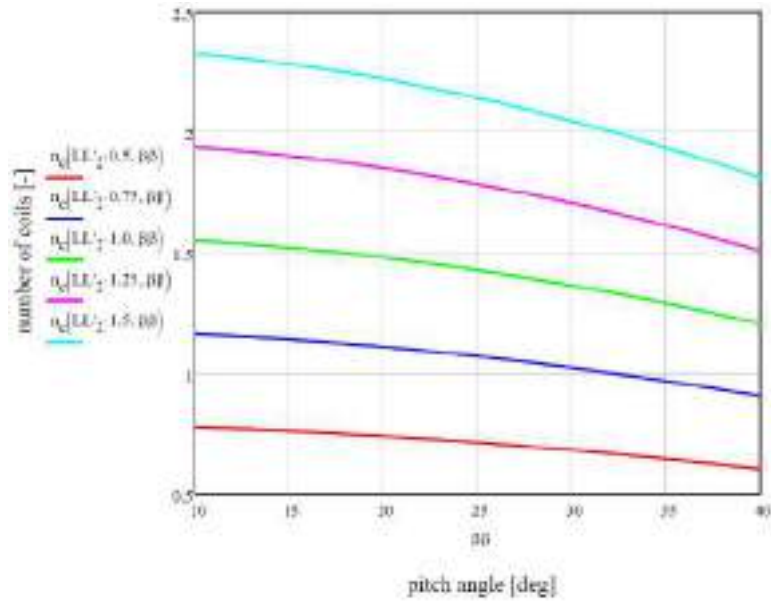
Figure 6.27. Coil number function of total wire length and pitch angle: the pitch angle is on x axis, while different color lines correspond to different wire length

6.4   DESIGN EXAMPLE OF A SUPERELASTIC TECHNOLOGY ISOLATION BEARING

The result of a simulated design process for a superelastic technology based isolation system is presented in this section. The design process goal is to get an optimized superelastic isolation device configuration *equivalent* with respect to an existing isolation bearing. The equivalence is intended as providing the same design yielding and maximum shear force and the same design displacement capability, of course with a different force-displacement relation.

Basically, a process related to the content of Chapter 4 is performed in the present section. If in Chapter 4 a reference LRB system was considered and it was assumed the possibility to design an equivalent SMA device, inhere the real superelastic device design has been performed and then numerically validated.

The LRB device considered is the same one introduced in Chapter 4 and it is recalled in Section 6.4.1. The superelastic design is presented then in Section 6.4.2 and its numerical verification in Section 6.4.3. A comparison with other proposed superelastic isolation devices is then reported in Section 6.4.4.

6.4.1   Reference Lead Rubber Isolator Device

The isolator we consider as a reference is the same LRB device described in Section 4.2 and its design properties are listed in Table 4.1. Plot of the force-displacement relation of the model and comparison with experimental test results is shown in Figure 4.1.

6.4.2   Superelastic Isolator Device Design

The superelastic isolator device design has been performed considering as a target the properties reported in Table 4.1 in terms of shear and maximum displacement capability. The superelastic material properties assumed to be used are the ones reported in Table 6.1.

(a)   Flat Slider

In this example we assume to use a low friction slider device, for example a lubrificated device (see Dolce *et al.* [2005]), whose friction coefficient is about $\mu_s \simeq \mu_f = 0.25\%$. Being based on the seismic weight reported in Table 4.1 and using this friction coefficient, the slider yielding shear is about 3% of the yielding shear. Hence its contribution for the base shear is negligible.

Provided this, the slider has just to be designed to be able to accommodate the maximum design displacement, and considering an acceptable pressure value in the device which has been estimated as 30MPa. The final configuration is characterized by a circular section of diameter 270mm, as shown in Figure 6.29.

(b)   *Lateral Restraining Superelastic Springs*

The optimum spring configuration for a lateral restraining system having the needed displacement capability and providing the same yielding and maximum force with respect to the reference device has been investigated. The eight radial configuration has been used considering fixed-hinged springs. The spring wire section is a pipe section with external diameter $d_w = 30$mm and an internal diameter $d_p = 20$mm. The coil radius is $R = 50$mm and the height of the spring axis is $h_s = 200$mm. The number of coils is $n_c = 1.85$.

The springs are clamped to the isolator core, which is connected to the upper (isolated) level using an allen screw internal with respect to the last coil and ending in a steel plate fastening the spring end. The same connection is used for the other end, the one clamped to the base of the isolation device, but this allen screw is connected to a hinge which is able to rotate along its vertical axis, as shown in Figure 6.29.

(c)   *Issues on Geometrical Configuration*

The final device configuration is shown in a tri-dimensional view in Figure 6.28, and in a bi-dimensional scheme in Figure 6.29. Evaluating its geometrical properties it turns out
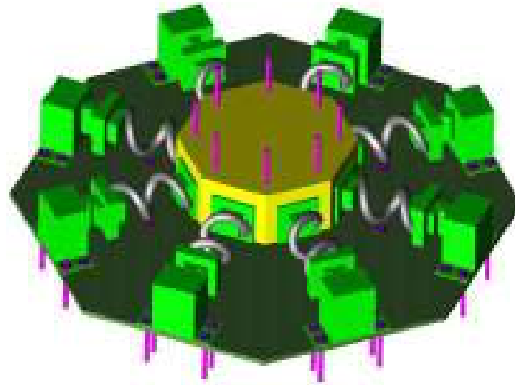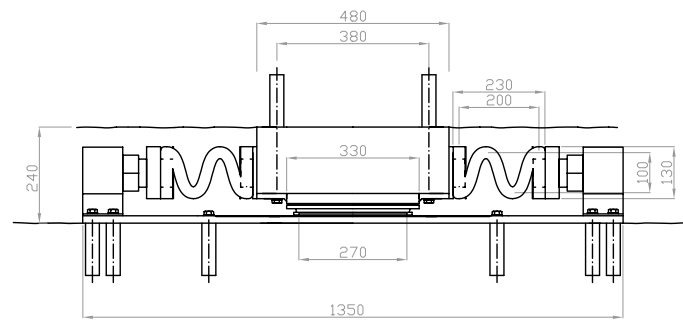
Figure 6.28. Superelastic isolator device: 3d view
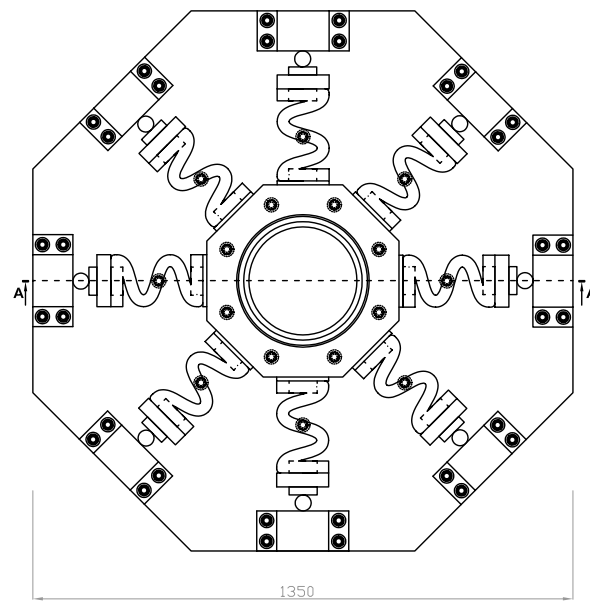
that such a system width is more than twice larger than the original device width, whose diameter is 500mm. This could be an important drawback for this system, because it is more difficult to accommodate such a large device in structures.

Anyway, even in this part the design objective was to get a single superelastic isolation device equivalent with respect to a single given LRB, a smart structural design could be characterized by some bearings with the lateral superelastic restrainers and other being composed only by the slider bearing system, carrying the vertical load without recentering restrainers. Therefore this problem could affect only some devices, not all the bearings.

(a) lateral view

(b) top view

Figure 6.29. Superelastic isolator device equivalent to LRB500

Moreover, other spring positioning systems could be designed, again decoupled from the sliding bearing system, for example around a rigid first level slab and fixed to a foundation wall, or to other locations.

The hinge is supposed to be rotating only around the vertical axis and this guarantees the spring deformation occurring mainly in the horizontal plane, leading to a relatively small vertical space demand to be accommodate in. The height of the device is therefore similar to the one of the actual LRB.

The possibility of replacement of the spring restrainer device has been taken into account in the geometrical configuration. As shown in the top view in Figure 6.29b, there is space enough to replace the coils from the lateral bounds clamped to the base using bolded connection. Looking at the lateral view in Figure 6.29a, it can be noticed that the slider surfaces are easily replaceable as well, being available enough space to position the needed jacks.

6.4.3   Superelastic Isolator Device Response

The superelastic isolator device response has been predicted using numerical tests using a finite element analysis program (ABAQUS [2003]). The only contribution of the spring lateral restrainer has been considered for carrying the shear force, being the friction yielding force negligible.

Superelastic device system response is shown in Figure 6.30, together with the plot of the experimental test results on the actual LRB. The results show that the superelastic device
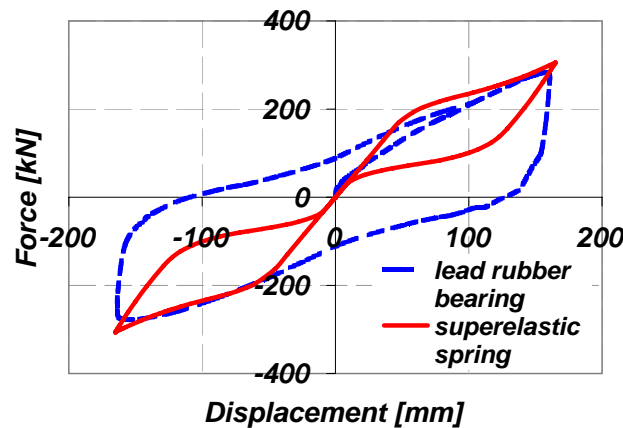
Figure 6.30. LRB 500 and superelastic isolation bearing force-displacement relation comparison

system provides the same yielding force and maximum force than the LRB, therefore the secant stiffness to the design displacement is the same. Looking at the hysteretic area of the force-displacement relation, the superelastic spring response hysteretic damping is of

the order of $\xi_h = 9\%$, hence very much smaller than the LRB one. The spring system is also characterized by a lower initial stiffness. The maximum displacement ductility is about $\mu_\Delta \simeq 3$.

The system numerical response shows that the superelastic device is perfectly recentering. On the contrary a LRB system is characterized by large residual displacements which imply the needing for reparation of the structure. This is a main advantage of the superelastic bearing, because it implies that at the end of the seismic event the isolation system would recover the original position. Possibility of avoiding expensive and time consuming reparations is quite attractive and this is the main advantage in using this superelastic devices with respect to traditional high dissipating but not recentering devices.

6.4.4 Comparison of the Proposed Device with Other Superelastic Isolators

In the present section, the device configuration as introduced in Section 6.4.2 is compared with respect to the solutions already presented in previous works, referring in particular to the theoretical or real design examples reported in Section 3.6.2.

Several configurations have been proposed based on *SMA wires*. Between the others, an exemplification list consists of the devices in Dolce *et al.* [2000] (see Figure 3.18), in Choi *et al.* [2006] (Figure 3.20), and in Liu *et al.* [2008b]. Of course an important advantage in this class of device is the easiness in producing wires with respect to more complex devices, like springs.

Anyway, the limitation of maximum deformation in tension of SMA wires implies the use of long wires in which an uniform deformation along all their length has to be guaranteed. To get an elongation of 200mm, which is the design displacement of the device proposed in Section 6.4.2 (whose axis length is 200mm and geometrical properties are reported in the previous section) assuming to limit the available strain in the wire to 7%, a total wire length of 2857mm is needed. To provide an uniform wire deformation seems not trivial.

A solution like the one in Choi *et al.* [2006], represented in Figure 3.20, seems not suitable to avoid stress and strain concentrations in the wire corners. The proposal in Liu *et al.* [2008b], which does consist of SMA wires diagonally around rubber bearing (hence it is very similar to the previous one) seems applicable only for small displacements. The both of them are anyway not efficient, because the SMA force resultant acts diagonally so it does not carry only the shear force but its component increases also the axial load. The solution in Dolce *et al.* [2000] (represented in Figure 3.18) it is probably the most efficient application based on SMA wires and it has been demonstrated to work properly, but in this case the concern is on the device manufacturing complexity.

A different implementation based on *flexural SMA bar* response is the one reported in Casciati *et al.* [2007]. Even if the device configuration motivation is not very clear from the paper, the proposal is close to the SMA bending bar conception approach, as presented in Bondonet and Filiatrault [1997]. The obtained results are anyway not recentering, hence

such a type of device conception is not interesting from our point of view.

The authors believe the spring configuration a smart solution to get the design goals. The large number of spring geometrical free parameters makes it possible to find suitable device configurations to meet the needed requirements. Moreover, an important advantage consists of the spring capability in reaching very large elongations with respect to its axis length.

In Dolce and Cardone [2001a] it was recognized that because of the material transformation occurring slowly the torsional response of superelastic material is very interesting. Nevertheless the complexity in manufacturing torsionally responding device it is an important limitation to their application is seismic engineering. The spring shape is considered an optimized compromise from this point of view. Firstly because it works in torsion, leading to a favorable material utilization. Then because it is relatively easy to be manufactured needing only a SMA bar to be coiled around another large diameter bar.

6.5 Conclusions

The design of an innovative superelastic isolation bearing has been investigated. The design result is a very flexible innovative device which is composed by an independent element for the transmission of the vertical load and by another system working as a lateral restrainer. The first element is a flat sliding bearing, a traditional device well known for civil engineering applications. The lateral restrainer is a superelastic device system composed by SMA coil springs. The restraining system is demanded to carry the design shear force being able to accommodate the design displacement. A simplified design procedure has been proposed for the innovative SMA springs.

A design example has been performed as well, assuming to design a superelastic device characterized by the same response in terms of period elongation than an actual lead rubber bearing. The design goals were reached and the final device results to be very attractive. The global isolation device is theoretically able to satisfy all the design requirements, carrying the vertical load, accommodating the design displacement avoiding residuals, limiting the transmittable base shear to the superstructure, providing suitable initial and lateral stiffness affecting the system period elongation, and making possible to replace components which need to be substituted. According to the author point of view, it is more suitable for base isolation applications that the other previously proposed based on shape memory alloy devices.

7. Evaluation of Superelastic Seismic Isolation Device Response in Single Degree of Freedom Systems

7.1 INTRODUCTION

The effectiveness of a superelastic isolation system device is investigated in the present chapter considering the response of a single degree of freedom system (*SDOF*). The term superelastic (*SE*) isolation system device refers to a bearing characterized by a nonlinear horizontal displacement-shear force relation which can be described by a *flag-shaped* hysteresis. This hysteresis has been demonstrated to be provided by a lateral restrainer system composed by *shape memory alloys* manufactured devices as reported in Chapter 6.

The objective of the investigation is to compare the innovative device capability in reaching the structural goals with respect to traditional isolation devices. In this context the traditional isolation bearing is a lead rubber bearing (*LRB*). The superelastic device has been designed to be equivalent to an actual LRB.

The investigation consists of a series of time history analyses. Direct computation of the response in time of the system subjected to a suitable ground motion set and evaluation of force and displacement envelopes and energy balance is considered the best way to evaluate the response of the innovative system with respect to the traditional one.

The investigated isolation devices are described in Section 7.2. Technical properties of the LRB system are reported together with the properties of the two superelastic device configurations which are considered. Section 7.3 reports the modeling issues for the time history analyses. Section 7.4 introduces the ground motion set which has been used in the analysis procedure. Section 7.5 presents the investigation results and Section 7.6 reports the main conclusions.

7.2 ISOLATION SYSTEM MODELS

In this work, the response of an existing device is compared with the response of two innovative superelastic system devices. The actual isolation bearing is described in Section 7.2.1 and it is an high dissipation device. The superelastic devices have been designed in order to be equivalent to the previous one in terms of displacement and force capability. They are composed by a flat slider to carry the vertical load and by superelastic lateral restrainers.

The solution we consider in this context for the lateral restraining system is the one reported in Chapter 6, characterized by radial lateral spring devices manufactured using shape memory alloys which has already been described in Section 6.4.2. A proposed device configuration scheme is shown in Figure 6.28 and in Figure 6.29. In this investigation anyway, two possibilities for the superelastic device design shear force are investigated:

- in the first isolator device configuration, the superelastic restraining system is supposed to carry all the shear force, being the friction coefficient of the slider very low and the breakaway shear negligible with respect to the yielding shear force; the technical properties of this system are described in Section 7.2.2;

- in the second configuration, a relevant percentage of the shear force is carried by the friction force, which provides an additional lateral stiffness and force component too; the technical properties of this system are described in Section 7.2.3.

7.2.1 Reference Lead Rubber Isolator Device

The isolator we consider as a reference is the same LRB device described in Section 4.2 and its design properties are listed in Table 4.1. Plot of the force-displacement relation of the model and comparison with experimental test results is shown in Figure 4.1. Elastoplastic model is commonly used as an approximation of the real behavior of the isolator. The lead core contribution provides a large and highly dissipating hysteresis. In fact this device is characterized by a nominal hysteretic damping equal to $\xi_h = 28\%$ which is the damping computed from the hysteresis area evaluation. The isolated device is designed for a EC8 design spectra (CEN [2004]) for $PGA = 0.35$g, 5% damping ratio type 1 soil type GTC. Given the device properties reported in Table 4.1, the effective period of the isolated system computed considering the secant stiffness of the actual LRB would be:

$$T_e = 2\pi\sqrt{\frac{W}{gK_e}} = 2.03\text{s} \tag{7.1}$$

based on the reduction factor η as defined in the EC8 (CEN [2004]) as a function of the hysteretic damping ξ_h:

$$\eta = \sqrt{\frac{10}{5 + \xi_h}} = 0.55 \tag{7.2}$$

and the design displacement of the system:

$$u_d = \eta S_d(T_e) = 0.55 \cdot 0.3\text{m} = 0.165\text{m} \tag{7.3}$$

in which S_d is the design spectral displacement at effective period.

This isolation system is considered suitable for the comparison because it is characterized both by an high dissipation capability and by a non-recentering force-displacement

relation. In theory its response is very different with respect to the superelastic device which is recentering but characterized by a lower hysteretic damping. Hence, provided that a superelastic device would be more attractive with respect a LRB because of the recentering, the goal of the comparison is to evaluate how much the dissipation capability differences affect the envelope response.

7.2.2 Innovative Superelastic Isolator Device with Negligible Friction Force

The first superelastic isolator device consists of a lateral restraining SMA system and of a sliding system carrying the vertical load and permitting the lateral displacement without any contribution in terms of shear and stiffness. This device conception has been defined *SL system*.

The optimum device configuration for a lateral restraining system having the needed displacement capability and providing the same yielding and maximum force with respect to the reference device has been investigated and it is shown in Figure 6.29. In Chapter 6 it has been demonstrated that using a radial configuration of eight superelastic hinge-connected springs, the resulting force-displacement relation from finite element analysis using ABAQUS [2003] is the one reported in Figure 7.1. In this one the innovative
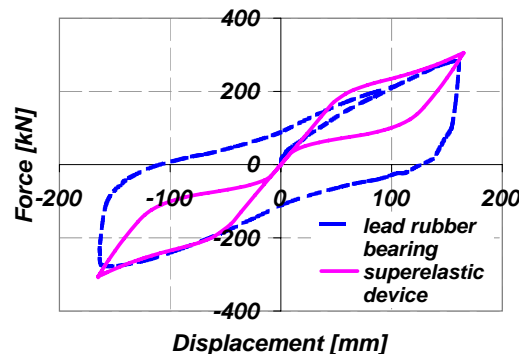
Figure 7.1. LRB 500 and superelastic isolation bearing with no friction (SL system) force-displacement relation comparison

superelastic hysteresis is also compared with the actual LRB experimental test results. It is shown that the superelastic device system provides the same yielding force and maximum force than the LRB. This implies that the secant stiffness to the design displacement is the same in the two systems. Moreover, the innovative system is perfectly recentering.

On the other side the superelastic system is characterized by an initial stiffness smaller than the one of the LRB. Because of this, at the design displacement the SE system ductility is smaller. Obviously, looking at the force-displacement relation, the SE hysteretic dissipation is significantly lower than the one of the LRB.

7.2.3   Innovative Superelastic Isolator Device with Relevant Friction Force

A second option for the innovative superelastic device design is to consider a flat slider characterized by a non-negligible friction coefficient and therefore contributing to the shear force capacity of the device. This system conception has been defined *FR system*. The yielding design shear force is assumed to be given by the sum of two different contributions:

$$V_{fr} = V_{se} + V_{bf} \tag{7.4}$$

in which V_{fr} is the total system shear force, V_{bf} is the shear force carried by the flat slider through friction, and V_{se} is the shear force carried by the superelastic restrainer device system.

The force-displacement relation of a friction device is very close to a rigid plastic hysteresis in which the yielding force is the breakaway force of the device. It has to be summed to the superelastic force-displacement relation to get the final device configuration hysteresis. This is shown in Figure 7.2, in which the separate contributions of the friction and of the superelastic force are reported, and in Figure 7.3 which reports the final system hysteresis compared with the LRB model one.

To guarantee an high recentering effect in the device even if the rigid-plastic friction component is taken into account, the following relation is suggested:
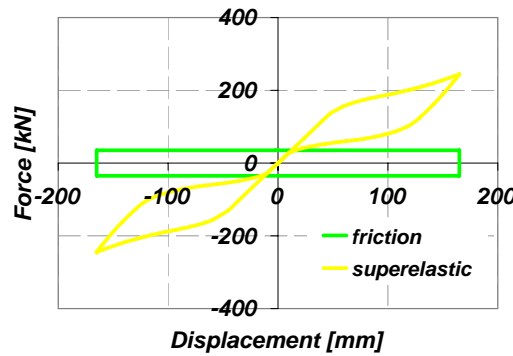
Figure 7.2. Superelastic isolation bearing with friction contribution (FR system): superelastic and friction components

$$V_{se} \geq 0.7 \, V_{fr} \tag{7.5}$$

and for the limit condition $V_{se} = 0.7 \, V_{fr}$ the result is the one shown in Figure 7.3.

Summing a rigid-plastic force-displacement relation with the flag-shaped one, provided that the design shear force is the same as the actual LRB system, the final FR system hysteresis is characterized by an higher initial stiffness and lower hardening due to the
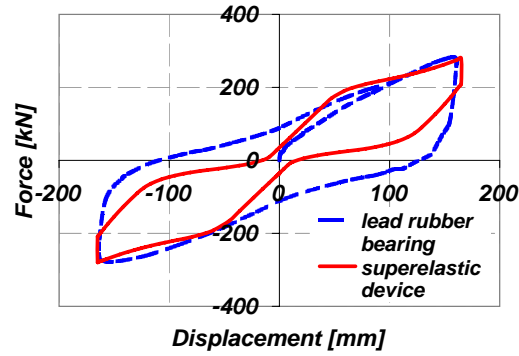
Figure 7.3. LRB 500 and superelastic isolation bearing with friction contribution (FR system): force-displacement relation comparison

rigid plastic contribution, and by an higher dissipation capability with respect to the SL system. FR system is not fully recentering due to the friction component. Nevertheless, the maximum residual displacement is very small if compared with the maximum residual of the LRB: residuals are about the 10% of the maximum displacement in FR system versus about the 100% of the maximum displacement in LRB.

7.3   TIME HISTORY ANALYSIS SYSTEM MODELING

The time history analyses are performed comparing for each ground motion input the response of single degree of freedom systems, as shown in Figure 7.4. The system mass, m_e is constant in all the tests and it has been computed from the seismic vertical load W reported in Table 4.1. Four different hysteresis have been considered, as reported in Section 7.3.1. The nonlinear time history analysis have been performed using the finite element program Ruaumoko (Carr [2007]). The viscous damping model is described in Section 7.3.2.
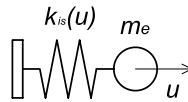
Figure 7.4. Analysis model for rigid superstructure base isolation

7.3.1   Hysteretic Constitutive Relations

The hysteresis modeled in the analysis are listed next.

- Elasto-plastic model (Figure 7.5). The elastoplastic model is representative of the real lead rubber bearing device and the parameters we use are those reported in Table 7.1.
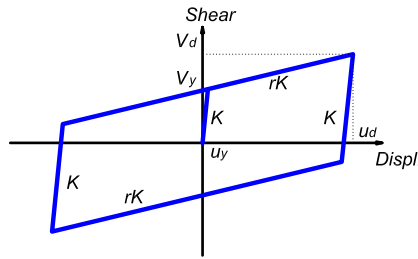
Figure 7.5. Base shear horizontal displacement relation for lead rubber bearing isolation device

- Flag-shaped model SL (Figure 7.6). The flag-shaped model reproduces the shear-horizontal displacement relation of the pure superelastic device (SL). The used parameters are summarized in Table 7.2.
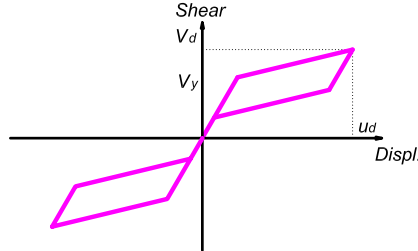
Figure 7.6. Base shear horizontal displacement relation for superelastic no friction isolation device

- Flag-shaped model FR (Figure 7.7). The flag-shaped model reproduces the shear-horizontal displacement relation of the superelastic device and frictional flat slider (FR). The numerical model was obtained using two spring in parallel, one reproducing the superelastic device (*SE*) and the other the friction bearing device (*BF*). The used parameters are summarized in Table 7.3.

- Linear elastic model (Figure 7.8). Considering the design displacement u_d and the design shear V_d, which are the same for the previous models, we carry out the analysis of the equivalent linear system, considering a secant stiffness to the design point which is common to the previous modes. The used parameters are summarized in Table 7.4.
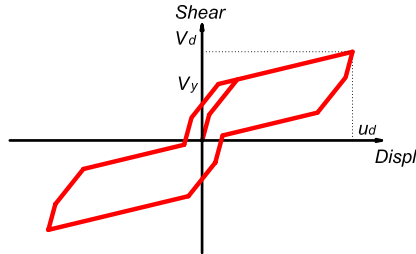
Figure 7.7. Base shear horizontal displacement relation for superelastic with friction isolation device
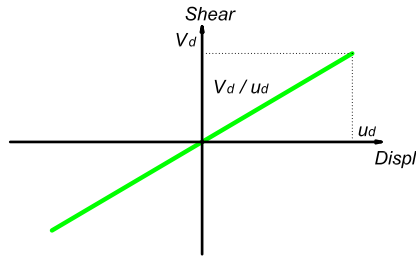
Figure 7.8. Base shear horizontal displacement relation for equivalent linear elastic with secant stiffness isolation device

7.3.2   Viscous Damping Modeling

To focus on the hysteretic dissipation, and to avoid the viscous damping component affecting significantly the system response, low viscous damping coefficient has been modeled.

Regarding the elastic damping component in the nonlinear elements, a constant damping proportional to the initial stiffness is used to have the same energy dissipation in the three models if the velocity history is the same. The damping ratio of the linear elastic system, in which the stiffness is constant, is assumed equal to $\xi_{le} = 2\%$. To get the same damping coefficient c in the equation of motion taking into account that the critical damping is different, the following relations have been used:

$$c = 2\xi_{le}\sqrt{k_e\frac{W}{g}} = 2\xi_{nl}\sqrt{k_{nl}\frac{W}{g}} \Longrightarrow \xi_{nl} = \xi_{le}\sqrt{\frac{k_e}{k_{nl}}} \tag{7.6}$$

in which, being ξ_{le} and k_e respectively the viscous damping and stiffness of the equivalent linear elastic system, k_{nl} is the initial stiffness and ξ_{nl} is the viscous damping coefficient of a nonlinear force-displacement relation.
The viscous damping coefficients for the all the nonlinear force-displacement relations consistently with this procedure resulted to be smaller than 2% given that their initial

stiffness is higher. Summary of the elastic viscous damping coefficients is reported in Table 7.1, Table 7.2, Table 7.3, and Table 7.4.

Table 7.1. Hysteretic properties of *EP* system

LRB 500 (EP system)		
Elastoplastic model		
yielding shear	V_{ep}	147 kN
initial stiffness	k_{ep}	8.4 kN/mm
second stiffness	rk_{ep}	0.8 kN/mm
viscous damping ratio	ξ_{ep}	0.88%
seismic vertical load	W	1653 kN

Table 7.2. Hysteretic properties of *SL* system

Superelastic no friction (SL System)		
Flag-shaped model		
yielding shear	V_{sl}	195 kN
initial stiffness	k_{sl}	3.68 kN/mm
second stiffness	rk_{sl}	0.26 kN/mm
viscous damping ratio	ξ_{sl}	1.32%
seismic vertical load	W	1653 kN

7.4 CONSIDERED GROUND MOTIONS

Time history analysis procedure is based on the structural response evaluation considering suitable earthquake ground motions. In this section the choice of ground motion set is reported.

7.4.1 Earthquake Records

Suites of earthquake ground motions from the *SAC* database (SAC [1997]) have been considered for the isolation bearing system response comparison evaluation. All the considered ground motions are natural records.
In particular, two sets of records have been used in this work:

- earthquake natural ground motions with 10% probability of exceedence in 50 years for the area of Los Angeles: 20 records, whose properties are reported in Table 7.5;

Table 7.3. Hysteretic properties of *FR* system

Superelastic with friction (FR System)		
Flag-shaped model - restrainer		
yielding shear	V_{se}	136 kN
initial stiffness	k_{se}	2.57 kN/mm
second stiffness	rk_{se}	0.18 kN/mm
Elastoplastic model - friction		
yielding shear	V_{bf}	59 kN
initial stiffness	k_{bf}	11.7 kN/mm
second stiffness	rk_{bf}	0.0 kN/mm
Total system		
yielding shear	V_{fr}	195 kN
initial total stiffness	k_{fr}	14.27 kN/mm
viscous damping ratio	ξ_{fr}	0.67%
seismic vertical load	W	1653 kN

Table 7.4. Hysteretic properties of *LE* system

Linear Elastic to design point (LE System)		
Linear model		
stiffness	k_{le}	1.62 kN/mm
viscous damping ratio	ξ_{le}	2.00%
seismic vertical load	W	1653 kN

- impulsive near-field earthquake ground motions: 12 records, whose properties are reported in Table 7.6.

Hence in total, 32 earthquake ground motions have been considered for the analysis. Some of them are relative to the same seismic event recorded in two different directions or in different stations. A large number of records has been chosen to take into account as much as possible the variability of the seismic input.

7.4.2   Ground Motion Scaling Procedure

The records are from large set of seismic events characterized by different seismological sources and recording conditions. Hence a scaling procedure is needed to permit the result comparison at the design level.

Table 7.5. Characteristics of Los Angeles area compatible ground motions

#	SAC Name	Seismic Event Magnitude	Year	Name	Recording Data Station	Dist.(km)	Scale Factor
1	LA01	6.9	1940	El Centro	Imperial Valley	10	1.11
2	LA02	6.9	1940	El Centro	Imperial Valley	10	1.66
3	LA03	6.5	1979	Imperial Valley	El C. array 5	4.1	0.58
4	LA04	6.5	1979	Imperial Valley	El C. array 5	4.1	0.64
5	LA05	6.5	1979	Imperial Valley	El C. array 6	1.2	0.40
6	LA06	6.5	1979	Imperial Valley	El C. array 6	1.2	0.75
7	LA07	7.3	1992	Landers	Barstow	36	2.18
8	LA08	7.3	1992	Landers	Barstow	36	2.96
9	LA09	7.3	1992	Landers	Yermo	25	1.49
10	LA10	7.3	1992	Landers	Yermo	25	1.68
11	LA11	7.0	1989	Loma Prieta	Gilroy	12	0.74
12	LA12	7.0	1989	Loma Prieta	Gilroy	12	2.85
13	LA15	6.7	1994	Northridge	Rinaldi RS	7.5	0.93
14	LA16	6.7	1994	Northridge	Rinaldi RS	7.5	0.51
15	LA17	6.7	1994	Northridge	Sylmar	6.4	0.43
16	LA18	6.7	1994	Northridge	Sylmar	6.4	0.44
17	LA19	6.0	1986	North Palm	Spring	6.7	1.81
18	LA20	6.0	1986	North Palm	Spring	6.7	0.63
19	LA13	6.7	1994	Northridge	Newhall	6.7	2.53
20	LA14	6.7	1994	Northridge	Newhall	6.7	1.77

Given that the lead rubber bearing device properties are compatible with a EC8 for $PGA =$ 0.35g type 1 soil type GTC design spectra (CEN [2004]), the same spectra has been used as a target for the scaling. The type 1 EC8 spectra are shown in Figure 7.9.

The scaling procedure we followed is the simply approach suggested in BSSC [1997]. The original records have been analyzed and then scaled by an uniform coefficient given by the ratio between the original record spectra the design spectra. The input database in SAC [1997] is not homogenous, because some records are proposed already scaled and others have not been modified. The scaling coefficients reported in Table 7.5 and Table 7.6 are anyway referred to the original ground motions, hence they are comprehensive of both the SAC and following scaling.

The displacement and acceleration spectra of the ground motions as reported in SAC [1997] and defined *original*, are shown in Figure 7.10, compared with the design spectra from EC8. The final *scaled* ground motion displacement and acceleration spectra are then

Table 7.6. Characteristics of impulsive near-field earthquake ground motions

	SAC	Seismic Event			Recording Data		Scale
#	Name	Magnitude	Year	Name	Station	Dist.(km)	Factor
21	NF01	7.4	1978	Tabas		1.2	0.50
22	NF02	7.4	1978	Tabas		1.2	0.40
23	NF09	6.7	1992	Erzican		2.0	0.43
24	NF10	6.7	1992	Erzican		2.0	0.78
25	NF11	7.3	1979	Landers		1.1	0.46
26	NF12	7.3	1979	Landers		1.1	1.59
27	NF13	6.7	1994	Nothridge	Rinaldi	7.5	0.46
28	NF14	6.7	1994	Nothridge	Rinaldi	7.5	0.66
29	NF15	6.7	1994	Nothridge	Olive View	6.4	0.40
30	NF16	6.7	1994	Nothridge	Olive View	6.4	1.00
31	NF19	6.9	1995	Kobe	Takatori	4.3	0.19
32	NF20	6.9	1995	Kobe	Takatori	4.3	0.64
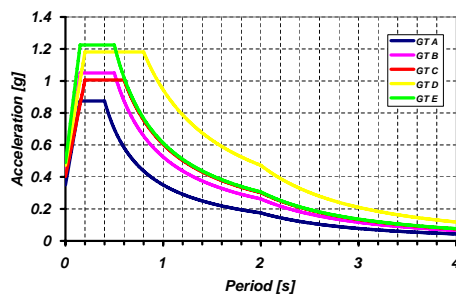
(a) acceleration spectra
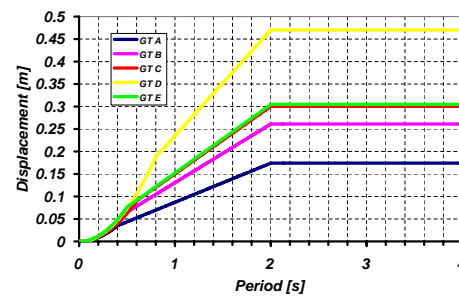
(b) displacement spectra

Figure 7.9. Elastic design spectra for $PGA = 0.35$g, 5% damping ratio type 1 (far field event) from EC8 (CEN [2004])

reported in Figure 7.11, again compared with EC8 design spectra.

7.4.3   Scaled Ground Motion Properties

The scaling of the ground motions has been performed following the spectrum compatibility requirement with the design spectra. The result consists of input records scaled even by large coefficients, from a minimum of 0.19 in record number 31 and a maximum of 2.96 in record number 8. Moreover, as shown in Table 7.7 and Table 7.8, the

(a) acceleration spectra (5% damping)   (b) displacement spectra (5% damping)
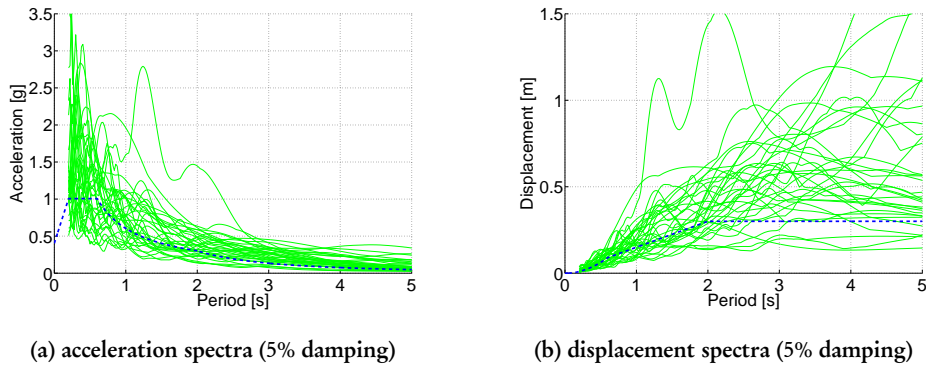
Figure 7.10. Original record (from SAC [1997]) spectra compared with the design spectra

(a) acceleration spectra (5% damping)   (b) displacement spectra (5% damping)
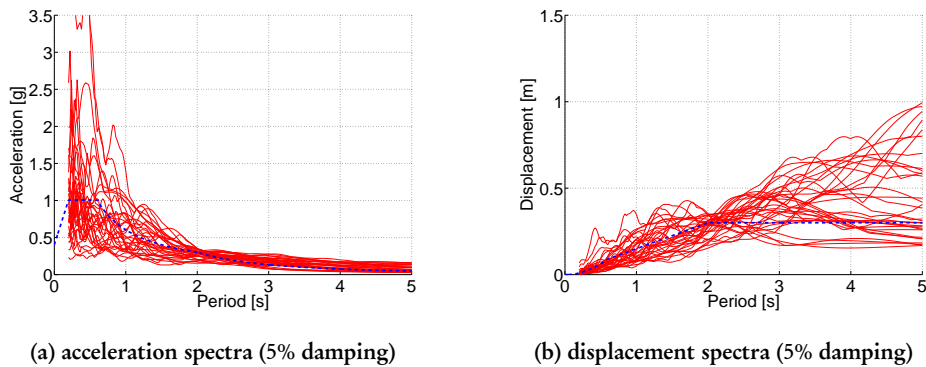
Figure 7.11. Scaled record spectra compared with the design spectra

spectra compatibility condition leads to ground motions characterized by large variability in terms of peak ground acceleration, velocity and displacement.

The point of the comparison is anyway to check the structural response of different isolation system device also being the records very different. Therefore, given that the record set is large enough to consider the variability of the input, the comparison is valid even if the ground motions properties are very different. All the record spectra in terms of acceleration and displacement have been plotted in Figure 7.10 and Figure 7.11. Nevertheless, due to the large number of considered ground motions, the statistics of the spectra are reported too.

Displacement spectra statistics are shown in Figure 7.12. In Figure 7.12a the data from

Table 7.7. Details of scaled Los Angeles area compatible ground motions

Number	Name	Scale Factor	PGA [g]	PGV [mm/s^2]	PGD [mm]
1	LA01	1.11	0.255	345	153
2	LA02	1.66	0.558	495	118
3	LA03	0.58	0.226	476	192
4	LA04	0.64	0.308	487	304
5	LA05	0.40	0.145	429	232
6	LA06	0.75	0.208	422	267
7	LA07	2.18	0.287	450	226
8	LA08	2.96	0.393	607	366
9	LA09	1.49	0.357	628	387
10	LA10	1.68	0.279	467	359
11	LA11	0.74	0.277	329	118
12	LA12	2.85	1.542	891	262
13	LA15	0.93	0.479	885	160
14	LA16	0.51	0.286	497	131
15	LA17	0.43	0.307	433	93
16	LA18	0.44	0.451	656	148
17	LA19	1.81	1.859	1245	285
18	LA20	0.63	0.632	665	164
19	LA13	2.53	0.577	813	169
20	LA14	1.77	0.392	484	213

the original records are reported and in Figure 7.12b the statistics after the record scaling are shown. It is immediately appreciable the fact that the mean and the median spectral ordinates are very close, at least for periods up to 3.5s. For longer periods, still differences are not large.

The effects of scaling procedure are evident from the comparison between Figure 7.12a and Figure 7.12b. The mean record spectra is very close to the design displacement spectra after scaling, moreover the scaling procedure reduces very much the standard deviation of the spectra ordinates.

The resulting mean displacement spectra is also characterized by a constant slope up to 3s period. Even if this is non consistent with respect to the design spectra, whose corner

Table 7.8. Details of scaled impulsive near-field earthquake ground motions

Number	Name	Scale Factor	PGA [g]	PGV [mm/s^2]	PGD [mm]
21	NF01	0.50	0.454	555	259
22	NF02	0.40	0.391	423	301
23	NF09	0.43	0.188	518	184
24	NF10	0.78	0.358	455	231
25	NF11	0.46	0.329	627	1059
26	NF12	1.59	1.271	1118	2923
27	NF13	0.46	0.408	800	179
28	NF14	0.66	0.255	396	121
29	NF15	0.40	0.293	490	124
30	NF16	1.00	0.597	541	91
31	NF19	0.19	0.149	329	106
32	NF20	0.64	0.273	409	150

period is 2s (CEN [2004]), this property is more realistic and useful in the comparison of the structural response of isolation devices, as previously observed in Attanasi *et al.* [2009b].

Acceleration spectra statistics are reported in Figure 7.13. Figure 7.13a and Figure 7.13b reports respectively the statistics before and after the record scaling.

The scaling procedure reduces the differences between the design spectra and the mean value of the record ordinates. In this case anyway the standard deviation and the difference between mean and median are increased after scaling for high frequencies and decreased for periods which are interesting for the base isolation procedure.
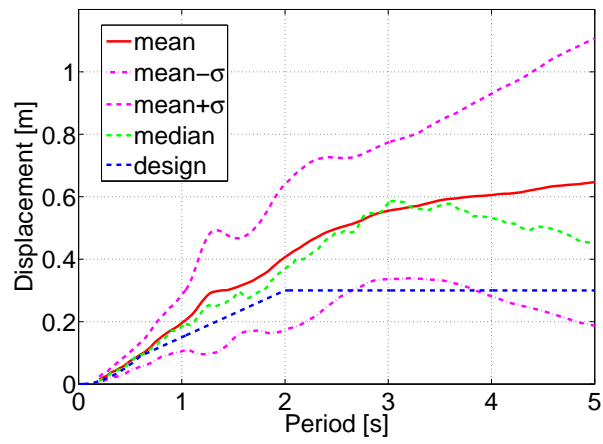
(a) original
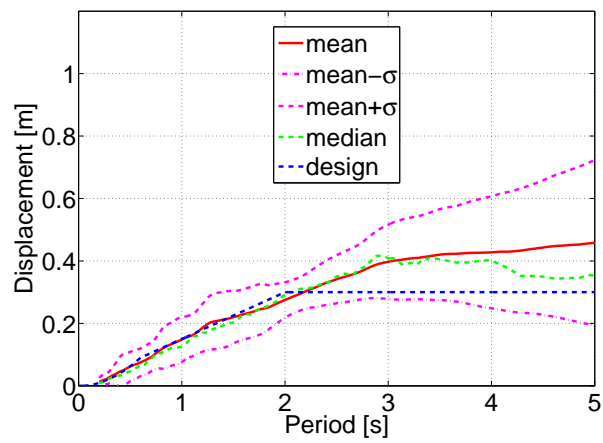
(b) scaled

Figure 7.12. Displacement spectra statistics (5% damping) over the considered ground motions compared with the design spectra
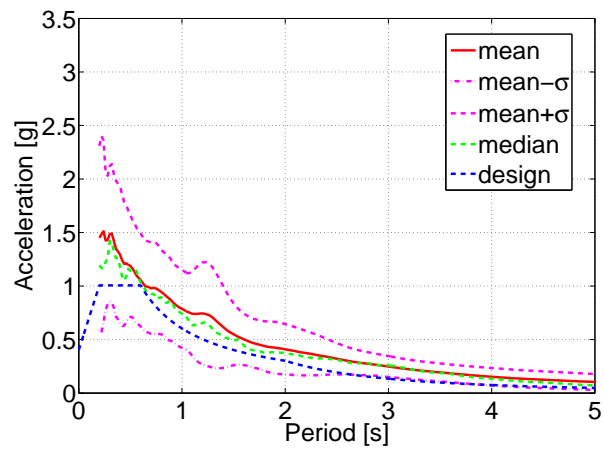
(a) original
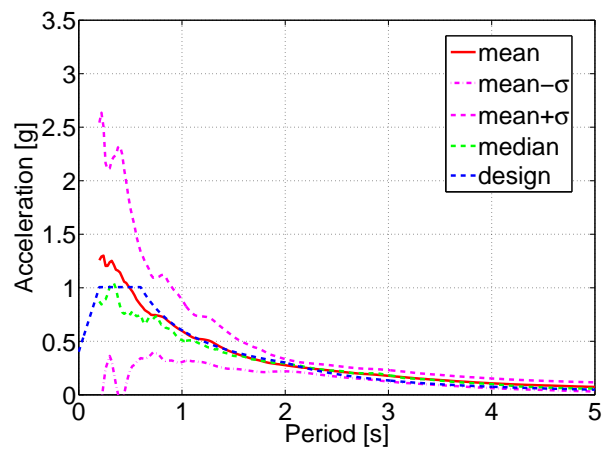
(b) scaled

Figure 7.13. Acceleration spectra statistics (5% damping) over the considered ground motions compared with the design spectra

7.5   NONLINEAR TIME HISTORY ANALYSIS RESULTS

Nonlinear time history analyses investigating and comparing the response of SDOF systems with hysteresis described in Section 7.3 subjected to ground motion set reported in Section 7.4 are performed. In this part, Section 7.5.1 presents the parameters which have been taken into account and on which the investigation is based; some of the exemplificative results are then reported in Section 7.5.2. Section 7.5.3 contains an overview summary on the global investigation findings.

7.5.1   Result Processing

The results have been reported and analyzed for each ground motion, to correlate the record properties to the system response. Mean results have been then considered over all the ground motion set. In the SDOF investigation data postprocessing the most important history parameters are the displacement, the shear force and the energy ratio.

The displacement history comparison between the different systems is useful to determine the maximum displacement demand and the reduction due to the force-displacement relation nonlinearity with respect to the linear secant system to the design displacement. Moreover it is useful to evaluate the presence and the magnitude of the residual displacements.

The displacement history plot provides informations also about the effective period of vibration. Checking the time in between two cycles the eventual period elongation can be evaluated.

The shear force is checked too. This is one of the most important design parameter and the maximum demand is fundamental for capacity design considerations. In the SDOF it is equal to the inertia force of the mass, hence it is significative for the system acceleration as well. Shear force and displacement plot have been considered also together to define the effective hysteresis.

The system energy balance is also taken into account. The input energy, has been computed together with the kinetic, damping and strain energy components. Since the input energy changes if the hysteresis rule is different even if we consider the same ground motion, the ratio between the strain energy and the input energy is a direct measure of the dissipation capability of the system.

7.5.2   Exemplificative Results

Four study examples are reported in this section to introduce the study procedure and to present some of the results. The considered ground motions are:

- ground motion LA03 (result summary reported in Figure 7.14);

- ground motion LA12 (Figure 7.15);

- ground motion NF16 (Figure 7.16);

- ground motion NF19 (Figure 7.17).

(a) displacement histories

(b) force histories

(c) force-displacement relations

(d) energy ratio balances
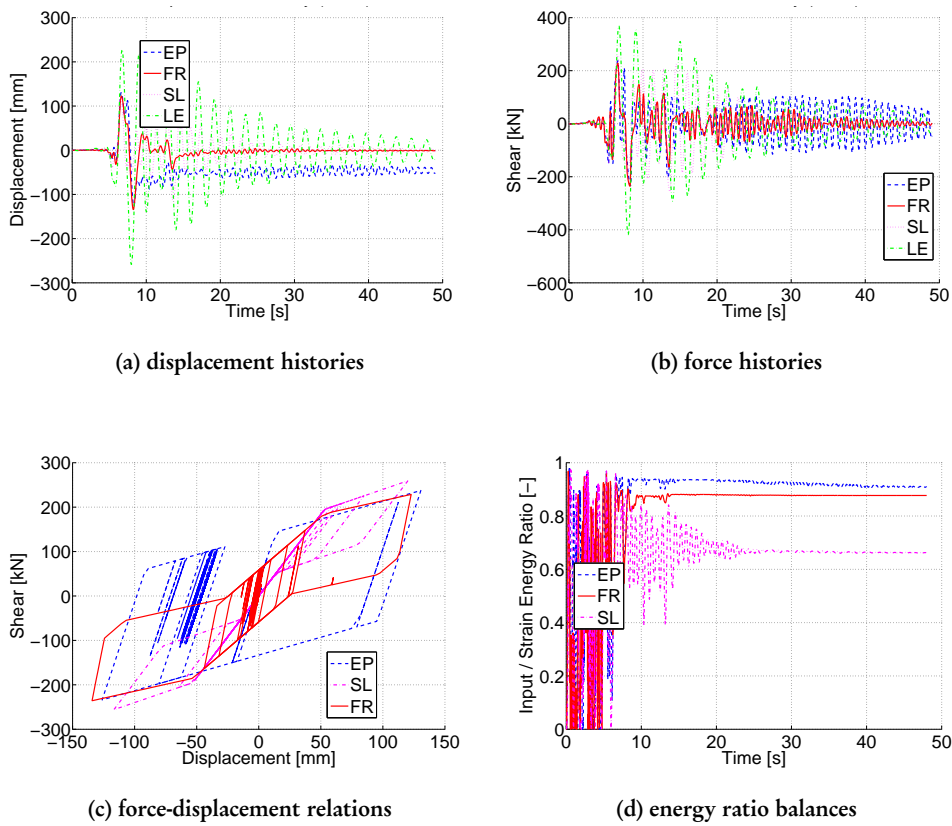
Figure 7.14. Isolation system response comparison subjected to ground motion LA03

In these, the following data are shown:

- displacement histories: the plot showing the mass displacement in time of the four system subjected to the same ground motion is reported;

- force histories: the shear in time is reported for the four ground motions;

- force-displacement relations: this plot provides hysteresis comparison together with immediate information about the maximum displacement and shear demands for the nonlinear systems (the linear elastic model has not been reported in the figures);

(a) displacement histories

(b) force histories

(c) force-displacement relations

(d) energy ratio balances
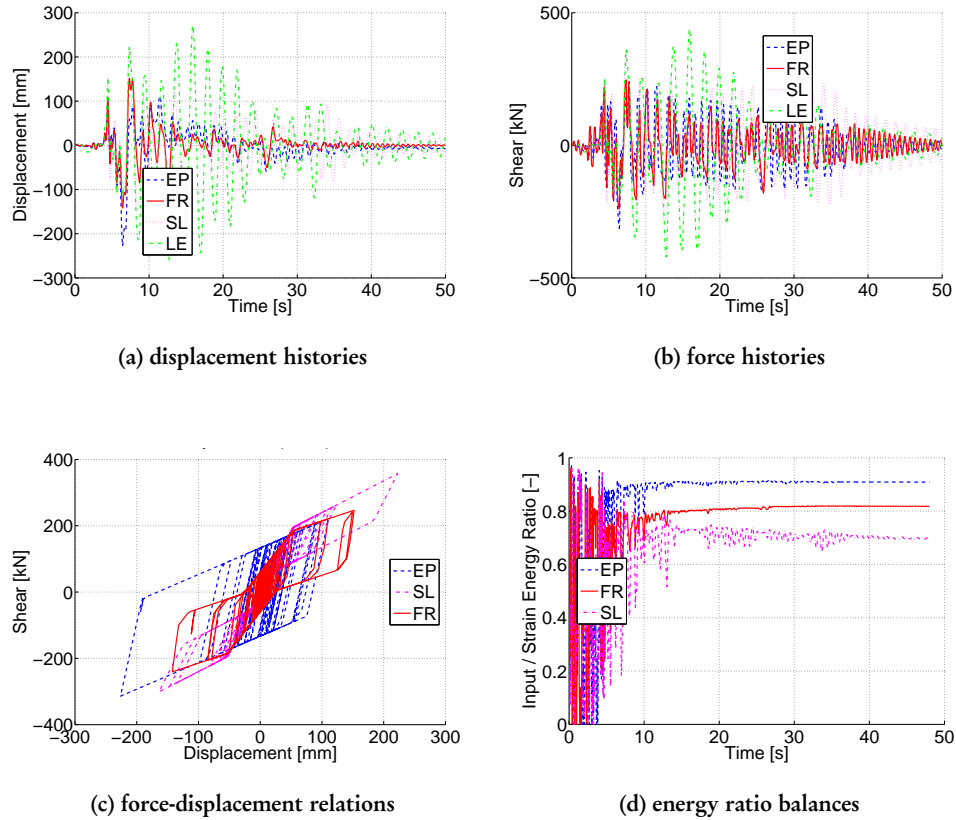
Figure 7.15. Isolation system response comparison subjected to ground motion LA12

- energy ratio balance: the ratio between hysteresis dissipated energy and input energy is shown for the nonlinear system, given that the ratio is zero for the linear one; the interesting value is the one at the end of the plot time, after some free vibration, when the elastic energy and kinetic contributions are negligible.

From the few examples, it is possible to point out some of the main findings of the investigation. The response is very different given the different isolation systems, even if in theory the all of them are characterized by the same design displacement and secant stiffness. The number of cycles and their displacement and force levels turned out to be completely independent from a system to an other.

From the investigation resulted that the nonlinear properties are very important only in few cycles, being the response controlled in most of the record duration by the

(a) displacement histories

(b) force histories

(c) force-displacement relations

(d) energy ratio balances
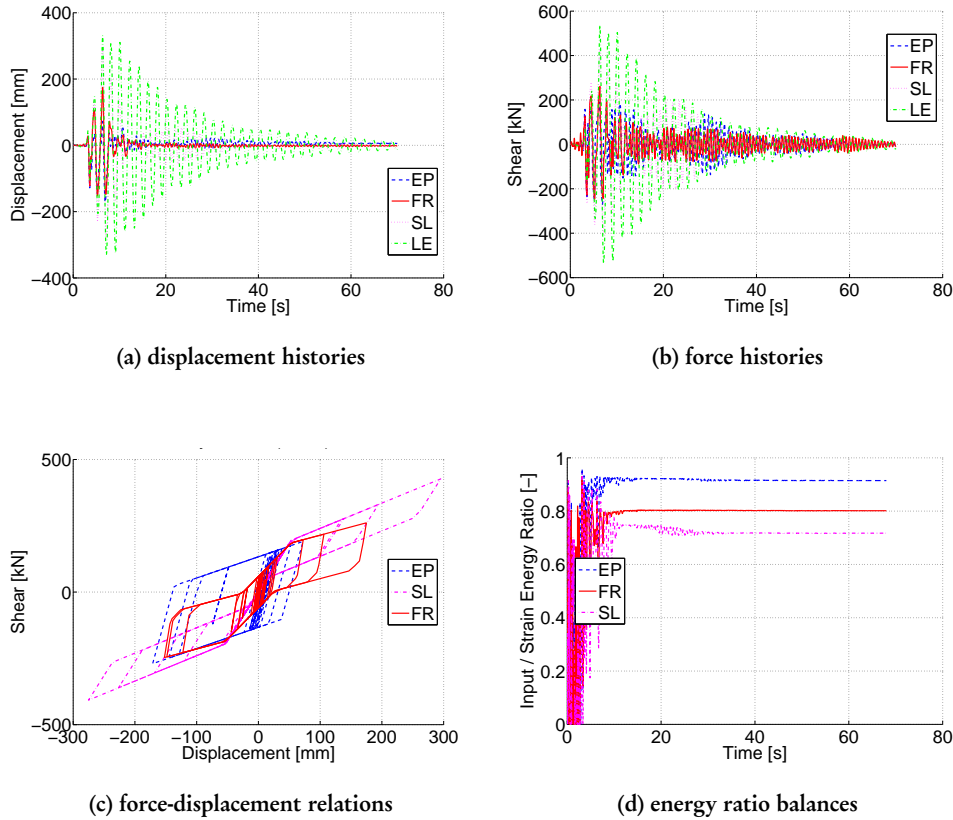
Figure 7.16. Isolation system response comparison subjected to ground motion NF16

initial stiffness. This is demonstrated considering the effective period computed from the displacement histories: the period of vibration is generally the initial stiffness period for most of the displacement history. Provided this, it turns out that the initial properties are relevant in the total energy dissipation and not only the maximum displacement force-displacement relations can be taken into account. Some response amplification effects due to the ground motion frequency are also shown, for example in the SL system in Figure 7.16b.

The SL system and FR system are equivalent in avoiding residuals in all the ground motion response. On the contrary the EP residual displacements are often significative, as shown in Figure 7.14a.

The examples report some of the most significative hysteresis comparisons. In Figure 7.14c a symmetrical positive-negative displacement response is shown, being the maximum

(a) displacement histories

(b) force histories

(c) force-displacement relations

(d) energy ratio balances
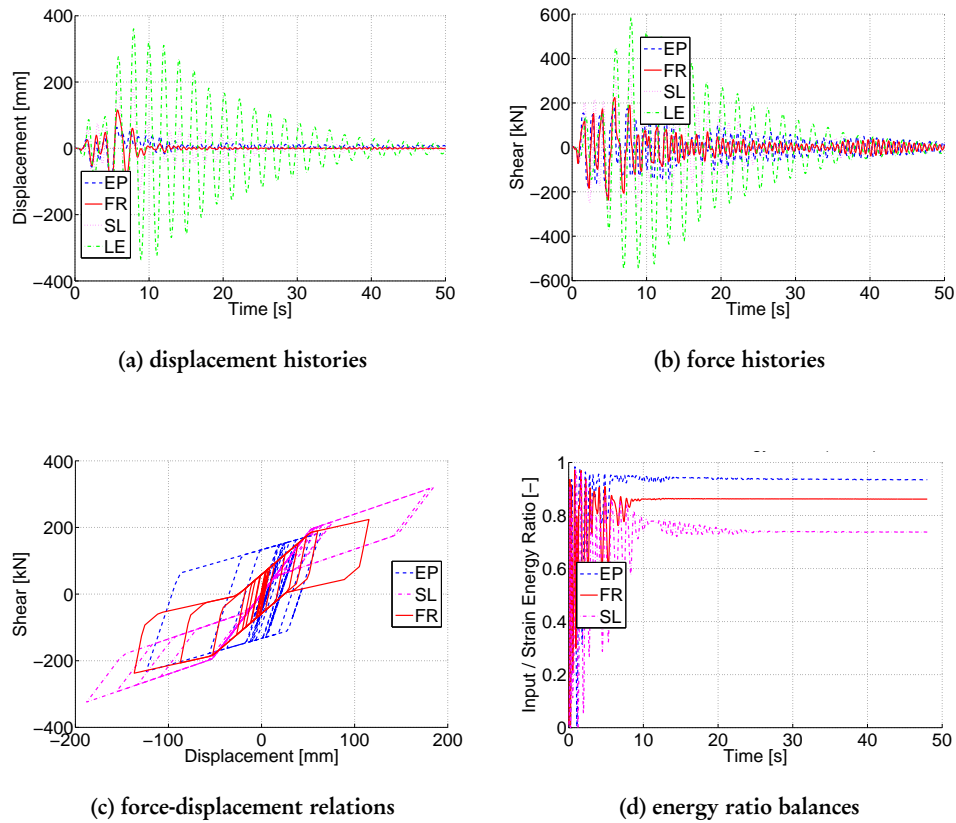
Figure 7.17. Isolation system response comparison subjected to ground motion NF19

positive and negative cycles about of the same magnitude for all the systems. The maximum displacement and force demand is about the same in the three nonlinear systems, being a bit lower in the SL; in general this is a not common result, being usually the SL the most demanding nonlinear system. Nevertheless, while the flag-shaped systems oscillate about the zero displacement value at the end of the record, the elastoplastic reaches as an equilibrium point about 50mm displacement, hence important residuals are present, of the order of 30% of the design displacement.

Figure 7.15c reports a system response characterized by a EP and SL system hysteresis asymmetric and more demanding than the FR systems. The design displacement is exceeded in EP and SL models. Due to the difference in response it is interesting to notice that the maximum displacement occurs in different phases in SL and EP model, and this can be seen in 7.15a: a negative peak is reported for EP and then a positive peak for SL,

FR and LE. This is probably a consequence of the recentering capability of the last three models with respect to the first one.

Figure 7.16c and Figure 7.17c show the typical force-displacement response. The EP and FR system maximum demands are about the same but while the EP is usually asymmetric and eventually producing some residuals, the FR system is quite symmetric with respect to the origin. Beside this, the SL model results more demanding both in terms of force and displacement demand than the previous two.

Concerning the energy balance plot, the EP dissipation capability is the highest in all the records. The FR and SL are a bit lower but differences are not as large as the hysteretic area at the maximum displacement cycle would suggest. The fact that usually the SL system reaches the energy ratio equilibrium at longer times is due to the fact that the SL system shows an important velocity content and kinetic energy contribution for larger time interval.

7.5.3   Result Summary

Envelopes in terms of displacement and shear force and the final dissipated energy ratio have been reported to summarize the system response and to provide an overall comparison. The scatter plot has considered the most suitable way to show the results reporting data for all the ground motions and their mean value. Moreover, the standard deviation is reported to estimate the variability in the response over the investigation sample set.

Figure 7.18 reports the displacement envelope values. Figure 7.18a is a scatter plot in which for each ground motion the maximum absolute displacement demand is reported for the EP, FR, SL and LE systems. Mean values for the systems are reported as well. It can be noticed that the EP and FR mean displacement is compatible with the design displacement, while the SL system is characterized by a mean displacement slightly larger. The ratio between the nonlinear system displacement normalized with respect to the linear elastic system to the design displacement provides a direct measure of the hysteretic damping effectiveness. In fact, the displacement reduction factor should be the same of the η coefficient defined and computed in Equation (7.2). The reduction ratio plot is shown in Figure 7.18b. It turns out that the reduction factor of the EP system is consistent with the previous computed value. Even more important is anyway that the difference between EP and FR reduction factor is very small. This is despite the fact that computing the same coefficient η being based on the ξ_h of the flag-shaped system we would get a significantly smaller value.

Figure 7.18c reports the overall displacement mean values for the four systems together with standard deviation indication. Roughly, it is about the 25% of the mean value in all the systems.

The shear force envelopes are reported in Figure 7.19. In Figure 7.19a the absolute values are reported for the four systems and in Figure 7.19b the maximum values for the

nonlinear systems normalized with respect to the linear elastic system.

It turns out that the mean shear force demand is about the same between EP and FR, and it is larger in SL system with respect to the other two. This can be easily explained considering the displacement demand results and the fact that due to the friction contribution in the FR system the stiffness after the superelastic device yielding is significantly lower than the EP and SL second stiffness. For the same reason, looking at the mean shear force values and their standard deviation in Figure 7.19c, it turns out that the FR standard deviation is the lowest, hence the shear force is about the same in all the record set results. The EP standard deviation is quite low as well, while in the SL system it is larger.

Again, the design shear value is compatible with the mean shear value in EP and FR systems while it has been exceeded in SL system. Referring to the reduction factor computed using Equation (7.2), it is close to the reduction for EP and FR systems despite the fact FR system is supposed to provide larger force demand based on hysteretic area.

Finally, looking at the energy dissipation ratio, Figure 7.20 reports the dissipation ratio of all the ground motions and the mean values for EP, FR and SL systems. The EP results to dissipate about the 90% of the input energy through hysteretic work and FR system about the 85%. Lower dissipation capability is shown by the SL system whose dissipation ratio is smaller than 70%. This is because the SL is characterized by a mean higher velocity with respect to the others and the damping dissipated energy is expected to be higher than in remaining hysteresis. This is also compatible with previous observations. Concerning the data scattering, the plot shows that the data dispersion is very small in the EP system and very large in the SL system values.
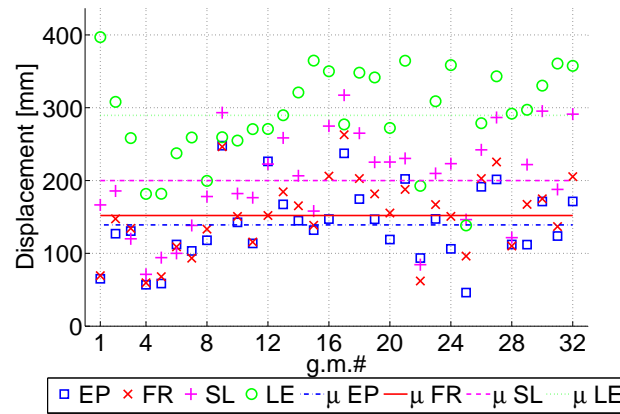
(a) displacement demand envelopes and mean values (absolute values of the four hysteresis)
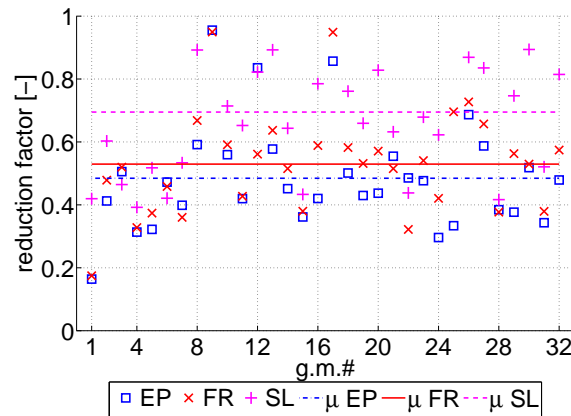
(b) displacement demand envelopes and mean values (normalized response w/r LE)
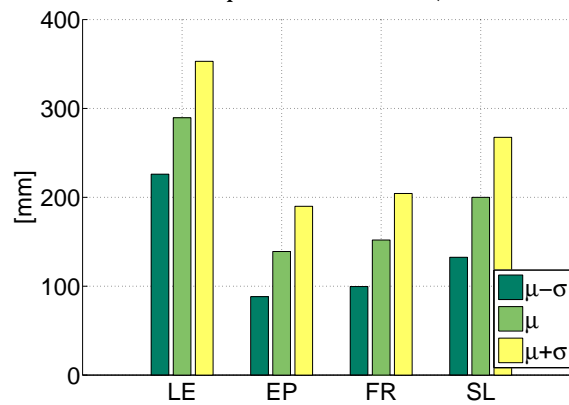
(c) mean value and standard deviation of displacement envelope values

Figure 7.18. Summary of system displacement demand over all the ground motions
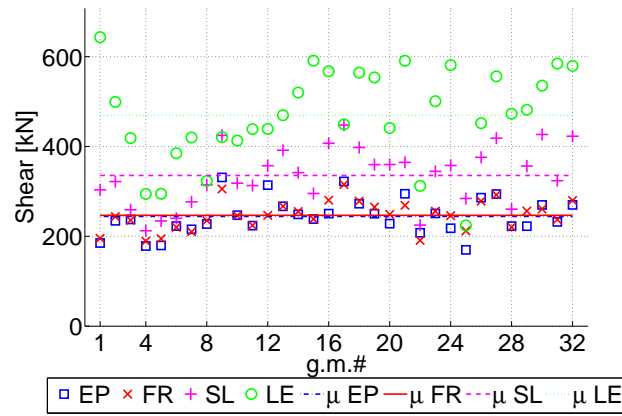
(a) shear demand envelopes and mean values (absolute values of the four hysteresis)
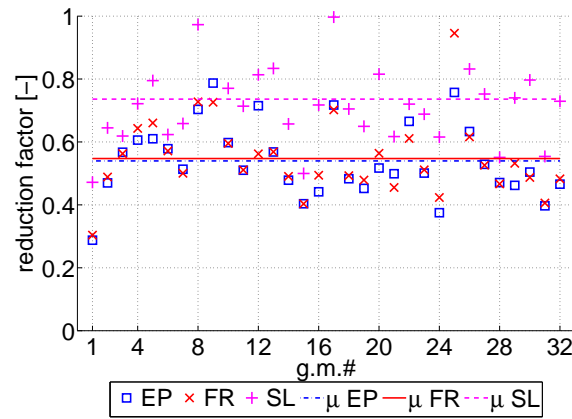
(b) shear demand envelopes and mean values (normalized response w/r LE)
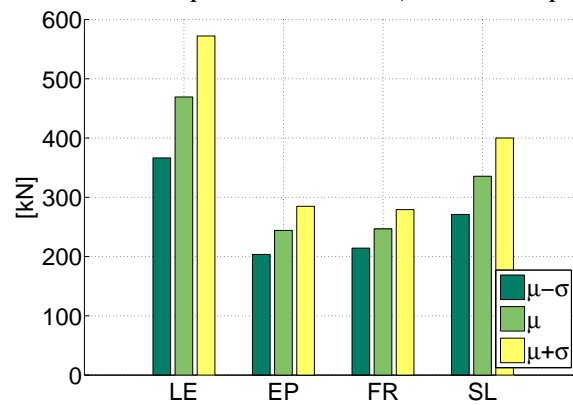
(c) mean value and standard deviation of shear envelope values

Figure 7.19. Summary of system force demand over all the ground motions
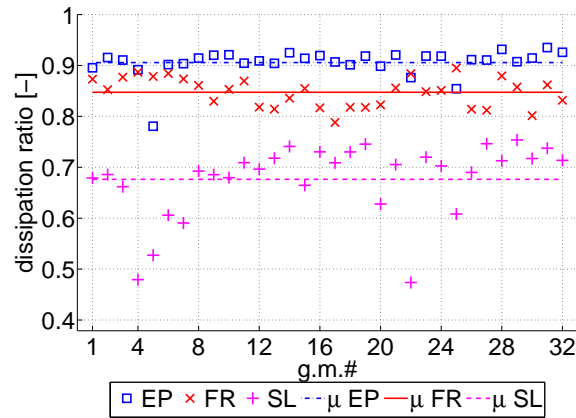
Figure 7.20. Summary of system energy balance over all the ground motions

7.6 CONCLUSIONS

An extensive campaign has been performed to evaluate the response of innovative isolation bearings. They are based on the response given by a lateral superelastic restrain and a flat slider system. Two configurations have been considered, one in which the flat slider is characterized by negligible friction coefficient (SL system) and another in which the friction is significant (FR system). Their response has been compared with an equivalent actual lead rubber bearing device and with the response of a linear elastic system secant to the design level.

Set of 32 natural but scaled ground motions has been considered. They are compatible with the design condition for the lead rubber bearing device.

The studied system is a single degree of freedom system. The mass is constant in all the configurations. The isolation systems have been described considering nonlinear force-displacement relations. Very low elastic damping has been considered and its amount has been determined to provide the same energy dissipation.

An important advantage in using flag-shaped isolation device is that the residual displacements are zero at the end of the event.

Despite the fact that theoretically the hysteretic damping in the elastoplastic system is very much larger than the hysteretic damping in flag-shaped systems, results show that if the friction contribution is about one third of the total base shear, the FR system shear envelope mean is about the same of the elastoplastic one, its displacement envelope mean is just slightly higher, and the mean energy dissipation is very close.

If no friction effect is taken into account the flag-shaped system is more demanding in terms of shear force and displacement envelopes than the elastoplastic system, but not as

much as an hysteretic area based computation would lead to.

This is due to the fact that maximum amplitude cycles are just few and the difference in hysteresis affects the displacement history significantly. Hence the same energy dissipation can be get in flag-shaped systems because of getting the same work having larger number of cycles.

Regarding the fact that the friction device performs better than the superelastic device without friction, this is due to the fact that its initial stiffness is higher, limiting this the displacement demand and increasing the energy dissipation, and its final stiffness is lower because the friction has no hardening. In this device the maximum theoretical residuals are of the order of 10% of the design displacement but in practise, no relevant residuals resulted from the analyses.

The conclusion of this investigation is that it is possible for an isolation system based on a superelastic lateral restrainer and a friction flat slider, which has been designed and whose model has been validates experimentally, to get a response very close to an actual high dissipation lead rubber bearing in terms of displacement and shear force envelopes. Moreover, the system is dissipating about the same percentage of input energy and it is almost totally recentering.

If we consider an isolation system based only on a superelastic restrainer, the systems is fully recentering but it is more demanding than the actual lead rubber bearing in terms of displacement and shear force; the dissipated energy ratio is lower too. Nevertheless, the differences are smaller than the one we would expect based on a hysteretic area based equivalent damping computation.

This page intentionally left blank.

8. Constant Ductility Spectra for Flag-Shaped Systems

8.1 INTRODUCTION

In previous chapters, superelastic bearing system application for seismic isolation has been investigated. It turned out that a device composed by a flat slider to transmit the vertical load and superelastic lateral restraining system can be a solution to meet the design requirements. The key aspect in the device design is the use of spring-shaped lateral restraining devices manufactured using shape memory alloys, as described in Chapter 5 and in Chapter 6. The system is recentering, energy dissipating and limiting the maximum transmittable shear in the structure, as the previous single degree of freedom system investigation in Chapter 7 has proved. Moreover, the lateral restraining system can be designed to accommodate the design displacement without any loss of strength in the system.

Nevertheless, given the adopted technology, limitation on the available displacement ductility has to be taken into account, being the displacement ductility the ratio between the lateral design displacement of the isolation system over the lateral displacement at which the restraining device yields. Previous investigations in Chapter 6 have demonstrated that it is possible to design a device for lateral restraining able to accommodate any design displacement, but due to the material properties and the device configuration, the maximum lateral displacement usable for design purpose is not larger than four or five times the lateral restrainer yielding displacement.

In this context, a constant ductility spectrum is a very useful tool for the preliminary design of device. Given a particular force-displacement relation and design conditions in terms of seismic demand compatible ground motions, it provides the required strength in the system not to exceed a fixed value of displacement ductility. The same force limit can be interpreted as a target as well, in order to take advantage of the most of the nonlinear available properties to optimize the design. For these reasons, in this work constant ductility spectra are computed and provided for superelastic system configurations.

Regarding the structure of the present chapter, generalities on the constant ductility spectra and on the way to compute them, and motivations are reported in Section 8.2. The considered design ground motions are then recalled in Section 8.3. Two device possible configurations are considered, corresponding to different force-displacement relations, and resulting data with the final spectra are reported for two systems respectively in Section

8.4 and Section 8.5. The main conclusions are drawn in Section 8.6.

8.2   CONSTANT DUCTILITY RESPONSE SPECTRA

Earthquake-resistant structure design is generally based on the assumption than the elements undergo nonlinear behavior under the design condition. This is to optimize the design procedure provided that the structure does not experience any critical strength reduction. An adequate design is accomplished when the elements are designed to sustain a displacement capacity larger than the design displacement demand. In this context, the constant ductility response spectra is useful because it provides the yield force or the maximum force to limit the inelastic demand to a given level.

8.2.1   Definitions and Presentation of the Problem

As reported in Riddell [2008], inelastic design spectra were first developed for elastic-perfectly plastic systems. Nonetheless they are computable and applicable for all the nonlinear force-displacement relations. Let us assume that a general nonlinear system
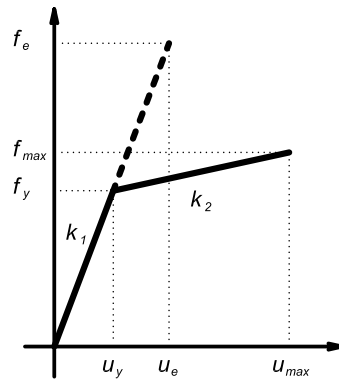
Figure 8.1. General nonlinear force-displacement relation

is characterized by an initial stiffness k_1, it yields when the force is f_y and the displacement is u_y and then it is characterized by a second stiffness k_2, as shown in Figure 8.1.
Let us assume that the system response is computed under the same design conditions considering different values for the yielding force f_y but being the stiffness k_1 and k_2 constant. If we assume a yielding force large enough to assure the response not to exceed the linear elastic limit, the system reaches the maximum force f_e and the maximum displacement u_e. Then, if we consider an yielding force $f_y < f_e$, under the same load conditions the system experiences the maximum displacement u_{max} and the maximum force f_{max}.

Given the nonlinear response, ductility μ can be defined as the maximum displacement over the yielding displacement:

$$\mu = \frac{u_{max}}{u_y} \tag{8.1}$$

and considering the maximum elastic response and the nonlinear one, the yielding strength ratio c_y is defined as:

$$c_y = \frac{f_y}{f_e} = \frac{u_y}{u_e} \tag{8.2}$$

For $c_y = 1$ or larger the system responds elastically. If we assume to keep the system and the external load constant and to compute the response changing the yielding force for $c_y < 1$, we can get a relation between c_y, or equivalently f_y, and the ductility μ. This implies that for every ductility value μ it is possible to find the corresponding c_y, and therefore the corresponding yielding strength f_y, for which the ductility value is not exceeded.

If we consider now as a load condition the base excitation of a ground motion and we refer to a single degree of freedom system as shown in Figure 8.2, characterized by a mass m_e and a nonlinear stiffness k_{is}, the process can be repeated to compute the maximum force demand in the elastic system subjected to the ground motion and to get the relation between the displacement ductility and the yielding strength coefficient. Moreover, the
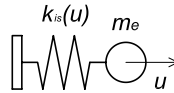
Figure 8.2. Single degree of freedom system

same process can be repeated for different ground motions. Finally, considering different period SDOFs, it is possible to define a spectra providing the yielding strength coefficient which for the considered ground motions guarantee not to exceed the wanted design ductility.

As a general comment, it has to be noted that the yield strength coefficient is the inverse of the strength reduction factor used in other works and it can be used to estimate the maximum inelastic displacement of structures from maximum elastic displacement combined with the ductility, as shown in Akkar and Miranda [2005]. More informations about the constant ductility spectra can be fount in Miranda and Bertero [1994] and observations about its application to performance-based seismic design are reported in Borzi and Elnashai [2000], Borzi et al. [2001], Miranda and Ruiz-Garcia [2002], Akkar and Miranda [2005], and Zhai and Xie [2005].

8.2.2   Construction of Constant-Ductility Response Spectrum

The procedure to construct the response spectra for a given hysteresis corresponding to specified level of displacement ductility has been presented in Chopra [2006] and can be summarized as a sequence of steps:

- definition of the analysis ground motion;

- definition of the SDOF damping ξ and period T_n;

- computation of the response in time for the linear system characterized by period T_n and damping ξ subjected to the ground motion; maximum displacement u_e and peak force f_e are stored;

- computation of the response of a nonlinear SDOF characterized by the given hysteresis, yielding force $f_y = f_e c_y$ with a selected $c_y < 1$, by period T_n, and damping ξ subjected to the ground motion; maximum displacement u_{max} (and therefore ductility μ) and peak force f_{max} are stored; the analysis is repeated for enough number of c_y data to develop data points (f_y, μ);

- for a selected μ, store the largest f_y value corresponding to this ductility which is a point in the plot (T_n, f_y) for the ductility μ;

- repeat the procedure for different periods T_n to get the full plot (T_n, f_y) for the ductility μ.

The procedure described refers to a single design ground motion and a single ductility value. Of course the investigation can be extended considering several ground motions and eventually considering the mean response or the envelope or can be repeated for several ductility values.

8.2.3   Motivations for the Investigation

This study is part of the investigation on the possibility of using superelastic lateral restrainers for seismic isolation application. These devices consist of shape memory alloy manufactured in coil spring shapes. This configuration results attractive because it provides the design lateral shear force together with the needed displacement capability through a flag-shaped force-displacement relation. Moreover the device is very flexible due to the large number of design parameters (the coil radius, the wire diameter, the pitch angle and the number of coils between the others) and therefore to the freedom in defining the final configuration to meet the design requirements. Nevertheless previous investigations demonstrated that a superelastic spring device is characterized by a limitation in the available displacement ductility which is of the order of $\mu = 4$ or $\mu = 5$ (see Chapter 6). This is reported for example in Figure 8.3, which shows a typical force-displacement
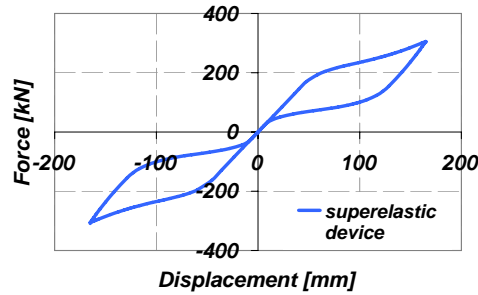
Figure 8.3. Force-displacement relation for a superelastic lateral restrainer

relation for a superelastic restrainer device computed using a finite element program (ABAQUS [2003]); in the previous, the resulting displacement ductility is $\mu = 3.5$.

In displacement-based seismic design, constant ductility spectra have demonstrated to be very useful for preliminary design when the maximum allowable ductility is given (Zhai and Xie [2005]). They let the designer to have a minimum trial base shear value to be used not to exceed the given limit. For this reason, this work is focused on the construction of constant ductility spectra for the innovative proposed systems, to provide this useful tool for the design procedure.

8.3   ANALYSIS GROUND MOTIONS

Constant ductility spectra have been computed considering a large set of compatible ground motions and evaluating the mean value of the results and their statistical properties. In this section the used earthquake records are recalled, being the ground motion set the same already used for the investigation in Chapter 7 and described in Section 7.4.

Suites of earthquake ground motions from the *SAC* database (SAC [1997]) have been considered for the isolation bearing system response comparison evaluation, as reported in Section 7.4.1. All the ground motions are natural records.
In particular, two sets of records have been used in this work:

- earthquake natural ground motions with 10% probability of exceedence in 50 years for the area of Los Angeles: 20 records, whose properties are reported in Table 7.5;

- impulsive near-field earthquake ground motions: 12 records, whose properties are reported in Table 7.6.

Hence in total, 32 earthquake ground motions have considered for the analysis. A large number of records has been chosen to take into account as much as possible the variability of the seismic input.

The records are from seismic events characterized by different seismological sources and recording conditions. Thus a scaling procedure is needed to permit the result comparison at the design level and the process has been described in Section 7.4.2. The EC8 spectra for $PGA = 0.35$g type 1 soil type GTC design spectra (CEN [2004]) has been used as a target for the scaling.

The resulting scaled ground motion properties are reported in Section 7.4.3. In particular, the scaling factors are reported in Table 7.5 and Table 7.6, while the final scaled ground motion displacement and acceleration spectra are shown in Figure 7.11, compared with EC8 design spectra.

8.4 INNOVATIVE SUPERELASTIC FLAG-SHAPED SYSTEM WITH NEGLIGIBLE FRICTION

The first nonlinear hysteresis which has been investigated for the constant ductility response spectra is the flag-shaped force-displacement relation relative to the *SL system*, as already defined in Section 7.2.2. This is an isolation system composed by a lateral superelastic restrainer system and a flat sliding device to carry the vertical load. The slider is supposed to have negligible friction coefficient and not to contribute for shear force and lateral stiffness.

8.4.1 Modeling Issues

The considered flag-shaped force-displacement relation is shown in Figure 8.4. This has been used in time history analyses performed considering a SDOF system subjected to the considered ground motion set.
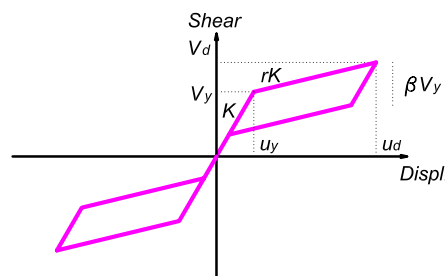
Figure 8.4. Base shear horizontal displacement relation for superelastic no friction isolation device

The system stiffness has been defined at the beginning and then kept constant. Referring to Figure 8.4, the initial stiffness is $k = 3.68$kN/m, the second stiffness coefficient is $r = 0.26$, the dissipation parameter is $\beta = 0.73$. The period of vibration has been obtained through variation of the system mass.

For each ground motion and period, the first run has been elastic and then 12 yielding strength coefficient values have been considered, from $c_y = 1$ to $c_y = 0.02$, to compute the yielding force $f_y = c_y f_e$ being the other hysteretic properties constant.

Analyses are performed considering system periods T_n spanning between $T_{min} = 0.5s$ and $T_{max} = 3s$ for a total of 41 different periods. In this context *period* refers to the initial period, computed considering the initial stiffness. The effective period T_e, based on the stiffness secant to the design displacement as defined in Priestley *et al.* [2007] is therefore given from the T_n as a function of the ductility μ:

$$T_e = T_n \sqrt{\frac{\mu}{1 + r(\mu - 1)}} \tag{8.3}$$

Given that the investigated hysteresis is relative to an isolation system, the proposed period set is suitable to describe the period range in interest.

The viscous damping in the analyzed systems has been modeled as tangent stiffness proportional damping, accordingly to suggestions in Grant *et al.* [2005] and Petrini *et al.* [2008]. It has been considered a damping ratio $\xi = 2\%$ of the critical one.

Analyses were performed using a nonlinear finite element program *Ruaumoko* (Carr [2007]).

8.4.2   Single Ground Motion Result Example

Referring to one single ground motion, the *LA*01 as defined in Table 7.5 and in SAC [1997], results are reported in the present section.

Figure 8.5 and Figure 8.6 show the comparison of the responses in term of force-displacement relation, considering the same system characterized by an initial period $T_n = 0.5$s. Figure 8.5a reports the elastic case showing the maximum force demand f_e for the given ground motion and period. The other sub-figures the response considering the nonlinear hysteresis defined in Figure 8.4 in which the yielding force is defined as $f_y = c_y f_e$ being the yielding coefficient c_y spanning from 1 to 0.02. In this case the response in Figure 8.5a and 8.5b are exactly the same.

Comparison of the positive quadrant of all the yielding reduction force coefficient c_y hysteresis is reported in Figure 8.7, from which is clear that reducing the c_y, both the displacement demand and the displacement ductility are increased, this one more than proportionally with respect to the previous, being the yielding displacement reduced at the same time.

For the given ground motion and the system which is being investigated, the relation of the yielding force normalized with respect to the weight of the structure (the lateral strength yielding coefficient) versus the displacement ductility is shown in Figure 8.8. Plot is provided up to a displacement ductility $\mu = 10$. Obviously in this case the elastic case and the $c_y = 1$ case are characterized by the same point in correspondence of $\mu = 1$.

Due to the fact that the hysteresis investigated is characterized by a second hardening after the yielding, the maximum shear force demand is not the same than the yielding force. The maximum force is related to the ductility, nevertheless additional plot showing the maximum force level versus the yielding force level is provided in Figure 8.9. If the hysteresis were elastoplastic with no hardening the line in Figure 8.9 would be the quadrant bisector. Given that the maximum shear experienced by the SDOF is larger than the yielding force which is reported normalized with respect to the weight of the structure, the line is at the right part of it, being the maximum force normalized with respect to the system weight reported in the horizontal axis. Only for $c_y = 1$, the line is on the bisector.

8.4.3   Mean Results over all the Ground Motion Set

The same results presented in Section 8.4.2 have computed for all the 32 records as defined in Section 8.3 and SAC [1997]. In this section the results for period $T_n = 0.5$s are reported considering the mean value over all the record set and the relative standard deviation.

Figure 8.10 reports the plot of the mean plus and minus a standard deviation over all the 32 ground motions, lateral strength yielding coefficient as a function of the displacement ductility. Yielding force ratio values corresponding to some given ductility values have been highlighted in the same figure, for $\mu = 3$, $\mu = 4$, and $\mu = 5$. Mean plot in therm of yielding force ratio and ductility resulted quite smooth in this case; nevertheless if different force levels correspond to the same ductility value, the largest one is considered.

In Figure 8.11 the relation between lateral strength yielding coefficient and maximum shear coefficient is reported again considering the mean value of the given system over all the 32 records and the mean value plus and minus a standard deviation.

In general, the data dispersion resulted to be larger for short period structures than for long period ones. Hence in this example case the standard deviation is characterized by a large value.

8.4.4   Resulting Constant Ductility Spectra

The procedure described in Section 8.4.3 has then been repeated for all the period vector spanning between $T_n = 0.5$s and $T_n = 3$s. The final result are constant ductility spectra computed for the ductility values of interest, which are $\mu = 3$, $\mu = 4$, and $\mu = 5$.
Two spectra are provided:

- yielding force constant ductility spectra: this is the spectra reporting the minimum yielding force not to exceed the given ductility value in the design conditions;

- maximum force constant ductility spectra: this is the spectra reporting the maximum force demand in the design conditions in a system reaching the given ductility value.

(a) elastic case

(b) inelastic $c_y = 1.00$

(c) inelastic $c_y = 0.75$

(d) inelastic $c_y = 0.50$

(e) inelastic $c_y = 0.40$

(f) inelastic $c_y = 0.30$

Figure 8.5. Comparison of the different force-displacement relations, ground motion LA01, $T_n = 0.5$s, $\xi = 2\%$ - part 1

(a) inelastic $c_y = 0.25$

(b) inelastic $c_y = 0.20$

(c) inelastic $c_y = 0.15$

(d) inelastic $c_y = 0.10$

(e) inelastic $c_y = 0.05$

(f) inelastic $c_y = 0.02$

Figure 8.6. Comparison of the different force-displacement relations, ground motion LA01, $T_n = 0.5$s, $\xi = 2\%$ - part 2

Figure 8.7. Comparison of the different force-displacement relations, ground motion LA01, $T_n = 0.5$s, $\xi = 2\%$ - part 3

Figure 8.8. Maximum displacement ductility demand vs lateral strength yielding coefficient, ground motion LA01, $T_n = 0.5$s, $\xi = 2\%$

Spectra are proposed reporting the force value normalized with respect to the weight of the structure. The design conditions are intended to be defined by the ground motion set which is used for the analysis.

Figure 8.12, Figure 8.13, and Figure 8.14 reports in the same axis scale the constant ductility spectra respectively for ductilities $\mu = 3$, $\mu = 4$, and $\mu = 5$. For each period ordinate, the mean value and the mean plus and minus a standard deviation over the 32 record is shown. Obviously, increasing the ductility level the spectral ordinate reduces for the same period value, even if differences are smaller for long period structures and higher for short period ones. For short period structures, the yielding force spectral ordinate is about two-third of the maximum force for $\mu = 3$ and about one-half for $\mu = 5$. Differences between the yielding and maximum force spectra get almost negligible in long period range for all the ductility values considered.
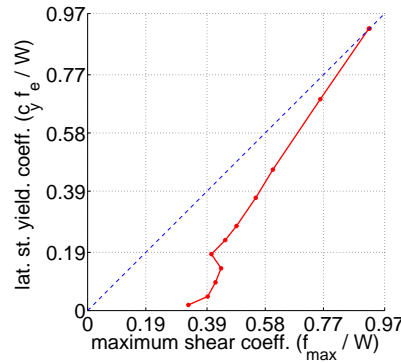
Figure 8.9. Maximum shear demand vs lateral strength yielding coefficient, ground motion LA01, $T_n = 0.5$s, $\xi = 2\%$

As already noticed, the standard deviation is quite high for short period range and decreases for long period range.

Figure 8.15 and Figure 8.16 shows respectively the yielding force ratio spectra and the maximum force ratio spectra data. The same plots underline the fact that differences between the considered ductility levels are larger in the yielding force ratio than in the maximum force ratio.

Moreover, from the data reported, it is clear that both the yielding force and the maximum force spectra can be described through a polynomial function decreasing as the period increases. Hence, in the same plot the polynomial regression for the data is presented interpolating the mean spectra ordinate data. Third order polynomial have been used for the purpose of expressing as a function of the period T the spectra ordinates $p(T)$ in the form:

$$p(T) = p_1 T^3 + p_2 T^2 + p_3 T + p_4 \tag{8.4}$$

The interpolating polynomial coefficients are reported in Table 8.1 for the yielding ratio spectra and in Table 8.2 for the maximum force ratio spectra to provide an analytical form for the yielding and maximum force ratio spectra.

(a) mean value

(b) mean and mean ± st. dev.

Figure 8.10. Maximum displacement ductility demand given by lateral strength yielding coefficient, mean value over all the records: values for $\mu = 3$, $\mu = 4$ and $\mu = 5$ are highlighted

Table 8.1. Yielding force lateral strength spectra polynomial coefficients for SL system hysteresis

Yielding Force Ratio (SL system)				
μ	p_1	p_2	p_3	p_4
3	-0.0247	0.1942	-0.5511	0.6283
4	-0.0245	0.1829	-0.4904	0.5286
5	-0.0244	0.1754	-0.4509	0.4656

(a) mean value   (b) mean and mean ± st. dev.
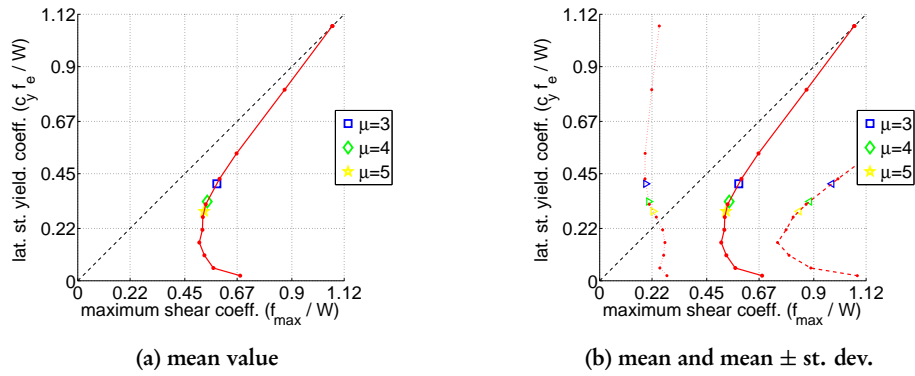
Figure 8.11. Maximum shear demand given by lateral strength yielding coefficient; mean value over all the records: values for $\mu = 3$, $\mu = 4$ and $\mu = 5$ are highlighted

(a) yielding force

(b) maximum shear force
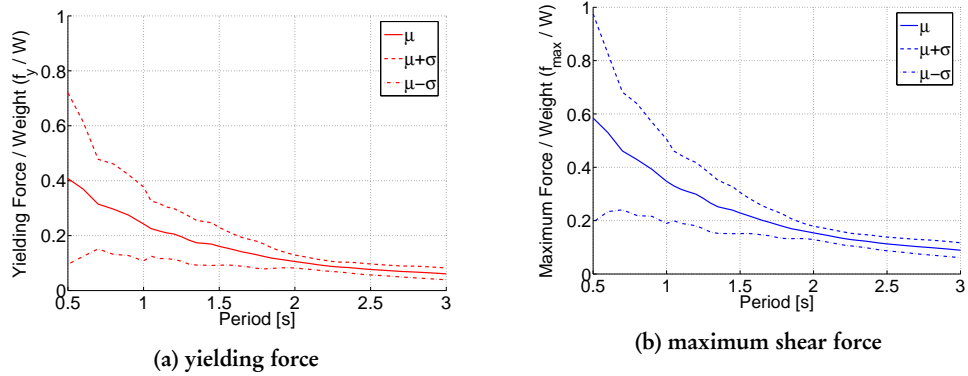
Figure 8.12. Yielding and maximum shear force coefficient spectra for ductility $\mu = 3$: mean value and mean ± standard deviation

Table 8.2. Maximum force lateral strength spectra polynomial coefficients for SL system hysteresis

Maximum Force Ratio (SL system)				
μ	p_1	p_2	p_3	p_4
3	-0.0363	0.2847	-0.8025	0.9097
4	-0.0396	0.2978	-0.8025	0.8695
5	-0.0444	0.3215	-0.8301	0.8613

(a) yielding force

(b) maximum shear force
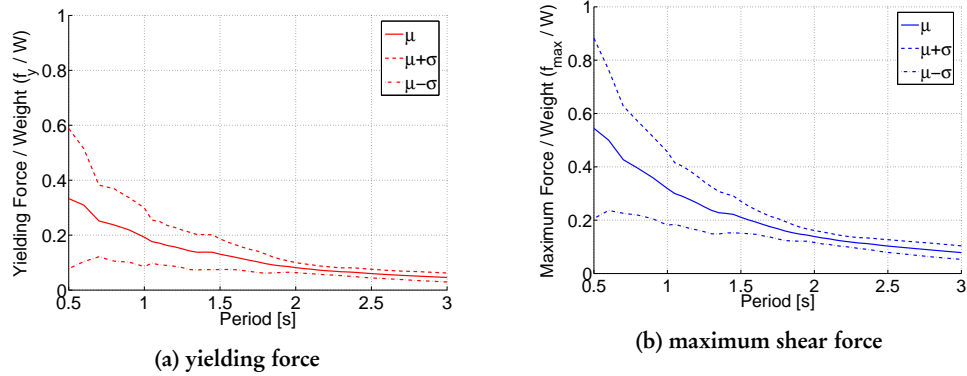
Figure 8.13. Yielding and maximum shear force coefficient spectra for ductility $\mu = 4$: mean value and mean $\pm$ standard deviation

(a) yielding force

(b) maximum shear force
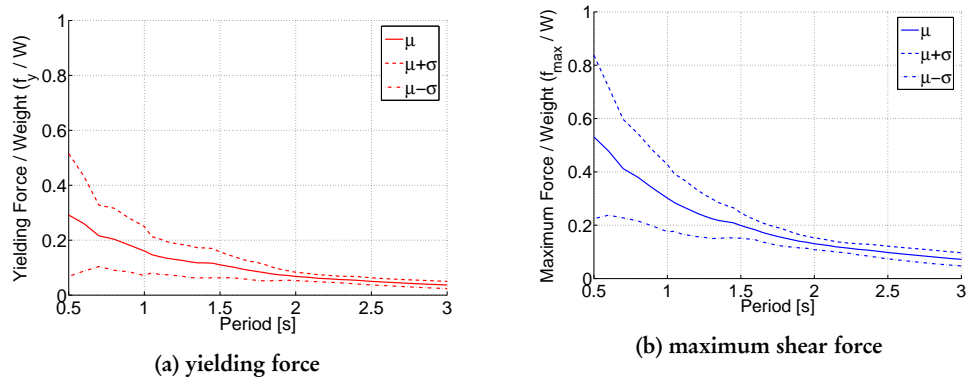
Figure 8.14. Yielding and maximum shear force coefficient spectra for ductility $\mu = 5$: mean value and mean $\pm$ standard deviation
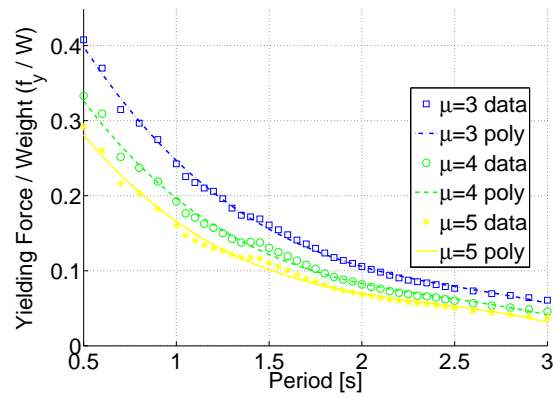
Figure 8.15. Yielding constant ductility spectra: data and polynomial regression
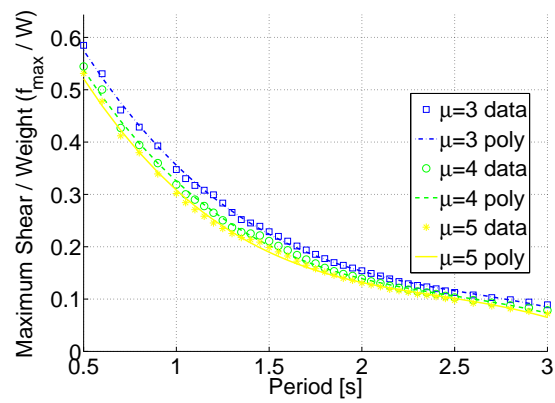
Figure 8.16. Maximum shear constant ductility spectra: data and polynomial regression

8.5 Innovative Superelastic Flag-shaped System with Relevant Friction

The constant ductility response spectra has been then investigated for the flag-shaped force-displacement relation relative to the *FR system*, as already defined in Section 7.2.3. This is an isolation system conception in which the device is composed by a lateral superelastic restrainer system and a flat slider to carry the vertical load and part of the shear force. The slider is characterized by a relevant friction coefficient and it contributes both in shear force and lateral stiffness response.

8.5.1 Modeling Issues

The considered flag-shaped force-displacement relation is shown in Figure 8.17. This has been used in time history analyses performed considering a SDOF system subjected to the considered ground motion set. It is composed by two contributions, the one from a
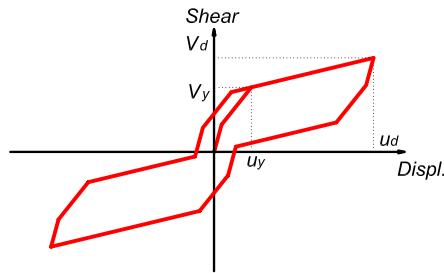
Figure 8.17. Base shear horizontal displacement relation for superelastic with friction isolation device

superelastic device (*SE*, shown in Figure 8.18a), and another one from the friction bearing (*BF*, shown in Figure 8.18b). In the considered device, the total yielding shear V_y as defined

(a) superelastic contribution   (b) frictional contribution
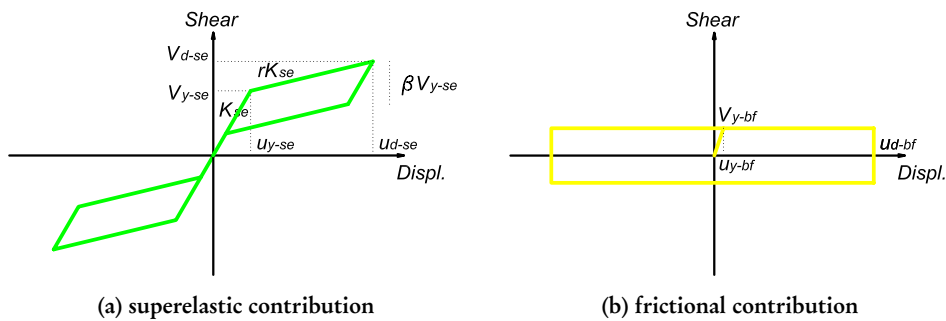
Figure 8.18. Superelastic with friction isolation device hysteresis components

in Figure 8.17, is shared between the two elements according to the following ratios:

$$V_{se} = \quad 0.7\ V_y$$
$$V_{bf} = \quad 0.3\ V_y \tag{8.5}$$

even changing the yielding level of force V_y, these ratios have been considered constant. For the sake of the investigation, the yielding shear value V_y has been considered equivalent to the yielding force f_y defined in Section 8.2.

The superelastic component (*SE*) properties have been defined as in the previous Section 8.4, with exception of the initial stiffness k_{se}, which has been reduced by the same coefficient used to reduce the superelastic shear V_{se} over the total shear V_y.

The friction component (*BF*) has been modeled considering an elastic perfectly plastic force-displacement relation characterized by an initial stiffness about four times larger than the superelastic one and by the yielding shear V_{bf}.

Given that the resulting loading curve is trilinear, as shown in Figure 8.17, a fictitious yielding point has been considered in correspondence of the superelastic device yielding $u_{y-se} = u_y$ (as reported respectively in Figure 8.17 and Figure 8.18a). The global system has then been identified considering a stiffness k_{sys} which is the secant stiffness to the superelastic device yielding displacement:

$$k_{sys} = \frac{\left(V_{y-se}\right) + \left(V_{y-bf}\right)}{u_{y-se}} = \frac{V_y}{u_y} \tag{8.6}$$

This stiffness neglects the bilinear contribution of the friction yielding effect, but it is considered the most significative parameter to define the initial system. Accordingly to this assumption, the period T_n has been computed based on k_{sys}, as shown in Equation (8.7) being M the mass of the system and neglecting the large stiffness provided by the friction device.

$$T_n = 2\pi \sqrt{\frac{M}{k_{sys}}} \tag{8.7}$$

For each ground motion and period value, the first run has been elastic, referring to stiffness k_{sys} as defined in Equation (8.6). Then 12 yielding strength coefficient values have been considered, from $c_y = 1$ to $c_y = 0.02$, to compute the yielding force $f_y = V_y$, being the other hysteretic properties constant and allocating the total force between the two contributions according to coefficients in Equation (8.5).

Analyses are performed considering system periods T_n, computed as defined previously, spanning between $T_{min} = 0.5s$ and $T_{max} = 3s$ for a total of 41 different periods. The effective period T_e, computed considering the stiffness secant to the design displacement as defined in Priestley *et al.* [2007], is given again as a function of T_n and of the ductility μ by Equation (8.3). Given that the investigated hysteresis is relative to

an isolation system, the investigated period set is suitable to describe the period range of interest.

The viscous damping in the analyzed systems has been modeled considering tangent stiffness proportional damping, as suggested in Grant *et al.* [2005] and Petrini *et al.* [2008]. A damping ratio $\xi = 2\%$ of the critical one has been considered.

Analyses were performed using a nonlinear finite element program *Ruaumoko* (Carr [2007]).

8.5.2   Single Ground Motion Result Example

Referring to one single ground motion, the *LA*01 as defined in Table 7.5 and in SAC [1997], results are reported in this section.

Figure 8.19 and Figure 8.20 show the comparison of the responses in term of force-displacement relation, considering the same system characterized by an initial period $T_n = 0.5$s. Figure 8.19a reports the elastic case and the other sub-figures the response considering the nonlinear hysteresis defined in Figure 8.17 changing the yielding coefficient c_y from 1 to 0.02.

In this case, due to the fact that the force-displacement relation is characterized by two yielding points, and the elastic system is conventionally defined considering the secant stiffness to the second yielding, for high values of c_y coefficient not all the hysteretic cycle is developed. Looking at Figure 8.19b, relative to $c_y = 1$, it is clear for example that the system does not reach the superelastic device elastic limit. This is mainly due to the high initial stiffness and the high yielding limit which turn out to limit the maximum displacement. Hence in this case different response is recorded between the linear elastic system in Figure 8.19a and the $c_y = 1$ system in Figure 8.19b. Moreover, in this particular ground motion case and for $T_n = 0.5$s, no yielding is reached in the superelastic restrainer for $c_y > 0.3$. Therefore for all the cases in which $c_y > 0.3$ the displacement ductility computed according assumptions reported in Section 8.5.1, results $\mu < 1$.

This is also shown in the comparison of the positive quadrant of the elastic and of all the yielding reduction force coefficient c_y hysteresis reported in Figure 8.7.

For the given ground motion and the system which is being investigated, the relation of the yielding force normalized with respect to the weight of the structure (the lateral strength yielding coefficient) versus the displacement ductility is shown in Figure 8.8. Plot is provided up to a displacement ductility $\mu = 10$. Again, the ductility plot presents a jump from the elastic case to the $c_y = 1$ case due to the reduction of displacement due to the high stiffness of the friction component.

Additional plot reporting the maximum force level versus the yielding force level is provided in Figure 8.23. In the cases in which the superelastic system does not yield the maximum force ratio is on the left of the bisector, while if yielding force ration is exceeded the point is at the right of it. The first point, the one on the top in the bisector, is the linear elastic point.

(a) elastic case

(b) inelastic $c_y = 1.00$

(c) inelastic $c_y = 0.75$

(d) inelastic $c_y = 0.50$

(e) inelastic $c_y = 0.40$

(f) inelastic $c_y = 0.30$
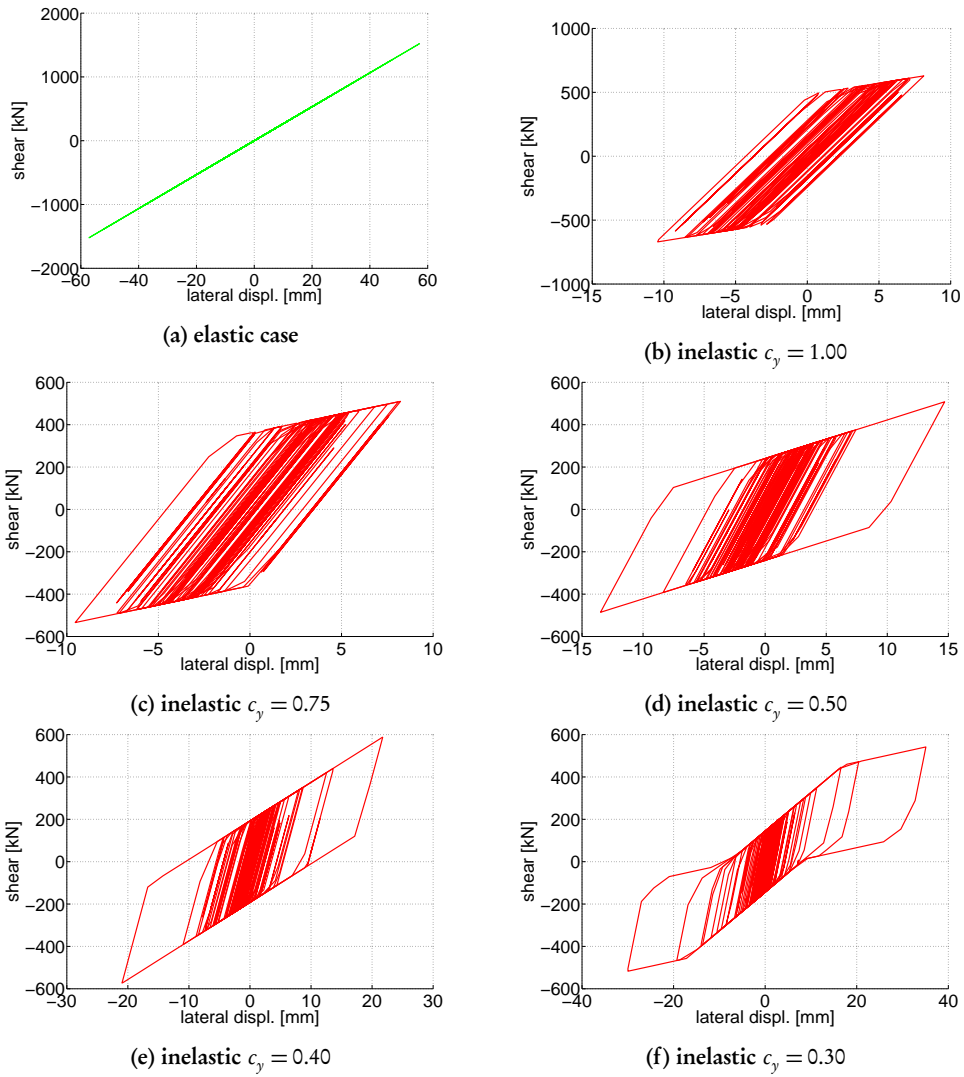
Figure 8.19. Comparison of the different force-displacement relations, ground motion LA01, $T_n = 0.5$s, $\xi = 2\%$ - part 1

(a) inelastic $c_y = 0.25$

(b) inelastic $c_y = 0.20$

(c) inelastic $c_y = 0.15$

(d) inelastic $c_y = 0.10$

(e) inelastic $c_y = 0.05$

(f) inelastic $c_y = 0.02$
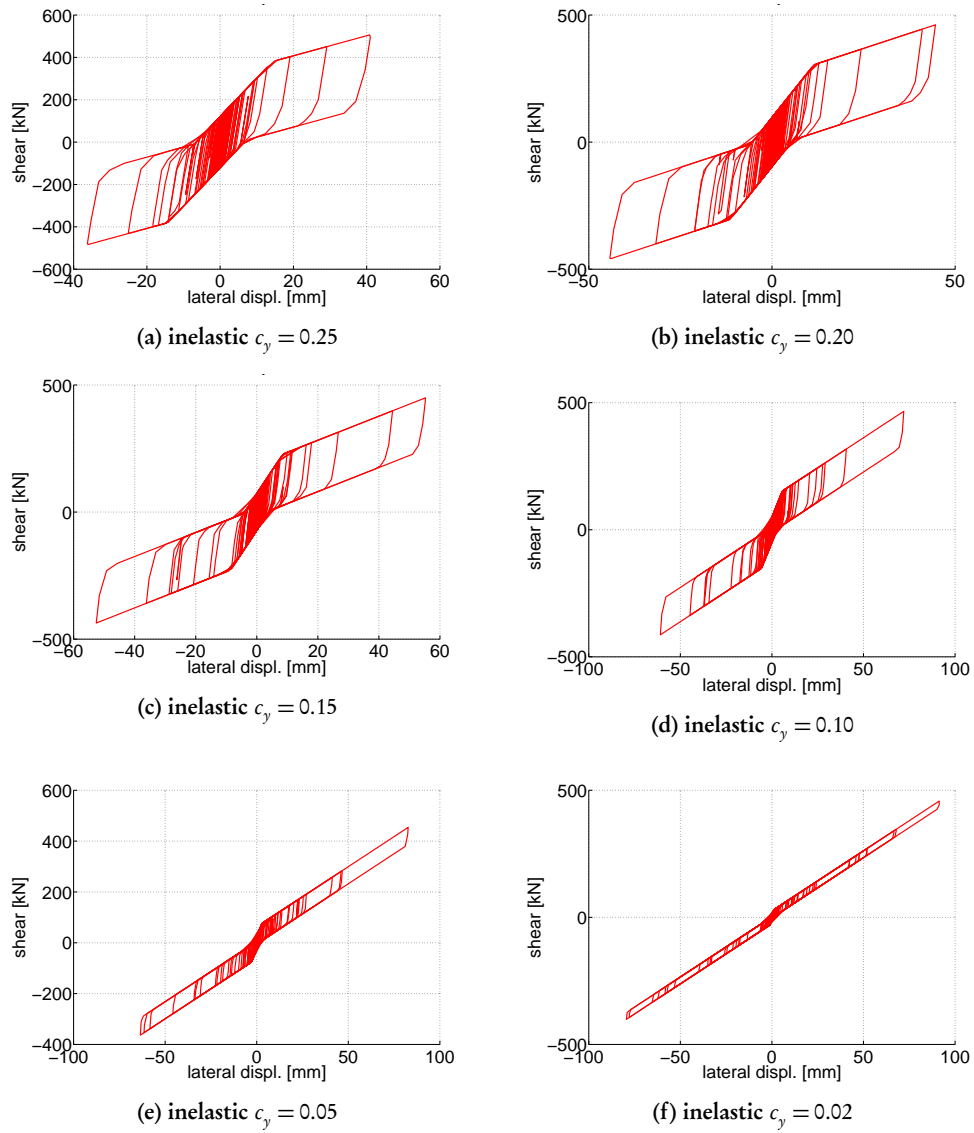
Figure 8.20. Comparison of the different force-displacement relations, ground motion LA01, $T_n = 0.5$s, $\xi = 2\%$ - part 2
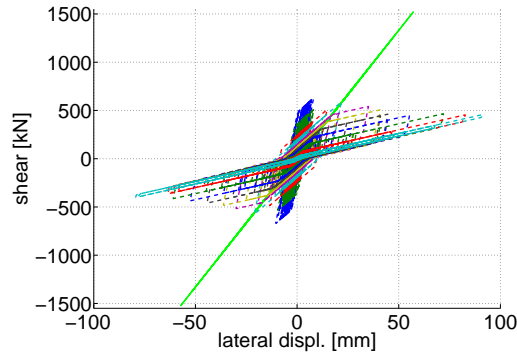
Figure 8.21. Comparison of the different force-displacement relations, ground motion LA01, $T_n = 0.5$s, $\xi = 2\%$ - **part 3**
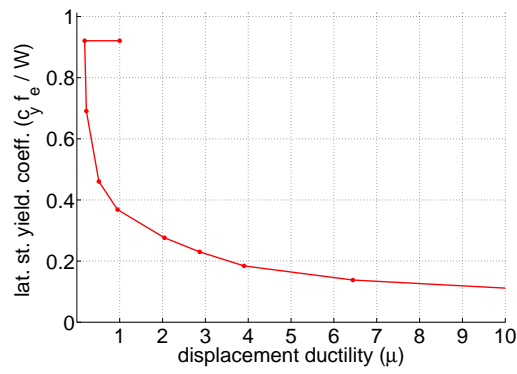
Figure 8.22. Maximum displacement ductility demand vs lateral strength yielding coefficient, ground motion LA01, $T_n = 0.5$s, $\xi = 2\%$
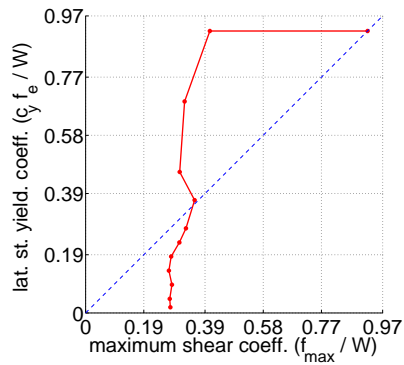
Figure 8.23. Maximum shear demand vs lateral strength yielding coefficient, ground motion LA01, $T_n = 0.5$s, $\xi = 2\%$

8.5.3 Mean Results over all the Ground Motion Set

The same results presented in Section 8.5.2 have computed for all the 32 records as defined in Section 8.3 and SAC [1997]. In this section the results for period $T_n = 0.5$s are reported considering the mean value over all the record set and the relative standard deviation.

Figure 8.24 shows the mean value plus and minus the standard deviation computed over all the 32 ground motions. Yielding force ratio values corresponding to some given ductility values have been highlighted in the same figure, for $\mu = 3$, $\mu = 4$, and $\mu = 5$. In this case the mean plot in therm of yielding force ratio and ductility resulted quite smooth. nonetheless if different force level corresponds to the same ductility value the largest one is considered.

In Figure 8.25 the relation between lateral strength yielding coefficient and maximum shear coefficient is reported again considering the mean value of the given system over all the 32 records and the mean value plus and minus a standard deviation. The data dispersion resulted to be larger for short period structures than for long period ones. Because of this, in this example case the standard deviation shows its highest value.

8.5.4 Resulting Constant Ductility Spectra

The procedure described in Section 8.5.3 has then been repeated for all the period vector spanning between $T_n = 0.5$s and $T_n = 3$s.

The final result are constant ductility spectra computed for the ductility values of interest, which are $\mu = 3$, $\mu = 4$, and $\mu = 5$.
Two spectra are provided:

- yielding force constant ductility spectra: this is the spectra reporting the minimum yielding force not to exceed the given ductility value in the design conditions;

- maximum force constant ductility spectra: this is the spectra reporting the maximum force demand in the design conditions in a system reaching the given ductility value.
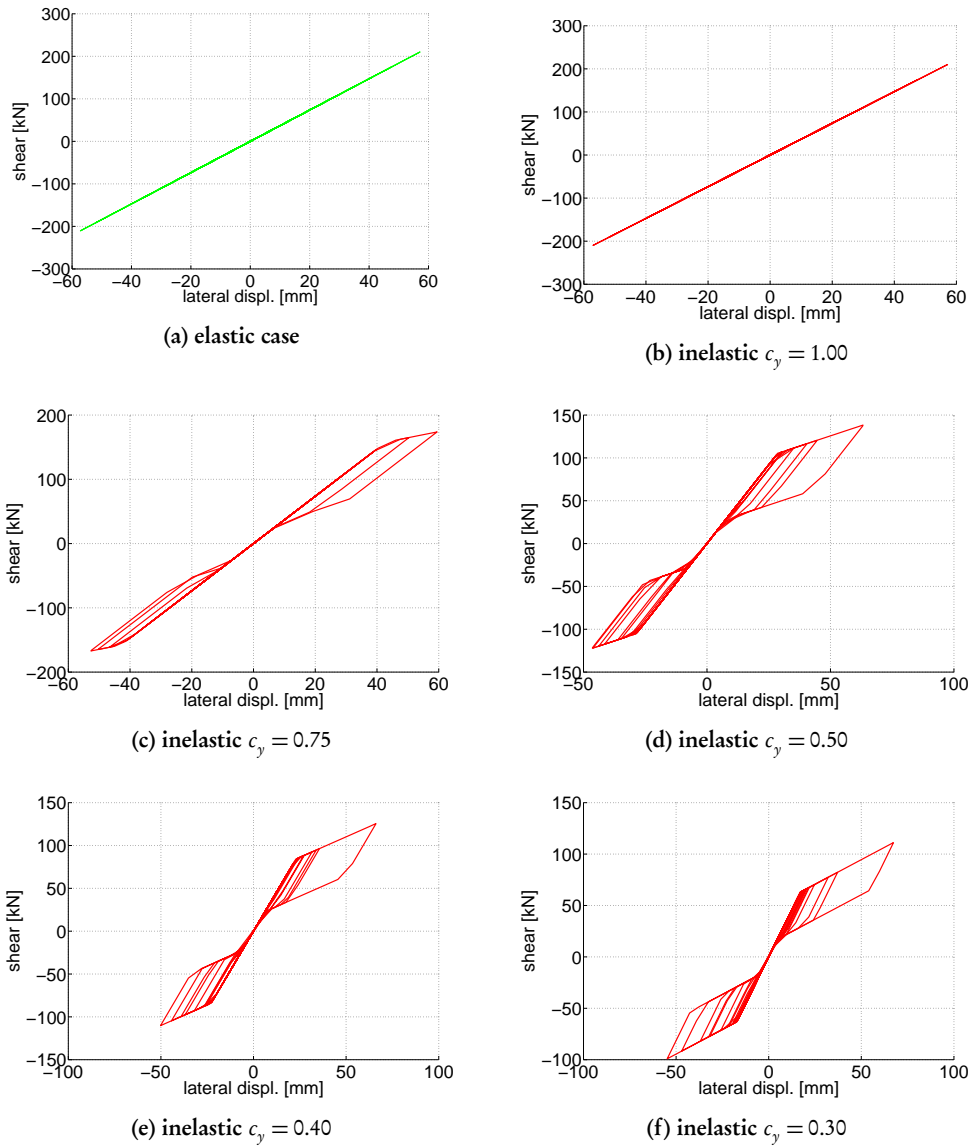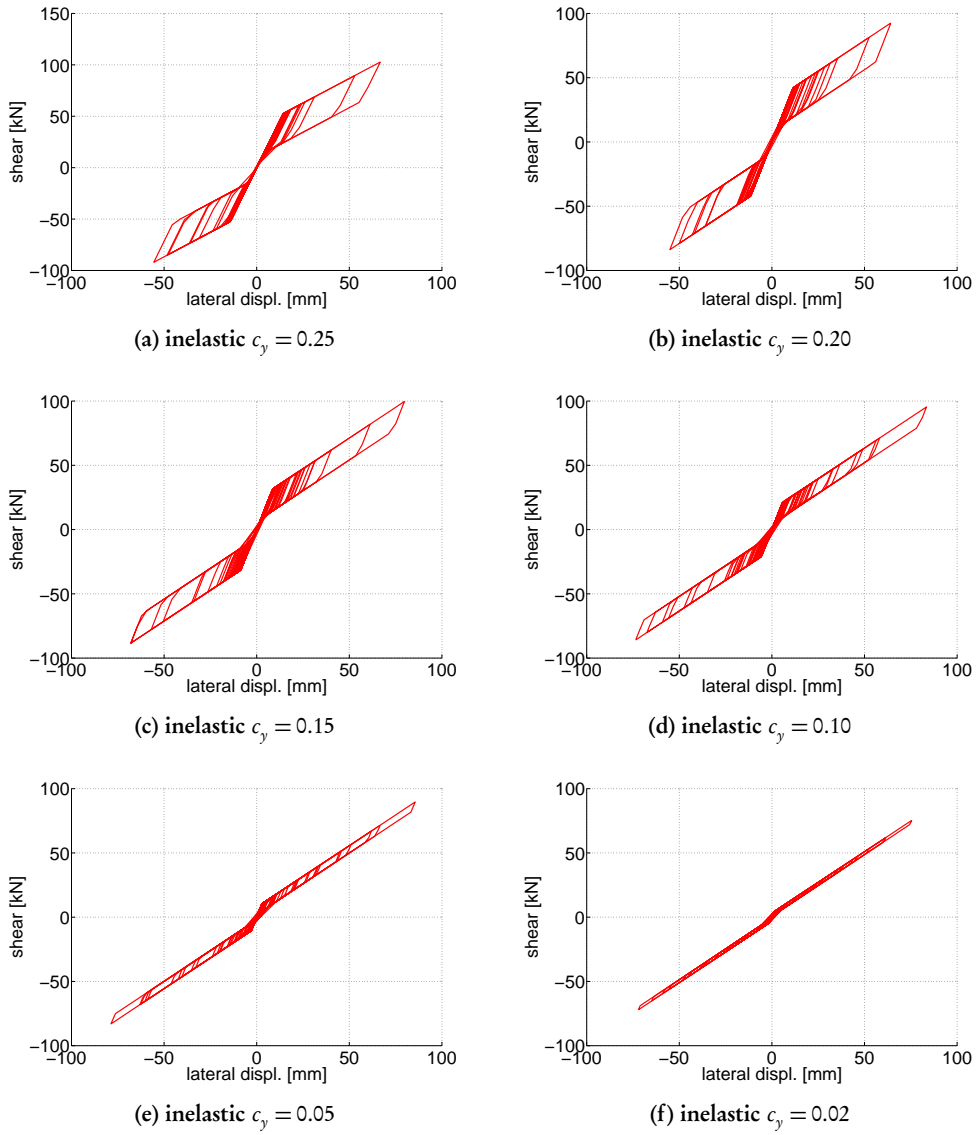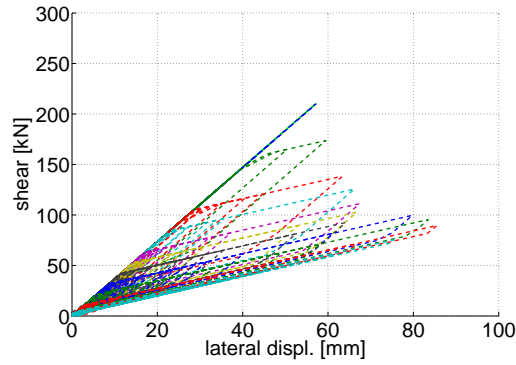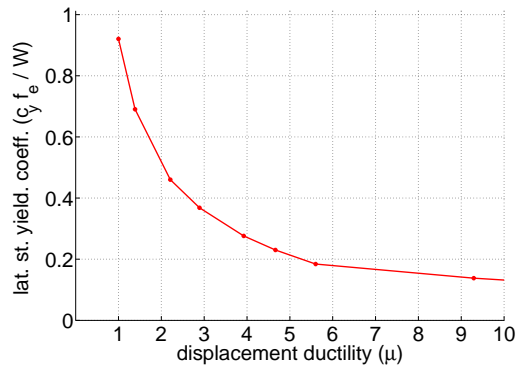
Spectra are proposed reporting the force value normalized with respect to the weight of the structure, and the design conditions are assumed to be the ones provided by the used record set. Figure 8.26, Figure 8.27, and Figure 8.28 reports in the same axis scale the constant ductility spectra respectively for ductilities $\mu = 3$, $\mu = 4$, and $\mu = 5$. For each period ordinate, the mean value and the mean plus and minus a standard deviation over the 32 record is shown.

The spectral shape is similar to the one found in Section 8.4.4 for the SL system. The main difference is anyway that the yielding force and maximum force coefficient for a given ductility is smaller than in the previous case. Again, differences between the yielding and maximum force spectra get almost negligible for long period range for all the ductility values considered; the standard deviation is large for short period range and

(a) mean value

(b) mean and mean ± st. dev.
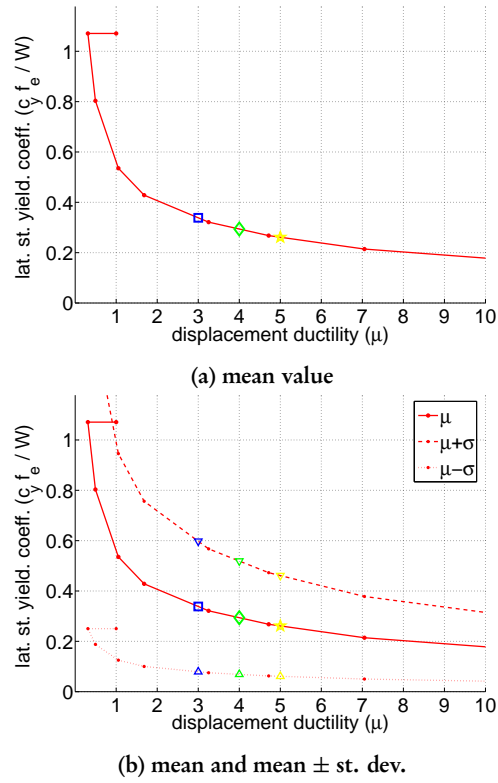
Figure 8.24. Maximum displacement ductility demand given by lateral strength yielding coefficient, mean value over all the records: values for $\mu = 3$, $\mu = 4$ and $\mu = 5$ are highlighted

(a) mean value

(b) mean and mean ± st. dev.
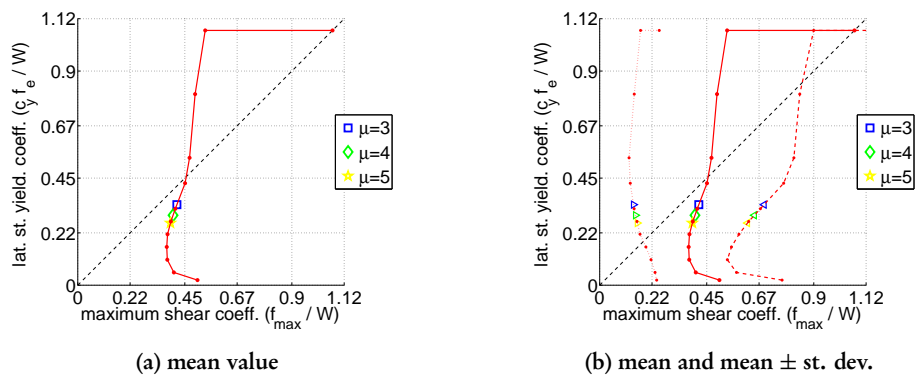
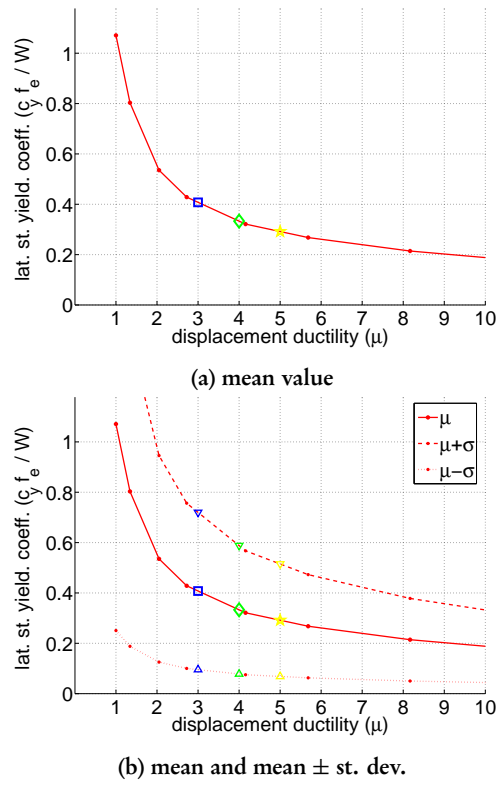**Figure 8.25.** Maximum shear demand given by lateral strength yielding coefficient; mean value over all the records: values for $\mu = 3$, $\mu = 4$ and $\mu = 5$ are highlighted

(a) yielding force

(b) maximum shear force
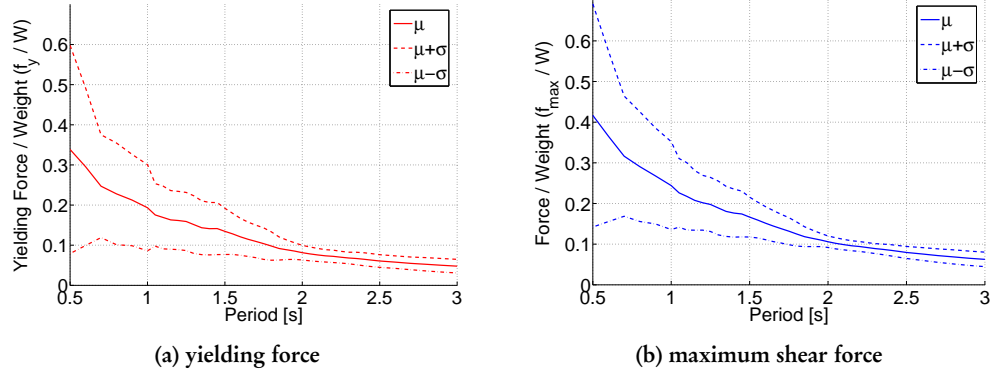
Figure 8.26. Yielding and maximum shear force coefficient spectra for ductility $\mu = 3$: mean value and mean $\pm$ standard deviation

(a) yielding force

(b) maximum shear force
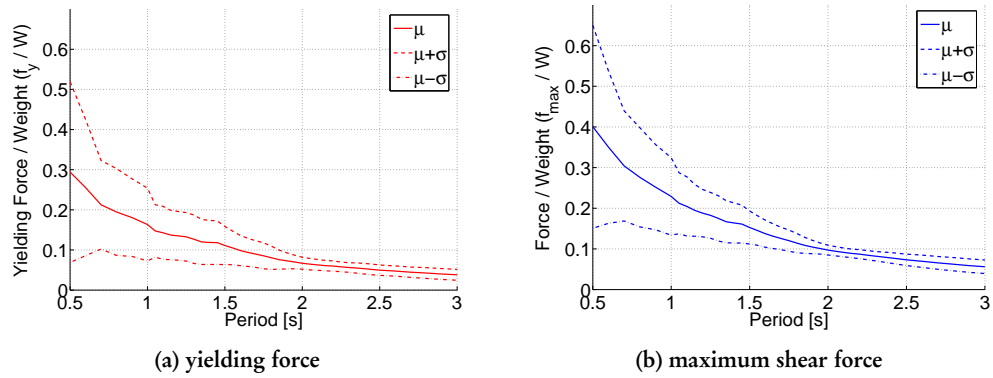
Figure 8.27. Yielding and maximum shear force coefficient spectra for ductility $\mu = 4$: mean value and mean $\pm$ standard deviation

almost negligible for long period structures.

Figure 8.29 and Figure 8.30 shows respectively the yielding force ratio spectra and the maximum force ratio spectra data. From the data reported it is clear that both the yielding force and the maximum force spectra can be described through a polynomial function decreasing as the period increases. In the same plot the polynomial regression for the data is presented in interpolating the mean spectra ordinate data. Third order polynomial have been used for the purpose of expressing as a function of the period T the spectra ordinates $p(T)$ in the form:

$$p(T) = p_1 T^3 + p_2 T^2 + p_3 T + p_4 \tag{8.8}$$

(a) yielding force　　　　　　　　　　　　　　　(b) maximum shear force
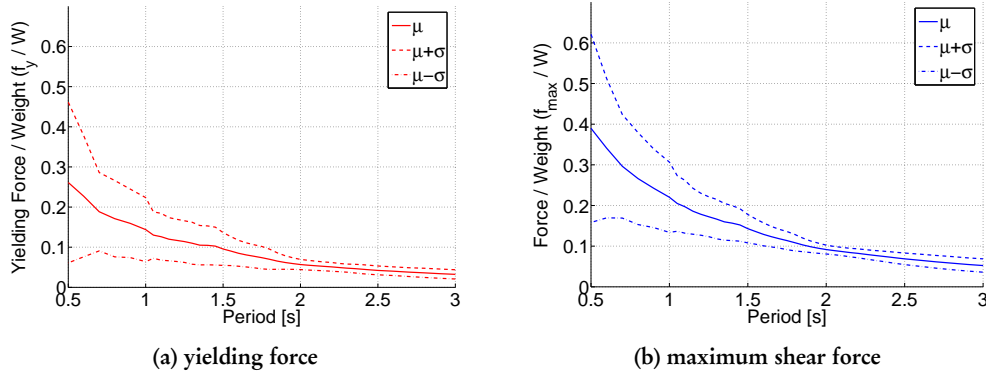
Figure 8.28. Yielding and maximum shear force coefficient spectra for ductility $\mu = 5$: mean value and mean $\pm$ standard deviation
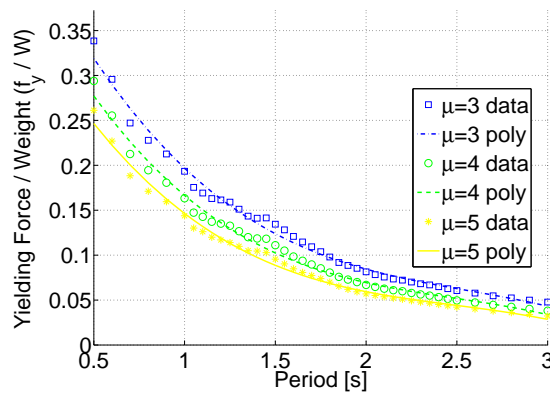
Figure 8.29. Yielding constant ductility spectra: data and polynomial regression

The interpolating polynomial coefficients are reported in Table 8.3 for the yielding ratio spectra and in Table for the maximum force ratio spectra to provide an analytical form for the yielding and maximum force ratio spectra.

8.6 CONCLUSIONS

Constant ductility spectra have been computed for innovative seismic isolation systems based on flag-shaped force-displacement response. The lateral restraining superelastic system is characterized by limited available ductility and informations are required for the design process on the minimum yielding shear force and on the minimum base shear not to exceed it.
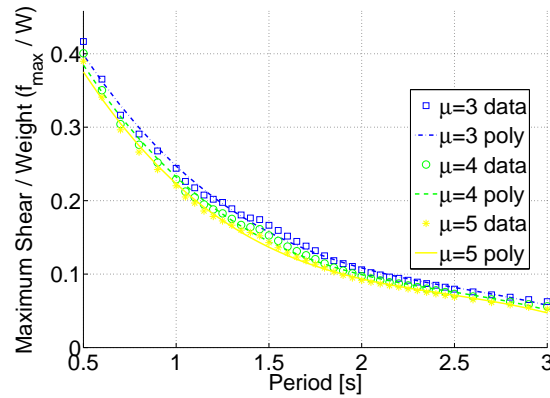
Figure 8.30. Maximum shear constant ductility spectra: data and polynomial regression

Table 8.3. Yielding force lateral strength spectra polynomial coefficients for FR system hysteresis

		Yielding Force Ratio (FR system)		
μ	p_1	p_2	p_3	p_4
3	-0.0209	0.1612	-0.4495	0.5060
4	-0.0208	0.1556	-0.4182	0.4499
5	-0.0190	0.1419	-0.3800	0.4034

Table 8.4. Maximum force lateral strength spectra polynomial coefficients for FR system hysteresis

		Maximum Force Ratio (FR system)		
μ	p_1	p_2	p_3	p_4
3	-0.0260	0.2002	-0.5571	0.6302
4	-0.0287	0.2146	-0.5761	0.6225
5	-0.0299	0.2213	-0.5839	0.6156

Two isolation system configurations are investigated. In the first one (SL system) all the shear force is carried by lateral superelastic restrainer. In the second one (FR system) the contribution of slider friction in terms of shear force and lateral stiffness has to be taken into account.

Results show that the SL system is in general more demanding than the FR friction. Comparison between Figure 8.15 and Figure 8.29 supports the conclusion, because for the same condition the spectra ordinates of SL system are larger than the FR system ones.

This implies that given the design conditions and a maximum tolerable ductility demand, the minimum yielding force not to exceed the ductility capacity is larger in the SL system than in the FR system. So the isolation system of a structure isolated with SL device has to be designed for an higher yielding strength to control the maximum ductility demand below the ductility capacity than the same structure isolated with FR system.

Or, in other terms, if the same structure is designed isolated by SL and FR systems characterized by the same yielding force, the SL isolation system is characterized by a larger ductility demand.

The same conclusion can be obtained considering the maximum force demand, hence from the comparison between Figure 8.16 and Figure 8.30. Again, the spectral ordinates of the SL system are larger than the ones of the FR system. The maximum force is important because it is the maximum shear transmitted from the isolation system to the superstructure, therefore capacity design is affected by this term.

If the same displacement ductility capacity has not to be exceeded in the isolation system, more strong superstructure has to be designed if SL system is used than if FR system is used.

Or, if the same superstructure is designed being isolated by SL and FR system, provided that rupture does not occur at isolation level, the superstructure is going to reach the same damage level for lower displacement ductility using the SL system than using the FR system.

Presented spectra are an important design tool for the definition of an optimum isolation system configuration using superelastic lateral restrainer devices. Given the available superelastic device, the designer has the chance to optimize the configuration changing the number of devices and the type of the system to meet all the design requirements.

9. Evaluation of Superelastic Seismic Isolation Device Response for Stiff Buildings

9.1 INTRODUCTION

The effectiveness of superelastic isolation device as presented in Chapter 6 is investigated in the present chapter considering the response of a base-isolated structure modeled as a multi degree of freedom system. The term superelastic (*SE*) isolation refers to a bearing characterized by a nonlinear shear force-horizontal displacement relation which can be described by a *flag-shaped* hysteresis. This hysteresis has been demonstrated to be provided by a lateral restrainer system composed by *shape memory alloy* manufactured devices. An actual force-displacement relation computed from a real superelastic device design is considered. Its model has been investigated and experimentally validated. The response of a structural system isolated using innovative bearings is compared with respect to the same structure isolated using traditional isolation devices. In this context, the traditional isolation bearing is a lead rubber bearing (*LRB*) and the superelastic device has been designed to be equivalent to the existing LRB. Previous investigations on single degree of freedom systems reported in Chapter 7 have demonstrated that the response of superelastic isolation devices is very attractive for its effectiveness in modifying the structural behavior and avoiding the residual displacements after the seismic event. Nevertheless, a strong limitation was given by the fact that the superstructure has been considered only for the computation of the additional mass of the system, neglecting any flexibility contribution. On the contrary, in the present investigation, a two storey frame configuration response is considered. The aim is to focus not only on the isolation system, but also on the effects on the superstructure, which has been taken into account considering its real flexibility, strength, and mass contribution. A stiff superstructure is considered, which is the most common case for the base isolation technology applications.

Two cases are considered, one in which the superstructure is designed to respond elastically and a second one in which the design is performed accepting limited damage in it. The aim is to compare the differences in the response induced by the different isolation system both when the system has been designed properly, assuring no damage in the isolated part of the structure, but also to investigate them when the elastic strength of the superstructure members is exceeded.

The investigation consists of a series of time history analyses. Direct computation

of the response in time of the system subjected to a suitable ground motion set and evaluation of design parameters both at the isolation system level and in the superstructure is considered the best way to evaluate the response of the innovative system with respect to the traditional one.

Section 9.2 describes the building properties and modeling issues. Section 9.3 recalls the technical configurations and principles of the innovative isolation devices and Section 9.4 reports the isolation system modeling issues and the finite element procedure. Section 9.5 introduces the ground motion set which has been used in the analysis procedure. Section 9.6 and Section 9.7 present the main finding of the investigation and in Section 9.8 the conclusions are reported.

9.2   DESIGN ASSUMPTION AND BUILDING PROPERTIES

In this study, the seismic response for a base-isolated *stiff* building is considered. This is the case of a structure whose fundamental isolated period is several times longer than the fundamental period considering a fixed-base, as defined in Priestley *et al.* [2007].

The building example is taken with some changes from Priestley *et al.* [2007] in which the same structural configuration has been presented for a simulated design. It is a small residential building, a two storey reinforced concrete frame structure. In this work we
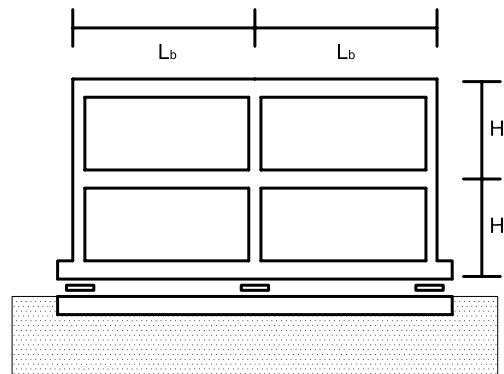
Figure 9.1. Building vertical section

assume for symmetry reasons to analyze only one frame of the resisting system, assuming the total weight and the forces to be distributed in the same proportion in all the resisting frames.

The vertical section geometry is shown in Figure 9.1, while the building plan is shown in Figure 9.2. The interstorey height is $H_s = 3$m and the beam span is $L_b = 6$m. All columns have sections of 400x400mm in plan; all beams are assumed to have a depth of 600mm.

(a) design case #1   (b) design case #2
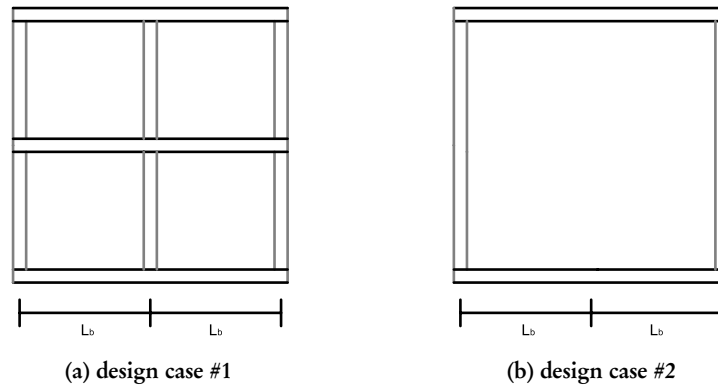
Figure 9.2. Building plan

Two cases are considered to investigate differences in the system response due to change in isolation technology and in superstructure behavior:

- case #1: *elastically responding superstructure.*
  This is the case of the proper design, when the superstructure has been designed to guarantee an elastic response under the design conditions. This imply that no damage is supposed to occur in the superstructure which maintains its initial properties during the motion.

- case #2: *inelastically responding superstructure.*
  This is the case in which the capacity design has not been applied between the isolation and the superstructure and the maximum design isolator shear force causes some damage in the superstructure. Being damaged, the superstructure changes its properties during the motions, and this affects its response.
  Of course this is not the proper design case, in which the superstructure damage has to be avoided, but it is an hypothetical design example case to evaluate how, and how much, the different isolation system affects the inelastic response of the superstructure too.

Given the design example structure, it is assumed that the total weight and the base shear is shared in the same proportion in all the resisting frames.

The case #1 has been considered first. The isolation system has been designed to meet the requirements, as described in Section 9.2.1. Then the superstructure has been designed considering a capacity design approach according to which it is supposed to respond elastically; this is reported in Section 9.2.2. In this first case *three* resisting frames have been considered, as shown in Figure 9.2a.

The case #2 consists then in verifying the same building than before, with the same

total weight and the same isolation system defined in Section 9.2.1, but considering only *two* resisting frames, as shown in Figure 9.2b. Moreover the frames in this second case are exactly the same than the previous case, hence they are the ones resulting from the design in Section 9.2.2. Obviously, being the total base shear the same than the case #1 but affecting only two frames, the force demand on them is significantly higher than in the previous case and the elastic limit is exceeded.

9.2.1 Isolated System Design

The goal of this investigation is to compare the structural response of a stiff building isolated using an actual bearing system with respect to the response of the same building isolated using superelastic devices. The isolation system is designed considering the actual device technical properties to determine the number of isolators to be placed. Then the same number of equivalent superelastic devices are used in the innovative system configuration.
The actual isolator device is a lead rubber bearing (LRB) produced by *AGOM International* and described in Section 4.2. Its technical properties have been reported in Table 4.1. The total weight to be considered for seismic design has been computed as $W_T = 4600 \text{kN}$ including the ground floor.

The building design is performed considering the *rigid superstructure* approach as defined in Priestley *et al.* [2007] according to which the superstructure is considered only as an additional mass for the system. In this design example we assume that the total isolation system is given by multiples of the properties of the model isolator as defined in Table 4.1. A single isolation device is supposed to be used for each frame, hence the isolation system is given by three isolators: $n_{is} = 3$. The needing of having redundancy is the vertical load sustaining elements implies that some sliders are positioned on the isolation layer as well to carry the vertical load without providing any lateral stiffness and shear force.

The design spectra is the Eurocode 8, $PGA = 0.35\text{g}$ soil C type 1 (CEN [2004]), reported in Figure 9.3. The effective design period T_d of the system is given by:

$$T_d = 2\pi \sqrt{\frac{W_T/g}{n_{is} \cdot k_e}} = 2\pi \sqrt{\frac{4600/9.81}{3 \cdot 1.62 \cdot 10^3}} = 1.95\text{s} \tag{9.1}$$

the point on the design spectra relative to the period T_d has been highlighted in Figure 9.3. Due to the equivalent damping ξ_b, the spectra reduction factor η, as defined in EC8 (CEN [2004]), is:

$$\eta = \sqrt{\frac{10}{5 + \xi_b}} = \sqrt{\frac{10}{5 + 28}} = 0.55 \tag{9.2}$$

(a) acceleration spectra   (b) displacement spectra
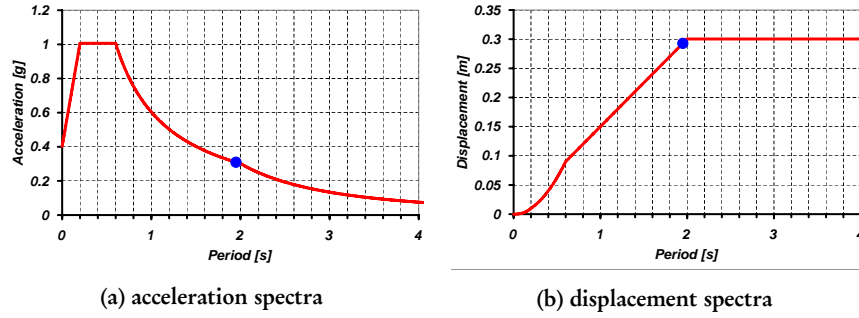
Figure 9.3. Elastic design spectra for $PGA = 0.35$g, 5% damping ratio type 1 (far field event) from EC8 (CEN [2004])

hence the design seismic displacement Δ_d from Figure 9.3b is:

$$\Delta_d = \eta S_d = 0.55 \cdot 0.29 = 0.16 \text{m} \tag{9.3}$$

in which S_d is the displacement spectra ordinate for the given period. The seismic base shear V_d from Figure 9.3a is given by:

$$V_{base} = W_T \eta S_a = 4600 \cdot 0.55 \cdot 0.31 = 784.3 \text{kN} \tag{9.4}$$

in which S_a is the acceleration spectra ordinate for the given period. The previous values are compatible with the design properties reported in Table 4.1, being on each isolator:

$$V_d = \frac{V_{base}}{n_{is}} = 261.4 \text{kN} \tag{9.5}$$

The final design base shear for the superstructure has been increased considering an overstrength factor $\phi^o = 1.2$ to assure its elastic response. Higher-mode effects have been neglected in the two-storey structural design.

9.2.2 Superstructure Design

The design of the superstructure has been performed considering the gravity loads and a base shear coefficient which resulted to be equal to 17% times the overstrength factor the total gravity load W_T:

$$\phi^o V_{base} = 17\% \cdot 1.2 \cdot W_T \simeq 930 \text{kN} \tag{9.6}$$

Consistently with design case #1, assuming to have three resisting frame $n_f = 3$ carrying the same shear proportion, the design shear for each frame V_{df} is given by:

$$V_{df} = \phi^o \frac{V_{base}}{n_f} = \frac{17\% \cdot 1.2 \cdot W_T}{3} \simeq 310 \text{kN} \tag{9.7}$$

The base shear has been used to compute base overturning moment and to distribute the actions in the frame members. The resulting design has been used both for case #1 and case #2 structure response evaluation.

(a)   Material Properties

Common material properties have been considered for the concrete and the steel in the design. The main parameters are reported in Table 9.1. Plot of the stress strain relations

Table 9.1. Material properties for RC *stiff* building design

Concrete Properties		
concrete compressive strength	f_{pc}	30 MPa
concrete modulus of elasticity	E_c	$5000\sqrt{f_{pc}}$
concrete unconfined strain	ϵ_{co}	0.002
concrete spalling strain	ϵ_{sp}	0.0064
Steel Properties		
steel yielding stress	f_y	400 MPa
steel max stress	f_{su}	600 MPa
steel modulus of elasticity	E_y	200 GPa
steel strain for strain hardening	ϵ_{sh}	0.008
steel maximum strain	ϵ_{su}	0.12

from the section analysis and member program *Cumbia* (see Montejo [2007]) are reported in Figure 9.4.
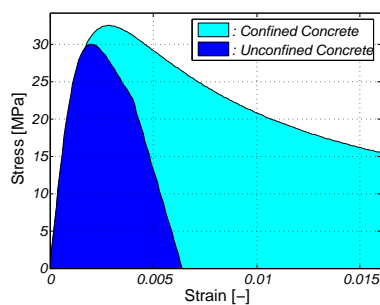
(a) confined and unconfined concrete   (b) reinforcing steel
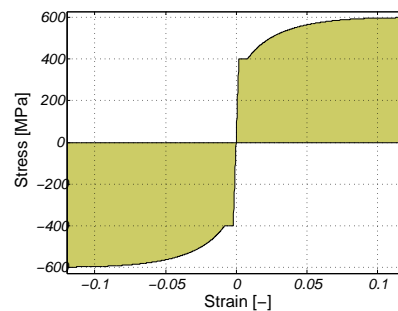
Figure 9.4. Material stress-strain relations (from Cumbia, see Montejo [2007])

(b)   Beam Design and Verification

The beams have been designed for the base shear and gravitational loads. Two designs have been performed for second level beam and first level beam considering and evaluating the reinforcement and the strength of the members in the plastic hinge zone. The considered section for beams is 400x600mm.

Second level beam plastic hinge zone is reinforced considering two 16mm bar layers, each one composed by five bars. Hence the reinforcement percentage is $\rho_{b2} = 0.84\%$. The relative moment curvature relation is shown in Figure 9.5a. The yielding moment is $M_{yb2} = 244.2\text{kNm}$ and the yielding curvature is $\Phi_{yb2} = 0.0057\text{m}^{-1}$.

First level beam plastic hinge zone is reinforced considering two 16mm bar layers, each one composed by five bars, and additional two bar layer. The reinforcement percentage is $\rho_{b1} = 1.01\%$. The relative moment curvature relation is shown in Figure 9.5b. The yielding moment is $M_{yb1} = 326.2\text{kNm}$ and the yielding curvature is $\Phi_{yb1} = 0.0067\text{m}^{-1}$.

(a) second level beam   (b) first level beam
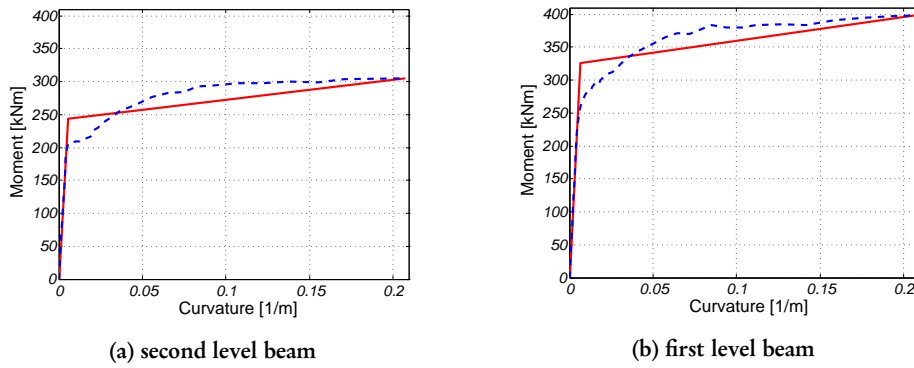
Figure 9.5. Moment curvature relation for beams: computed curve and linearization (from Cumbia, see Montejo [2007])

(c)   Column Design and Verification

Column were designed providing the same reinforcement in all the height of the building. Two cases have been considered, one for interior columns and one for exterior columns.

In the interior columns, 14 bars of 22mm diameter were used. The reinforcement ratio is $\rho_{cint} = 3.33\%$. Member analysis results of the interior columns are reported in Figure 9.6. Moment curvature relation for the plastic hinge zone at the base of the column, where the axial load is maximum $N_{cint} = 750\text{kN}$, is reported in Figure 9.6a. The moment axial load interaction diagram is then shown in Figure 9.6b.

In the exterior columns, 8 bars of 22mm diameter were used. The reinforcement ratio is $\rho_{cext} = 1.90\%$. Member analysis results of the exterior columns are reported in Figure 9.7. Moment curvature relation for the plastic hinge zone at the base of the column, where the

(a) moment curvature relation for $N_{cint} = 750$kN

(b) moment axial load interaction diagram
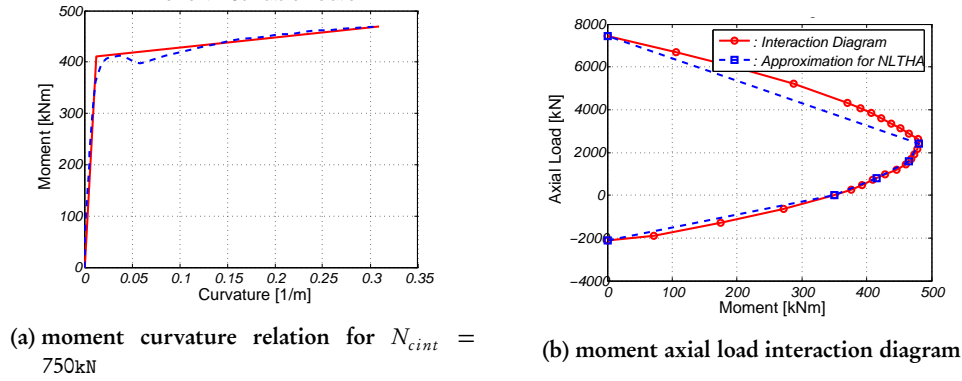
Figure 9.6. Interior column member analysis (from Cumbia, see Montejo [2007])

axial load is maximum $N_{cint} = 375$kN, is reported in Figure 9.7a. The moment axial load interaction diagram is then shown in Figure 9.7b.

(a) moment curvature relation for $N_{cext} = 375$kN

(b) moment axial load interaction diagram
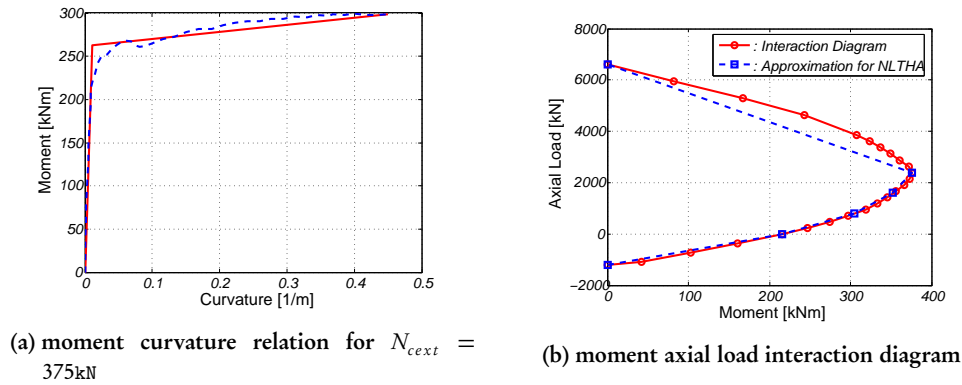
Figure 9.7. Exterior column member analysis (from Cumbia, see Montejo [2007])

9.3 INNOVATIVE SUPERELASTIC ISOLATION SYSTEMS

In this work the response of an existing device is compared with the response of two innovative superelastic system devices. The actual isolation bearing is described in Section 4.2 and it is an high dissipation device. The superelastic devices have been designed in order to be equivalent to the previous one in terms of displacement and force capabilities. They are based on a flat slider to carry the vertical load and on superelastic lateral restrainers. The solution we consider in this context for the lateral restraining system is the one reported in Chapter 6, characterized by radial lateral spring devices manufactured using

shape memory alloys which has already been described in Section 6.4.2. A proposed device configuration scheme is shown in Figure 6.29. In this investigation anyway, two possibilities for the superelastic device design shear force are investigated:

- in the first isolator device configuration, the superelastic restraining system is supposed to carry all the shear force in the device, being the friction coefficient of the slider very low and the breakaway shear negligible with respect to the yielding shear force; the technical properties of this system are described in Section 7.2.2;

- in the second configuration, an important part of the shear force is carried by the friction force, which provides an additional lateral stiffness and force component too; the technical properties of this systems are described in Section 7.2.3.

9.4 FINITE ELEMENT ANALYSIS PROCEDURE

The investigation has been performed considering the structural response in time history analyses. Global system modeling is described in Section 9.4.1 and details on the isolation system models are reported in Section 9.4.2. The considered response parameters are reported in Section 9.4.3.

9.4.1 Global System modeling

All seismic dynamic analyses are performed using the nonlinear dynamic analysis computer program *Ruaumoko* (Carr [2007]). The model includes only one exterior frame, together with one gravity column that eventually represents all interior frame columns. The total gravity loads acting on the interior columns are applied to the gravity column in the model and both the gravity column and the exterior frame are constrained to experience the same lateral deformation at each floor.

Only the bare concrete frame is included in the analyses, hence the slab participation as a composite beam is not included. The inelastic response is concentrated in plastic hinges that could form at both ends of the frame members. Rigid-end offsets are specified at the end of the frame members to account for the actual size of the members at the joints. The panel zones of the beam-column connections are assumed to be stiff and strong enough to avoid any panel shear deformation and yielding under strong earthquakes. This assumption represents the most critical condition as all the hysteretic energy must be dissipated only through plastic hinging in the beams and the columns. The columns are fixed at the slab levels, except the gravity column that is assumed pinned at the base and at each level. P-Δ effects are accounted for in the analyses, including P-Δ forces generated in the interior frames. Plot of the geometry and with the element numbering, location of plastic hinges and beam properties used is shown in Figure 9.8.

Concrete beam-column elements as defined in Carr [2007] have been used in the model. The yield interaction surface has been defined for each member accordingly to the section
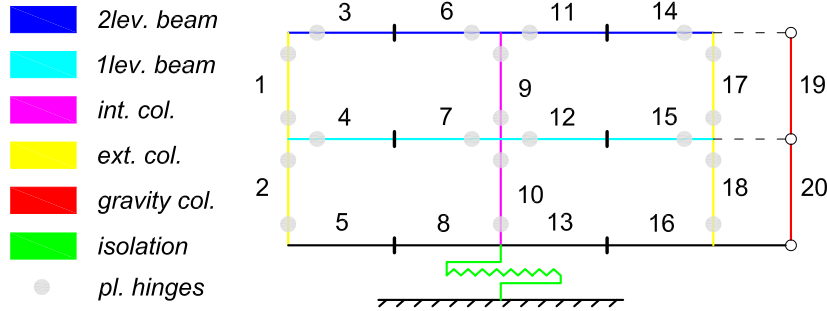
Figure 9.8. Frame example finite element model: element numbering, beam classes and plastic hinge locations are reported

analyses performed in Section 9.2.2 to determine the plastic hinge properties. Its nonlinear properties have been modeled using a Takeda (Carr [2007]) hysteresis. Isolation layer has been modeled considering a lateral spring characterized by the suitable force-displacement relation and representing the total isolation layer effect.

Rayleigh damping of $\xi = 1\%$ based on the first and third elastic modes of vibration of the structure is assigned.

Based on the assumption in Section 9.2.2, two cases have been considered. Even if the first case is supposed to investigate the elastically responding superstructure behavior and the second the inelastically responding one, same inelastic model has been used in the two of them. The only differences in the two models of the two cases regards the total weight and the isolation properties and are reported below.

- case #1.
  In the first case, when three resisting frames are considered, the weight acting on the frame is one third of the total weight $W_f = 0.33\,W_T$ and the one acting on the gravitational column is zero $W_{gc} = 0$, for a total weight in the superstructure $W_{ss} = 0.33\,W_T$. Assuming that the base shear acting on the single frame is one third of the total shear and being the total number of isolators from the design $n_{is} = 3$, the isolation system modeled in the analyses consists only of one isolator $n_{is-frame} = 1$.

- case #2.
  In the second case only two resisting frames are considered. Hence the weight acting on the frame is one third of the total weight $W_f = 0.33\,W_T$ and one sixth on the gravitational column $W_{gc} = 0.167\,W_T$, for a total weight in the superstructure $W_{ss} = 0.50\,W_T$. Assuming that the base shear acting on the frame is one half of the total shear and being the total number of isolators from the design $n_{is} = 3$, the isolation system modeled in the analyses considers the effects of $n_{is-frame} = 1.5$ isolators.

9.4.2   Isolation System Modeling

The responses of the two superstructure cases have been compared considering three different isolation systems corresponding to the actual LRB system described in Section 4.2, and the two innovative superelastic configurations described in Section 7.2.2 and Section 7.2.3, moreover an equivalent linear system secant to the design level has been considered.   Hence the isolation system described in Figure 9.8 has been modeling considering the following force-displacement relations.

- Elasto-plastic model (Figure 9.9). The elastoplastic model is representative of the real lead rubber bearing device defined in Section 4.2 and the parameters we use are those reported in Table 9.2.
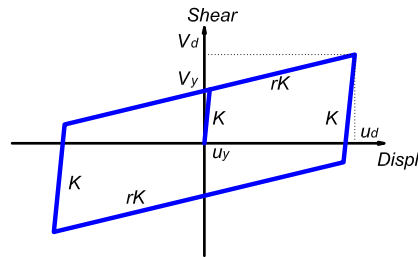
Figure 9.9. Base shear horizontal displacement relation for lead rubber bearing isolation device

Table 9.2. Hysteretic properties of *EP* system

LRB 500 (EP system)		
Elastoplastic model		
yielding shear	V_{ep}	147 kN
initial stiffness	k_{ep}	8.4 kN/mm
second stiffness	rk_{ep}	0.8 kN/mm

- Flag-shaped model SL (Figure 9.10). The flag-shaped model reproduces the shear-horizontal displacement relation of the pure superelastic device (SL) device defined in Section 7.2.2. The used parameters are summarized in Table 9.3.

- Flag-shaped model FR (Figure 9.11). The flag-shaped model reproduces the shear-horizontal displacement relation of the superelastic device and frictional flat slider (FR) defined in Section 7.2.3. The numerical model was obtained using two spring in parallel, one reproducing the superelastic device (*SE*) and the other the friction bearing device (*BF*). The used parameters are summarized in Table 9.4.
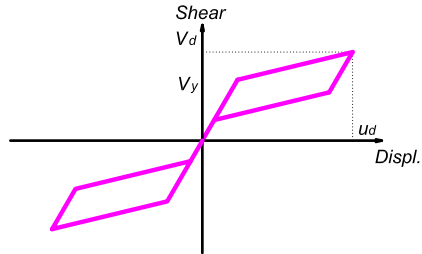
Figure 9.10. Base shear horizontal displacement relation for superelastic no friction isolation device

Table 9.3. Hysteretic properties of *SL* system

Superelastic no friction (SL System)		
Flag-shaped model		
yielding shear	V_{sl}	195 kN
initial stiffness	k_{sl}	3.68 kN/mm
second stiffness	rk_{sl}	0.26 kN/mm
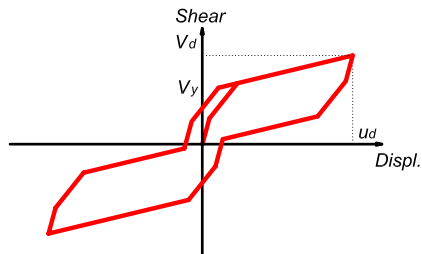
Figure 9.11. Base shear horizontal displacement relation for superelastic with friction isolation device

- Linear elastic model (Figure 9.12). Considering the design displacement u_d and the design shear V_d, which are the same for the previous models, we carry out the analysis of the equivalent linear system, considering a secant stiffness to the design point which is common to the previous modes. The used parameters are summarized in Table 9.5.

The proposed model parameters are relative to the case $n_{is-frame} = 1$. Therefore they have to be multiplied for the correct $n_{is-frame}$ value in the analyses.

For the sake of comparison the fixed base frame response has been computed as well, both in case #1 and in case #2.

Table 9.4. Hysteretic properties of *FR* system

Superelastic with friction (FR System)		
Flag-shaped model - restrainer		
yielding shear	V_{se}	136 kN
initial stiffness	k_{se}	2.57 kN/mm
second stiffness	rk_{se}	0.18 kN/mm
Elastoplastic model - friction		
yielding shear	V_{bf}	59 kN
initial stiffness	k_{bf}	11.7 kN/mm
second stiffness	rk_{bf}	0.0 kN/mm
Total system		
yielding shear	V_{fr}	195 kN
initial total stiffness	k_{fr}	14.27 kN/mm

Figure 9.12. Base shear horizontal displacement relation for equivalent linear elastic with secant stiffness isolation device

9.4.3   Response Parameters

The responses of the isolation devices and of the superstructure have been checked and compared. The design conditions are identified by the ground motion set records considered in the investigation.

Concerning the isolation device response to the design conditions, the maximum displacement and shear force demand have been considered the most significative parameters. They have been already analyzed in previous work on single degree of freedom system response.

Moreover, to check the superstructural response we consider:

- storey level shear demand: this is a parameter significative to evaluate the acting forces in the superstructure induced by the earthquake and their distribution in the superstructure;

Table 9.5. hysteretic properties of *LE* system.

Linear Elastic to design point (LE System)		
Linear model		
stiffness	k_{le}	1.62 kN/mm

- storey level drift demand: this is a parameter important to quantify the relative displacement of each slab with respect the one on the top and on the bottom and therefore to quantify the rotation of the columns and of the beams; it represents a direct measurement of the structural damage in the structure;

- floor acceleration: estimation of floor acceleration is useful to evaluate the nonstructural component damage in the superstructure; different base isolation technologies are supposed to affect this parameter significantly;

- ductility demand in the plastic hinge locations: the maximum ductility in curvature in all the inelastic members has been evaluated to compute both the plastic work done and the damage in the members;

- energy balance: the input energy has been compared with the strain energy dissipated in the isolation system and with the energy dissipated in the plastic hinge zones.

The previous framework is supposed to provide a suitable data set to compare the isolation system effectiveness in reaching the structural goals in a rigid MDOF superstructure design.

9.5 ANALYSIS GROUND MOTIONS

The design earthquake is represented in terms of elastic spectra. Design conditions are given by EC8 spectra for $PGA = 0.35$g type 1 soil type GTC design spectra (CEN [2004]). The seismic design level has been represented then considering a set of compatible ground motions.

In this section the used earthquake records are recalled, being the ground motion set the same already used for the investigation in Chapter 7 and described in Section 7.4.

Suites of earthquake ground motions from the *SAC* database (see SAC [1997]) have been considered for the isolation bearing system response comparison evaluation, as reported in Section 7.4.1. All the ground motions are natural records.

In particular, two sets of records have been used in this work:

- earthquake natural ground motions with 10% probability of exceedence in 50 years for the area of Los Angeles: 20 records, whose properties are reported in Table 7.5;

- impulsive near-field earthquake ground motions: 12 records, whose properties are reported in Table 7.6.

Hence in total, 32 earthquake ground motions have considered for the analysis. A large number of records has been chosen to take into account as much as possible the variability of the seismic input.

The records are from seismic events characterized by different seismological sources and recording conditions. Thus a scaling procedure is needed to permit the result comparison at the design level and the process has been described in Section 7.4.2. The EC8 spectra for $PGA = 0.35g$ type 1 soil type GTC design spectra (CEN [2004]) has been used as a target for the scaling.
The resulting scaled ground motion properties are reported in Section 7.4.3. In particular, the scaling factors are reported in Table 7.5 and Table 7.6, while the final scaled ground motion displacement and acceleration spectra are shown in Figure 7.11, compared with EC8 design spectra.

9.6   ELASTICALLY RESPONDING SUPERSTRUCTURE RESULTS

In this section the main results for the case #1 are reported. This is the case in which the resisting system of the superstructure is composed by three frames. In the member design, capacity design through suitable overstrength factor was applied, hence no inelastic demand is supposed to be developed.
Section 9.6.1 reports the main results regarding the isolation system response. Section 9.6.2 summarizes the main results of the isolated superstructure demand due to the earthquake action.

9.6.1   Isolation System Response

For each ground motion record the maximum displacement demand and the maximum shear force in the isolation layer were recorded for each one of the isolation system configurations described in Section 9.4.2.
Displacement envelopes are reported in Figure 9.13 and force envelopes in Figure 9.14.
The mean value and the standard deviation for the EP, FR, and SL systems are then plotted in terms of displacement in Figure 9.15a and in terms of shear in Figure 9.15b. The same plot reports also the absolute mean value on the top of the mean bars and the coefficient of variation, which is the ratio of the standard deviation over the mean, at the top of the standard deviation bars.

According to the rigid superstructure approach, the isolation system was design to reach a displacement of $\Delta_d = 160\text{mm}$ considering a dissipation capability function of the elastoplastic hysteresis. The mean demand in the EP, FR and SL systems shown in Figure 9.15a and normalized with respect to the design displacement are reported in Table 9.6. It can be seen that the design condition based on the theoretical dissipation capability of
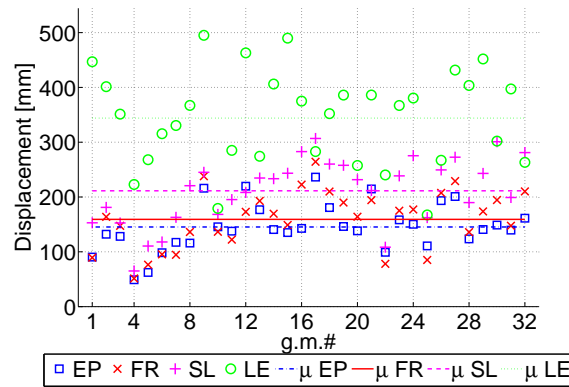
Figure 9.13. Displacement demand envelopes and mean values in the isolation system (absolute values of the four isolator hysteresis)
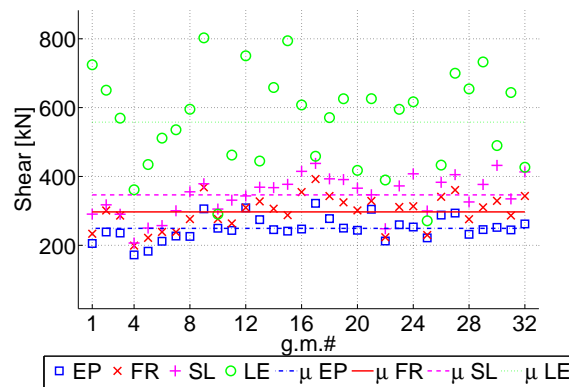
Figure 9.14. Shear demand envelopes and mean values in the isolation system (absolute values of the four isolator hysteresis)

Table 9.6. Mean displacement envelope over design displacement ratio

Displacement Demand over Design Displacement			
design	EP system	FR system	SL system
100%	90.6%	99.3%	131.8%

(a) displacement demand   (b) shear force demand
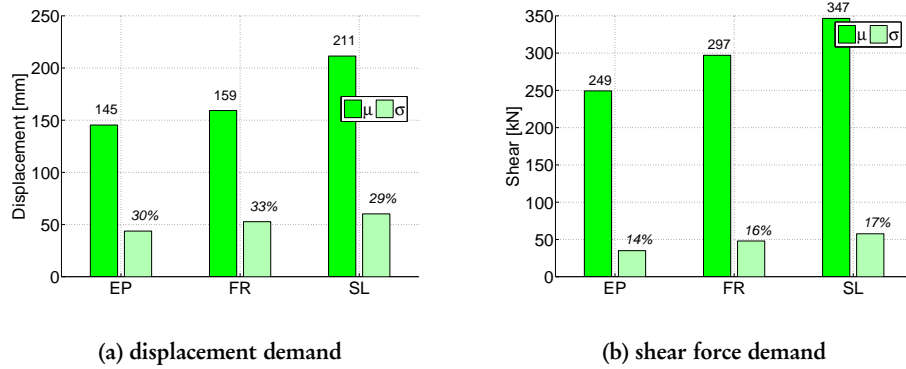
Figure 9.15. Isolation system displacement and shear demand envelope mean and standard deviation. The absolute values and the coefficients of variation are also reported respectively for the mean and the standard deviation bars

Table 9.7. Mean shear coefficient envelope over design displacement ratio

Shear Demand over Design Shear			
design	EP system	FR system	SL system
100%	95.0%	111.4%	129.0%

the LRB system is satisfied in EP and FR system response, while it is slightly exceeded in SL system. The coefficient of variation of the displacement demand over all the ground motion set is about the 30% in all the isolation systems as resulting from data of Figure 9.15a: hence the coefficient of variation is just slightly affected by the different hysteresis in the isolators.

Regarding the shear force demand, the design shear was the 17% of the structural weight which in this case is $W_{ss} = 0.33 W_T = 1533$kN leading to a design base shear in the isolation system of 261kN. The comparison between the design shear force and the mean envelope in the isolation system is reported in Table 9.7, from which results that the EP system shear coefficient is $16.2\% W_{ss}$ and that the FR and SL systems exceed the maximum design shear demanding respectively a mean shear force envelope equal to respectively the $19.4\% W_{ss}$ and $22.6\% W_{ss}$. The coefficient of variation of the shear force demand over all the ground motion set is about the 15% in all the isolation systems.

The comparison between the displacement and the shear force demand in the nonlinear force-displacement relation with respect to the linear elastic system to the design displacement is a direct measure of the hysteretic reduction factor η, which for the most

Table 9.8. Effectiveness of the isolation equivalent viscous damping in reducing the maximum displacement and force demand

Mean Reduction Factor from T.H.A.s			
Displacement			
LE system	*EP system*	*FR system*	*SL system*
100%	42%	46%	61%
Shear Force			
LE system	*EP system*	*FR system*	*SL system*
100%	45%	53%	62%

dissipating hysteresis, the EP one, resulted to be $\eta = 0.55$. Table 9.8 reports the different mean reduction factors for displacement and shear force. Again, generally the same coefficient computed for the EP system resulted to be applicable even for the FR systems. Slightly larger demand is confirmed to occur in SL system.

9.6.2 Superstructure Response

To evaluate the mean response of the superstructure being isolated considering different isolation systems, mean values over all the ground motion set of the main parameters are reported in Figure 9.16. The first check concerns the damage in the superstructure and it results that no plastic hinges have been developed in any inelastic location of the model, hence the design results to be performed properly.

The absence of superstructural damage is reported also in the energy balance shown in Figure 9.16d. This is a plot in which the input energy, which is the work done by the ground motion on the system, is compared with the energy dissipated through the work in the isolators and with the work done in the plastic hinges. Since in this case no energy dissipation occurs in the plastic hinges, no damage occurs in the structure.

Figure 9.16a reports the mean and the standard deviation of the interstorey drift. It is remarkable that the same superstructure modeled considering a fixed based would experience a mean interstorey drift of 1.2% at the first level and of 1% at the second level. Floor shear mean envelopes are reported in Figure 9.16b for the two levels. Normalized with respect to the superstructure weight the values correspond to percentages between $17 - 22\% W_{ss}$ in the first level and $13 - 16\% W_{ss}$ in the second level. In the fixed base case the mean values would be $659 \text{kN} = 43\% W_{ss}$ and $447 \text{kN} = 29\% W_{ss}$.

Acceleration mean envelopes are reported in Figure 9.16d, considering the three rigid slab acceleration have been considered. The comparison can be completed with the fixed base mean acceleration envelopes which is equal to 0.46g at the ground level, which is also the mean peak ground acceleration value, and it is amplified to 0.60g and 0.70g respectively

(a) interstorey drift demand

(b) floor level shear force demand

(c) floor acceleration demand

(d) energy balance
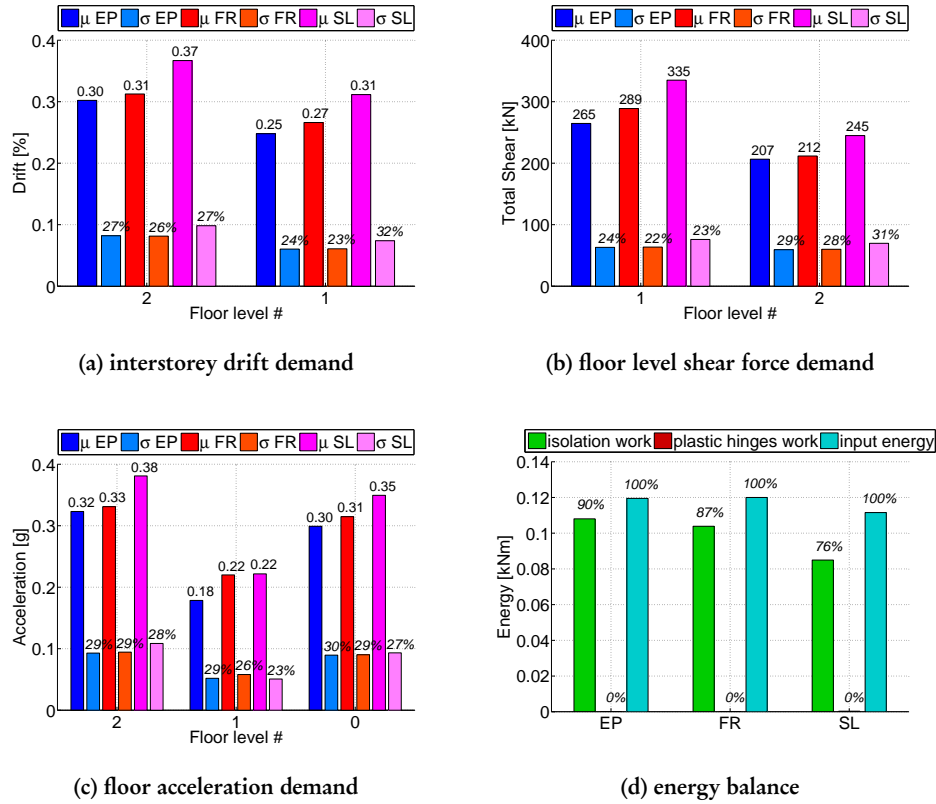
Figure 9.16. Superstructure response parameters.
In 9.16a, 9.16b, and 9.16c the mean values and the coefficient of variations are reported respectively on the μ and on the σ bars; in 9.16d each column percentage is normalized w/r the input energy

at the second level slab and at the roof level.

9.7 INELASTICALLY RESPONDING SUPERSTRUCTURE RESULTS

In this section the results for the case #2 are reported. This is the case in which the resisting system of the superstructure is composed by only two frames and it has been under-designed with respect to the capacity design principles on purpose to investigate the effects of different isolation system on the superstructure damage.

Section 9.7.1 reports the main results regarding the isolation system response. Section 9.7.2 summarizes the main results of the isolated superstructure demand due to the earthquake.

9.7.1 Isolation System Response

For each ground motion record the maximum displacement demand and the maximum shear force in the isolation layer were recorded for each one of the isolation system configurations described in Section 9.4.2.

Displacement envelopes are reported in Figure 9.17 and force envelopes in Figure 9.18.

The mean value and the standard deviation for the EP, FR, and SL systems are then
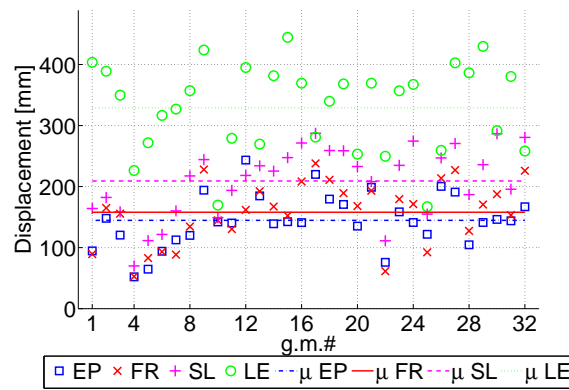
Figure 9.17. Displacement demand envelopes and mean values in the isolation system (absolute values of the four isolator hysteresis)
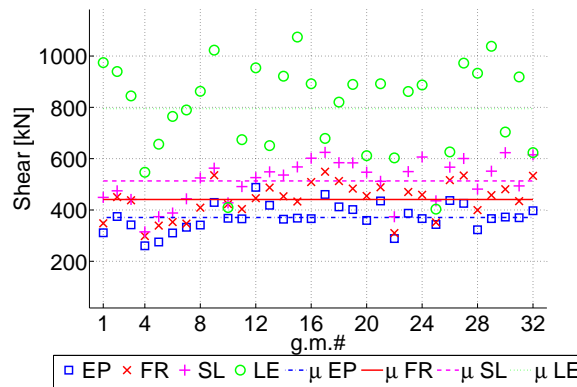
Figure 9.18. Shear demand envelopes and mean values in the isolation system (absolute values of the four isolator hysteresis)

reported in terms of displacement in Figure 9.19a and in terms of shear in Figure 9.19b.

The same plot reports also the absolute mean value on the top of the mean bars and the coefficient of variation, which is the ratio of the standard deviation over the mean, at the top of the standard deviation bars.

(a) displacement demand   (b) shear force demand
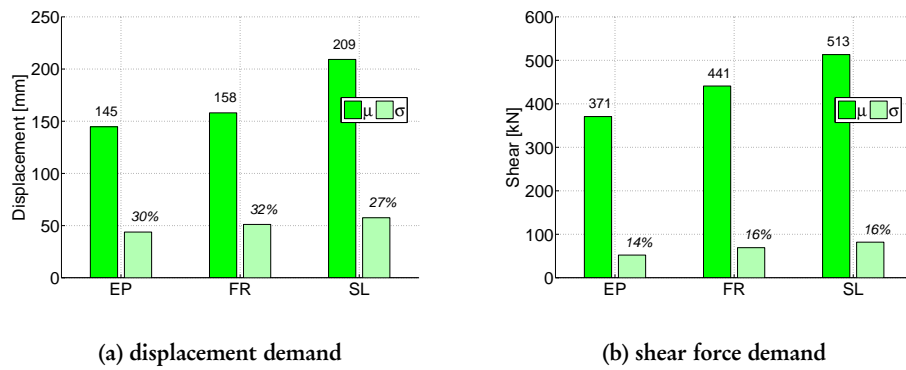
Figure 9.19. Isolation system displacement and shear demand envelope mean and standard deviation. The absolute values and the coefficients of variation are also reported respectively for the mean and the standard deviation bars.

Table 9.9. Mean displacement envelope over design displacement ratio

Displacement Demand over Design Displacement			
design	EP system	FR system	SL system
100%	90.6%	99.4%	130.6%

Table 9.10. Mean shear coefficient envelope over design displacement ratio

Shear Demand over Design Shear			
design	EP system	FR system	SL system
100%	94.6%	112.5%	130.8%

The isolation system was design to reach a displacement of $\Delta_d = 160$mm considering a dissipation capability function of the elastoplastic hysteresis. The mean demand in the EP, FR and SL systems shown in Figure 9.19a and normalized with respect to the design displacement are reported in Table 9.9. It can be seen that the design condition based on the theoretical dissipation capability of the LRB system is satisfied in EP and FR system

response, while it is slightly exceeded in SL system response. The coefficient of variation of the displacement demand over all the ground motion set is about the 30% in all the isolation systems as resulting from data of Figure 9.19a. Again the coefficient of variation is just slightly affected by the different hysteresis in the isolators.

Regarding the shear force demand, the design shear was the 17% of the structural weight which in this case is $W_{ss} = 0.50 W_T = 2300\text{kN}$ leading to a design base shear in the isolation system of 392kN. The comparison between the design shear force and the mean envelope in the isolation system is reported in Table 9.10, from which results that the EP system shear coefficient is 16.1%W_{ss} and the FR and SL systems exceed the maximum design shear demanding respectively a mean shear force envelope equal to respectively the 19.1%W_{ss} and 22.3%W_{ss}. The coefficient of variation of the shear force demand over all the ground motion set is about the 15% in all the isolation systems.

Table 9.11. **Effectiveness of the isolation equivalent viscous damping in reducing the maximum displacement and force demand**

Mean Reduction Factor from T.H.A.s			
Displacement			
LE system	EP system	FR system	SL system
100%	44%	48%	63%
Shear Force			
LE system	EP system	FR system	SL system
100%	46%	55%	64%

The direct hysteretic reduction factor computation is reported in Table 9.11, which reports the different mean reduction factors for displacement and shear force. Again, generally the same coefficient computed for the EP system $\eta = 0.55$ resulted to be applicable even for the FR systems. Slightly larger demand is confirmed to occur in SL system.

9.7.2   Superstructure Response

To evaluate the mean response of the superstructure being isolated considering different isolation systems, the mean value over all the ground motion set of main parameters are reported in Figure 9.20. Accordingly to the previous assumptions, in this case the superstructure experiences the development of some plastic hinges. Properties of plastic hinge zones in term of position of occurrence and mean curvature ductility demand have been investigated as well.

The presence of superstructural damage is reported this time also in the energy balance shown in Figure 9.20d. In this case some energy dissipation resulted to occur in the plastic

(a) interstorey drift demand

(b) floor level shear force demand

(c) floor acceleration demand

(d) energy balance
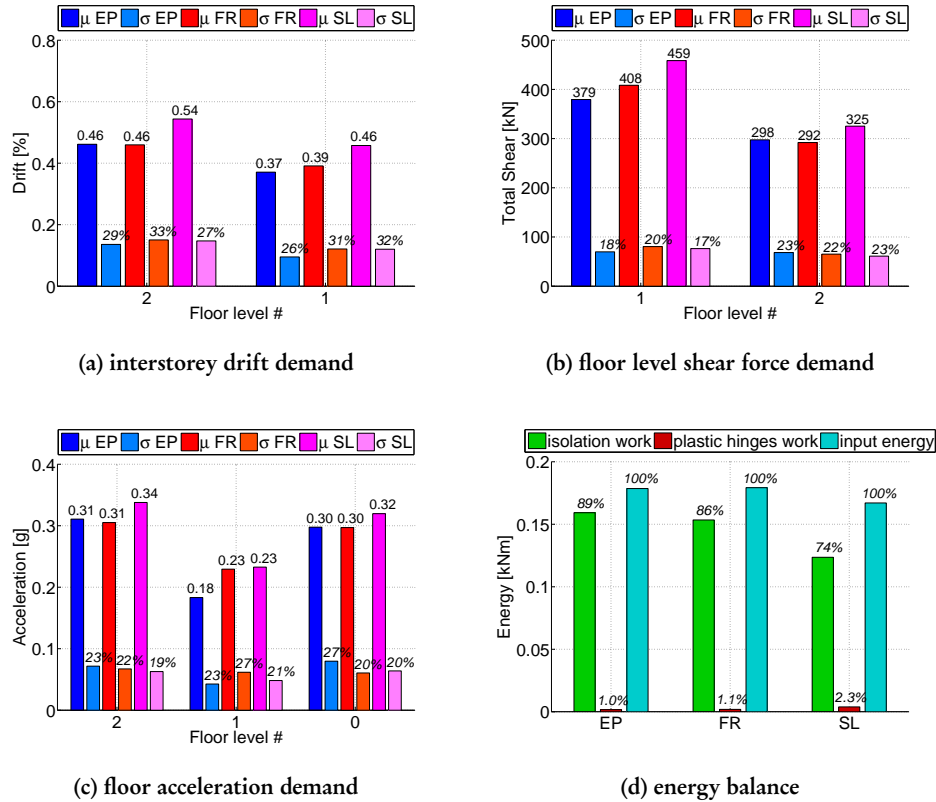
Figure 9.20. Superstructure response parameters.
In 9.20a, 9.20b, and 9.20c the mean values and the coefficient of variations are reported respectively on the μ and on the σ bars; in 9.20d each column percentage is normalized w/r the input energy

hinges. Anyway, the percentage is still very small with respect to the input energy and also with respect to the strain work done by the isolation systems. Moreover, it is possible to identify that a structure isolated using SL system dissipate more energy through plastic hinges, hence in this structure results to be more damaged.

Figure 9.20a reports the mean and the standard deviation of the interstorey drift. Again this is an important parameter to identify damage and the plot shows that in this case values are significantly higher than values recorded in the previous case and shown in Figure 9.16a. The same superstructure modeled considering a fixed based in this case would experience a mean interstorey drift of 1.63% at the first level and of 1.42% at the second level.

Floor shear mean envelopes are reported in Figure 9.20b for the two levels. The values

correspond to percentages in the range $16-20\% W_{ss}$ in the first level and $13-14\% W_{ss}$ in the second level, hence even if only slightly, they are smaller than in the previous case whose results are reported in Figure 9.16b. In the fixed base case the mean values would be $725\text{kN} = 31\% W_{ss}$ and $505\text{kN} = 22\% W_{ss}$.

Acceleration mean envelopes are reported in Figure 9.20d, where the three rigid slab acceleration have been considered. The comparison can be completed with the fixed base mean acceleration envelopes which is equal to 0.46g at the ground level (the mean peak ground acceleration value) and it is amplified to 0.49g and 0.53g respectively at the second level slab and at the roof level.

Therefore, regarding the comparison of the superstructural data of the damaged structure with respect to the previous case in which the superstructure is undamaged, the drift is significantly increased but the shear force and the floor acceleration are reduced, due to the damaging itself and the softening of the frame members.
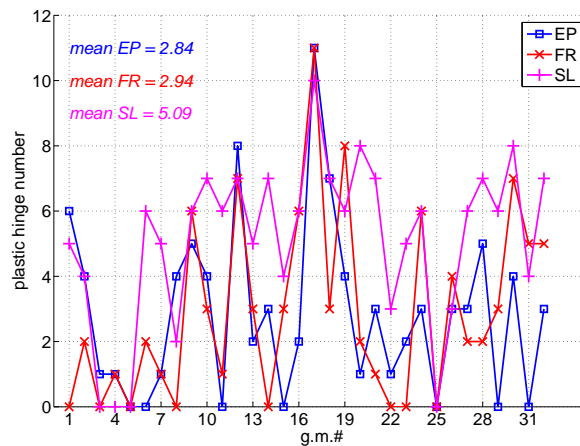
Figure 9.21. Plastic hinge occurrence in all ground motions for different isolation systems

Concerning the plastic hinge occurrence and mean curvature ductility demand, Figure 9.21 reports for each ground motion the total number of plastic hinges occurring for the three isolation system models. It turns out that the mean value of SL system is higher than the ones of EP and FR systems which are very close each other. This also matches with data in Figure 9.20d according to which the SL system is characterized by the highest damage in the superstructure.

Figure 9.22 reports then the number of plastic hinge occurrences in each frame location in all the ground motion records. For each location then the mean curvature ductility is reported in Figure 9.23. The three isolation system results together with the fixed base case, which of course is more severe, are reported too. Comparing the superstructure hinge response in the isolation configurations it turns out that the mean curvature ductility
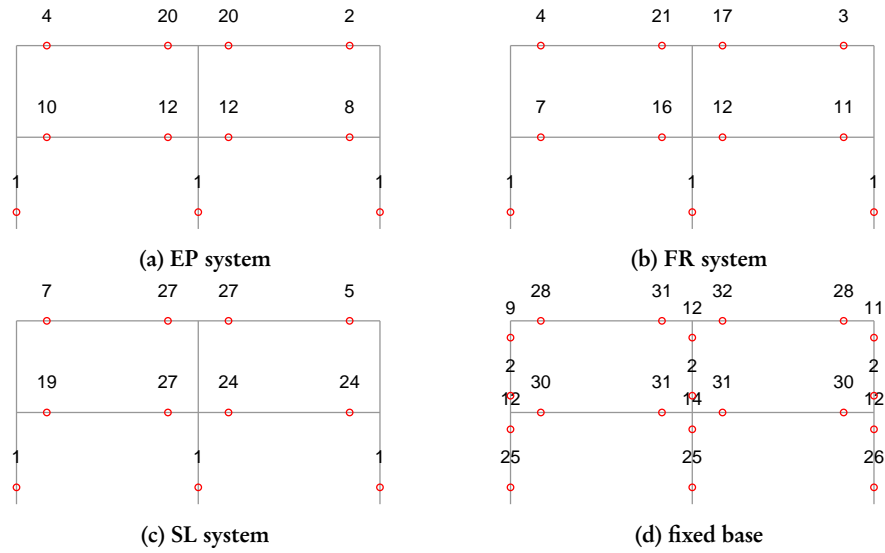
Figure 9.22. Superstructure plastic hinge occurrences
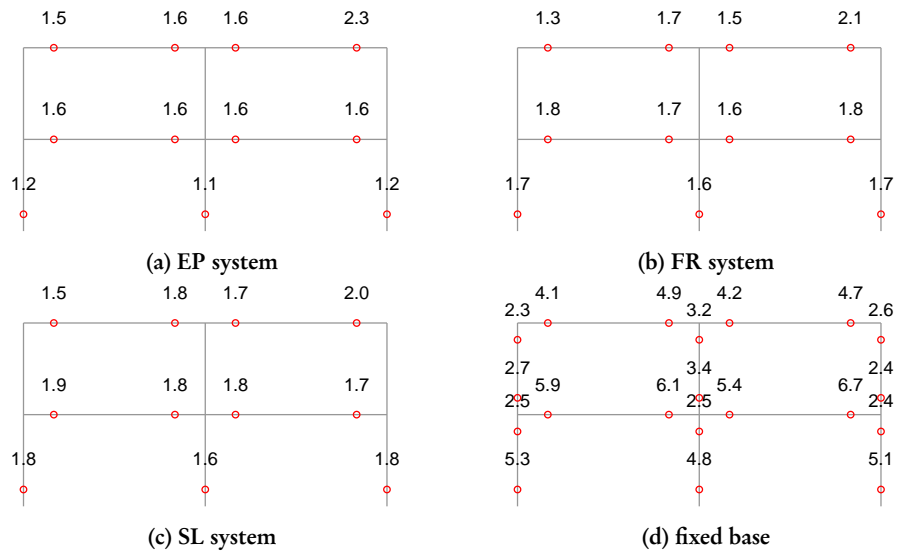
Figure 9.23. Superstructure plastic hinge mean curvature ductility demand

is about the same and generally quite small, not exceeding the value 2. Nevertheless the higher dissipation in the SL system is due to an higher number of inelastic demand occurrences in this configuration members.

9.8   CONCLUSIONS

The seismic response of a two-storey isolated concrete frame structure has been checked by considering different isolation technologies. The objective of the investigation is to evaluate and compare the effectiveness of the different isolation configurations in reaching the structural goals. In particular the design accomplished with an actual lead rubber bearing (EP system) has been compared with the response of the superstructure isolated with two equivalent innovative superelastic devices (FR system and SL system). Two cases have been considered, one in which the superstructure has been designed to elastically respond and another in which it was supposed to experience some damage to investigate also the effects of damaging.

Concerning the isolation system response, it results that the maximum displacement and shear force recorded in the isolation layer are very close between the three considered systems, regardless the fact that the theoretical hysteretic damping is supposed to be significantly different. The design parameters computed considering the largest dissipation capability, which is the one provided by EP system corresponding to LRB, are generally met even considering the flag-shaped FR system. The SL system demand is more severe but differences are very much smaller than what we would expect based on a equivalent hysteretic damping approach. Moreover, differences in response considering the damage in the superstructure or not are negligible, being the isolation layer response the same in the two investigated cases.

Looking at the superstructure response, the EP system and FR system responses are very close in all the cases. The isolation turns out to be very effective in terms of reduction of interstorey drift, floor shear and floor acceleration, both when the superstructure is damaged and when it responds elastically. On the other side, the SL isolation technology turned out to be more demanding in terms of the same quantities.

Given the previous results, the main conclusion is that based on the performed analysis the actual LRB system and the innovative flag-shaped with friction FR system are almost the same in terms of device and superstructure response. The main parameter envelopes, which are the values we accounted the most because they are at the base of the design procedure, are almost the same both at the isolation and superstructure level.
Slightly more demanding resulted the innovative flag-shaped without friction, the SL system. Nevertheless its response from time history analyses is more close to the LRB one than to the one which we would predict according to an equivalent hysteretic damping approach.

10. Evaluation of Superelastic Seismic Isolation Device Response for Flexible Buildings

10.1 INTRODUCTION

The effectiveness of superelastic isolation device as presented in Chapter 6 is investigated in the present chapter considering the response of a base-isolated structure. The term superelastic (*SE*) isolation refers to a bearing characterized by a nonlinear shear force-horizontal displacement relation which can be described by a *flag-shaped* hysteresis. This hysteresis has been demonstrated to be provided by a lateral restrainer system composed by *shape memory alloy* manufactured devices. An actual force-displacement relation computed from a real superelastic device design is considered. Its model has been investigated and experimentally validated. The response of a structural system isolated using innovative bearings is compared with respect to the same structure isolated using traditional isolation devices. In this context the traditional isolation bearing is a lead rubber bearing (*LRB*) and the superelastic device has been designed to be equivalent to the existing LRB.

Previous investigations on single degree of freedom systems reported in Chapter 7 have demonstrated that the response of superelastic isolation devices is very attractive for its effectiveness in modifying the structural behavior and avoiding the residual displacements after the seismic event. The response investigation on a base isolated stiff structure isolated using actual and innovative devices has been also performed in Chapter 9. The main conclusion was that the stiff superstructure affects with a relatively small influence the isolation device response, which is very close to the SDOF one. Concerning the superstructure response, its flexibility contribution was small in the total system displacement context. Similar responses in terms of interstorey drift, floor shear and floor accelerations has been recorded considering actual and innovative isolation devices.

In the present chapter, a six storey frame structure is considered. The aim is to focus on the effects of the different isolation technologies on the flexible superstructure response, which has been taken into account considering its real flexibility, strength, and mass distribution.

Two cases are considered, one in which the superstructure is designed to respond mainly elastically, and a second one in which the design is performed accepting some damage in the frame. This is to compare the differences in the response induced by the different

isolation systems both when the system has been designed properly, assuring no damage in the isolated part of the structure, and when the elastic strength of the superstructure members is exceeded.

The investigation consists of a series of time history analyses. Direct computation of the response in time of the system subjected to a suitable ground motion set and evaluation of design parameters both at the isolation system level and at the superstructure is considered the best way to evaluate the response of the innovative system with respect to the traditional one.

In Section 10.2 the building properties, some basis on the actual isolation system design procedure, and some modeling issues are summarized. Section 10.3 presents the technical configurations and principles of the innovative isolation devices. Section 10.4 recalls the ground motion set which has been used in the analysis procedure. Section 10.5 and Section 10.6 present the main finding of the investigation and in Section 10.7 the conclusions are reported.

10.2   DESCRIPTION OF BUILDING STRUCTURE AND DESIGN OF THE ISOLATION SYSTEM

In the present study, the seismic response for a base-isolated *flexible* building is considered. This is the case of a structure whose fundamental isolated period is less than 3 times longer than the fundamental period considering the fixed-base, according to the definition given in Priestley *et al.* [2007].

In this investigation it is assumed that the isolation technique is a retrofitting strategy for a given building. Therefore a structure already proposed in previous works is considered, being its material and geometrical characteristics described in Section 10.2.1. Its nonlinear static and main dynamic properties are then reported in Section 10.2.2 and in Section 10.2.3. A suitable isolation system configuration using LRB system has been proposed to meet the design goals and the design is presented in Section 10.2.4.

As a design target, an interstorey drift limitation has been considered. Nevertheless, two conditions have been investigated, referring to the expected superstructure damage:

- case #1: *elastically responding superstructure.*
  In this case the isolation system has been designed to limit as much as possible the inelastic response of the superstructure. In particular, plastic hinges occurrences are supposed to be very rare and they ductility demand low.

- case #2: *inelastically responding superstructure.*
  In this case the isolation system has been designed accounting for a relevant displacement and dissipation capability in the superstructure, hence extensive development of plastic hinges is expected.

10.2.1 Superstructure Properties

The considered building is a six storey structure originally studied in Tsai and Popov [1994] and then modified in Hall [1994]. Further investigations on the same structure have been presented in Filiatrault *et al.* [2001] and Wanitkorkul and Filiatrault [2008]. The building is rectangular in plan braced in the North-South direction by *two* exterior moment-resisting frames. The original design complies with the *1994 UBC* code requirements (ICBO [1994]) for a building located in Zone 4 on soil type *S2*. In its original configuration, each lateral resisting frame is characterized by a total weight for the seismic load condition of $W_{0,tot} \simeq 14500\text{kN}$. In this work, two conditions have been considered, changing the total seismic weight. In the first one, corresponding to *case #1*, the total considered weight in one half of the original structure weight, plus one half of the additional weight of the first rigid floor $W_{fr} = 2500\text{kN}$:

$$W_{1,tot} = 0.5 \left(W_{0,tot} + W_{fr} \right) \tag{10.1}$$

while in the second one, corresponding to *case #2*, the original total weight has been considered plus the additional weight of the first rigid floor:

$$W_{2,tot} = 1.0 \left(W_{0,tot} + W_{fr} \right) \tag{10.2}$$

(a)   Geometry and Member Schedule

In the present investigation only one frame of the building is modeled, as the structure is assumed symmetrical. The superstructure geometry with the main dimensions and the member assignment is shown in Figure 10.1. The steel grade is *A*36 characterized by nominal yielding stress of $f_y = 290\text{MPa}$ for all the members. The bilinear moment-curvature relationship adopted for all beam and column members is shown in Figure 10.2, based on the *AISC* design provisions for ductile steel moment resisting frames (AISC [1997]). The ultimate moment M_u is taken as the 20% higher than the yielding moment M_p and the bilinear factor is equal to $r = 0.02$. Summary of the main member properties is reported in Table 10.1, in which the yielding moment, the ultimate moment, the initial rotational stiffness, the yielding curvature, the ultimate curvature, and the plastic hinge length are reported for all the sections at zero axial load condition. The axial load-bending moment interaction is considered through a simplified diagram symmetrical in the two directions of bending. This can be defined using just 4 points and its shape is shown in Figure 10.3. Table 10.2 reports then the corresponding values in the interaction diagram for all the column sections.

(b)   Finite Element Analysis Model

All the design and the dynamic analyses are performed using the nonlinear dynamic analysis computer program *Ruaumoko* (Carr [2007]). The model includes the frame
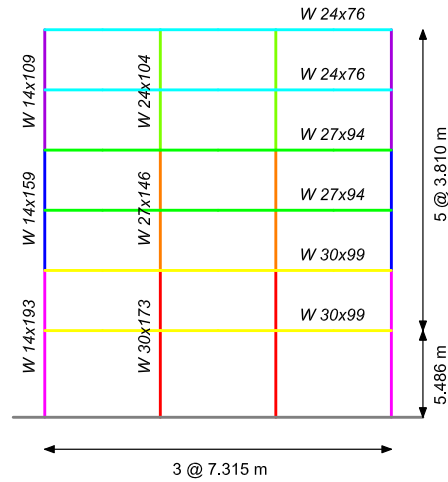
Figure 10.1. Superstructure geometrical properties: main dimensions and steel member assignments
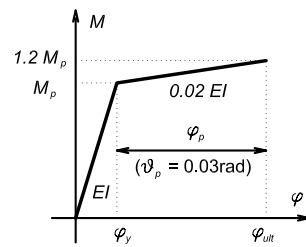
Figure 10.2. Bilinear moment-curvature model
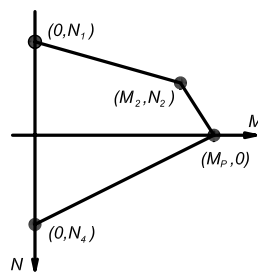
Figure 10.3. Axial force-bending moment interaction diagram model

together with one gravity column that represents all interior columns. The total gravity loads acting on the interior columns are applied to the gravity column in the model and both the gravity column and the exterior frame are constrained to experience the same lateral deformation at each floor.

Table 10.1. Superstructure member bending properties

Profile	M_p [kNmm]	M_{ult} [kNmm]	EI [kNmm^2]	φ_y [1/mm]	φ_{ult} [1/mm]	L_p [mm]
W14x109	$9.12 \cdot 10^5$	$1.09 \cdot 10^6$	$1.03 \cdot 10^{+11}$	$8.84 \cdot 10^{-6}$	$9.72 \cdot 10^{-5}$	328
W24x104	$1.37 \cdot 10^6$	$1.65 \cdot 10^6$	$2.58 \cdot 10^{11}$	$5.32 \cdot 10^{-6}$	$5.85 \cdot 10^{-5}$	550
W14x159	$1.36 \cdot 10^6$	$1.64 \cdot 10^6$	$1.58 \cdot 10^{11}$	$8.62 \cdot 10^{-6}$	$9.48 \cdot 10^{-5}$	343
W27x146	$2.19 \cdot 10^6$	$2.63 \cdot 10^6$	$4.69 \cdot 10^{11}$	$4.68 \cdot 10^{-6}$	$5.14 \cdot 10^{-5}$	626
W14x193	$1.69 \cdot 10^6$	$2.02 \cdot 10^6$	$2.00 \cdot 10^{11}$	$8.44 \cdot 10^{-6}$	$9.29 \cdot 10^{-5}$	354
W30x173	$2.88 \cdot 10^6$	$3.45 \cdot 10^6$	$6.83 \cdot 10^{11}$	$4.21 \cdot 10^{-6}$	$4.63 \cdot 10^{-5}$	696
W24x76	$9.50 \cdot 10^5$	$1.14 \cdot 10^6$	$1.75 \cdot 10^{11}$	$5.43 \cdot 10^{-6}$	$5.98 \cdot 10^{-5}$	547
W27x94	$1.32 \cdot 10^6$	$1.59 \cdot 10^6$	$2.72 \cdot 10^{11}$	$4.85 \cdot 10^{-6}$	$5.34 \cdot 10^{-5}$	616
W30x99	$1.48 \cdot 10^6$	$1.78 \cdot 10^6$	$3.32 \cdot 10^{11}$	$4.46 \cdot 10^{-6}$	$4.91 \cdot 10^{-5}$	678

Table 10.2. Superstructure member interaction diagram properties

Profile	N_1 [kN]	N_2 [kN]	M_2 [kNm]	M_p [kNm]	N_4 [kN]
W14x109	-5987	-1198	821	912	5987
W24x104	-5725	-1145	1236	1373	5725
W14x159	-8737	-1605	1972	2191	8027
W27x146	-8027	-1605	1972	2191	8027
W14x193	-10627	-2125	1518	1687	10627
W30x173	-9505	-1901	2588	2875	9505

Only the bare steel frame is included in the analyses, hence the slab participation as a composite beam is not included. The inelastic response is concentrated in plastic hinges that could form at both ends of the frame members.

Rigid-end offsets are specified at the end of the frame members to account for the actual size of the members at the joints. The panel zones of the beam-column connections are assumed to be stiff and strong enough to avoid any panel shear deformation and yielding under strong earthquakes. This assumption represents the most critical condition for the inelastic curvature demand on the welded beam-to-column joints, as all the hysteretic energy must be dissipated only through plastic hinging in the beams and the columns. The columns are fixed at the slab level, except the gravity column that is assumed pinned at the base and at each level. P-Δ effects are accounted for in the analyses, including P-Δ forces generated in the interior frames. Figure 10.4 reports the node and element numbering of the structural finite element model.

(a) nodes   (b) elements
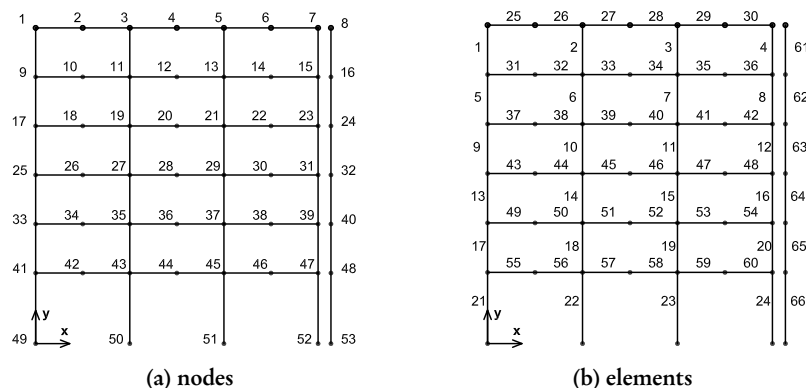
Figure 10.4. Structural model and numbering

10.2.2   Pushover Analysis

Pushover analyses have been performed to gain some insight on the behavior of the proposed structure when subjected to lateral loads. The failure mechanism and the ductility demand on the structural members are evaluated, as well as the ultimate base shear and the corresponding deformed shape.

In a pushover analysis, a lateral monotonic load is applied to a structure until the ultimate load is approached. This static analysis, much easier to perform than a dynamic analysis, allows the evaluation of the elastic and inelastic responses of the structure under lateral loads.

Adaptive pushover analyses have been performed considering the structural model defined in Section 10.2.1. Initial linear load distribution is used and it is applied in the positive direction of the x axis according to convention in Figure 10.4. Two structural models have been run, for the two different cases of gravitational loads $W_{1,tot}$ and $W_{2,tot}$. Results turned out to be the same for the two cases being the gravitational load influence negligible. For this reason only a capacity curve is reported in Figure 10.5 and it is relative to the case characterized by gravity load $W_{2,tot}$.

The first plastic hinging occur almost simultaneously in the beam and in the column. The first plastic hinge in a beam occurs at the first floor beam in the middle bay, as shown in Figure 10.6a, for a base shear of 2120kN (14.6% $W_{0,tot}$). The first plastic hinge in a column occurs at the base of an interior column of the ground floor, as shown in Figure 10.6b, for a base shear of 2180kN (15.1% $W_{0,tot}$). The first failure of a member occurs for a base shear of 3457kN (23.9% $W_{0,tot}$) in the same beam plastic hinge where the first yielding has been recorded. When this beam fails there are also several other members which have almost reached their curvature ductility capacity. These members are the other ends of all first floor beams and the base sections of the two interior columns.

The displaced shape and the interstorey drift at first yielding is reported in Figure 10.7.
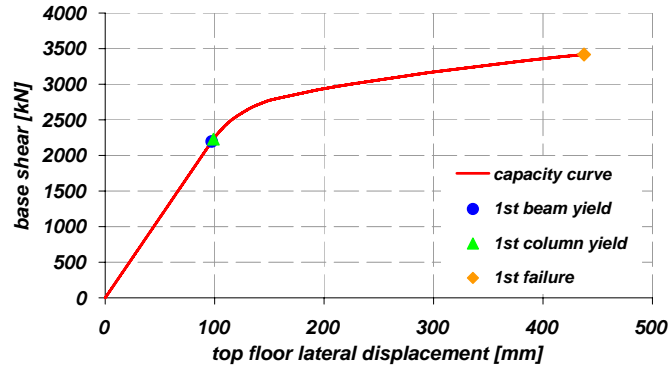
Figure 10.5. Capacity curve for the adaptive pushover analysis (gravity weight $W_{2,tot}$)

(a) yielding   (b) failure
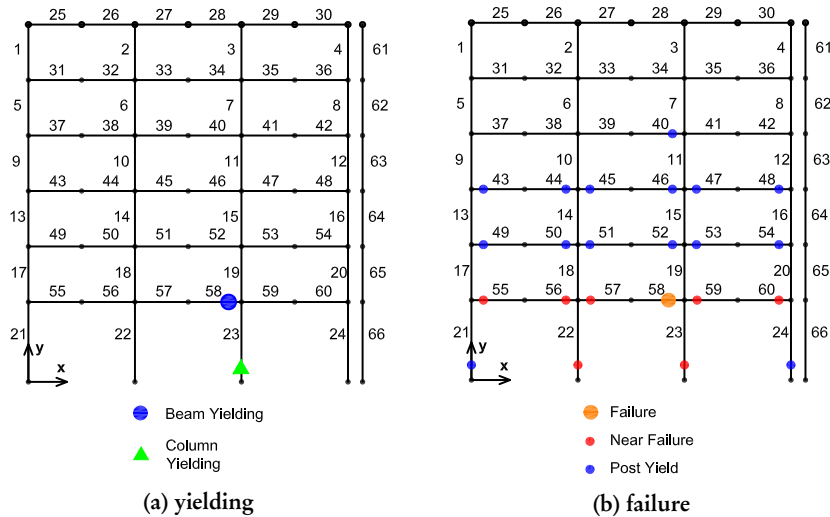
Figure 10.6. Pushover analysis: inelastic demand at yielding and failure conditions

The displaced shape is about linear at the lower floors and the maximum yielding drift is 0.45% at the first floor, which is also the one with the largest height. The displaced shape and the interstorey drift at first member failure is reported in Figure 10.8. The displaced shape follows the theoretical shape for frame buildings as reported in Priestley *et al.* [2007], and the maximum drift at failure is 3.36% again at the lowest floor.

As a general conclusion after the pushover analysis, despite the fact that the geometry and properties of the structure might suggest a soft story behavior at the ground floor, the results obtained from the adaptive pushover analyses show a very rational distribution of yielding, with plastic hinges forming at the base of the columns and week beam-strong

(a) floor displacement

(b) interstorey drift
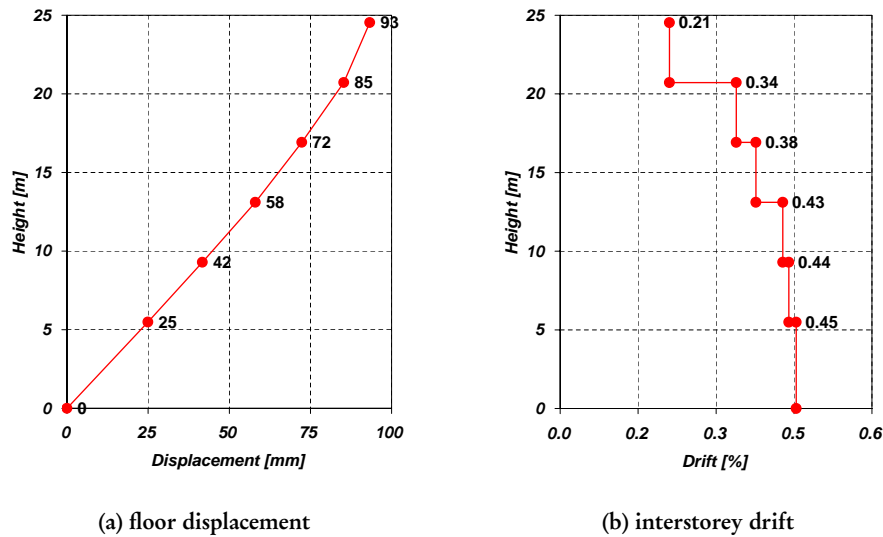
Figure 10.7. Pushover analysis: displaced shape and interstorey drift at first yielding conditions

(a) floor displacement

(b) interstorey drift
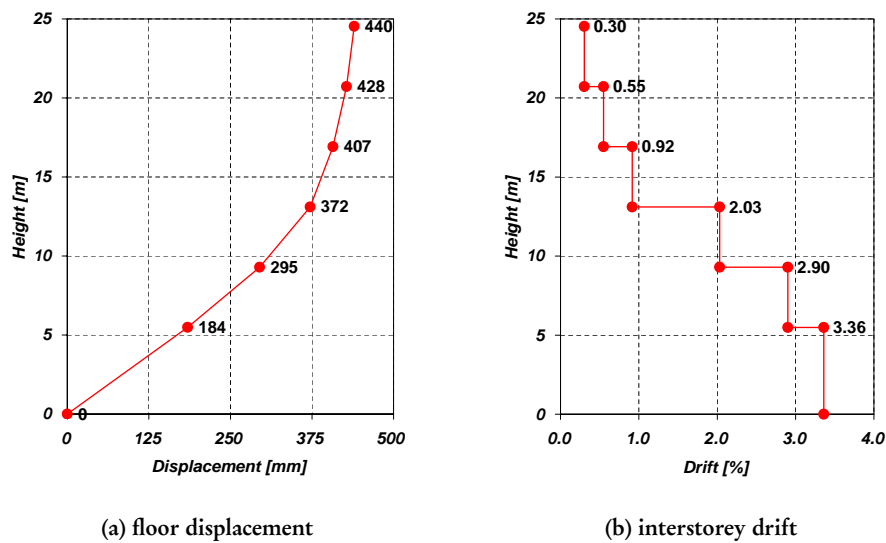
Figure 10.8. Pushover analysis: displaced shape and interstorey drift at first member failure

column behavior at every yielded joint, as intended for a building designed with capacity design concepts. However the ductility capacity is not large enough to reach a plastic mechanism before the failure of the first member.

10.2.3 Fixed Base Dynamic Properties

The dynamic properties of the initial elastic system are investigated performing a modal analysis. The two gravitational load conditions are considered, $W_{1,tot}$ in the case #1 and $W_{2,tot}$ in the case #2. The modal properties for case #1 and case #2 are listed in Table 10.3.

Table 10.3. Dynamic characteristics of the fixed base building structure

Mode	*case* #1		*case* #2	
	Frequency [Hz]	Period [s]	Frequency [Hz]	Period [s]
1	1.087	0.920	0.767	1.304
2	3.120	0.320	2.204	0.453
3	5.717	0.175	4.040	0.247
4	9.071	0.110	6.411	0.156
5	12.74	0.078	9.002	0.111

Regarding the damping modeling, a *Rayleigh* (Priestley *et al.* [2007]) damping model was adopted in the analyses, using $\xi_v = 1\%$ coefficient for the first and the fifth mode.

10.2.4 Isolation System Design

In the present work the superstructure is given, hence the isolation system design has to be interpreted as a retrofitting strategy of the proposed building. In the isolation system design, we assume to use the actual device and the isolation configuration is designed. Then the same configuration but considering the equivalent superelastic devices is considered and the responses are compared.

The actual isolator device is a lead rubber bearing (LRB) produced by *AGOM International* described in Section 4.2 and its technical properties are reported in Table 4.1.

The building design is performed according the *flexible superstructure* approach as defined in Priestley *et al.* [2007], and the superstructure is taken into account for its additional mass and flexibility contribution to reach the design displacement. The design spectra is the Eurocode 8, $PGA = 0.35g$ soil C type 1 (CEN [2004]), reported in Figure 7.9.

The floor weight distribution for case #1 and case #2 are shown in Figure 10.9a. It resulted $W_{1,tot} = 8487$kN and $W_{2,tot} = 16970$kN.

The displaced profile for the superstructure has been defined accordingly to suggestions in Priestley *et al.* [2007] for frame buildings. As a design drift limit, maximum interstorey drift of $\vartheta_d = 0.5\%$ at the first floor is considered. Following a *direct displacement based design* approach (Priestley *et al.* [2007]), the design displacement profile turned out to be the one in Figure 10.9b which it is assumed to be the same in the two cases. The displacement at the isolation layer is supposed to be $\Delta_{is} = 150$mm and the roof

displacement $\Delta_{roof} = 232$mm. The interstorey drift from this displacement distribution is shown in Figure 10.9c.

Based on the displacement profile, the effective height is $H_e = 16.12$m and its design displacement is $\Delta_e = 208$mm as reported in Figure 10.9b. The effective mass of the equivalent single degree of freedom system has been computed as well based on the displacement profile.

(a) floor weights   (b) displacement profile   (c) interstorey drift
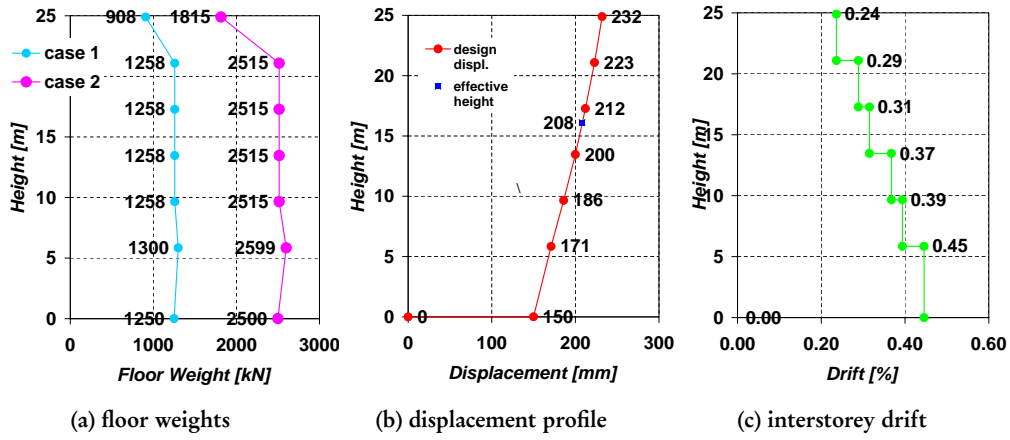
Figure 10.9. Design weights in case #1 and case #2 and design displacement and drift target for the isolation system

Sum of the viscous damping contribution weighted accordingly to the design displacement to estimate the global system equivalent viscous damping has been used, accordingly to suggestions in Priestley *et al.* [2007]. Considering a hysteretic damping $\xi_h = 28\%$ for the isolation system (as reported in Table 4.1) and $\xi_v = 1\%$ for the superstructure, the resulting equivalent damping is $\xi_e = 19.8\%$.

The resulting effective period is very close to the design corner period $T_e = 2.022$s $\simeq T_c$.

(a)   Case #1

Considering the first case and its effective mass $m_{1,e} = 2647$kN, the design base shear would be:

$$V_{1,d} = 4\pi^2 \frac{m_{1,e}\Delta_e}{T_e^2} = 5322\text{kN} \tag{10.3}$$

nevertheless, given that the effective period is larger than the corner period $T_e > T_c$, there is not unique solution in the design and the effective stiffness could correspond to any period larger than T_c. As reported in Priestley *et al.* [2007], any value of design base shear less than $V_{1,d}$ satisfies the design assumptions.

In the first case the design assumption is to consider *five* isolators $n_{1,is} = 5$. The design displacement is compatible with the one in Table 4.1 and the isolation system secant stiffness to the design displacement is:

$$k_e n_{1,is} = 8.10\text{kN/mm} \tag{10.4}$$

considering the previous stiffness at the isolation level, the modal analysis of the global structure identifies a fundamental period $T_{1,is} = 2.21\text{s}$ (being $T_{1,is} = 2.4 T_{1,0}$ in which $T_{1,0}$ if the fundamental period of the case #1 fixed base structure as reported in Table 10.3). The base shear in the isolation system is:

$$V_{1,base} = k_e n_{1,is} \Delta_{is} = 1215\text{kN} \tag{10.5}$$

The effective superstructure shear is supposed to be larger than the previous due to dynamic amplification, higher-mode and overstrength effects as described in Priestley *et al.* [2007]. Based on recommendations in Paulay and Priestley [1992], the dynamic amplification factor can be estimated for one-way frames as $\omega_s = 1.3$. Being the overstrength factor in this case about $\phi^o = 1.25$ the maximum shear demand can be estimated as $\omega_s \phi^o V_{1,base} = 1974\text{kN}$. Hence the design base shear is about the same then the one from the pushover analysis and this should prevent large inelastic demand in the superstructure.

(b)   Case #2

The effective mass in the second case is $m_{2,e} = 5294\text{kN}$. The design base shear in this case would be:

$$V_{2,d} = 4\pi^2 \frac{m_{2,e}\Delta_e}{T_e^2} = 10640\text{kN} \tag{10.6}$$

Again, any value of design base shear less than $V_{2,d}$ satisfies the design assumptions, as in Priestley *et al.* [2007]. In particular, being the total weight in the second case twice with respect to the weight in the first case, we decide to consider *ten* isolators $n_{2,is} = 10$. The isolation system secant stiffness to the design displacement is:

$$k_e n_{2,is} = 16.20\text{kN/mm} \tag{10.7}$$

considering the previous stiffness at the isolation level, the modal analysis of the global structure identifies a fundamental period $T_{2,is} = 2.36\text{s}$ (being $T_{2,is} = 1.8 T_{2,0}$ in which $T_{1,0}$ if the fundamental period of the case #2 fixed base structure as reported in Table 10.3). The base shear in the isolation system is:

$$V_{2,base} = k_e n_{2,is} \Delta_{is} = 2430\text{kN} \tag{10.8}$$

The design superstructure shear needs to be computed from the previous considering the dynamic amplification, which can be estimated as $\omega_s = 1.3$ from Paulay and Priestley

[1992], and the overstrength factor which in this case has been estimated as $\phi^o = 1.00$. the maximum shear demand can be estimated as $\omega_s \phi^o V_{2,base} = 3159\text{kN}$. Being the superstructure properties constant even if the design base shear in case #2 is the double with respect to case #1, and after the pushover analysis results, some inelastic demand in the superstructure is expected in the dynamic response. This implies that the interstorey drift is supposed to be exceeded in the analysis.

10.3   INNOVATIVE SUPERELASTIC ISOLATION SYSTEMS

In this work the response of the base isolated structure using actual lead rubber isolation bearings is compared with the response of two innovative superelastic system devices. The superelastic devices are based on a flat slider to carry the vertical load and on superelastic lateral restrainers. The solution considered for the lateral restraining system is the one reported in Chapter 6, characterized by radial lateral spring devices manufactured using shape memory alloys which has already been described in Section 6.4.2. A proposed device configuration scheme is shown in Figure 6.29.
In this investigation anyway, two possibilities for the superelastic device design shear force are investigated:

- in the first isolator device configuration, the superelastic restraining system is supposed to carry all the shear force in the device, being the friction coefficient of the slider very low and the breakaway shear negligible with respect to the yielding shear force; the technical properties of this system are described in Section 7.2.2;

- in the second configuration, an important part of the shear force is carried by the friction force, which provides an additional lateral stiffness and force component too; the technical properties of this systems are described in Section 7.2.3.

As reported in Section 10.2.4, the isolation system design has been accomplished assuming to use LRB. Superelastic devices have been designed in order to be equivalent to the actual LRB in terms of displacement and force capabilities. Thus, in the verification procedure, the same number of isolators with respect to the LRB design is assumed.

The responses of the two superstructure cases have been compared considering three different isolation systems corresponding to the actual LRB system described in Section 4.2, and the two innovative superelastic configurations described in Section 7.2.2 and Section 7.2.3. Moreover a linear elastic system secant to the isolation system design point has been considered. The implemented isolation models are the same used in the previous rigid-superstructure investigation reported in Chapter 9 and reproposed inhere.

- Elasto-plastic model (EP system, in Figure 10.10). The elastoplastic model is representative of the real lead rubber bearing device defined in Section 4.2 and the parameters we use are those reported in Table 10.4.
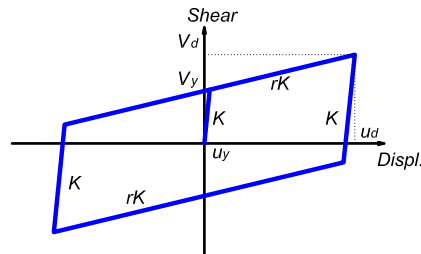
Figure 10.10. Base shear horizontal displacement relation for lead rubber bearing isolation device

Table 10.4. Hysteretic properties of *EP* system

LRB 500 (EP system)		
Elastoplastic model		
yielding shear	V_{ep}	147 kN
initial stiffness	k_{ep}	8.4 kN/mm
second stiffness	rk_{ep}	0.8 kN/mm

- Flag-shaped model (SL system, in Figure 10.11). The flag-shaped model reproduces the shear-horizontal displacement relation of the pure superelastic device (SL) device defined in Section 7.2.2. The used parameters are summarized in Table 10.5.
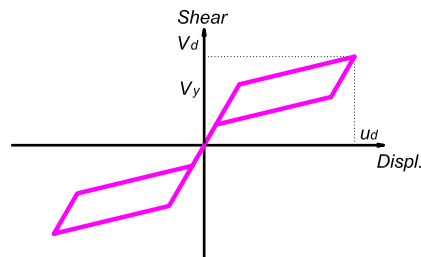
Figure 10.11. Base shear horizontal displacement relation for superelastic no friction isolation device

- Flag-shaped model (FR system, in Figure 10.12). The flag-shaped model reproduces the shear-horizontal displacement relation of the superelastic device and frictional flat slider (FR) defined in Section 7.2.3. The numerical model was obtained using two spring in parallel, one reproducing the superelastic device (*SE*) and the other the friction bearing device (*BF*). The used parameters are summarized in Table 10.6.

- Linear elastic model (LE system, in Figure 10.13). Considering the design displacement u_d and the design shear V_d, which are the same for the previous

Table 10.5. Hysteretic properties of *SL* system

Superelastic no friction (SL System)		
Flag-shaped model		
yielding shear	V_{sl}	195 kN
initial stiffness	k_{sl}	3.68 kN/mm
second stiffness	rk_{sl}	0.26 kN/mm
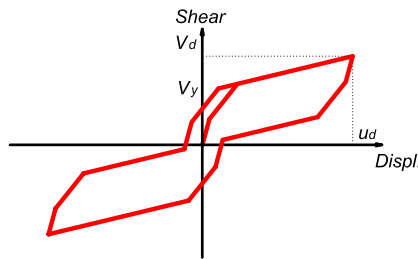
Figure 10.12. Base shear horizontal displacement relation for superelastic with friction isolation device

models, we carry out the analysis of the equivalent linear system, considering a secant stiffness to the design point which is common to the previous modes. The used parameters are summarized in Table 10.7.
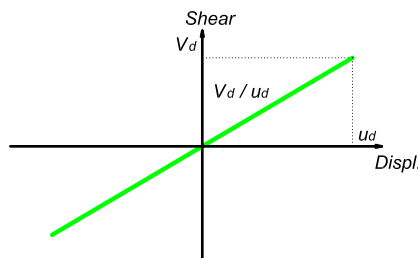
Figure 10.13. Base shear horizontal displacement relation for equivalent linear elastic with secant stiffness isolation device

The proposed model parameters are relative to the case $n_{is-frame} = 1$. Therefore they have to be multiplied for the correct $n_{is-frame}$ value in the analyses.
For comparison the fixed base frame response has been computed too, both in case #1 and in case #2.

Table 10.6. Hysteretic properties of *FR* system

Superelastic with friction (FR System)		
Flag-shaped model - restrainer		
yielding shear	V_{se}	136 kN
initial stiffness	k_{se}	2.57 kN/mm
second stiffness	rk_{se}	0.18 kN/mm
Elastoplastic model - friction		
yielding shear	V_{bf}	59 kN
initial stiffness	k_{bf}	11.7 kN/mm
second stiffness	rk_{bf}	0.0 kN/mm
Total system		
yielding shear	V_{fr}	195 kN
initial total stiffness	k_{fr}	14.27 kN/mm

Table 10.7. hysteretic properties of *LE* system.

Linear Elastic to design point (LE System)		
Linear model		
stiffness	k_{le}	1.62 kN/mm

10.4   ANALYSIS GROUND MOTIONS

The design earthquake is represented in terms of elastic spectra. Design conditions are given by EC8 spectra for $PGA = 0.35$g type 1 soil type GTC design spectra (CEN [2004]). The seismic design level has been represented then considering a set of compatible ground motions.

In this section the used earthquake records are recalled, being the ground motion set the same already used for the investigation in previous chapters and described in Section 7.4.

Suites of earthquake ground motions from the *SAC* database (see SAC [1997]) have been considered for the isolation bearing system response comparison evaluation, as reported in Section 7.4.1. All the ground motions are natural records.

In particular, two sets of records have been used in this work:

- earthquake natural ground motions with 10% probability of exceedence in 50 years for the area of Los Angeles: 20 records, whose properties are reported in Table 7.5;

- impulsive near-field earthquake ground motions: 12 records, whose properties are reported in Table 7.6.

Hence in total, 32 earthquake ground motions have considered for the analysis. A large number of records has been chosen to take into account as much as possible the variability

of the seismic input.

The records are from seismic events characterized by different seismological sources and recording conditions. Thus a scaling procedure is needed to permit the result comparison at the design level and the process has been described in Section 7.4.2. The EC8 spectra for $PGA = 0.35$g type 1 soil type GTC design spectra (CEN [2004]) has been used as a target for the scaling.

The resulting scaled ground motion properties are reported in Section 7.4.3. In particular, the scaling factors are reported in Table 7.5 and Table 7.6, while the final scaled ground motion displacement and acceleration spectra are shown in Figure 7.11, compared with EC8 design spectra.

10.5 Limited-Damage Responding Superstructure Results

The results of the time history analyses are reported in this section for the case #1 in which the total seismic weight of the superstructure is $W_{1,tot} = 8487$kN and the isolation system for the investigated frame is composed by $n_{1,is} = 5$ isolators. In this case the superstructure is supposed to mainly respond elastically and the interstorey drift demand to be close to the design profile, at least for the EP isolation system configuration. Response of innovative isolation technology systems is checked and compared. In particular, in Section 10.5.1 the isolation system response comparison is reported, while in Section 10.5.2 the main results of the isolated superstructure demand values are summarized.

10.5.1 Isolation System Response

For each ground motion record the maximum displacement demand and the maximum shear force in the isolation layer were recorded for all the isolation system configurations described in Section 10.3.

Displacement envelopes for the different isolation systems and the linear system secant system to the design displacement and for all the ground motions are reported in Figure 10.14 and base shear force envelopes in Figure 10.15. The mean value and the standard deviation for the EP, FR, and SL systems are then plotted in terms of displacement in Figure 10.16a and in terms of shear in Figure 10.16b. The same plots report also the absolute mean value on the top of the mean bars and the coefficient of variation, which is the ratio of the standard deviation over the mean, at the top of the standard deviation bars.

According to the design procedure and referring to the maximum dissipation capability, which was the one function of the elastoplastic hysteresis, the isolation system was design to reach a displacement of $\Delta_{is} = 150$mm. The mean demand in the EP, FR and SL systems shown in Figure 10.16a and normalized with respect to the design displacement are reported in Table 10.8. The design displacement is not exceeded in the EP and FR systems, while the mean SL demand is about one third higher than the design value.
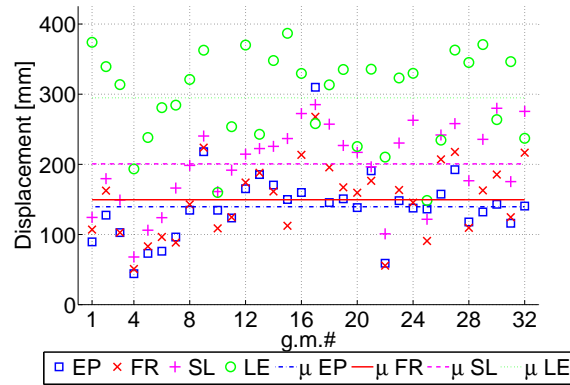
Figure 10.14. Displacement demand envelopes and mean values in the isolation system (absolute values of the three isolator hysteresis and the linear system secant to the design displacement)
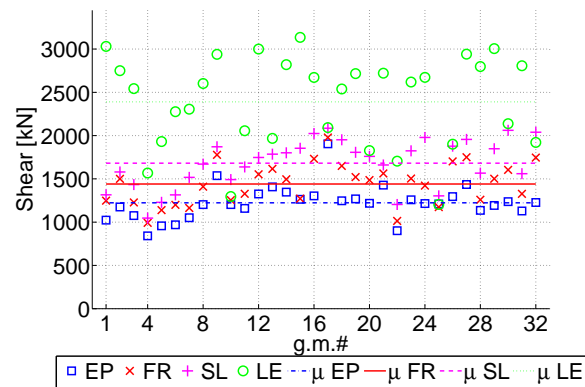
Figure 10.15. Shear demand envelopes and mean values in the isolation system (absolute values of the three isolator hysteresis and the linear system secant to the design displacement)

Table 10.8. Mean displacement envelope over design displacement ratio

Displacement Demand over Design Displacement			
design	EP system	FR system	SL system
100%	93.3%	100.0%	134.0%

(a) displacement demand

(b) shear force demand
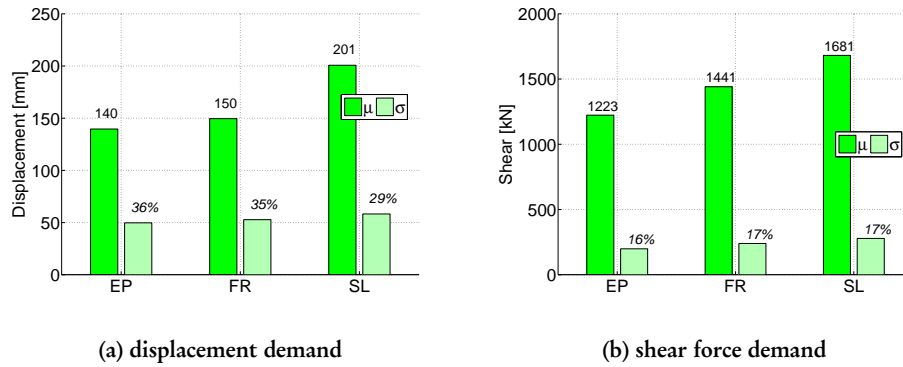
Figure 10.16. Isolation system displacement and shear demand envelope mean and standard deviation. The absolute values and the coefficients of variation are also reported respectively for the mean and the standard deviation bars

Table 10.9. Mean shear coefficient envelope over design displacement ratio

Shear Demand over Design Shear			
design	EP system	FR system	SL system
100%	100.6%	118.6%	138.3%

Regarding the shear force demand, the design shear in the isolation system constituted by $n_{1,is} = 5$ isolators is $V_{1,base} = 1215$kN. Considering the dynamic amplification and the overstrength factor $(\omega_s \phi^o)_1 = 1.62$, we would expect to design the superstructure for a base shear which is significantly larger with respect to the value $V_{1,base}$. Anyway in Table 10.9 the maximum shear force demand in the isolation system is compared with respect to the value $V_{1,base} = 1215$kN. Results show that the mean demand is very close to the design force in the EP system while it is exceeded for one-fifth in the FR system on for two-fifth in the SL system.

Coefficients of variation are about the same in the three systems both in terms of displacement demand (about 30%) and force demand (about 17%).

10.5.2 Superstructure Response

The superstructure response has been checked to investigate and underline differences in the response given by the various base isolation system force-displacement relations.

(a)   Superstructure Deformation

The deformation of the superstructure has been investigated. This consists in particular in the evaluation of the different displacement profiles, of their envelope, and in the computation of the maximum interstorey drift demands. The obtained values are then compared with the design ones.

Figure 10.17, Figure 10.18, and Figure 10.19 report the floor displacement profile envelope and the maximum interstorey drift demand respectively for EP, FR, and SL systems.

(a) floor displacement profile   (b) interstorey drift demand
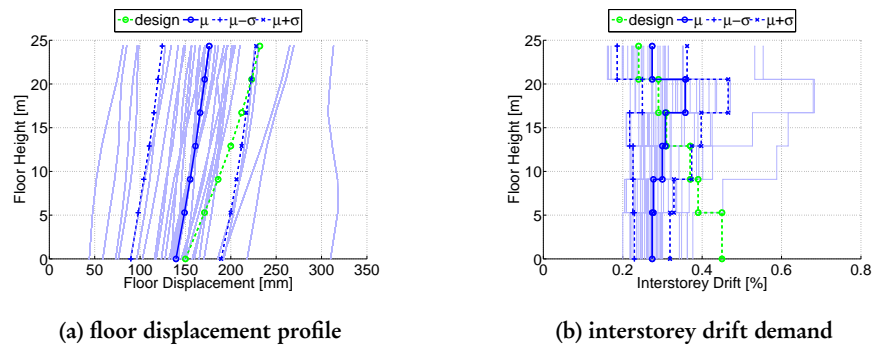
Figure 10.17. Time history analyses on EP system: displacement and drift results

(a) floor displacement profile   (b) interstorey drift demand
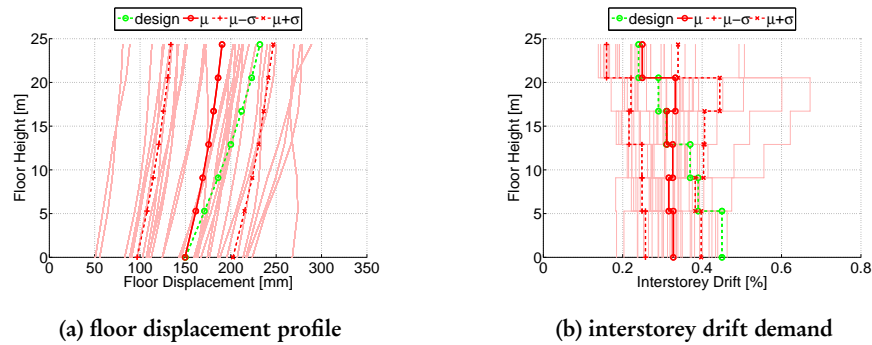
Figure 10.18. Time history analyses on FR system: displacement and drift results

Figure 10.20 reports, just for comparison, the same values considering the fixed-base superstructure. The values for all the ground motions are shown, together with the mean and mean plus and minus a standard deviation and the design values.

Looking at the results and referring mainly to the mean displacement and drift, the conclusion is that the design targets are respected for the EP and FR system, while they are exceeded for the SL system. This is proved in particular by the fact that the interstorey

(a) floor displacement profile   (b) interstorey drift demand
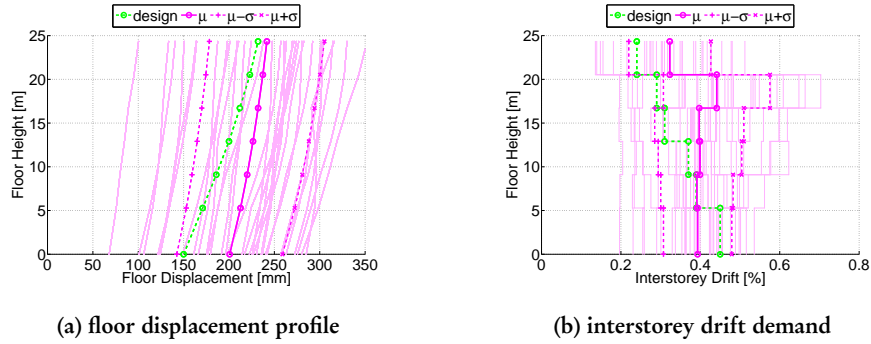
Figure 10.19. Time history analyses on SL system: displacement and drift results

(a) floor displacement profile   (b) interstorey drift demand
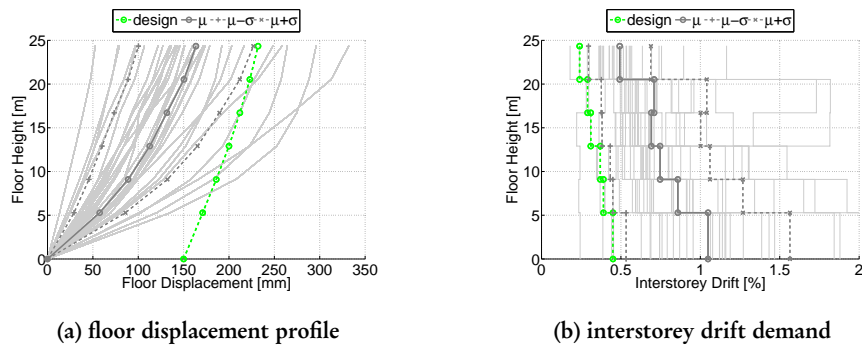
Figure 10.20. Time history analyses on fixed base structure: displacement and drift results

drift in the SL system is higher than in the previous ones, and being this closely related to the superstructure damage, it implies some plastic hinging. Moreover, as already mentioned looking at Table 10.8, the floor displacement profile shows that the isolation system demand is higher than the design one.

Globally, it can be noted that the mean drift profile is quite constant along the height of the building in all the systems, regardless the fact that the building is not regular in height and the masses are not uniform at every level. On the other side, the deformed shape computation according to the approach proposed in Priestley *et al.* [2007] leads to higher drift design at the lower floor and lower drift at the top floors. This difference has been interpreted as a consequence of two different factors. It is a proof of the isolation strategy effectiveness because the structure, responding mainly elastically, is deformed linearly. Moreover, it is also given by higher mode effects on the superstructure. Higher-modes produce large drift demand, in particular at the fifth floor.

Overall comparison of the interstorey drift demand at each floor level for all the isolation

system showing the mean value and the standard deviation over all the ground motion set is reported in Figure 10.27a. The conclusion is that the EP and FR systems are characterized by a very close response and the SL system is more demanding in terms of superstructure interstorey drift.

(b)   Floor Shear Force and Overturning Moment

The shear force envelopes for all the ground motions together with their mean values and the design values are reported for all the isolation systems and the fixed base in Figure 10.21. Two design values are reported. The lowest is the distribution along the building height according to the floor masses and the deformed shape of the base shear $V_{1,base}$. The highest is the previous one amplified considering the overstrength factor ϕ^o and the dynamic amplification ω_s; this would be the design values if the superstructure was to be designed according to the isolation system base shear, hence it is the value which we checked not to be exceeded during the time histories.

(a) EP system

(b) FR system

(c) SL system

(d) fixed base
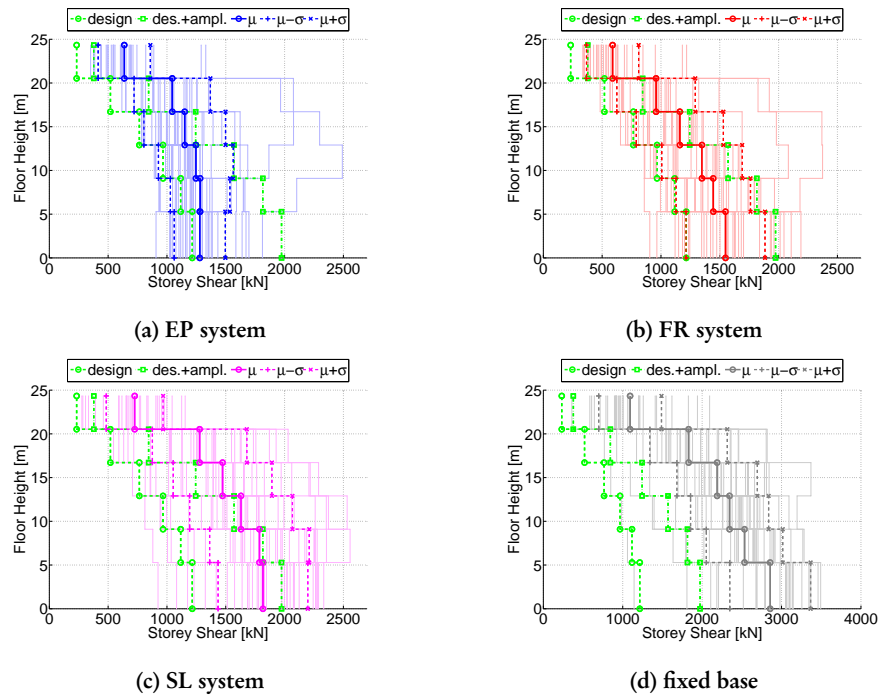
Figure 10.21. Time history analyses: floor shear demand values

The effects of the almost constant drift envelope along the height of the building affects the shear distribution as well, being this one quite small at the base of the building, close to the value $V_{1,base}$. Moreover, the higher modes influence in the superstructure response

is proved also looking at the shear distribution. Nevertheless the mean shear demand is compatible and does not exceed the amplified design limit significantly both in EP and FR system. Higher mode effects cause a mean value from time histories higher than design value in SL system, which also is in general more demanding than the previous ones.

In Figure 10.27b the mean floor shear demand, its standard deviation and the coefficient of variation are reported for all the isolation systems and for all the storeys. It can be noted that while in FR and SL systems the shear distribution is quite stepping along the building height, the mean envelope of the EP system is characterized by a more uniform shear demand, which is lower at the lower floors than the FR one and higher at the top floors.

(a) overturning moment (equivalent SDOF moment is $M_{OV} = 19.6\text{MN}$).

(b) exterior column axial force envelopes (the static axial force is $N_{stat} = 450\text{kN}$).
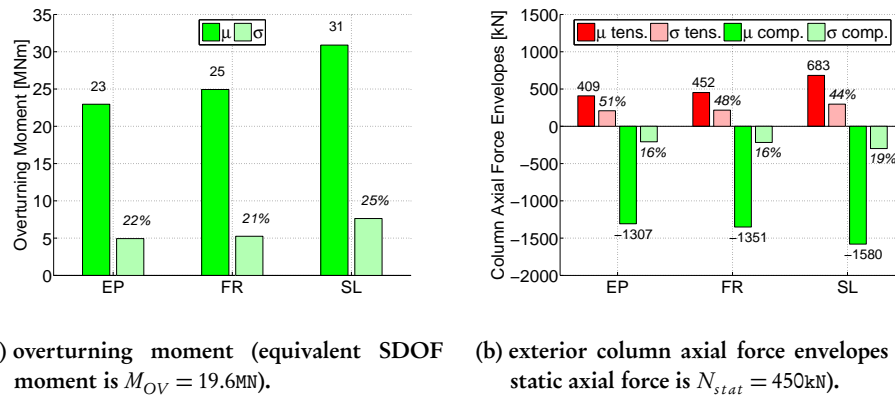
Figure 10.22. Maximum overturning effects on the isolated superstructure considering different isolation systems (the mean values and the coefficients of variation are reported respectively on the μ and on the σ bars)

Basically the design of base isolated flexible frames is governed by the base shear and its repartition along the building height. Nevertheless even in the isolated base frames an issue can be the maximum overturning moment in the superstructure. This is particularly relevant in the case of tall buildings with a short base length, for which the overturning moment is relevant because the effective height is high and it affects the superstructure response critically changing the axial force in the base columns which provide mainly the base moment to resist the overturning. For this reason, in all the time history analyses the overturning moment has been monitored computing the axial force in the base columns and their base moment. Being $L_b = 7315\text{mm}$ the span length in a single bay, the overturning moment M_{OV} has been computed as:

$$M_{OV} = M_{21} + M_{22} + M_{23} + M_{24} +$$
$$+ N_{21} \cdot 1.5L_b + N_{22} \cdot 0.5L_b - N_{23} \cdot 0.5L_b - N_{24} \cdot 1.5L_b \tag{10.9}$$

in which N_i and M_i are intended as the axial force and the bending moment at the base of elements i referring to numbering in Figure 10.4b.

Results are reported in Figure 10.22. In particular Figure 10.22a shows the mean value of all the maximum overturning moments recorded for all the ground motions together with their standard deviation and coefficient of variation. Figure 10.22b then shows the mean and standard deviation of the maximum axial force in the exterior columns, both in tension and in compression. Again, it can be noted that the EP and FR systems are characterized by close responses, while the SL system produces higher overturning moment demand. Also the axial force in the exterior columns are higher considering the SL system. The axial force produced by the static loading is about $N_{stat,21} \simeq 450 \text{kN}$. The mean axial load variation envelopes are reported in Table 10.10 in which the mean axial load due to overturning ΔN_{OTM} over the static axial load N_{stat} for the three systems are reported. Results show that the overturning moment and variation of the axial force

Table 10.10. **Mean axial load variation in exterior columns ratio:** $\Delta N_{OTM}/N_{stat}$

Axial load variation Ratio		
EP system	*FR system*	*SL system*
190%	200%	251%

from time histories are close to the design values considering an equivalent single degree of freedom system and applying the base shear $V_{1,base}$ at the equivalent height H_e defined in Section 10.2.4. The larger demand in the SL system is probably due to the fact that in this system the base shear is larger.

(c)   Floor Acceleration

Horizontal inertia forces that develop at each level of a building are proportional to the absolute horizontal accelerations experienced by the building. The floor acceleration is therefore important to assess the performance of non-structural elements.

The results in terms of floor accelerations are reported for all the ground motions and for all the isolations systems and also for the fixed base case in Figure 10.23. The mean values for all the systems and for all the floors and their standard deviation is also shown in Figure 10.27c.

As a conclusion, SL system is the more demanding in terms of floor acceleration too. EP and FR system responses are again quite close, even if the FR system is less demanding at the isolation and at the roof levels. The fact that if the superstructure responds elastically in the SL system the floor acceleration is the highest, it is related to the shear force developed at the base, which it is the highest.

(a) EP system

(b) FR system

(c) SL system

(d) fixed base
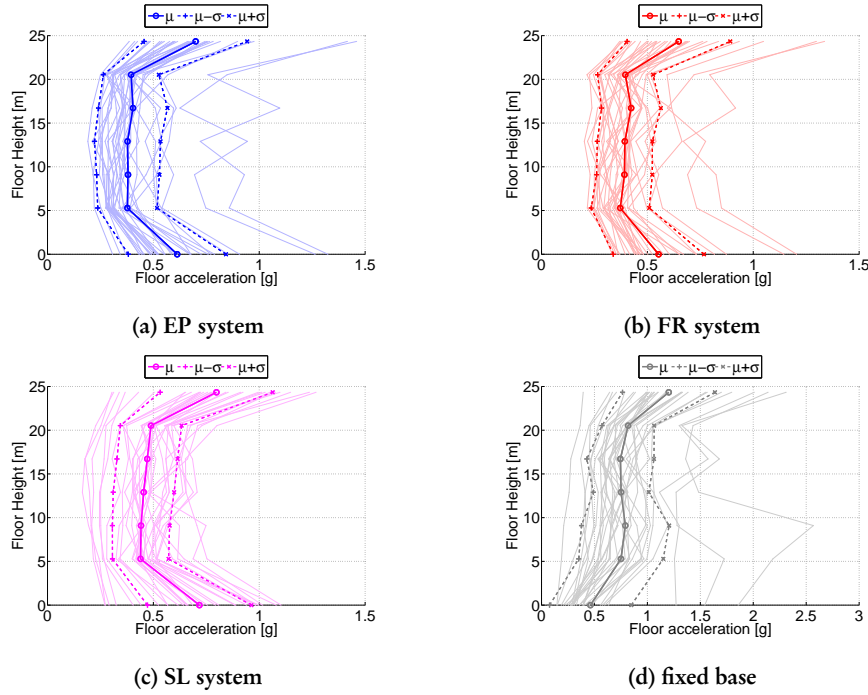
Figure 10.23. Time history analyses: floor acceleration demand values

(d)   Superstructure Damage and Energy Balance

In this design verification example, the superstructure is not intended to experience serious damage. Nevertheless the plastic hinge occurrence has been checked and it is reported in Figure 10.24. From this one the development of some plastic hinges in SL system it is shown, even if almost only in few ground motions. The occurrences in EP and FR systems are negligible. The mean curvature ductility demand for each plastic hinge location is then reported in Figure 10.25 for the isolation systems and for comparison in the fixed base case.

The superstructure damaging has been investigated considering the global energy balance as well. In this, the work done by the plastic hinge location and by the isolation system has been computed and then compared with the input energy from each ground motion. Comparison of the dissipated over input energy is shown in Figure 10.26. Accordingly to the design goals, the plastic hinge occurrences, and their mean ductility demand, the input energy dissipated through the plastic hinges is very low. It is not negligible only in the SL system case.
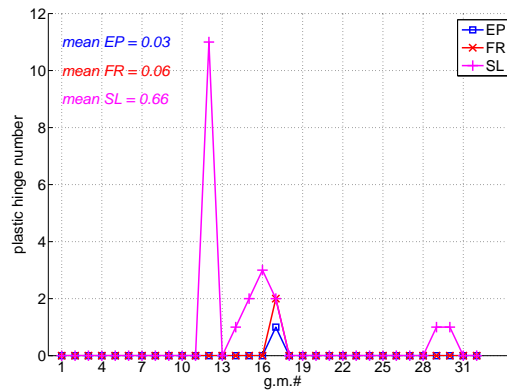
Figure 10.24. Plastic hinge occurrence in all ground motions for different isolation systems

(a) EP system

(b) FR system

(c) SL system

(d) fixed base
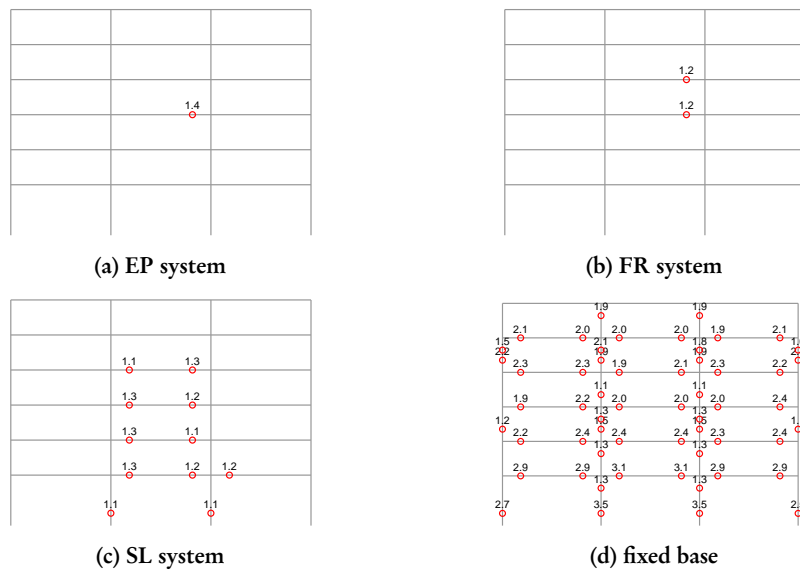
Figure 10.25. Superstructure plastic hinge mean curvature ductility demand
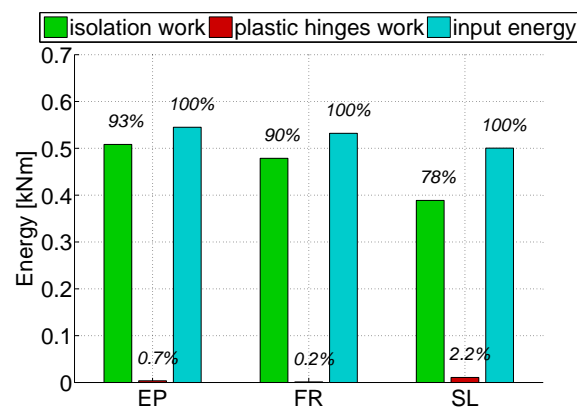
Figure 10.26. Different isolation system structure energy balance (each column percentage is normalized w/r the input energy
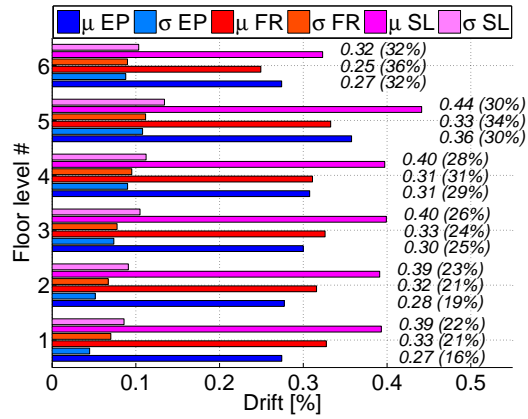
(a) interstorey drift demand
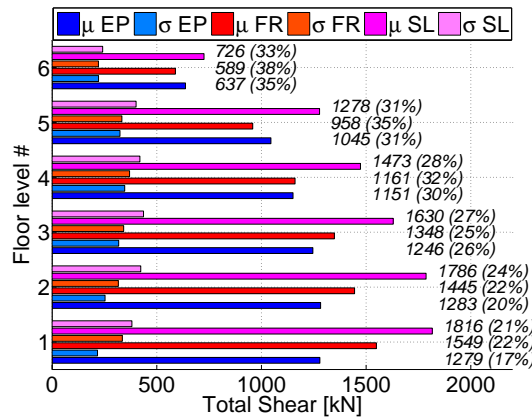
(b) floor level shear force demand
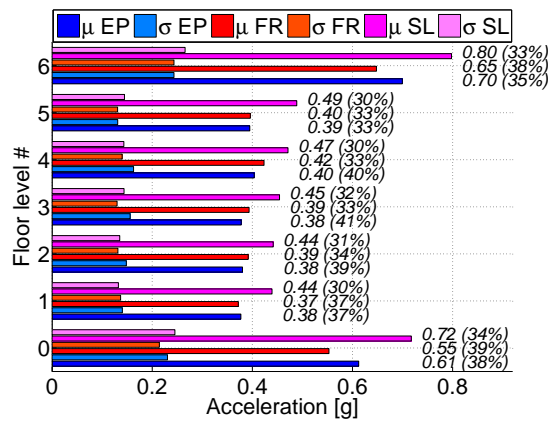
(c) floor acceleration demand

Figure 10.27. Superstructure main response parameters (mean values and coefficient of variations are reported too for each level and isolation system)

10.6 Inelastically Responding Superstructure Results

The time history results are reported in this section for the case #2. In this case the total seismic weight of the superstructure is $W_{2,tot} = 16970 \text{kN}$ and the isolation system is composed by $n_{is} = 10$ isolators. The case is investigated to get comparison about the different inelastic superstructure response as a function of the isolation system adopted. In fact, design shear force in the isolation system is supposed to produce some plastic demand in the superstructure with consequent development of plastic hinges.

10.6.1 Isolation System Response

For all the ground motion records, the maximum displacement demand and the maximum shear force in the isolation layer were recorded for all the isolation system configurations described in Section 10.3.
Displacement envelopes are reported in Figure 10.28 and force envelopes in Figure 10.29.
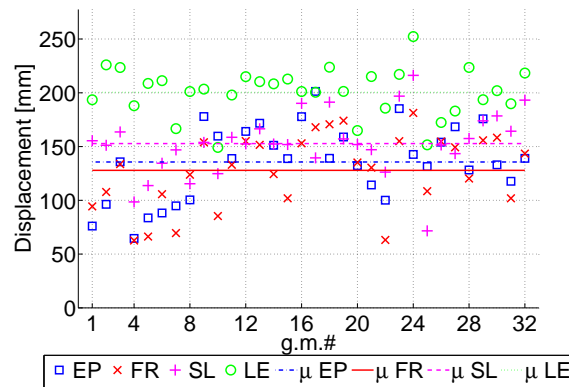
Figure 10.28. Displacement demand envelopes and mean values in the isolation system (absolute values of the three isolator hysteresis and the linear system secant to the design displacement)

The mean value and the standard deviation for the EP, FR, and SL systems are then plotted in terms of displacement in Figure 10.30a and in terms of shear in Figure 10.30b. The same plots report also the absolute mean value on the top of the mean bars and the coefficient of variation, which is the ratio of the standard deviation over the mean, at the top of the standard deviation bars.

According to the design procedure and considering a dissipation capability function of the elastoplastic hysteresis, the isolation system was supposed to reach a displacement equal to $\Delta_{is} = 150 \text{mm}$. The mean demand in the EP, FR and SL systems shown in Figure 10.30a and normalized with respect to the design displacement are reported in Table 10.11.
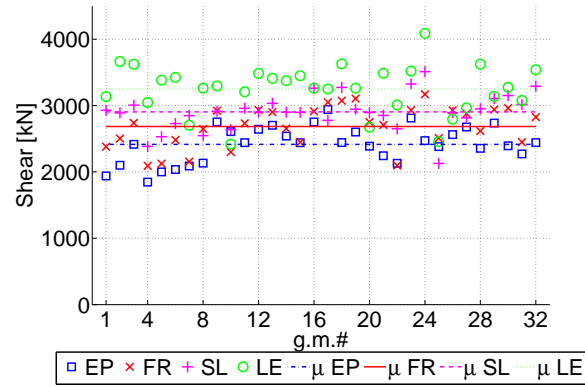
Figure 10.29. Shear demand envelopes and mean values in the isolation system (absolute values of the three isolator hysteresis and the linear system secant to the design displacement)

(a) displacement demand

(b) shear force demand
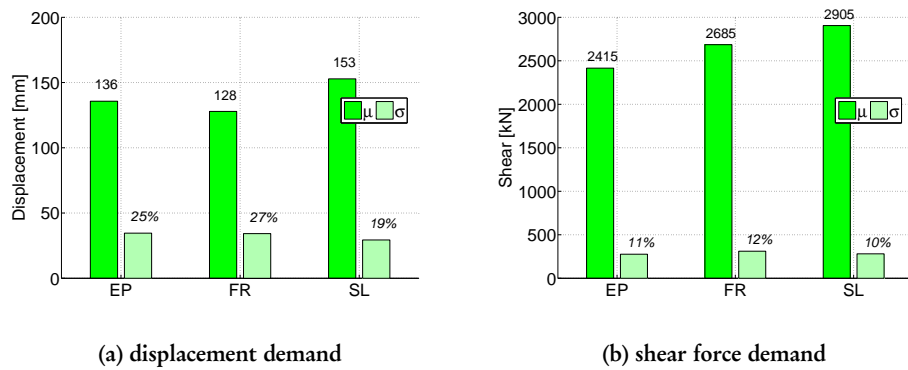
Figure 10.30. Isolation system displacement and shear demand envelope mean and standard deviation. The absolute values and the coefficients of variation are also reported respectively for the mean and the standard deviation bars

Table 10.11. Mean displacement envelope over design displacement ratio

Displacement Demand over Design Displacement			
design	EP system	FR system	SL system
100%	90.6%	85.3%	102.0%

Table 10.12. Mean shear coefficient envelope over design shear ratio

Shear Demand over Design Shear			
design	EP system	FR system	SL system
100%	99.4%	110.5%	119.5%

Like in the previous case in Section 10.5, the SL system displacement demand is the highest. In this case anyway, the mean displacement demand at the isolators in the FR system is lower than the mean displacement demand in the EP system. Moreover, in general in all the systems, the mean displacement is lower than the mean displacement in the isolation system recorded in case #1. The reason is probably that the damaging occurring at the superstructure level reduces the displacement demand at the isolators and the design level is reached through an higher contribution in terms of superstructure displacement.

Regarding the shear force demand, the design shear in all the isolation system composed by $n_{2,is} = 10$ isolators is $V_{2,base} = 2430\text{kN}$. The comparison between the design shear force and the mean envelope in the isolation system is reported in Table 10.12. The reduction in terms of displacement demand with respect to the design values affects the shear demand as well, which is lower in terms of percentage to the design shear force compared with the previous case shown in Table 10.9. Nevertheless the design condition is exceeded again considering the mean response in FR and SL systems.

Both in terms of displacement and in terms of shear force the coefficient of variation in this case is lower than in the previous case, implying a more uniform response at the isolation system layer when the superstructure is damaged.

10.6.2   Superstructure Response

Again the superstructure response has been investigated. The same parameters compared in the previous section have been checked to evaluate the main effects in using different isolation systems when the superstructure experiences some damage.

(a)   Superstructure Deformation

Floor displacement envelope profiles and interstorey drift profiles have been evaluated. They are reported in Figure 10.35a, Figure 10.35b, Figure 10.35c, and Figure 10.35d respectively for the EP, FR, SL isolation system and for the fixed base case. The values for all the ground motions are shown, with their mean value and mean plus and minus a standard deviation. The design displacement profile was computed based on a maximum drift at the lowest floor to prevented the damaging. On the contrary in this context the superstructure is supposed to be damaged, so the drift is expected to be exceeded. In fact the interstorey mean drift envelope is larger than the design one for all the isolation

(a) floor displacement profile
(b) interstorey drift demand
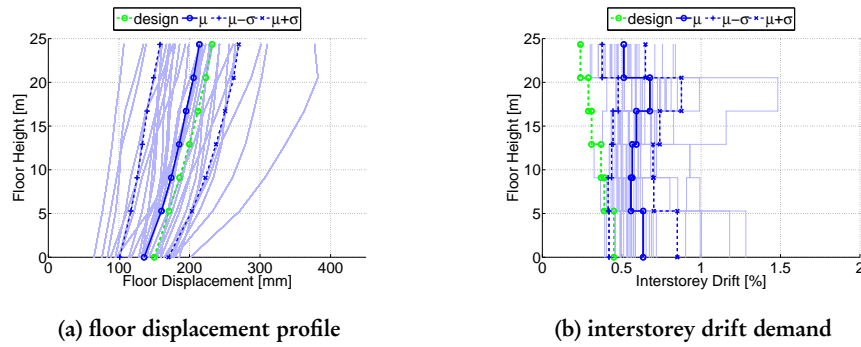
Figure 10.31. Time history analyses on EP system: displacement and drift results

(a) floor displacement profile
(b) interstorey drift demand
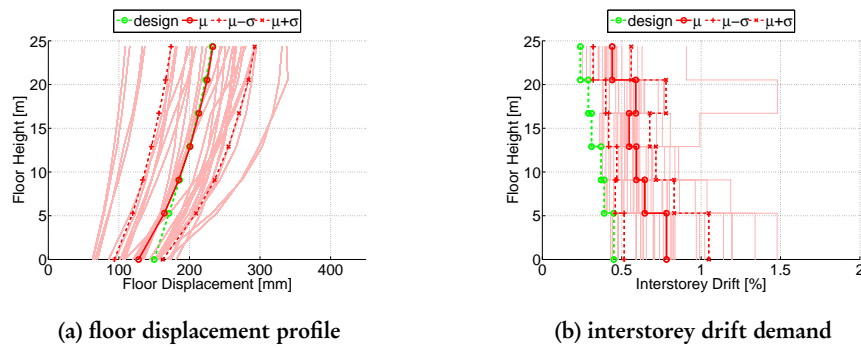
Figure 10.32. Time history analyses on FR system: displacement and drift results

(a) floor displacement profile
(b) interstorey drift demand
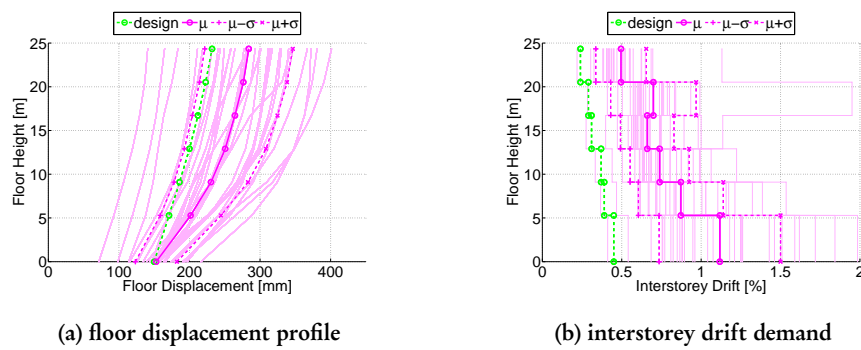
Figure 10.33. Time history analyses on SL system: displacement and drift results

systems. Anyway again the EP system response is the less severe, while the SL system is the most demanding. Higher mode effects are still quite important looking at the drift

(a) floor displacement profile   (b) interstorey drift demand
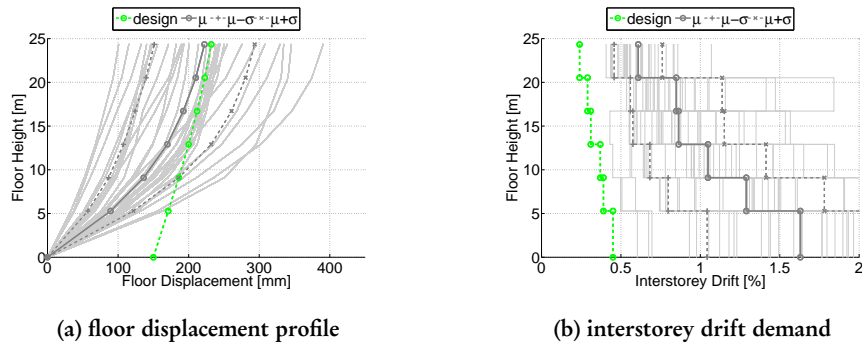
Figure 10.34. Time history analyses on fixed base structure: displacement and drift results

envelopes and at their peak values in some of the responses.

Mean drift envelope for all the floors and all the isolation systems with standard deviation and their coefficient of variation are reported in Figure 10.42a. Also based on this, we can conclude that the FR and EP mean responses are very close, with exception to the first storey drift, and characterized by a mean drift demand of the order of 0.6%. In the first storey the FR response is characterized more than the EP one by a soft storey mechanism, increasing the mean drift demand. The SL system floor drift is significantly larger in all the floors, implying a large damage in the superstructure.

(b)   Floor Shear Force and Overturning Moment

The shear force envelopes for all the ground motions together with their mean value and the design value are reported for all the isolation systems and the fixed base in Figure 10.35. Two design values are reported. The lowest is the distribution along the building height according to the floor masses and the deformed shape of the base shear $V_{2,base}$. The highest is the previous one amplified considering the overstrength factor ϕ^o and the dynamic amplification ω_s; this would be the design values if the superstructure was to be designed according to the isolation system base shear, hence it is the main value which we checked not to be exceeded in the time histories. Anyway the floor shear values are based on an elastic superstructure response, therefore the design values are just reported for comparison, being the superstructure not designed to respond elastically to these values. In Figure 10.42b the mean floor shear demand, its standard deviation and coefficient of variation are reported for all the isolation systems and for all the storeys. In this case the shear distribution along the building height is more regular than in the previous case, differences between different isolation systems are lower and the coefficient of variation for each value is lower with respect to the previous case.

The overturning moment and the variation of axial load in the exterior columns has been investigated in this case too and main results are reported in Figure 10.36.

(a) EP system

(b) FR system

(c) SL system

(d) fixed base
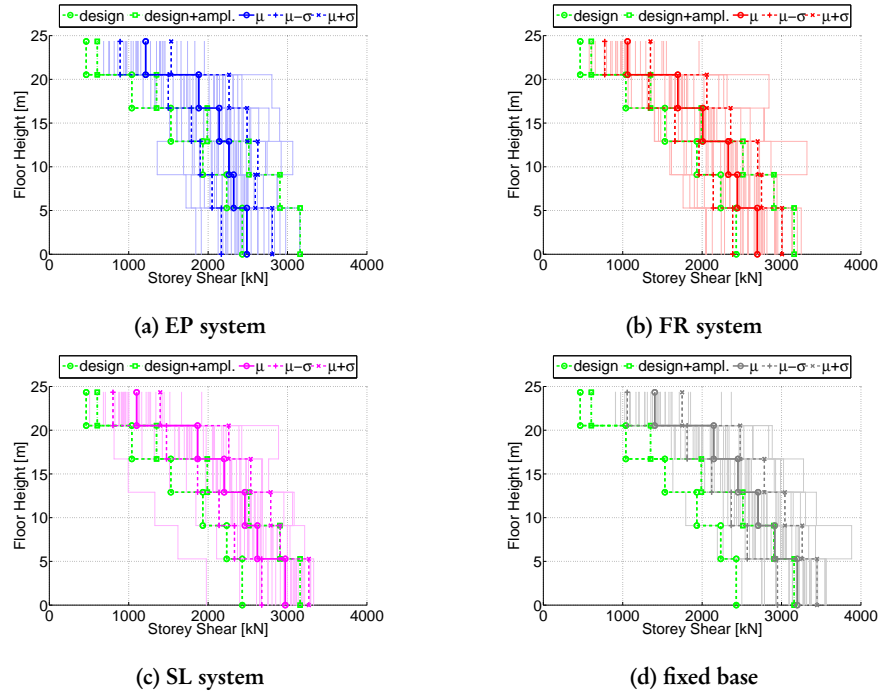
Figure 10.35. Time history analyses: floor shear demand values
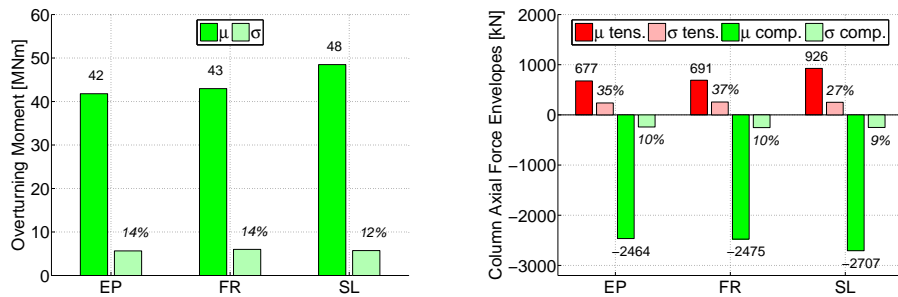
(a) overturning moment (equivalent SDOF moment is $M_{OV} = 39.2\text{MN}$).

(b) exterior column axial force envelopes (the static axial force is $N_{stat} = 900\text{kN}$).

Figure 10.36. Maximum overturning effects on the isolated superstructure considering different isolation systems (the mean values and the coefficients of variation are reported respectively on the μ and on the σ bars)

Mean overturning moment M_{OV} defined accordingly to Equation (10.9) and its standard deviation are reported in Figure 10.36a. EP and FR system demands are close to the theoretical M_{OV} computed considering equivalent SDOF system; the SL system one is bit larger, being this caused by the higher base shear demand. Figure 10.36b shows the mean and the standard deviation of the maximum axial force in the exterior columns, both in tension and in compression. Again SL system is more demanding. Table 10.13 reports the mean axial load variation in the exterior columns with respect to the static axial load which in this case is $N_{stat,21} = 900\text{kN}$. The high variation in the column axial force is

Table 10.13. Mean axial load variation in exterior columns ratio: $\Delta N_{OTM}/N_{stat}$

Axial load variation Ratio		
EP system	FR system	SL system
174%	176%	201%

lower than before in percentage because of the increasing weight. It is expected to affect the superstructure dynamic response also with some plastic hinging at the column base.

(c)   Floor Acceleration

Figure 10.37 shows the floor acceleration at all the levels for the entire ground motion set and for all the isolation system. The mean values and standard deviation and coefficient of variations are then reported in Figure 10.42c.

Two main points can be underlined in this case with respect to results in previous case. First of all the floor acceleration demand is in this case lower than in the previous case. Then, if in the results of case #1 the SL system was the more demanding, in this case differences are lower and anyway the EP system mean demand is higher. The reason for both the points can be identified in the damaging of the superstructure. It is supposed to produce a softening effect in the superstructure which causes the reduction of the floor acceleration. Moreover, being the SL system characterized by the largest inelastic response as expected from the interstorey drift demand which is usually proportional to the plasticization, it is the system which experience the largest softening.

(d)   Superstructure Damage and Energy Balance

The analysis of this structure and of its isolation strategy through different systems have been performed to evaluate differences in the response when the superstructure is expected to be damaged. The investigation on the plastic hinge occurrence is therefore quite significant in this context, together with the system energy balance.

Figure 10.38 reports the number of plastic hinge occurrences for all the ground motion set and for all the isolation systems. It turns out that the mean number of occurrences in the

(a) EP system

(b) FR system

(c) SL system

(d) fixed base
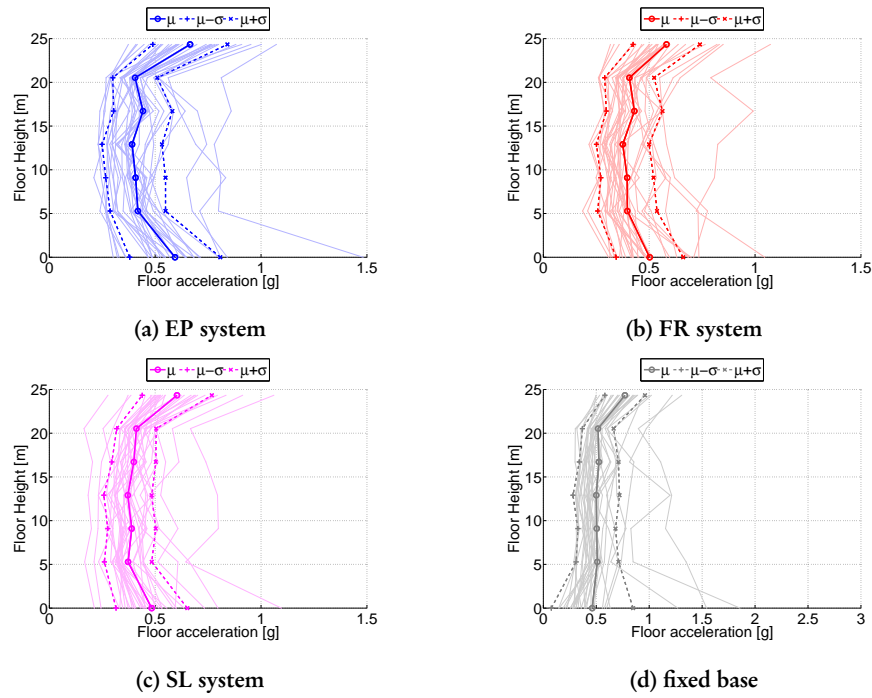
Figure 10.37. Time history analyses: floor acceleration demand values
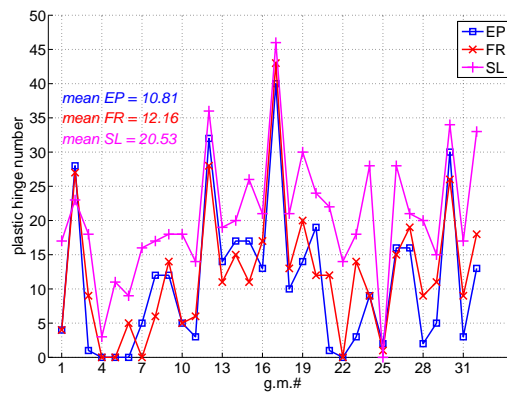
Figure 10.38. Plastic hinge occurrence in all ground motions for different isolation systems

EP system is less than 11, it is more than 12 in the FR system and it is more than 20 in the SL system.

(a) EP system

(b) FR system

(c) SL system

(d) fixed base
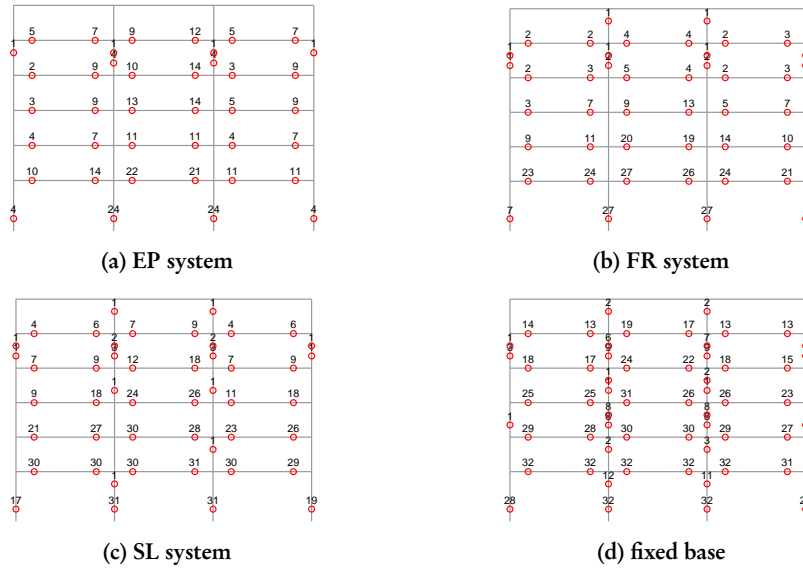
Figure 10.39. Superstructure plastic hinge occurrences

(a) EP system

(b) FR system

(c) SL system
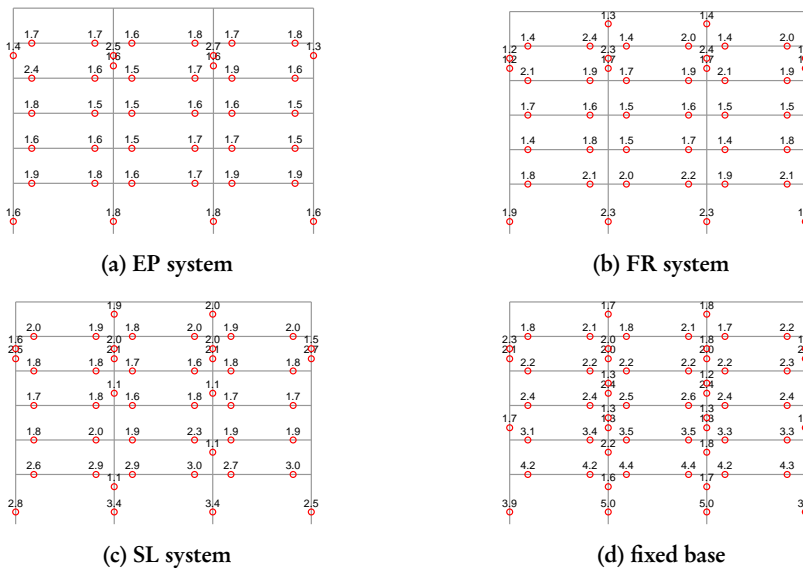
(d) fixed base

Figure 10.40. Superstructure plastic hinge mean curvature ductility demand

Figure 10.39 reports then the plastic hinge occurrence locations for all the isolation systems and the fixed base case, and Figure 10.40 the mean curvature ductility demands
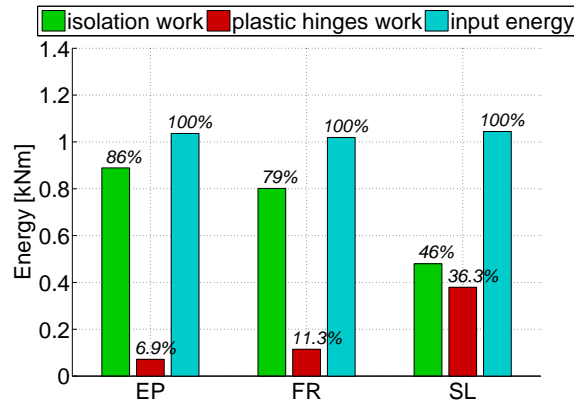
Figure 10.41. **Different isolation system structure energy balance (each column percentage is normalized w/r the input energy**

in the same locations and in the same cases.

The main conclusion is that as expected the superstructure experiences in this case severe damage. Nevertheless the capacity design is mostly respected and the superstructure is usually characterized by ductile mechanisms. Due to higher mode effects, already identified through the drift result plot, a soft storey is developed for a single ground motion at the fifth floor and this in all the isolation systems. The maximum curvature ductility is in general quite low and no member flexural collapse is recorded in any isolation system configuration.

The system energy balance is shown in Figure 10.41. In this case the mean input energy in the three systems is very close, hence the comparison is quite immediate. In all the systems a relevant part of the input energy is dissipated through plastic hinge work in the superstructure and this confirms the damage results shown before. In particular, the SL system dissipates a similar amount of energy in the isolation non linear system and in the plastic hinges and this is the highest plastic hinge work percentage. Values for EP and FR system are closer, nevertheless the second one is the double with respect to the first one.
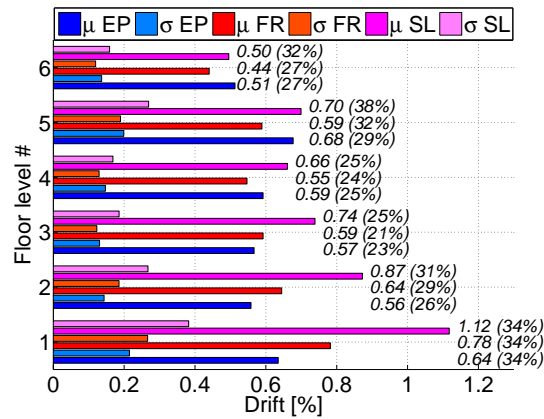
(a) interstorey drift demand
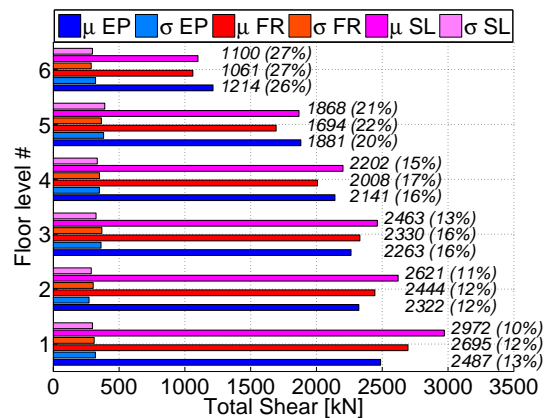
(b) floor level shear force demand
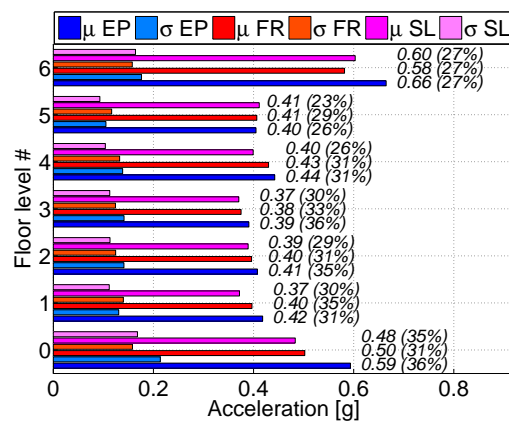
(c) floor acceleration demand

Figure 10.42. Superstructure main response parameters (mean values and coefficient of variations are reported too for each level and isolation system)

10.7 CONCLUSIONS

The seismic response of a six storey isolated steel frame structure has been checked considering different isolation technologies. Retrofitting processes have been simulated considering a superstructure defined in literature and assuming two different gravitational load distributions. Based on this, isolation systems have been defined using actual lead rubber bearings (EP system). Consequently, it has been assumed to use innovative superelastic devices (FR system and SL system) equivalent with respect to LRB. The objective of the investigation is to evaluate and compare the effectiveness of the different isolation configurations in reaching the structural goals. Two cases have been considered, one in which the superstructure has been designed to elastically respond and another in which it was supposed to experience some damage.

Regarding the isolation system response, it results that the maximum displacement and shear force recorded in the isolation layer are very close between the three considered systems. This despite the fact that the theoretical hysteretic damping and therefore the response envelopes are supposed to be significantly different, given the differences in the force-displacement relations. The flag-shaped FR system response is very close to the high dissipation LRB system response. The SL system is more demanding but the differences are very much smaller than what would be expected based on a equivalent hysteretic damping approach. A reduction in the force and displacement isolation system demand has been recorded when the superstructure experiences extensive damage, as a consequence of the fact that the design displacement is in this case reached through a larger superstructure contribution.

Looking at the superstructure response, EP system and FR system responses are very close in all the cases. The isolation turns out to be very effective in terms of reducing interstorey drift, floor shear and floor acceleration, both when the superstructure is damaged and when it responds elastically.

Based on the presented results, the main conclusion is that from the performed analysis the actual LRB system and the innovative flag-shaped with friction (FR system) are almost equivalent in terms of device and superstructure response. The main parameter envelopes, which are the values we accounted the most because they are at the base of the design procedure, are almost the same both at the isolation and superstructure level.
Slightly more demanding results are from the innovative flag-shaped without friction (SL system). Nevertheless its response from the time history analyses is closer to the LRB one than to the one predicted according to an equivalent hysteretic damping approach.

This page intentionally left blank.

11. Seismic Displacement Based Design of Base Isolated Structures with Superelastic Bearings

11.1 INTRODUCTION

In previous chapters, the effectiveness of different superelastic isolation device configurations has been investigated. Time history analyses were performed on single degree of freedom systems in Chapter 7, on rigid superstructure systems in Chapter 9, and on flexible superstructure systems in Chapter 10. Two possible isolation configurations have been considered, one in which all the restraining force is demanded at a superelastic system and another in which the superelastic system works in parallel with a friction device. The structural response of buildings isolated using innovative systems were compared with the results of the same buildings isolated using actual high dissipative isolation devices.

The main conclusion is that the superelastic isolation devices is very attractive for its effectiveness in modifying the structural response and avoiding the residual displacements after the seismic event. Nevertheless, the system with the friction elements turns out to be less demanding in terms of displacements and forces with respect to the pure superelastic restrainer. Moreover, using this superelastic plus friction device, differences in response with respect to high dissipative bearing are very small.
Based on that, the possibility of using the superelastic plus friction device configuration for base isolation can be a valid option in seismic engineering. For this reason, its design process is investigated in the present chapter, based on the displacement design approach as presented in Priestley *et al.* [2007].

An overall description summary of the innovative superelastic device is proposed in Section 11.2. The review of the seismic base isolation design procedure and the practical modifications to be used in case of superelastic device are then proposed in Section 11.3. A simulated design example using superelastic device and its comparison with the design example of the same structure considering an actual isolation system is described in Section 11.4. The results of the design process are then assessed through time histories analyses in Section 11.5. Finally, the main conclusions are reported in Section 11.6.

11.2 INNOVATIVE SUPERELASTIC DEVICE

The proposed superelastic isolation device is recalled in this section after being designed in Chapter 6. The described configuration feasibility in improving the structural response has been investigated in previous chapters even in comparison with another superelastic device configurations, which resulted less effective, and with actual high dissipating isolation systems.

11.2.1 Device Conception and Components

The basic principle for the superelastic device isolation bearing is to ideally use two elements, one to carry the vertical load and to permit the lateral displacement, and the other to work as a flexible and dissipative restrainer, i.e. providing lateral restoring force opposite to the bearing motion.
The first one is a sliding system transmitting the vertical load and permitting the lateral displacement with a non-negligible friction coefficient.
The other is a superelastic material lateral restraining system. This is composed by radial lateral springs manufactured using shape memory alloys whose design has been described in Chapter 6.
A possible device configuration scheme is shown in Figure 11.1. This is a general lay out of the system considering a restraining system and a friction slider. Obviously the two elements are not required to be used together at all the bearing locations and the design can be performed also assuming sliders without the restraining system or some superelastic restraining systems without the corresponding sliders.
This system conception has been defined in Section 7.2.3 as *FR system* and its peculiarity is that the slider contributes also in terms of shear force. It turned out to be more favorable in terms of seismic performance with respect to the same configuration but with negligible slider friction coefficient (*SL system*, as defined in Section 7.2.2). Referring to superelastic isolation system (*SE system*) we refer here to FR system.

11.2.2 Resulting Hysteresis

The total shear force V_{is} response of the SE system is made up of two different contributions:

$$V_{is} = V_{se} + V_{bf} \tag{11.1}$$

in which:

- V_{se} is the shear force carried by the superelastic spring restrainer system;

- V_{bf} is the shear force provided by the flat slider through friction.

The two different components are reported in Figure 11.2. The superelastic shear force-lateral displacement relation can be obviously described through a flag-shaped

(a) lateral view

(b) top view

Figure 11.1. Superelastic isolator device configuration
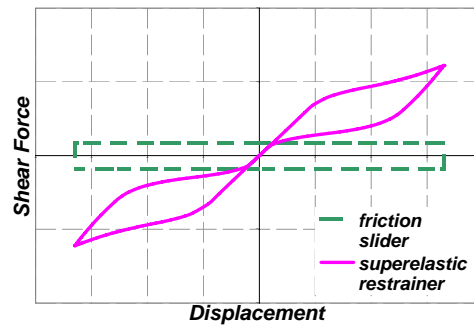
Figure 11.2. Superelastic isolation bearing with friction (SE system) contribution: superelastic and friction components

hysteresis. The friction component can be modeled using a rigid-plastic relation in which the yielding force is the breakaway force of the slider.

As focused from Figure 11.2, a particular issue of the SE isolation system design is to balance the friction and the superelastic shear force component to limit the residual displacements.

In Figure 11.3, the final system hysteresis given by the sum of the two components of Figure 11.2 is shown. This is also compared with a lead rubber bearing (*LRB*) response model characterized by the same design force and displacement (see Section 4.2). Summing rigid-plastic and flag-shaped force displacement relations, the final SE
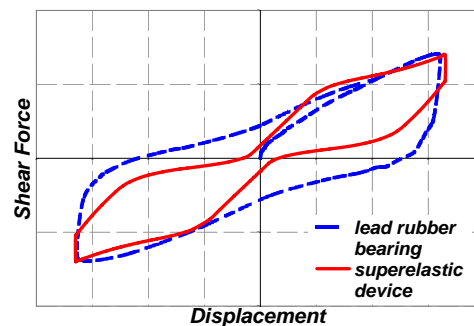
Figure 11.3. LRB 500 and superelastic isolation bearing with friction contribution (FR system): force-displacement relation comparison with equivalent LRB system

system hysteresis is characterized by an high initial stiffness and low hardening due to the rigid plastic contribution, and an higher dissipation capability with respect to the system without friction. Evidently, the comparison with LRB system shows that this last one is characterized by a larger hysteretic dissipation with respect to the proposed SE system.

As a final remark, Figure 11.3 also proves that SE system is not fully recentering due to the friction component. Nevertheless, the maximum residual displacement is very small if compared with the maximum residual of the LRB.

11.3   DESIGN PROCEDURE FOR ISOLATED STRUCTURES

In the present section the design procedure for base isolated structures is reviewed. The Direct Displacement Based Design approach is reported in Section 11.3.1 as presented in Priestley *et al.* [2007]. In Section 11.3.2 the suggested approach for SE system isolation design is then proposed. Design provisions for superelastic base isolated structures are then summarized in Section 11.3.3.

11.3.1   Direct Displacement Based Design Procedure for Isolated Structures

The displacement based design consists firstly in modeling the structure with an equivalent single degree of freedom system (SDOF) characterized by an equivalent mass (m_e) lumped at an equivalent height (h_e), an effective stiffness for lateral load (K_e), and an equivalent viscous damping (ξ_e).

The design displacement is usually computed assuming the elastic response in the superstructure and all the essential nonlinear phenomena taking place in the isolation system. Hence, large part of the displacement demand is expected to occur at the isolation level. Based on the structural configuration, a theoretical deformed shape for the lateral load condition can be assumed, and an example is shown in Figure 11.4. The deformed

(a) displacement profile   (b) equivalent SDOF system
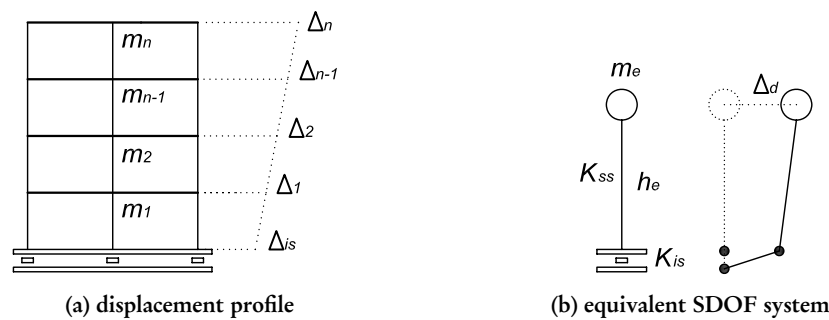
Figure 11.4. Base isolated flexible structure model

shape $\mathbf{\Delta}$ of a general structure with n_f floors and mass m_j at each storey can be estimated. $\mathbf{\Delta}$ is a vector having n_f components corresponding to the displacements of each floor as shown in Figure 11.4a.

The generalized displacement coordinate is defined as:

$$\Delta_d = \frac{\sum_{j=1}^{n_f} m_j \Delta_j^2}{\sum_{j=1}^{n_f} m_j \Delta_j} \tag{11.2}$$

and the effective mass is:

$$m_e = \frac{\sum_{j=1}^{n_f} m_j \Delta_j}{\Delta_d} \tag{11.3}$$

while the effective height is given by:

$$h_e = \frac{\sum_{j=1}^{n_f} m_j \Delta_j h_j}{\sum_{j=1}^{n_f} m_j \Delta_j} \tag{11.4}$$

and can be interpreted as the height of the resultant of the lateral forces to produce at the base of the SDOF a bending moment equal to the base moment of original MDOF. Equation (11.2), Equation (11.3), and Equation (11.4) are applicable for all the structures, not only the isolated ones, even if the design displacement profile is supposed to be different.

For small buildings or tanks, fundamental period of base-isolated structure is several times larger than fixed-base structure. Hence the isolation system horizontal stiffness K_{is} is several times smaller than the superstructure stiffness K_{ss}.

$$K_{is} >> K_{ss} \tag{11.5}$$

If Equation (11.5) is verified, the assumption of rigid superstructure is reasonable (this was the case of the investigation in Chapter 9). Separate design for superstructure and isolation system can be performed, assuming that all the displacement occurs only at the isolation level, as shown in Figure 11.5. In this case the superstructure affects the isolation system

(a) displacement profile   (b) equivalent SDOF system
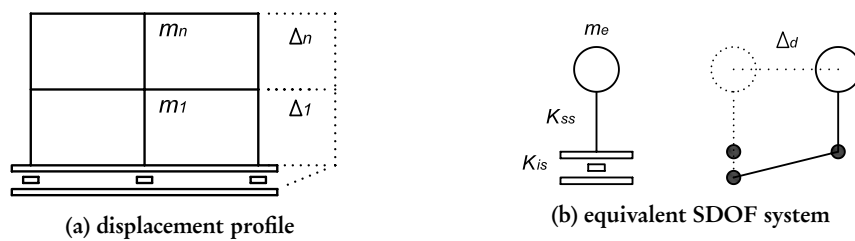
Figure 11.5. Base isolated rigid structure model

design only as an additional mass. The effective mass m_e is equal to the total mass and the effective height h_e is one half of the total height.

Given the shear force-lateral displacement relation of the system, which can be general and mostly given by the isolation system response contribution, the effective stiffness K_e is the secant stiffness to the design displacement. This definition is shown in Figure 11.6 in which the single degree of freedom system has been modeled assuming an initial elastic stiffness K and a post yielding stiffness which is a fraction rK of the previous. The design displacement Δ_d is a function of the limit state condition we are interested in
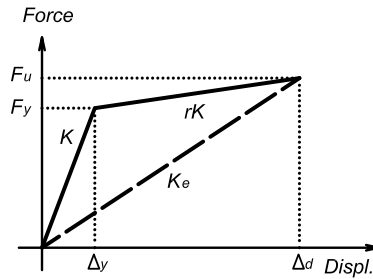
Figure 11.6. Effective stiffness concept for a bilinear force displacement relation envelope

and it can be computed using Equation (11.2). Considering the real structure properties such as materials and cross sections, the control point displacement is related to structural performance. Still referring to SDOF, we also compute the loss of linearity displacement Δ_y, corresponding to the first yielding in the structure. Then the displacement ductility of the equivalent system is given by:

$$\mu = \frac{\Delta_d}{\Delta_y} \tag{11.6}$$

In displacement based design procedure the structure is modeled as a SDOF system with a linear elastic stiffness equal to the effective stiffness. Nevertheless, real inelastic properties cannot be neglected because they are related to energy dissipation. Therefore an equivalent viscous damping ratio ξ_e representative of the elastic damping and of the hysteretic energy absorbed during the real response is used. In some researches (for example Grant *et al.* [2005]) empirical relations between the equivalent damping ratio for different structural system and the design displacement ductility have been developed and are accessible. They are based on the proportionality between the hysteretic area of the lateral force-displacement loops and the energy dissipation as recognized for the first time in Jacobsen [1960].
Assuming that the 5% damping design displacement spectra is given, the effectiveness of damping ξ_e is in reducing the displacement ordinates. An estimation of the relative damping ratio spectra multiplying the original spectra ordinates by a factor $R_\xi(\xi_e)$. This is a reduction factor increasing as the equivalent viscous damping increases. The most

common formulation, which is also reported in CEN [2004], is:

$$R_\xi = \left(\frac{10}{5 + \xi_e} \right)^\alpha \tag{11.7}$$

in which $\alpha = 0.5$ for far field events and $\alpha = 0.25$ for near field events as proposed in Priestley *et al.* [2007].

Using the design displacement for the structure and referring to the design spectra for the given damping, effective structural period T_e can be computed as shown in Figure 11.7. According the previous assumption, the effective stiffness K_e is given by:
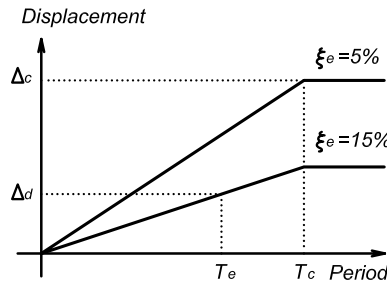
Figure 11.7. Displacement design spectra for different damping ratios (reported on the curves) and computation of the effective structural period T_e given the design displacement Δ_d

$$K_e = \frac{4\pi^2 m_e}{T_e^2} \tag{11.8}$$

and the base shear of the structure is:

$$V_{base} = K_e \Delta_d \tag{11.9}$$

Computation of the design shear force for the equivalent SDOF can be straight using the relation:

$$V_{base} = \frac{4\pi^2 m_e}{\Delta_d} \left(\frac{\Delta_c}{T_c} \right)^2 R_\xi^2 \tag{11.10}$$

being Δ_c and T_c the coordinate of the corner period in the 5% damping design displacement spectra as reported in Figure 11.7.

11.3.2 Superelastic Isolation System Design

The design procedure for a base isolated structure using superelastic device is presented in this section. Some suggestions are proposed in the general framework of the direct displacement based procedure for base isolated structures.

Major concerns are in particular related to the equivalent single degree of freedom modeling issues in terms of equivalent viscous damping and effective stiffness. In previous works (see Attanasi *et al.* [2009b] and Attanasi *et al.* [2009a]) the concept that in a base isolated system the dissipation was directly a function of the hysteretic area was debunk. Moreover, differences in superstructural performance induced by the different isolation system hysteresis was underlined. The superelastic system response was identified as characterized by large number of cycles and therefore in average by an high velocity content. Finally, the large importance of cycles in which the design displacement is not reached was recognized.

The aim for the suggested procedure is to provide some design tools preserving the DDBD basic approach. Assuming that the equivalent SDOF system is characterized by a linear elastic stiffness secant to the design displacement, an appropriate expression for the system hysteretic damping is investigated. This is supposed to take into account all the contributions in energy dissipation given by the device components considering a suitable weight for the all of them.

(a)   Shear Force Contribution Balancing

As already recognized, the isolation system device response is made by the contribution of the friction shear force V_{bf} and of the superelastic restrainer force V_{se}. The shear force-lateral displacement relations can be approximated as a flag-shaped hysteresis and as a rigid-plastic hysteresis respectively, as shown in Figure 11.8, in which the first quadrat for both of them is reported. In the design procedure, a first step is to design the force

(a) superelastic restrainer hysteresis   (b) friction device hysteresis
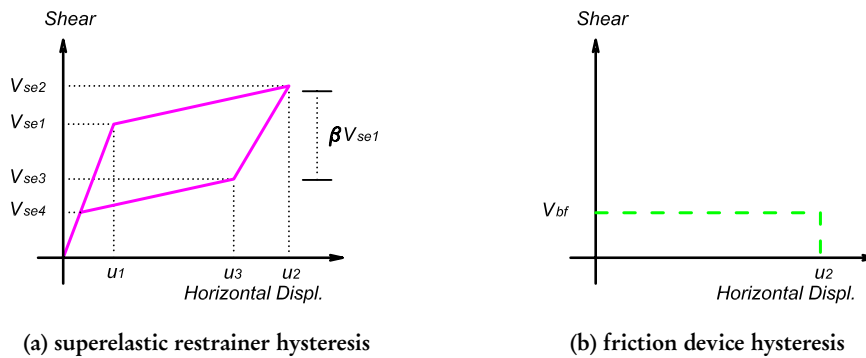
Figure 11.8. SE system base isolation components

contributions in order to provide an acceptable level of residual displacements. Referring to quantities in Figure 11.8, this condition can be formalized as follows:

$$V_{bf} \leq V_{se4} \tag{11.11}$$

being V_{se4} the force at which the initial linear branch is reached looping in unloading.

A parameter to quantify the relative weight of the superelastic restrainer shear force with respect to the friction force is needed. Due to the different hardening coefficient in the superelastic contribution (in which the second stiffness is relevant, as shown in Figure 11.8a) and in the friction model (in which it is negligible, as shown in Figure 11.8b), this ratio changes as the design displacement changes.

Assuming u_2 the design displacement in the isolators, and referring to quantities reported in Figure 11.8, the following expression is proposed for the superelastic contribution ratio λ_{se}:

$$\lambda_{se} = \frac{\psi_{se}}{2}\left(\frac{V_{se1}}{V_{se1} + V_{bf}} + \frac{V_{se2}}{V_{se2} + V_{bf}}\right) \tag{11.12}$$

in which ψ_{se} is a given coefficient. Its suggested value is $\psi_{se} = 0.90$.

The friction contribution λ_{bf} is simply given by:

$$\lambda_{bf} = 1 - \lambda_{se} \tag{11.13}$$

Parameters λ_{se} and λ_{bf}, have been proposed in an approximate expression which is intended to weight the different force contributions considering the nonlinear response.

For $\psi_{se} = 1$, Equation (11.12) is simply the mean value of the superelastic force ratio at yielding and at design condition, i.e. the mean value in the nonlinear superelastic range. The ψ_{se} coefficient is intended to take into account in a simplified manner for the different relative weight in the range of displacement in which the superelastic yielding is not exceeded. Due to the recentering effect, the system response is often in this close-to-zero displacement range, in which most of the dissipation is demanded only to friction. Hence the ψ_{se} factor reduces the superelastic contribution and increases the friction one.

The condition already recognized in Equation (11.11), can be also expressed in terms of λ_{se} or λ_{bf}. The suggested relation is:

$$\lambda_{se} = \left(1 - \lambda_{bf}\right) \leq \frac{0.35}{\psi_{se}} \tag{11.14}$$

(b)   Isolation System Equivalent Hysteretic Damping

The two different isolation device shear force contributions are considered separately in the proposed expression to compute the equivalent hysteretic damping of the system. Considering the hysteretic area based approach for the damping estimation as suggested in Grant et al. [2005], Attanasi et al. [2009b] contains the expression to compute the equivalent damping as a function of the ductility. For the superelastic flag-shaped force-displacement relation, the expression is:

$$\xi_{se}(\mu) = \frac{\beta}{\pi}\frac{(\mu - 1)(1 - r_{se})}{\mu(1 + \mu r_{se} - r_{se})} \tag{11.15}$$

in which β is a measure of the dissipation capability of the flag-shaped relation. Referring to quantities in Figure 11.8 it can be defined as:

$$\beta = \frac{V_{se1} - V_{se4}}{V_{se1}} \tag{11.16}$$

and r_{se} is the system hardening, hence the second stiffness over initial stiffness ratio, i.e:

$$r_{se} = \frac{V_{se2} - V_{se1}}{u_2 - u_1} \frac{u_1}{V_{se1}} \tag{11.17}$$

Figure 11.9 reports the hysteretic damping-ductility relation for the flag-shaped force-displacement relation computed considering Equation (11.15) and the values $\beta = 0.70$ and $r_{se} = 0.20$.
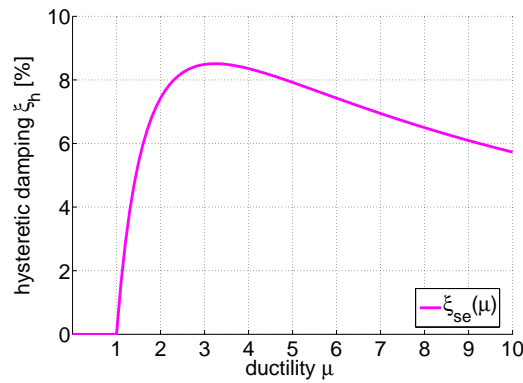
Figure 11.9. Hysteretic damping for flag-shaped force-displacement relation (from Equation (11.15))

The friction damping component is considered assuming that the hysteresis can be assimilated to a fictitious elastoplastic relation. For this one, in Grant *et al.* [2005] the damping expression is proposed. It has to be noted anyway that the friction device ductility is not the same ductility than the flag-shaped system. Obviously the fictitious yielding in the friction system occurs for a lower displacement than the flag-shaped hysteresis yielding point. Moreover, there is no point to consider the friction system ductility as an independent variable because it does not have any physical meaning. Therefore in the design procedure is suggested to consider as the isolation system ductility the superelastic restrainer ductility. The friction system ductility can be assumed to be ten times the system ductility. This is leading to good approximation considering superelastic device yielding displacement from 50 to 100 mm.
Based on the previous assumptions, the suggested expression for the friction component

as a function of the system ductility i.e. the superelastic device ductility, is:

$$\xi_{bf}(\mu) = \frac{2}{\pi} \frac{((10\mu)-1)\left(1-r_{bf}\right)}{(10\mu)\left(1+(10\mu)r_{bf}-r_{bf}\right)} \tag{11.18}$$

in which r_{bf} is the hardening coefficient of the elastoplastic relation. Considering $r_{bf} = 0$ i.e. relation elastic-perfectly plastic, Figure 11.10 reports the hysteretic damping-ductility relation for the flag-shaped force-displacement relation computed considering Equation (11.18). As expected the viscous damping tends to the maximum limit which is $\xi_h = 2/\pi$.
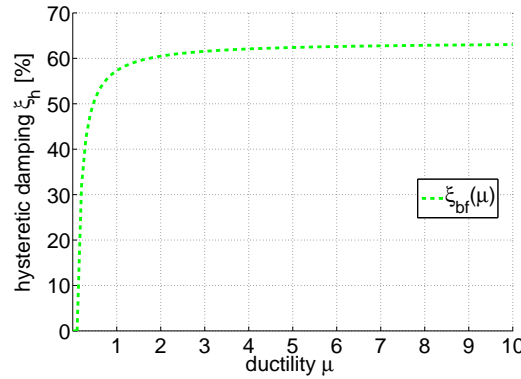
Figure 11.10. Hysteretic damping for friction elasto-plastic force-displacement relation (from Equation (11.18))

It is remarkable that given the previous assumptions the damping has non zero values for $\mu \geq 0.1$.

To combine together the superelastic and the friction hysteretic damping components the weighted sum is suggested using the contribution weights defined in Equation (11.12) and in Equation (11.13). Hence the final expression to estimate the SE isolation system damping is:

$$\xi_{is}(\mu) = \xi_{bf}(\mu)\lambda_{bf} + \xi_{se}(\mu)\lambda_{se} \tag{11.19}$$

In Figure 11.11 the separate weighted contributions are reported together with the system damping, assuming $\lambda_{se} = 0.70$ and $\lambda_{bf} = 0.30$. It is possible to note how the friction contribution, although weighted for a low contribution coefficient, is effective in significantly increase the system equivalent viscous damping. For usual ductility range of coil spring superelastic restraining device, i.e. from $\mu \simeq 3$ to $\mu \simeq 5$, and for the parameters considered in the previous plots, which are quite typical, the system hysteretic damping is $\xi_{is} \simeq 24\%$.
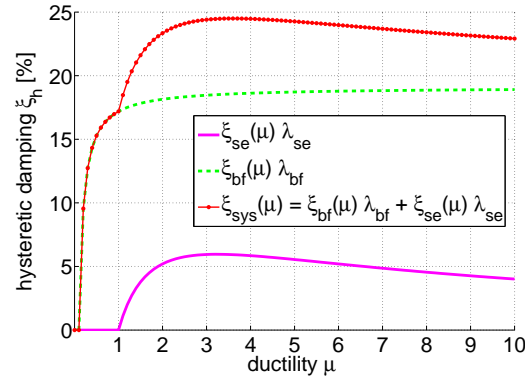
Figure 11.11. Hysteretic damping for SE isolation system device: superelastic, friction, and total system hysteretic damping

11.3.3   Design Provisions for Base Isolated Structures using Superelastic Devices

Based on contents of Section 11.3.1 and Section 11.3.2, the design provisions for base isolated structure using SE system are summarized in the present section.

- *Superstructure modeling.*
  The first assumption concerns the superstructure modeling, considering a *rigid* superstructure or a *flexible* superstructure.

  - Rigid case: this is the case in which the superstructure is very stiff with respect to the isolation system; the design choice means to consider it only as an additional mass on the isolation layer neglecting all its flexibility contributions; the total superstructure mass provides the value for the effective mass m_e and all the design displacement $\Delta_d = \Delta_{is}$ is supposed to occur at the isolation layer.

  - Flexible case: based on the damage level acceptable in the superstructure and on its structural system, an approximate displacement profile $\boldsymbol{\Delta}$ is assumed; referring to the displacement profile and to the seismic mass distribution in the superstructure it is possible to compute the system design displacement Δ_d (Equation (11.2)), the effective mass m_e (Equation (11.3)), and the equivalent height h_e (Equation (11.4)). The design displacement has to be shared between the isolation system and the superstructure according to the design assumption $\Delta_d = \Delta_{is} + \Delta_{ss}$.

- *Isolation Device Design.*
  From the design displacement demand in the isolation system, taking into account the ductility and force limitations, a suitable SE system is designed. The full hysteresis of the friction system and of the superelastic restraining system has to

be defined accordingly to provisions oriented to guarantee recentering (Equation (11.11) or Equation (11.14)).
The system ductility μ is computed as a ratio between the design displacement in the isolators Δ_{is} and the yielding displacement of the superelastic restrainer. The relative weight for the shear force contribution needs to be determined (Equation (11.12) and Equation (11.13)) to find the global SE system damping ξ_{is} according to Equation (11.19).

- *Equivalent SDOF Hysteretic Damping.*
  The global isolation system and superstructure damping ξ_{sys} is computed as a weighted sum of their displacement contribution (in case of rigid superstructure, its contribution is neglected).

- *Definition of the Reduced Design Spectra.*
  Based on the seismological conditions, a reduction coefficient is found (Equation (11.7)) to reduce the design 5% damping design spectra and get the design spectra relative to the considered hysteretic damping.

- *Computation of the Base Shear Force.*
  Considering the reduced spectra and the design displacement the base shear force is computed from Equation (11.10).

- *Isolation System and Superstructure Design.*
  The number of needed SE system is obtained assuming to share the base shear between the different isolators. The superstructure base shear is computed considering proper overstrength factors. Shear force and bending moment distribution in the superstructure is used for the member design.

11.4   Base Isolated System Design Example Comparison

To formalize the design procedure for the superelastic base isolation system, a design example is reported in the present section. The object of the design is a structure already presented in literature and for which a simulated base isolation design is available. The aim of the investigation is also to compare the design procedure and results considering traditional isolators and superelastic devices.

11.4.1   Building Properties and Expected Performance

The building we consider in the present work has been presented in Priestley *et al.* [2007] and it is reproposed here with some minor changes. The building is shown in plan in Figure 11.12 and it has $n_f = 6$ storeys with uniform storey height of $h_f = 2.8\text{m}$ and equal seismic floor weight of 3000kN at each level, including the roof. Plan building dimensions are reported in Figure 11.12. The structural system consists of four boundary walls, with
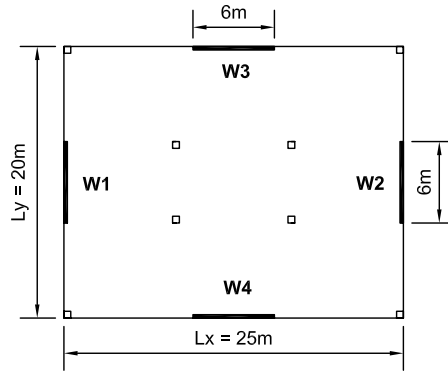
Figure 11.12. Design example building floor plan

internal columns and flat-slab floors which do not contribute significantly to the lateral resistance. In the original example the walls where different in length because the aim of the study was to evaluate the torsional eccentricity. In this context anyway, given the purpose of the investigation, the resisting walls are all of the same length, $l_w = 6\text{m}$. Specified material strength are $f_c' = 30\text{MPa}$ and $f_y = 420\text{MPa}$. Flexural reinforcing steel will be $d_{bl} = 20\text{mm}$ diameter with a steel elastic modulus $E_s = 200\text{GPa}$.

The isolation layer is supposed to be positioned between the foundation and the first slab (base isolation). The concept of isolation itself as discussed in Priestley *et al.* [2007], is based on the assumption that the superstructure responds elastically and that only the isolation system responds non-linearly and dissipates energy. As a consequence, in the design the superstructure is assumed to deform according its yield deformed shape and the maximum drift (which in a cantilever wall system occurs at the top floor) is limited to a value lower than the yielding drift.

Based on the material properties, the reinforcing steel yielding strain is:

$$\epsilon_y = \frac{f_{ye}}{E_s} = 2.31 \cdot 10^{-3} \tag{11.20}$$

being $f_{ye} = 1.1 f_y = 462\text{MPa}$ the steel expected yield stress. The wall yield curvature is then given as:

$$\varphi_y = \frac{2\epsilon_y}{l_w} = 7.7 \cdot 10^{-4} \; 1/\text{m} \tag{11.21}$$

estimating the strain penetration l_{sp} as

$$l_{sp} = 0.022 f_{ye} d_{bl} = 0.203\text{m} \tag{11.22}$$

the roof yielding displacement is:

$$\Delta_{y-roof} = \varphi_y \frac{\left(n_f \cdot h_f + l_{sp}\right)^2}{3} = 0.074 \text{m} \qquad (11.23)$$

In Figure 11.13a the superstructure displacement profile Δ_{y-ss} is shown. In 11.13b the interstorey drift distribution is reported when the top floor yields.

(a) displacement profile (Δ_{y-ss})   (b) interstorey drift
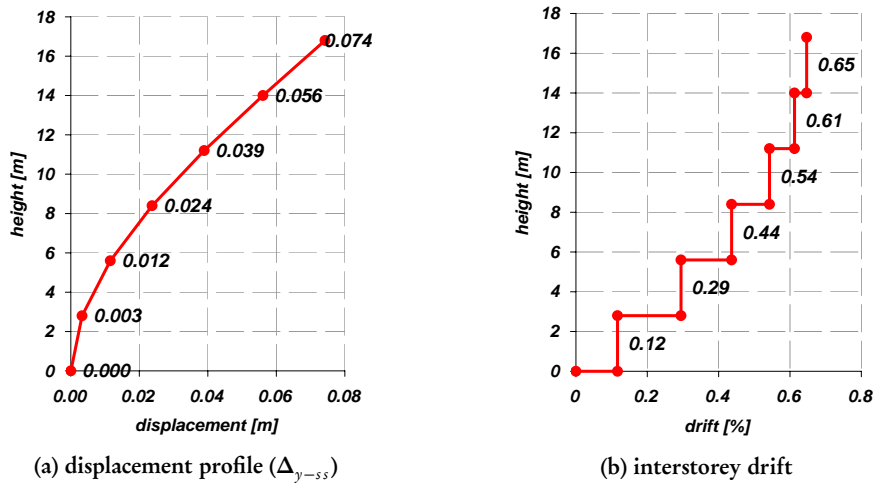
Figure 11.13. Superstructure yielding displacement and drift profiles

As in the design example in Priestley *et al.* [2007], the isolation system design displacement is $\Delta_{is} = 0.200$m. To capacity protect the superstructure, its design profile is the design profile at yielding scaled by a factor equal to 80%.

The global design displacement profile is therefore:

$$\Delta = \Delta_{is} + 0.80\Delta_{y-ss} \qquad (11.24)$$

The resulting design floor displacements are reported in Figure 11.14a, while the design interstorey drifts is in Figure 11.14b.

Given the design displacement profile Δ, using Equation (11.4), Equation (11.3), and Equation (11.2), the effective height h_e, the effective mass m_e, and the equivalent system design displacement Δ_d are computed and resulted:

$$
\begin{aligned}
h_e &= & 8.90 \text{ m} \\
m_e &= & 20820 \text{ kN/g} \\
\Delta_d &= & 0.221 \text{ m}
\end{aligned}
\qquad (11.25)
$$

The effective height h_e and the generalized displacement Δ_d are reported in Figure 11.14a as well.

(a) displacement profile (Δ) (b) interstorey drift
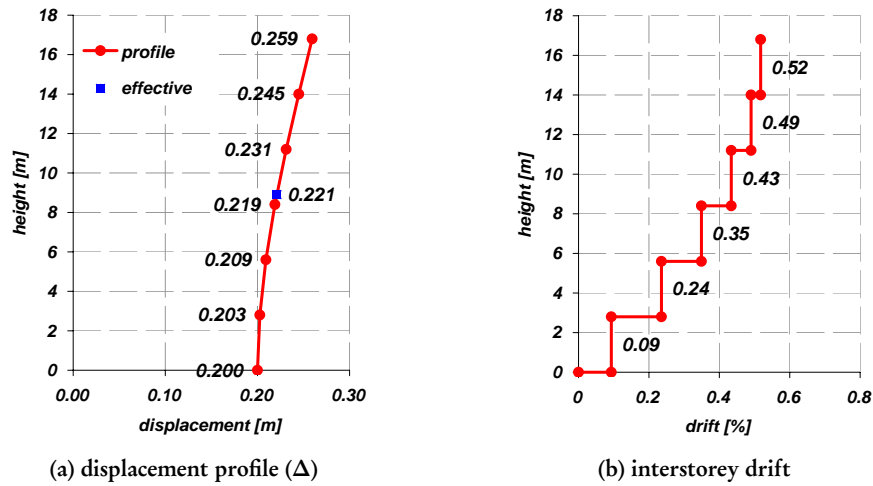
Figure 11.14. Isolation system and superstructure design displacement and drift profiles

11.4.2 Design Conditions

The structure is to be constructed in a region of high seismicity, corresponding to a PGA of 0.6g with the displacement-spectrum for the 5% damping given in Figure 11.15. Displacement reduction for damping conforms to Equation (11.7).
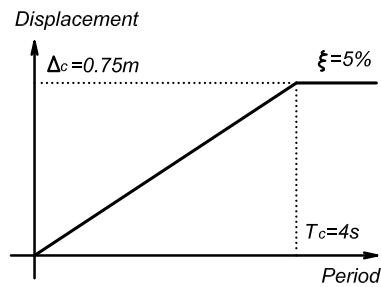
Figure 11.15. Design displacement spectra

The seismic design is performed both for the traditional and the superelastic isolation system either in a *far field* condition, and this is reported in Section 11.4.4 and Section 11.4.5, and in a *near fault* condition in which directivity velocity pulse characteristics might be expected, as reported in Section 11.4.6 and Section 11.4.7.

11.4.3   Superelastic Isolation Device Design

As a superelastic isolation device we refer to the SE system device configuration shown in Figure 11.1.

Using the simplified procedure described in Section 6.3.4 for the eight spring lateral restrainer system, the device design has been accomplished considering as a displacement capability $\Delta_{is} = 200$mm, and ensuring the capability to reach larger displacements without any strength loss.
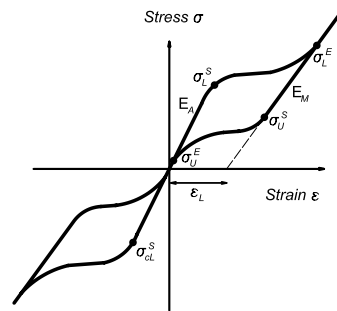
Figure 11.16. SMA superelastic uni-axial stress-strain

Table 11.1. SMA superelastic uni-axial stress-strain parameters

SMA superelastic					
$E_A \; [MPa]$	45000	$\sigma_L^S \; [MPa]$	600	$\sigma_U^E \; [MPa]$	200
$E_M \; [MPa]$	15000	$\sigma_L^E \; [MPa]$	800	$\sigma_{cL}^S \; [MPa]$	600
$\nu_A = \nu_M$	0.33	$\sigma_U^S \; [MPa]$	400	$\epsilon^L \; [-]$	0.05

The design has been checked with a finite element analysis (ABAQUS [2003]) referring to a model which has been validated in reproducing the superelastic spring response as reported in Chapter 5. For the device design and check, the material model shown in Figure 11.16 has been considered using the values reported in Table 11.1.

The final spring configuration is a pipe section with $d_w = 30$mm external diameter and $d_p = 20$mm internal diameter, $R = 50$mm coil radius, $h_s = 250$mm long, and and $n_c = 1.96$ coils for each spring. The hinged-fixed condition has been considered. In the analysis we assumed that the perimetric hinges does not limit the spring displacement even for displacement larger than the spring axis. Even if the design displacement is $\Delta_{is} = 200$mm the device response has been numerically checked till a displacement $\phi_{is}\Delta_{is} = 300$mm, being $\phi_{is} = 1.5$. The resulting superelastic system composed by eight springs in radial position is characterized by the response reported in Figure 11.17.
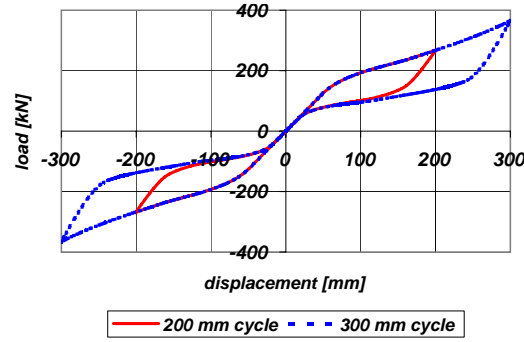
Figure 11.17. Superelastic restraining system shear force-lateral displacement response
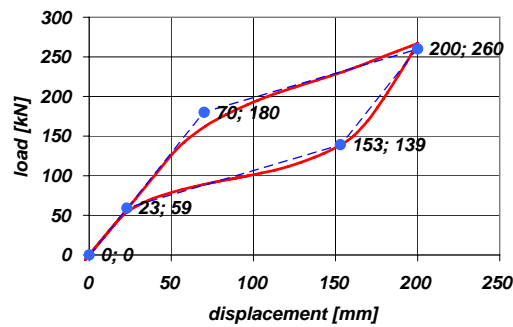
Figure 11.18. Superelastic restraining system response model

The shear force-lateral displacement relation for the radial spring system has been modeled in the structural analysis for the design and the verification of the global isolation system response as a flag-shaped hysteresis, like the one shown in Figure 11.8a. The matching between the superelastic response from analysis using finite elements ABAQUS [2003] and the corresponding flag-shaped model is reported in Figure 11.18. The SE isolation system response model parameters are then summarized in Table 11.2.

11.4.4 Far Field Seismic Design using LRB System

The isolation system design for the far field condition using lead rubber bearing isolators has been described for the given structure in Priestley *et al.* [2007]. The simulated design in the present work differs slightly from the original one because of the reduction factor formula. Here, Equation (11.7) is used because it is the formula proposed in CEN [2004], while in the previous design another expression was proposed. Moreover, in the present investigation the superstructure damping coefficient is assumed $\xi_{ss} = 1\%$, based on the

Table 11.2. Superelastic restraining system response model parameters

Isolation SE system Flag-shaped Model		
initial stiffness	k_0	2571.43 kN/m
hardening factor	r	0.239
secant stiffness	k_e	1300 kN/m
dissipation factor	β	0.67
yielding displacement	u_y	0.070 m
design ductility	μ	2.857
yielding force	V_y	180 kN
design force	V_d	260 kN

consideration that the superstructure is supposed to respond elastically and therefore its damping is negligible. In Priestley *et al.* [2007], a damping of $\xi_{ss} = 5\%$ was proposed.

(a)   Isolation System Design

From the previous investigation in Priestley *et al.* [2007], the resulting ideal shear force-lateral displacement of the isolation devices was the hysteresis reported in Figure 11.19 and the response parameters in Table 11.3. The global system hysteretic damping is
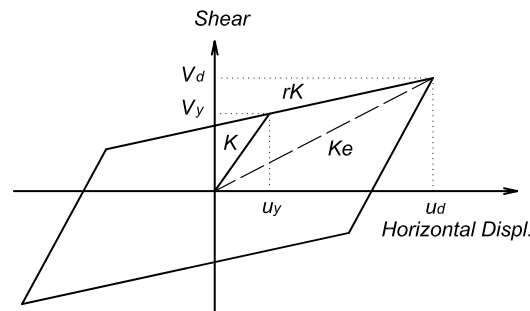
Figure 11.19. Ideal hysteresis for the design LRB (from Priestley *et al.* [2007])

estimated as:

$$\xi_{sys} = \frac{\Delta_{is}\xi_{is} + (\Delta_d - \Delta_{is})\xi_{ss}}{\Delta_d} =$$
$$= \frac{0.200 \cdot 26\% + (0.222 - 0.200) \cdot 1\%}{0.222} = 23.51\% \quad (11.26)$$

Table 11.3. LRB model parameters (as defined in Priestley *et al.* [2007])

LRB Isolators Elastoplastic Model		
initial stiffness	k_0	8636 kN/m
hardening factor	r	0.105
secant stiffness	k_e	1500 kN/m
yielding displacement	u_y	0.015 m
design ductility	μ	13.33
yielding force	V_y	133 kN
design force	V_d	300 kN
hysteretic damping	h_e	26 %

the reduction factor is:

$$R_\xi = \left(\frac{10}{5 + \xi_{sys}} \right)^{0.5} = 0.592 \tag{11.27}$$

and the corresponding effective period results:

$$T_e = \frac{\Delta_d T_c}{\Delta_c R_{xi}} = \frac{0.222 \cdot 4}{0.750 \cdot 0.592} = 2.00 \text{s} \tag{11.28}$$

the effective stiffness is:

$$K_e = \frac{4\pi^2 m_e}{T_e^2} = 20940 \text{kN/m} \tag{11.29}$$

hence the base shear is:

$$V_{base} = K_e \Delta_d = 4651 \text{kN} \tag{11.30}$$

To carry the base shear V_{base}, $n_{is} = 16$ isolators are to be positioned at the base of the building. The isolation system at the design displacement Δ_{is} is supposed to develop a shear force $V_d = 4800 kN = 103.2\% V_{base}$.

(b)   Cantilever Wall Design

As a function of the design displacement shape $\mathbf{\Delta}$, the design shear at the isolation level V_d is distributed at each floor level. The obtained distribution is shown for a single resisting wall as a *floor shear* (V_b) in Figure 11.20a. To capacity design the superstructure an overstrength factor of $\phi^o = 1.25$ is applied and the resulting *overstrength shear* ($\phi^o V_b$) is shown in Figure 11.20a as well. Then, relative bending moment distributions are reported in Figure 11.20b as *floor moment* (M_b) and *overstrength moment* ($\phi^o M_b$). To compute the

(a) shear force   (b) bending moment
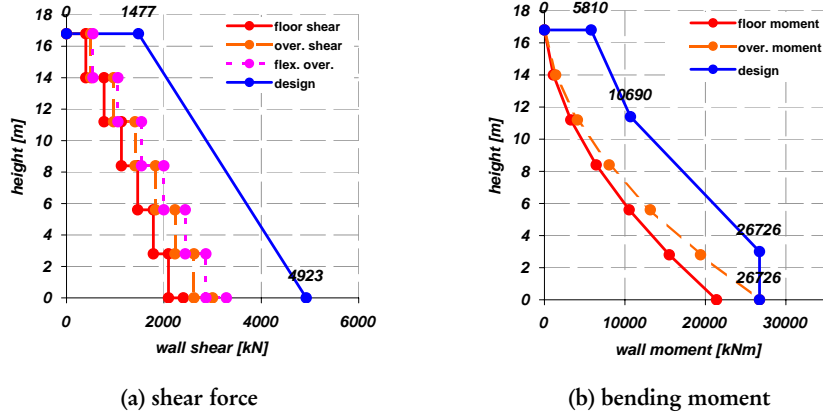
Figure 11.20. Far field EP system wall design actions

design moment capacity envelope, suggestions from Priestley *et al.* [2007] are considered. The mid-height moment results from:

$$M^o_{0.5H} = 0.4\phi^o M_b \tag{11.31}$$

A tension shift for a length equal to $l_w/2 = 3$m has then been considered. The design moment profile is also reported in Figure 11.20b.

Based on this, the flexural reinforcement has been computed considering the seismic axial load condition as well. In this case a total number $n_b = 68$ of $d_b = 20$mm longitudinal bars are used. 22 bars are positioned at each one of the two ends of the wall for a length 1.2m; the remaining reinforcement is positioned in the remaining wall portion 3.6m long. The resulting reinforcement ratio is $\rho_l = 1.42\%$, and the flexural section properties are shown in Figure 11.21. From the comparison between the design moment $\phi^o M_b$ at the base and the resisting moment, a flexural overstrength ratio $\phi^f = 1.09$ results. In Figure 11.20a the *flexural overstrength* shear value ($\phi^f \phi^o V_b$) is reported too.

The design shear capacity envelope is obtained considering the value $\omega_v \phi^f \phi^o V_b$ at the base, and the value $0.3\omega_v \phi^f \phi^o V_b$ at the wall top, being the dynamic amplification factor $\omega_v = 1.5$ computed according to expression in Paulay and Priestley [1992]. The resulting design shear profile is also reported in Figure 11.20a.

11.4.5   Far Field Seismic Design using SE System

The design of the isolation system and of the cantilever wall is performed in the same conditions reported in Section 11.4.4, but now considering the SE system.

(a) moment curvature

(b) interaction diagram

Figure 11.21. Far field EP system wall flexural capacity

(a) Isolation System Design

The superelastic restraining system described in Section 11.4.3 is assumed to be used for the SE system isolation device. Referring to variables defined in Figure 11.8a, for the present design, as reported in Figure 11.18, it resulted:

$$
\begin{array}{llll}
V_{se1} & = & 180 & \text{kN} \\
V_{se3} & = & 139 & \text{kN}
\end{array}
\qquad
\begin{array}{llll}
V_{se2} & = & 260 & \text{kN} \\
V_{se4} & = & 59 & \text{kN}
\end{array}
\tag{11.32}
$$

The friction slider design has to be performed. Its breakaway shear force V_{bf} is assumed as:

$$
V_{bf} = \frac{V_{se1}}{3} = 60\text{kN}
\tag{11.33}
$$

being $V_{bf} \simeq V_{se4}$, the condition from Equation (11.11) is satisfied. From Equation (11.12) and Equation (11.13) respectively:

$$
\begin{aligned}
\lambda_{se} & = & \frac{0.9}{2}\left(\frac{180}{180+60}+\frac{260}{260+60}\right)=0.70 \\
\lambda_{bf} & = & 0.30
\end{aligned}
\tag{11.34}
$$

The flag-shaped hysteretic damping component from Equation (11.15), computed considering parameters reported in Table 11.2, is:

$$
\xi_{se}(\mu=2.86)=\frac{0.67}{\pi}\frac{(2.86-1)(1-0.24)}{2.86(1+2.86\cdot0.24-0.24)}=7.3\%
\tag{11.35}
$$

while for the friction damping, Equation (11.18) considering $r_{bf} = 0.0$ leads to:

$$\xi_{bf}(\mu = 2.86) = \frac{2}{\pi} \frac{(10 \cdot 2.86 - 1)}{10 \cdot 2.86} = 61.4\% \tag{11.36}$$

hence the global isolation system damping from Equation (11.19) is:

$$\xi_{is}(\mu = 2.86) = 7.3\% \cdot 0.70 + 61.4\% \cdot 0.3 = 23.5\% \tag{11.37}$$

Still assuming that the superstructure responds elastically with only a 1% viscous damping contribution, the total structural equivalent damping is:

$$\xi_{sys} = \frac{\Delta_{is}\xi_{is} + (\Delta_d - \Delta_{is})\,\xi_{ss}}{\Delta_d} =$$
$$= \frac{0.200 \cdot 23.5\% + (0.222 - 0.200) \cdot 1\%}{0.222} = 21.3\% \tag{11.38}$$

the reduction factor is:

$$R_\xi = \left(\frac{10}{5 + \xi_{sys}}\right)^{0.5} = 0.617 \tag{11.39}$$

and the corresponding effective period is:

$$T_e = \frac{\Delta_d T_c}{\Delta_c R_{xi}} = \frac{0.222 \cdot 4}{0.750 \cdot 0.617} = 1.92\text{s} \tag{11.40}$$

the effective stiffness is:

$$K_e = \frac{4\pi^2 m_e}{T_e^2} = 22710\text{kN/m} \tag{11.41}$$

hence the base shear results:

$$V_{base} = K_e \Delta_d = 5043\text{kN} \tag{11.42}$$

To carry the shear V_{base}, $n_{is} = 16$ isolators are positioned at the base of the building. The isolation system at the design displacement Δ_{is} develops a shear force $V_d = 5120kN = 101.5\% V_{base}$.

(b)   Cantilever Wall Design

As a function of the design displacement shape $\mathbf{\Delta}$, the design shear and bending moment on the cantilever wall are reported in Figure 11.22. The overstrength and the dynamic amplification factors are the same than in Section 11.4.4: $\phi^o = 1.25$ and $\omega_v = 1.5$. At the end of the flexural design the flexural overstrength ratio resulted $\phi^f = 1.10$. In this case

(a) shear force   (b) bending moment
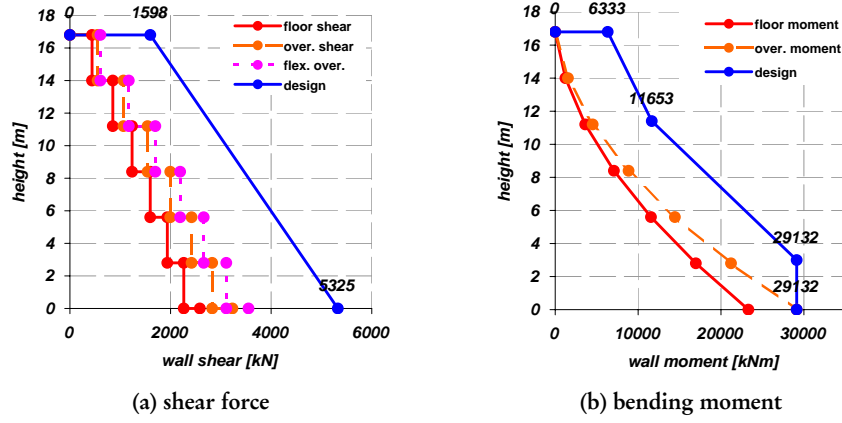
Figure 11.22. Far field SE system wall design actions

a total number $n_b = 76$ of $d_b = 20\text{mm}$ longitudinal bar are used. 26 bars are positioned at each one of the two ends of the wall for a length 1.2m; the remaining reinforcement is positioned in the remaining wall portion 3.6m long. The resulting reinforcement ratio is $\rho_l = 1.59\%$, and the section flexural properties are reported in Figure 11.23.

(a) moment curvature   (b) interaction diagram
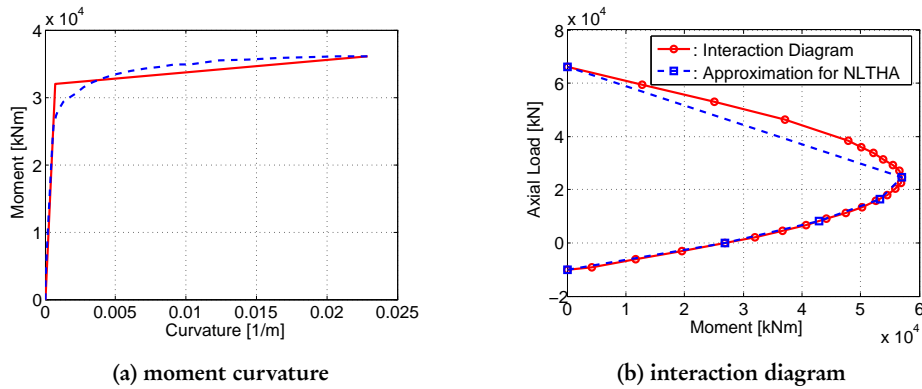
Figure 11.23. Far field SE system wall flexural capacity

11.4.6   Near Fault Seismic Design using LRB System

In the near fault design condition the same procedure with respect to Section 11.4.4 is followed. Also the same isolator configuration is used.

(a)   Isolation System Design

The system hysteretic damping is the same than in the case of Section 11.4.4, i.e.:

$$\xi_{sys} = 23.51\% \tag{11.43}$$

the difference is in the computation of the reduction factor, which turns out to be:

$$R_\xi = \left(\frac{10}{5 + \xi_{sys}}\right)^{0.25} = 0.77 \tag{11.44}$$

and the corresponding effective period is:

$$T_e = \frac{\Delta_d T_c}{\Delta_c R_{xi}} = \frac{0.222 \cdot 4}{0.750 \cdot 0.77} = 1.54\text{s} \tag{11.45}$$

the effective stiffness is:

$$K_e = \frac{4\pi^2 m_e}{T_e^2} = 36820\text{kN/m} \tag{11.46}$$

hence the base shear results:

$$V_{base} = K_e \Delta_d = 8178\text{kN} \tag{11.47}$$

The base shear V_{base}, is distributed between $n_{is} = 26$ isolators at the base of the building. The isolation system at the design displacement Δ_{is} is supposed to develop a shear force $V_d = 7800kN = 99.3\% V_{base}$. Even if this is a bit smaller than the design value, it is considered close enough to be acceptable.

(b)   Cantilever Wall Design

The design shear force and bending moment on the cantilever wall are reported in Figure 11.24. The overstrength and the dynamic amplification factors are the same than previous Section 11.4.4: $\phi^o = 1.25$ and $\omega_v = 1.5$. At the end of the flexural design the flexural overstrength ratio resulted $\phi^f = 1.16$.
In this case a total number $n_b = 136$ of $d_b = 20$mm longitudinal bar are used. 50 bars are positioned at each one of the two ends of the wall for a length 1.2m; the remaining reinforcement is positioned in the remaining wall portion 3.6m long. The resulting reinforcement ratio is $\rho_l = 2.85\%$, and the section properties are reported in Figure 11.25.

11.4.7   Near Fault Seismic Design using SE System

Finally, the near fault condition design has been performed also for SE system isolated building.

(a) shear force

(b) bending moment
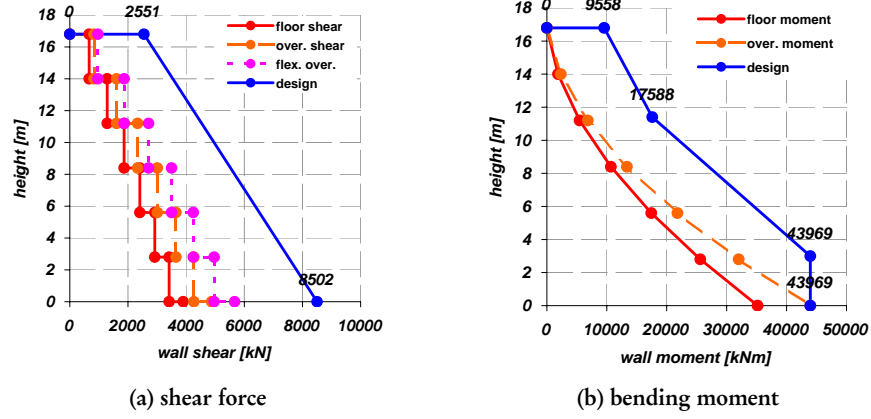
Figure 11.24. Near fault EP system wall design actions

(a) moment curvature

(b) interaction diagram
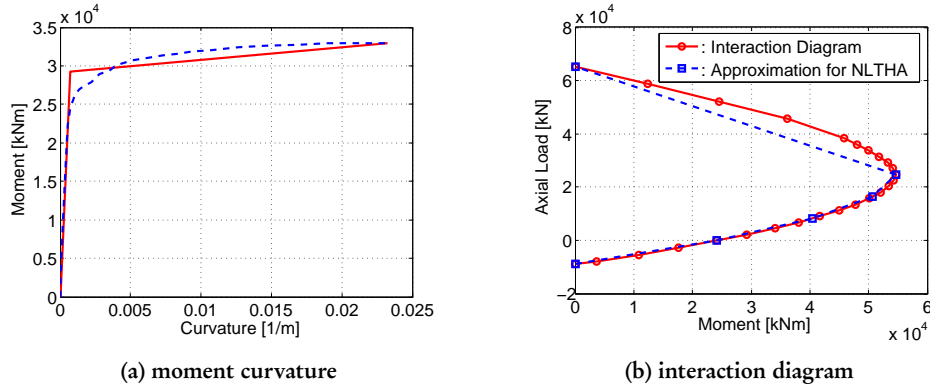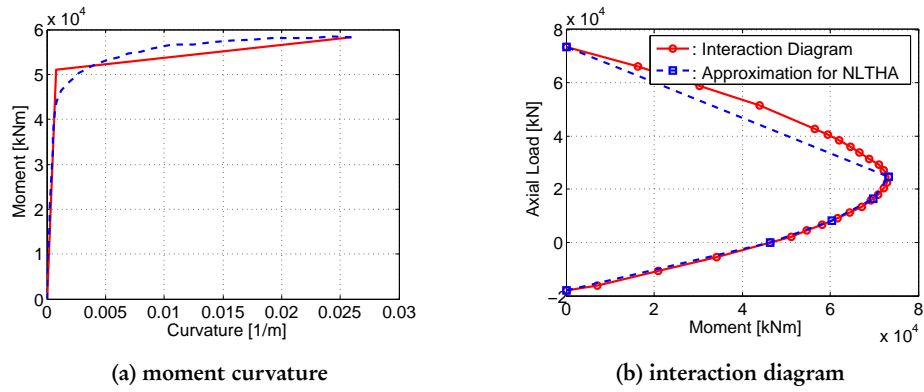
Figure 11.25. Near fault EP system wall flexural capacity

(a)   Isolation System Design

The same isolation system defined in Section 11.4.5 is used. The system hysteretic damping is the same than before:

$$\xi_{sys} = 21.3\% \tag{11.48}$$

while the reduction factor is:

$$R_\xi = \left(\frac{10}{5 + \xi_{sys}}\right)^{0.25} = 0.785 \tag{11.49}$$

and the corresponding effective period is:

$$T_e = \frac{\Delta_d T_c}{\Delta_c R_{xi}} = \frac{0.222 \cdot 4}{0.750 \cdot 0.785} = 1.51\text{s} \tag{11.50}$$

the effective stiffness is the same than in previous case of Section 11.4.6:

$$K_e = \frac{4\pi^2 m_e}{T_e^2} = 36820\text{kN/m} \tag{11.51}$$

as well as the base shear:

$$V_{base} = K_e \Delta_d = 8178\text{kN} \tag{11.52}$$

Again, $n_{is} = 26$ isolators are used. The isolation system design shear force is $V_d = 8320kN = 101.7\% V_{base}$.

(b) Cantilever Wall Design

The design shear and bending moment on the cantilever wall are reported in Figure 11.26. The overstrength and the dynamic amplification factors are the same than previous Section

(a) shear force (b) bending moment
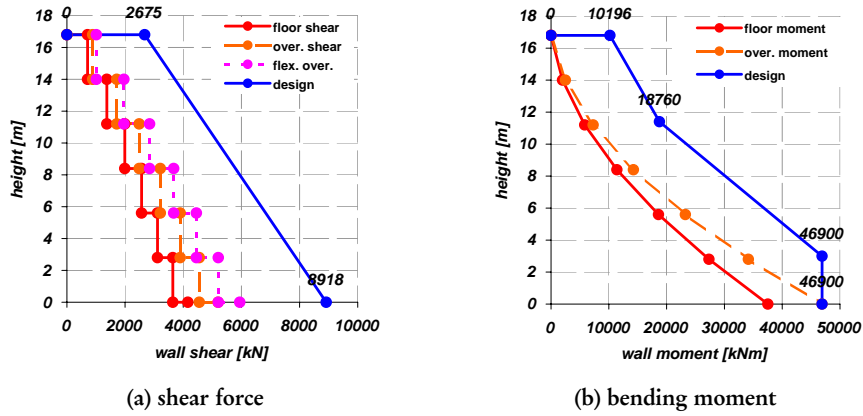
Figure 11.26. Near fault SE system wall design actions

11.4.5: $\phi^o = 1.25$ and $\omega_v = 1.5$. At the end of the flexural design the flexural overstrength ratio resulted $\phi^f = 1.14$.

In this case a total number $n_b = 148$ of $d_b = 20\text{mm}$ longitudinal bar are used. 50 bars are positioned at each one of the two ends of the wall for a length 1.2m; the remaining reinforcement is positioned in the remaining wall portion 3.6m long. The resulting reinforcement ratio is $\rho_l = 3.1\%$. This is a quite high reinforcement ratio, anyway it is

less than the maximum longitudinal reinforcement ratio for walls as suggested in Paulay and Priestley [1992]:

$$\frac{0.7}{f_y} \leq \rho_l \leq \frac{16}{f_y} = 3.8\% \tag{11.53}$$

The section properties are reported in Figure 11.27.

(a) moment curvature   (b) interaction diagram
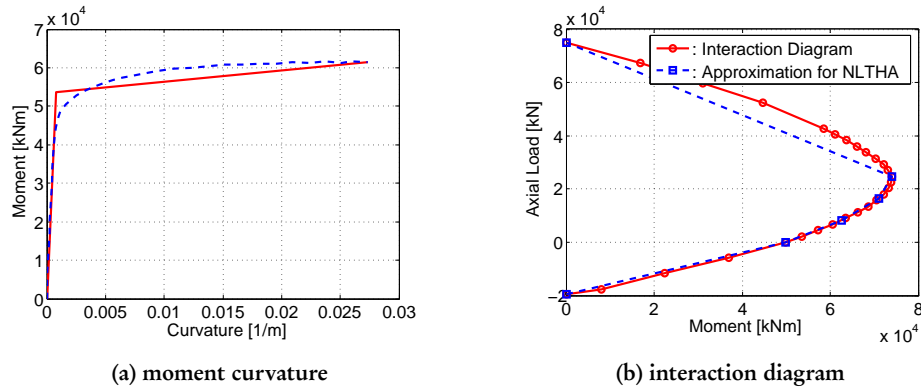
Figure 11.27. Near fault SE system wall flexural capacity

11.4.8 Conclusions on the Design Example Comparison

Four design procedure have been performed for the example structure. The result summary is reported in Table 11.4 for the far field condition and in Table 11.5 for the near fault condition.

Table 11.4. Design example summary for far field condition

Far Field Design Comparison						
System	Isolation Design				Wall Design	
	ξ_{sys}	R_ξ	V_{base}	n_{is}	$\phi^o M_b$	ρ_l	$\phi^o \phi^f V_b$
EP	23.51%	0.59	4651 kN	16	26.7 MNm	1.42%	4923 kN
SE	21.30%	0.62	5043 kN	16	29.1 MNm	1.59%	5325 kN
SE / EP	0.91	1.05	1.08	1.00	1.09	1.12	1.08

As a general conclusion, it can be noted that the system equivalent hysteretic damping is about the same, leading to a isolation system design which is very close. Even if the same number of isolators are used, being the ratio between design force in the SE system over the EP system about 1.07, there are some differences in the wall base design actions.

Table 11.5. Design example summary for near fault condition

Near Fault Design Comparison							
System	Isolation Design				Wall Design		
	ξ_{sys}	R_ξ	V_{base}	n_{is}	$\phi^o M_b$	ρ_l	$\phi^o \phi^f V_b$
EP	23.51%	0.77	8178 kN	26	44.0 MNm	2.85%	8502 kN
SE	21.30%	0.78	8178 kN	26	46.9 MNm	3.10%	8918 kN
SE / EP	0.91	1.01	1.00	1.00	1.07	1.09	1.05

Nevertheless differences are smaller than 10%, therefore the design of EP and SE system can be considered *equivalent*.

11.5 ISOLATED BUILDING DESIGN ASSESSMENT

The isolation system design results as performed in Section 11.4 are assessed in the present section using time history analysis.

11.5.1 Building Modeling

The nonlinear dynamic finite element program *Ruaumoko* (Carr [2007]) is used for the numerical simulation of the case-study structure. The model includes only one resisting wall (as shown in Figure 11.28a), taking advantage of the symmetry of the building in plan and assuming that the interaction with the gravity resisting frame is negligible. Torsional effects were not considered in the analyses. The seismic floor weight is assumed to be shared between the two resisting walls, therefore at each slab level one half of the floor mass is applied.

The wall inelastic response is concentrated in the plastic hinge S_{wall}, that can form at the base of the wall, as reported in Figure 11.28b. The inelastic flexural spring has been characterized in the different cases as a function of the longitudinal reinforcement and of the flexural strength provided in each design case. The wall flexural stiffness has been computed considering the moment curvature properties as reported in Figure 11.21a, Figure 11.23a, Figure 11.25a, and Figure 11.27a. The axial load-bending moment interaction relations in Figure 11.21b, Figure 11.23b, Figure 11.25b, and Figure 11.27b were used for the yielding surface definition. The plastic hinge inelastic response was modeled considering a *Takeda* model (Carr [2007]). The foundation is supposed to be rigid and the base node is restrained from vertical displacement and rotation.

The effect of the isolation system is reproduced through the lateral displacement activated spring, S_{isol} (see Figure 11.28b). In the EP system case, the isolation system shear force-lateral displacement response has been modeled considering an equivalent

(a) idealized resisting system   (b) finite element model
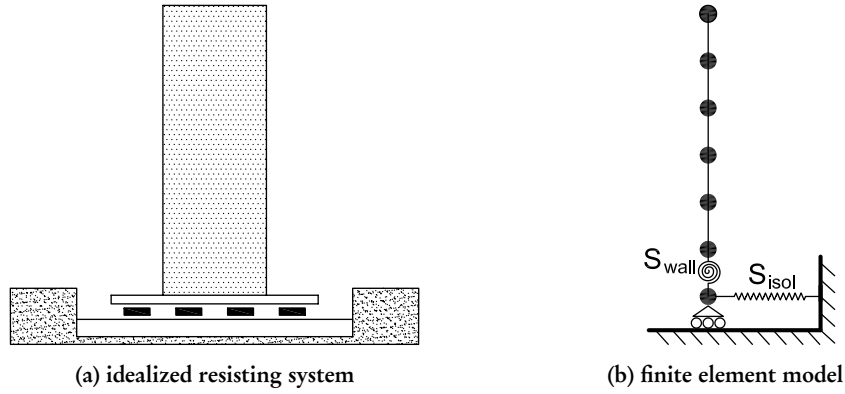
Figure 11.28. Finite element structural model

elastoplastic hysteresis as shown in Figure 11.19 and considering the parameters in Table 11.3. Obviously the effect of ($n_{is}/2$) elastoplastic isolators has been taken into account, being n_{is} different in the far field and near fault condition, and considering only one half of the total number of isolators because half of the building is investigated.

Modeling the SE system, the S_{isol} spring behavior results from the ($n_{is}/2$) contributions of the friction and of the superelastic component as reported in Figure 11.8, considering the final design values defined in Section 11.4.5. Concerning the friction rigid-plastic hysteresis, it is modeled considering a elastoplastic relation with very small hardening ($r_{bf} = 10^{-5}$) and yielding displacement $u_{bf} = 2$mm.

A *Rayleigh* damping proportional to the initial stiffness has been considered, fixing $\xi_{\omega 1} = 1\%$ at the first mode and $\xi_{\omega 2} = 3\%$ at the second mode. The very low first mode damping is based on the consideration that in the fundamental mode the dissipation is demanded to the isolator system and this is directly taken into account with nonlinear hysteresis. More important is the superstructure contribution in higher modes, hence a larger damping coefficient is considered. Nevertheless, due to the isolated building system, the participating mass in higher modes is almost negligible

11.5.2   Ground Motions for Numerical Analyses

Suites of earthquake ground motions from the *SAC* database (SAC [1997]) have been considered for the isolation bearing system response comparison evaluation. All the ground motions are natural records.

The design conditions were defined in terms of displacement spectra in Section 11.4.2. It turns out that the design condition spectra matches the mean displacement spectra from the original ground motion set as proposed in SAC [1997]. Hence the structure assessment has been performed considering the ground motion database without any further scaling procedure.

Two sets of records have been used:

- earthquake natural ground motions with 10% probability of exceedence in 50 years for the area of Los Angeles: 20 records, used to perform only the far field design condition assessment, whose properties are reported in Table 11.6;

- impulsive near-field earthquake ground motions: 12 records, used to perform only the near fault design condition assessment, whose properties are reported in Table 11.7.

Hence in total, 32 earthquake ground motions have considered for the analysis, 20 to assess the far field design and 12 for the near fault one.

(a)   Far Field Condition Ground Motions

The ground motion set used for the far field assessment is reported in Table 11.6. In SAC [1997] it was proposed already scaled and the amplitude is reported. The displacement spectra properties of this set compared with the design one are reported in Figure 11.29. The acceleration spectra are then shown in Figure 11.30.   Both the mean and the

(a) 5% damping displacement spectra (all record set)

(b) 5% damping displacement spectra (statistics)
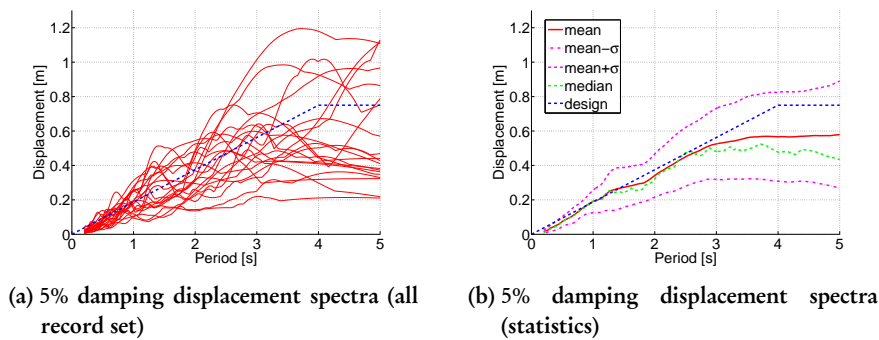
Figure 11.29. Far field ground motion records (from SAC [1997]) 5% damping displacement spectra compared with the design spectra

median displacement spectra matches the design conditions for period range larger than the effective period resulting in the simulated design. The ground motion set data is anyway characterized by a shorter corner period with respect to design spectra, around $T_c = 3$s.

(b)   Near Fault Condition Ground Motions

The ground motion set used for the near fault assessment is reported in Table 11.7. The original records are used, being the ground motion set for near fault condition proposed in SAC [1997] considering the recorded amplitude. The displacement spectra properties

Table 11.6. Characteristics of Los Angeles area compatible ground motions

#	SAC Name	Seismic Event			Recording Data		Scale Factor
		Magnitude	Year	Name	Station	Dist.(km)	
1	LA01	6.9	1940	El Centro	Imperial Valley	10	2.01
2	LA02	6.9	1940	El Centro	Imperial Valley	10	2.01
3	LA03	6.5	1979	Imperial Valley	El C. array 5	4.1	1.01
4	LA04	6.5	1979	Imperial Valley	El C. array 5	4.1	1.01
5	LA05	6.5	1979	Imperial Valley	El C. array 6	1.2	0.84
6	LA06	6.5	1979	Imperial Valley	El C. array 6	1.2	0.84
7	LA07	7.3	1992	Landers	Barstow	36	3.20
8	LA08	7.3	1992	Landers	Barstow	36	3.20
9	LA09	7.3	1992	Landers	Yermo	25	2.17
10	LA10	7.3	1992	Landers	Yermo	25	2.17
11	LA11	7.0	1989	Loma Prieta	Gilroy	12	1.79
12	LA12	7.0	1989	Loma Prieta	Gilroy	12	1.79
13	LA15	6.7	1994	Northridge	Rinaldi RS	7.5	1.03
14	LA16	6.7	1994	Northridge	Rinaldi RS	7.5	1.03
15	LA17	6.7	1994	Northridge	Sylmar	6.4	0.79
16	LA18	6.7	1994	Northridge	Sylmar	6.4	0.79
17	LA19	6.0	1986	North Palm	Spring	6.7	0.99
18	LA20	6.0	1986	North Palm	Spring	6.7	0.99
19	LA13	6.7	1994	Northridge	Newhall	6.7	2.97
20	LA14	6.7	1994	Northridge	Newhall	6.7	2.97
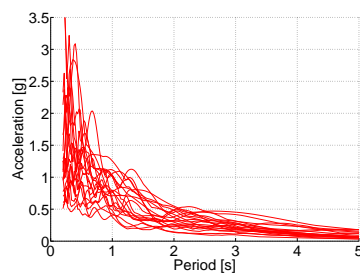
(a) 5% damping acceleration spectra (all record set)
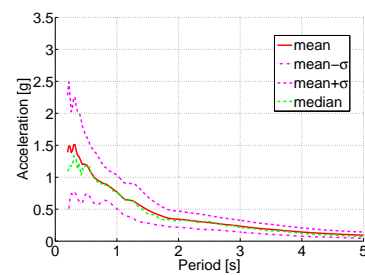
(b) 5% damping acceleration spectra (statistics)

Figure 11.30. Far field ground motion records (from SAC [1997]) 5% damping acceleration spectra

Table 11.7. Characteristics of impulsive near-field earthquake ground motions

#	SAC Name	Seismic Event			Recording Data		Scale Factor
		Magnitude	Year	Name	Station	Dist.(km)	
21	NF01	7.4	1978	Tabas		1.2	1.00
22	NF02	7.4	1978	Tabas		1.2	1.00
23	NF09	6.7	1992	Erzican		2.0	1.00
24	NF10	6.7	1992	Erzican		2.0	1.00
25	NF11	7.3	1979	Landers		1.1	1.00
26	NF12	7.3	1979	Landers		1.1	1.00
27	NF13	6.7	1994	Nothridge	Rinaldi	7.5	1.00
28	NF14	6.7	1994	Nothridge	Rinaldi	7.5	1.00
29	NF15	6.7	1994	Nothridge	Olive View	6.4	1.00
30	NF16	6.7	1994	Nothridge	Olive View	6.4	1.00
31	NF19	6.9	1995	Kobe	Takatori	4.3	1.00
32	NF20	6.9	1995	Kobe	Takatori	4.3	1.00

of this set compared with the design one are reported in Figure 11.31. The acceleration spectra are then shown in Figure 11.32.

The ground motion set used to evaluate the near fault condition is characterized by a

(a) 5% damping displacement spectra (all record set)

(b) 5% damping displacement spectra (statistics)
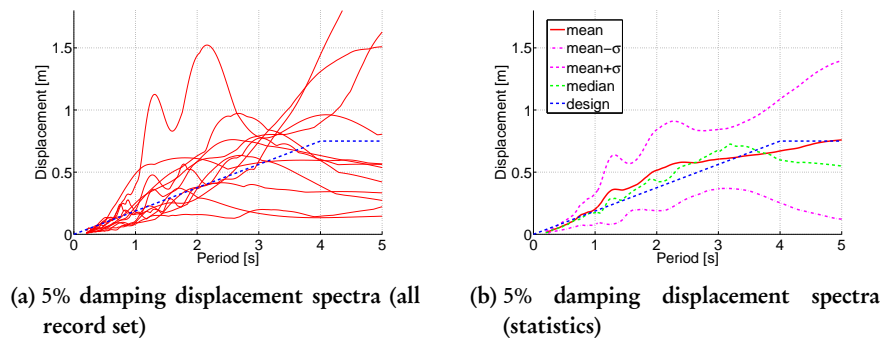
Figure 11.31. Near fault ground motion records (from SAC [1997]) 5% damping displacement spectra compared with the design spectra

spectral displacement demand a bit larger both in terms of mean and median values than the design one. Moreover the corner period is close to the design condition $T_c = 4\text{s}$. The standard deviation with respect to the records of the far field design condition is anyway a bit larger. Because of the previous, we expect a response in general more severe in this design condition both in terms of isolation system response and in terms of superstructure

(a) 5% damping acceleration spectra (all record set)

(b) 5% damping acceleration spectra (statistics)
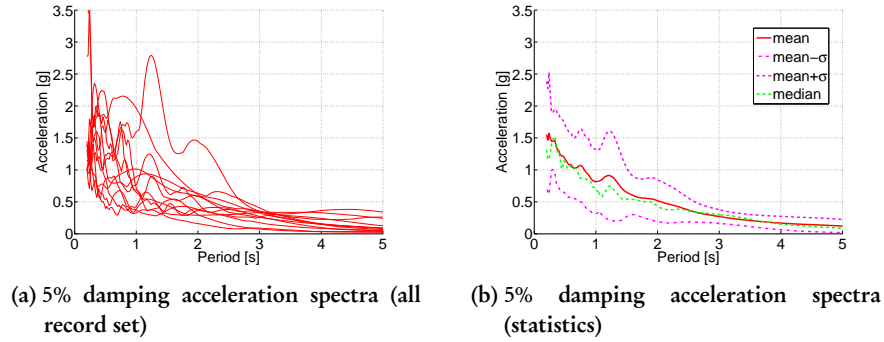
Figure 11.32. Near fault ground motion records (from SAC [1997]) 5% damping acceleration spectra

demand.

11.5.3   Far Field Design Assessment and Result Comparison

The far field condition design considering EP system as reported in Section 11.4.4 and considering SE system as reported in Section 11.4.5 has been compared considering the ground motion set in Table 11.4.

(a)   Isolation System Response

The isolation system response is compared in the present section.

Two examples of the resulting hysteresis from two time history analyses are reported in Figure 11.33. In the same plot the EP system and the SE system response are shown and the main hysteretic properties can be identified and compared. The EP system response is large and dissipative, but its maximum theoretical residual displacement can be of the same order of magnitude than the maximum displacement. On the other side, the SE system design has been accomplished consistently with the balancing of the friction force with respect to the superelastic force to reduce residuals. Consequently, the maximum residual displacement is $\Delta_R \simeq 20$mm, i.e. $\Delta_R \simeq 10\%\Delta_{is}$, and this regardless the maximum displacement demand, if it is larger than Δ_R.

Being the EP and SE system designed for the same design shear at the design displacement $\Delta_{is} = 200$mm, and therefore being the two of them characterized by the same secant stiffness, in Figure 11.33 the different stiffness in the two system can be analyzed. The SE system loading backbone curve is trilinear, characterized by a very high initial stiffness before the breakaway force is reached, by a large stiffness before the superelastic restrainer yielding, and then a quite low stiffness hardening to the design displacement. On the other side, the EP system is bilinear, yielding at a force lever lower than the SE system, but characterized by a larger hardening. Hence in the SE system the initial high stiffness and

(a) LA03 (ground motion #3)   (b) LA14 (ground motion #20)
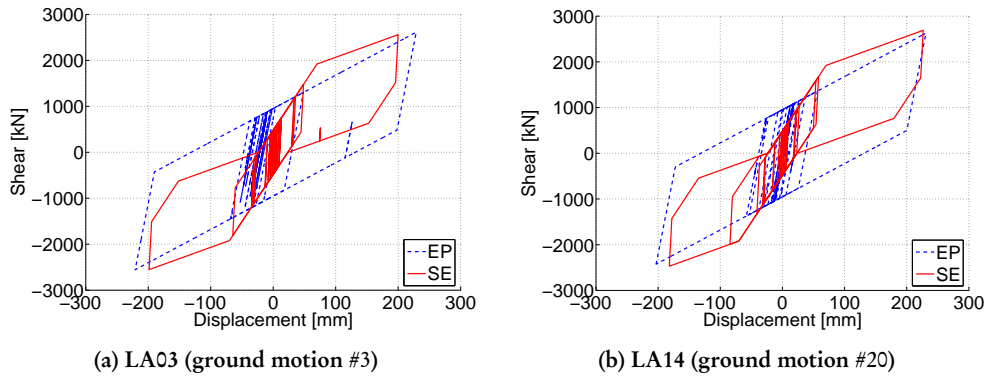
Figure 11.33. Isolation system force-displacement response example

the higher yielding force level are supposed to control the initial displacement very well. On the other side, the low hardening ratio is a less effective restrainer to large displacement demands but it controls the maximum force level in the device.

Finally, looking again at Figure 11.33, it can be concluded that for the design displacement level, if the SE system component design has been performed properly, its theoretical hysteretic damping is very close to the EP system one, taking advantage of the SE lower hardening and its larger yielding force. Moreover, the numerical tests proved that the effectiveness of the SE system is related to the modification of the displacement history. The superelastic device response is characterized by the largest velocity content, related to the recentering effect. In fact, in Figure 11.33a some oscillations around a non-zero displacement point are reported in the EP response, corresponding to zero displacement centered oscillations in the SE system.

(a) lateral displacement   (b) shear force
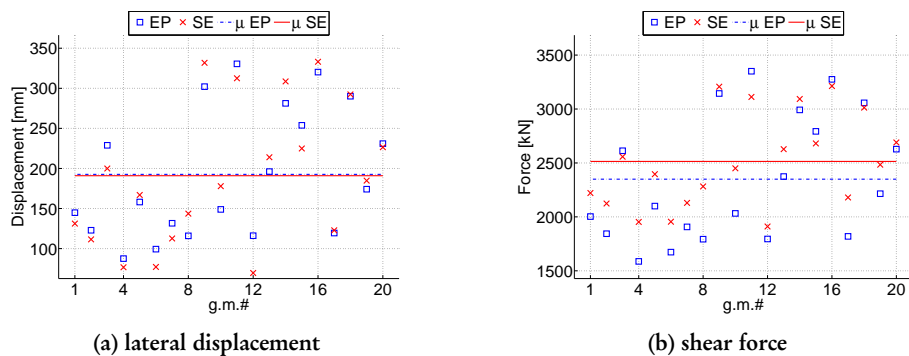
Figure 11.34. Isolation system ground motion set demand envelopes and mean values

(a) lateral displacement   (b) shear force
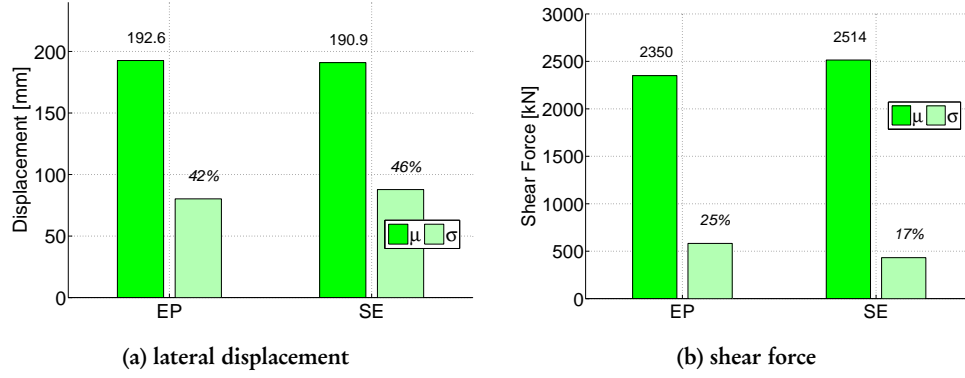
Figure 11.35. Isolation system mean and standard deviation demand envelopes: mean values and coefficient of variation are reported

A global view on the isolation system response is provided in Figure 11.34, in which for all the far field ground motion set the isolation system displacement demand (Figure 11.34a) and shear force demand (Figure 11.34b) are reported. The mean values over all the ground motion set is provided either in Figure 11.34 and in Figure 11.35, in which also the standard deviation and the coefficient of variations are reported for the displacement and the force demands.

As a general comment, it can be seen that the isolation system mean displacement is consistent with the design displacement. Being the mean displacement demand in the EP system Δ_{ep}:

$$\Delta_{ep} = 96.3\%\Delta_{is} \tag{11.54}$$

and considering the mean displacement demand in the SE system Δ_{se}:

$$\Delta_{se} = 95.4\%\Delta_{is} \tag{11.55}$$

Concerning the shear force demand in the isolation system, recalling that the model takes into account only one half of the entire building, the mean shear demand in the EP system V_{ep}:

$$V_{ep} = 97.9\%V_d/2 \tag{11.56}$$

recalling the $V_d = 2400$kN, as reported in Section 11.4.4. In the SE system the shear demand V_{se}:

$$V_{se} = 98.2\%V_d/2 \tag{11.57}$$

being in this case $V_d = 2560$kN as in Section 11.4.5.

Comparing the coefficients of variation, Figure 11.35 shows that the SE system standard deviation is larger in terms of displacement and smaller in terms of force with respect to

the EP system. This is ascribed to the SE system small final hardening effective in limiting the shear force but not effective in controlling the displacement demand.

(b)   Superstructure Response

The superstructure response is then assessed considering the time history analysis response.

The cantilever wall relative displacement profile envelopes are shown for all the ground

(a) EP system   (b) SE system
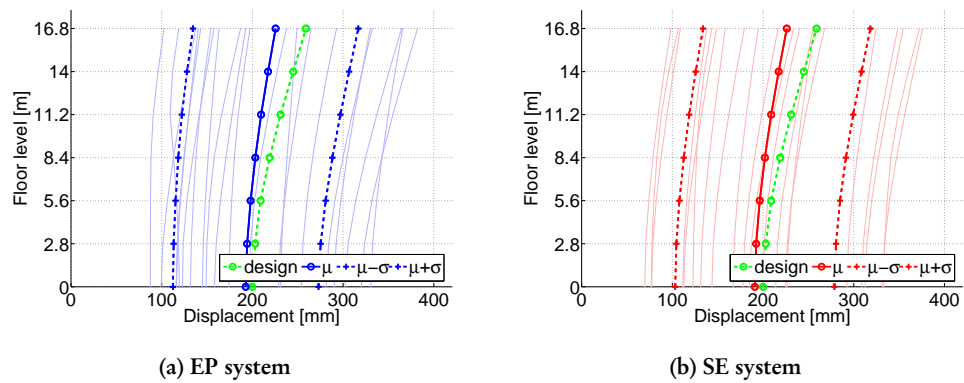
Figure 11.36. Storey displacement envelope

(a) EP system   (b) SE system
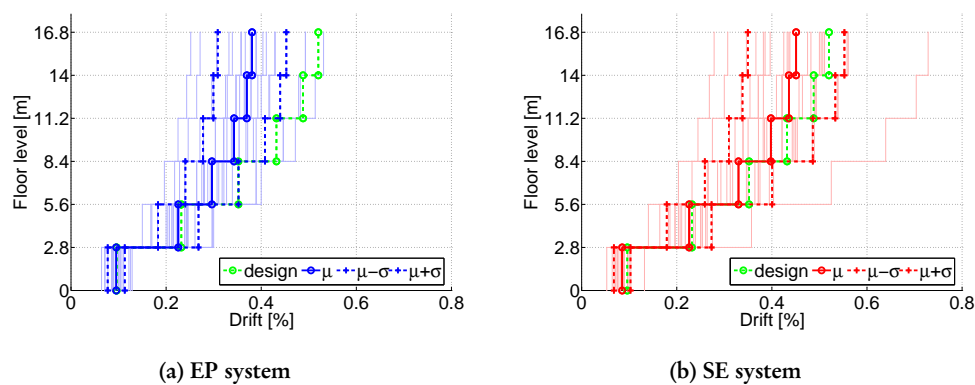
Figure 11.37. Interstorey drift demand

motions in Figure 11.36. EP system response (in Figure 11.36a) and SE system response (in

(a) EP system   (b) SE system
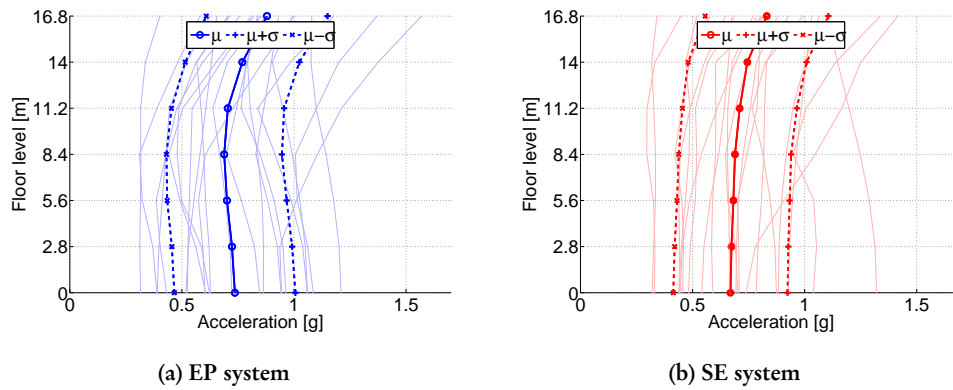
Figure 11.38. Storey acceleration demand

Figure 11.36b) are reported compared with the design displacement profile. Mean results are in the same plot, together with mean plus and minus a standard deviation. In general, the mean displacement SE system and EP system envelopes are very close and they are smaller than the design value. The standard deviation values are very close too.

A more important parameter to identify the structural damage is the interstorey drift. The superstructure design has been performed considering the design drift profile, reported together with the drift envelopes in Figure 11.37. The drift limit was fixed to avoid the superstructure inelastic response. It can be seen that the design condition is respected considering the mean values for both the EP and SE systems. Nevertheless, the SE system is closer to the design condition and its mean plus a standard deviation value exceeds the limit. This is due to the effect on the mean and standard deviation from a particular ground motion response characterized by a maximum drift demand of the order of 0.70%.
The mean drift value for all the floor levels and the relative standard deviation and coefficient of variations are reported for the EP and SE systems in Figure 11.39a. These values have to be compared with the drift computed at yielding which is 0.65% and the maximum design drift which is 0.52%. Both the isolation systems respect in mean the design condition. Being the SE system demand more severe, it also provides a more rational superstructural response, closer to the design condition.

As an important index for the non-structural damage, the floor acceleration has been computed at the different floor levels. Absolute acceleration envelopes are reported in Figure 11.38 for all the ground motions and their mean values and basic statistical properties are proposed in Figure 11.39b as well. Even if the coefficient of variation values
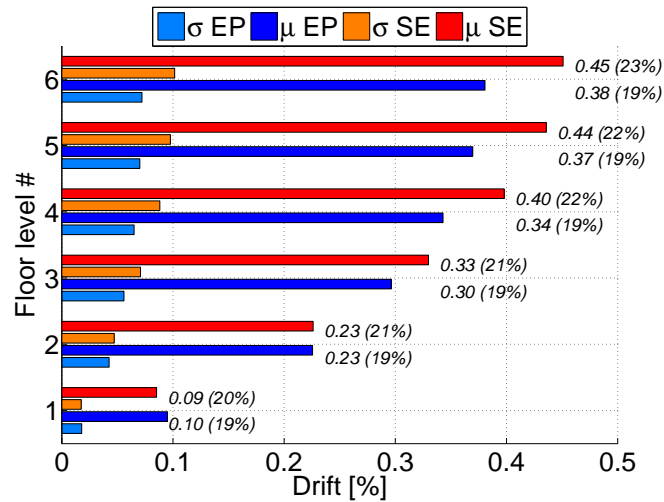
(a) interstorey drift demand comparison
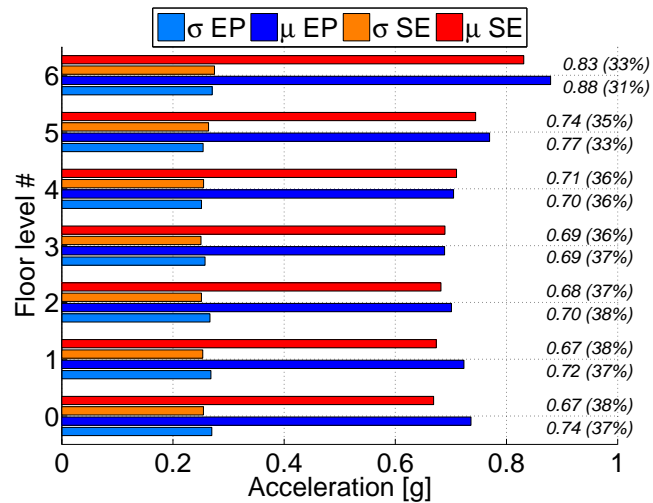
(b) floor acceleration demand comparison

Figure 11.39. Superstructure response comparison: mean values and standard deviation of interstorey drift and floor acceleration

are quite high in this case, being of the order of one third, the mean values do not differ very much between the EP and the SE systems and are lower than 0.9g. Hence we can conclude that no significative non-structural damage differences are expected changing one isolation system to the other in far field conditions.

(a) EP system   (b) SE system
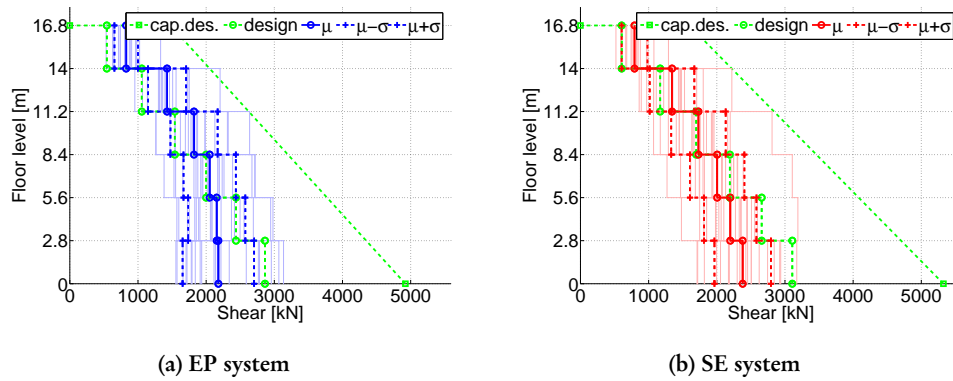
Figure 11.40. Wall shear envelope

(a) EP system   (b) SE system
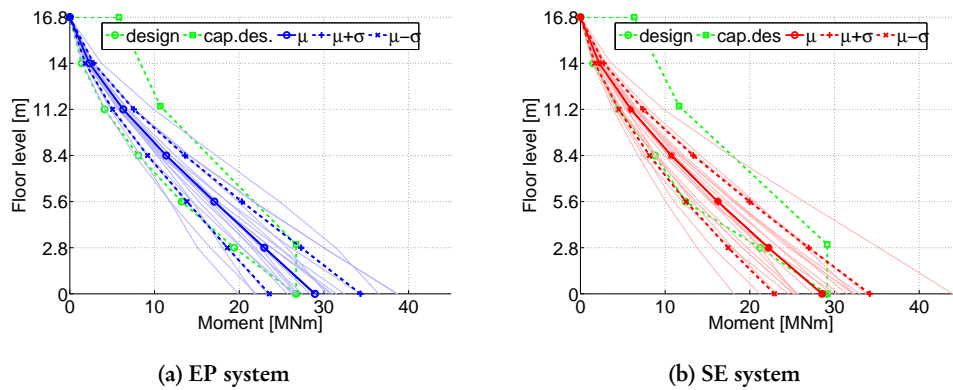
Figure 11.41. Wall moment envelope

The wall shear force envelopes are reported in Figure 11.40, compared with the design profile and with the capacity design profile which it is supposed to be used to dimensioning the reinforcement. It turns out that the mean shear demand exceeds the design values at the top floors both when the EP system and when the SE system are considered. Nevertheless the capacity design values are larger than the most severe ground motion demands, so the design check is verified. Considering the shear force mean values and statistics reported in Figure 11.42a, the floor shear demand considering the two isolation systems is about the same with exception of the first floor. The difference is due to the larger isolation design shear force the SE system; difference is anyway smaller than the 10% of the total value.

Bending moment envelopes are then reported in Figure 11.41. In this case it can be noted
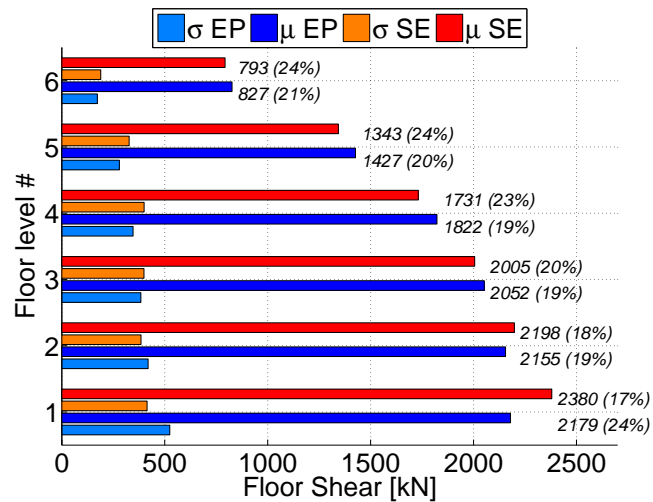
(a) shear force
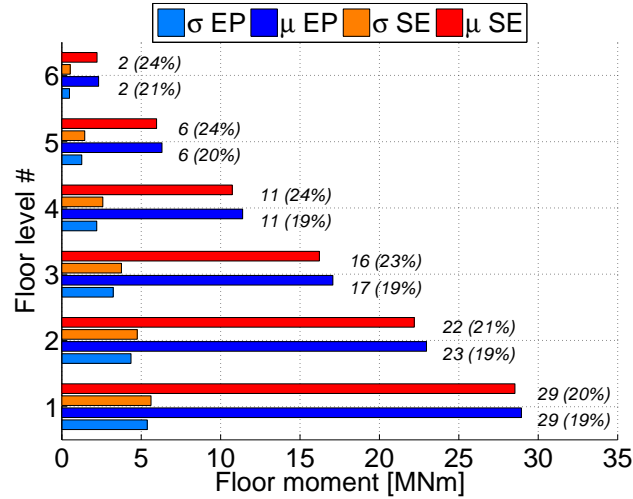
(b) bending moment

Figure 11.42. Wall bending moment and shear force comparison

that several ground motions cause a base moment which is larger than the design one, even significantly larger. In particular, the EP system mean base bending moment exceeds the design condition. The SE system mean demand is about the same with respect to the

previous system, as reported also in the comparison in Figure 11.42b. Nevertheless, due to the larger design bending moment, the mean values does not exceed the design values.
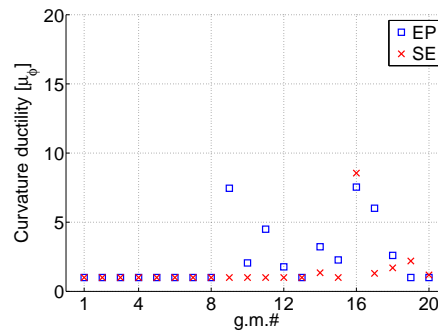
Figure 11.43. Maximum curvature ductility demand at the wall plastic hinge

The comparison of the maximum curvature ductility in the wall plastic hinge has been performed too. It is reported in Figure 11.43. As expected, the number of cases in which the EP system wall exceeds its elastic limit is larger than cases in SE system. Moreover, the mean curvature ductility in SE system is smaller. Nevertheless the plastic occurrences are few and the ductility demand is far away from the wall maximum ductility capacity as reported in Figure 11.21a and in Figure 11.23a.

11.5.4   Near Fault Design Assessment and Result Comparison

The near fault condition design considering the EP system as reported in Section 11.4.6 and the SE system as resulting from Section 11.4.7 has been assessed through time history analyses considering the ground motion set reported in Table 11.7. In the present section the main results concerning the isolation system response and the superstructure behavior are summarized.

(a)   Isolation System Response

(a) NF01 (ground motion #21)   (b) NF09 (ground motion #23)
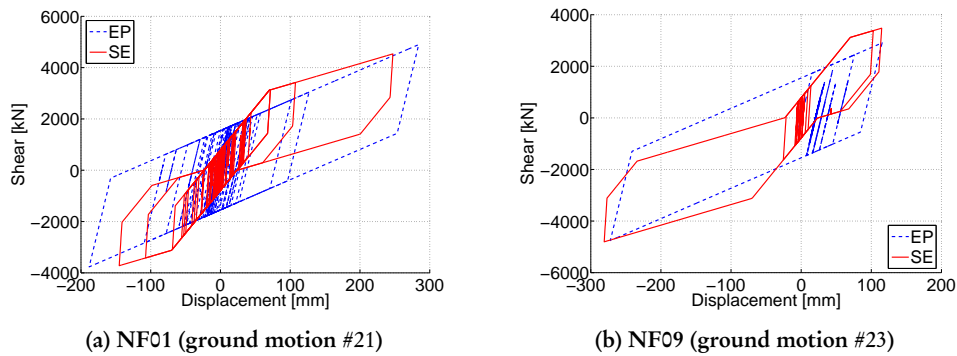
Figure 11.44. Isolation system force-displacement response example

(a) lateral displacement   (b) shear force
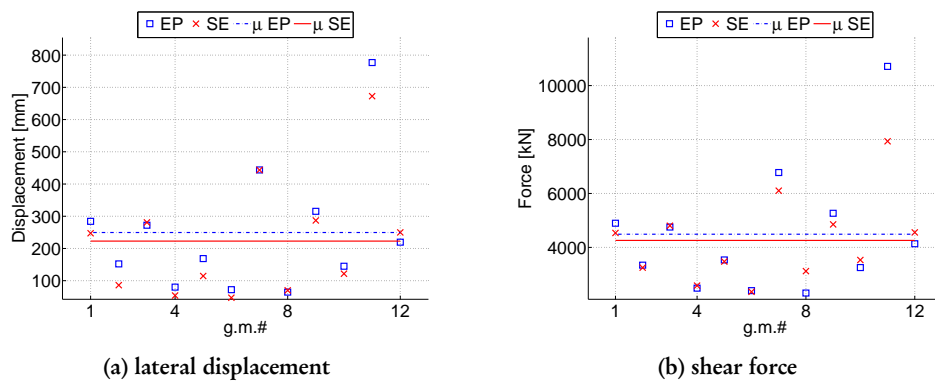
Figure 11.45. Isolation system ground motion set demand envelopes and mean values

The near fault ground motion set is generally characterized by a particular velocity content typical of impulsive strong motion records. Hence, the isolation system response can be characterized by large and asymmetric response.

Two hysteretic response examples are reported in Figure 11.44 and the pulse response is

(a) lateral displacement (statistics over 12 records)

(b) shear force (statistics over 12 records)

(c) lateral displacement (statistics over 10 records)

(d) shear force (statistic over 10 records)
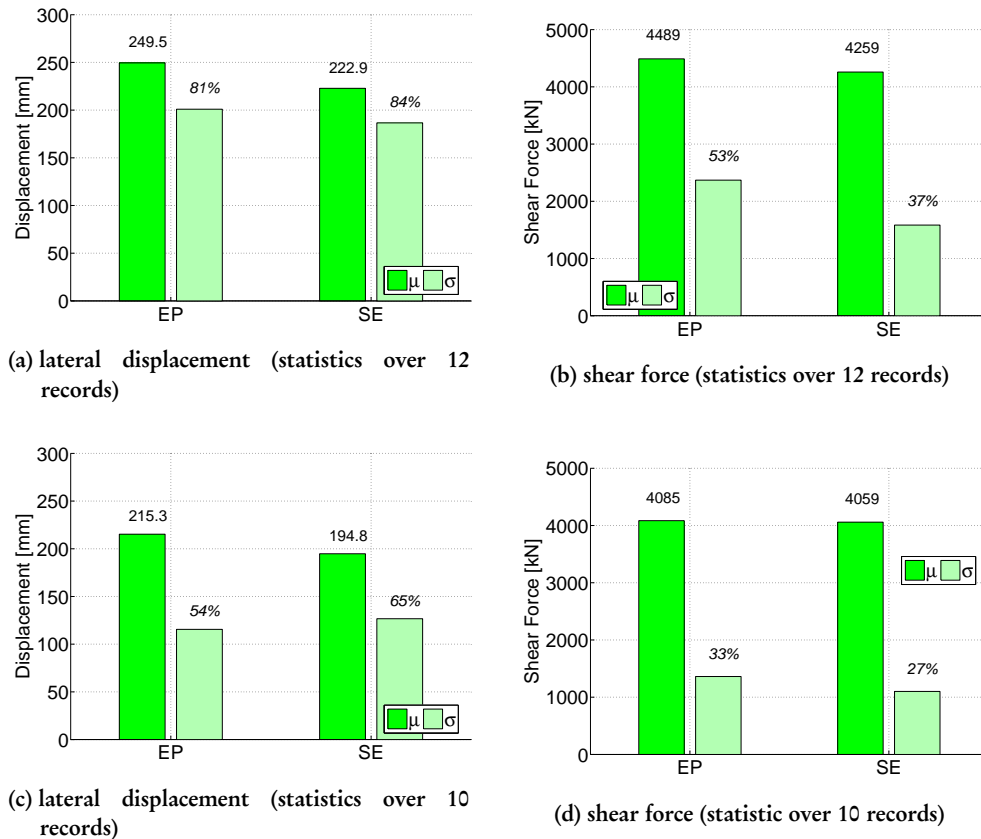
Figure 11.46. Isolation system mean and standard deviation demand envelopes: mean values and coefficient of variation are reported

evident, especially in Figure 11.44b which shows a particular case in which the design displacement is exceeded. In the near fault condition the recentering effect provided by SE system is particularly useful, record pulses producing large residual displacements in non-recentering devices.

The global overview on the isolations system response is provided in Figure 11.45 for all the ground motion set in terms of displacement (in Figure 11.45a) and in terms of shear force (in Figure 11.45b). In the same plots the mean displacement and force demand are reported as well. It can be seen that the near fault ground motion results are characterized by a large scatter. In particular a single ground motion is very severe, both in terms of displacement and force demand, and this is the record #11.

For this reason, the mean value and the standard deviation are computed in terms of

displacement and force either considering the 12 ground motions, but also referring to only 10 ground motions and deleting from the statics the most severe record (ground motion #11) and the less demanding (which has been considered the record #8 for the EP system and the record #4 for the SE system). The statistics over the entire ground motion set are reported in Figure 11.46a and Figure 11.46b in terms of displacement and force respectively. The same statistics but considering only the reduced ground motion set, composed by 10 records, are then reported in Figure 11.46c and Figure 11.46d. The reduced record set is very effective in decreasing the scatter. This is proved by the standard deviation comparison between Figure 11.46a and Figure 11.46c and between Figure 11.46b and Figure 11.46d.

If we compare the mean displacement and force demand based on the entire record set, the design values are exceeded both in terms of displacement and force. Being the mean displacement demand in the EP system Δ_{ep-12}:

$$\Delta_{ep-12} = 124.7\%\Delta_{is} \tag{11.58}$$

and considering the mean displacement demand in the SE system Δ_{se-12}:

$$\Delta_{se-12} = 111.4\%\Delta_{is} \tag{11.59}$$

Concerning the shear force demand in the isolation system, recalling that the model takes into account only one half of the entire building, the mean shear demand in the EP system V_{ep-12}:

$$V_{ep-12} = 115.1\%V_d/2 \tag{11.60}$$

recalling the $V_d = 3900\text{kN}$, as in Section 11.4.6. In the SE system the shear demand V_{se-12}:

$$V_{se-12} = 102.4\%V_d/2 \tag{11.61}$$

being in this case $V_d = 4160\text{kN}$, as in Section 11.4.7.

The comparison considering the reduced record set is then the following.
Displacement in the EP system Δ_{ep-10}:

$$\Delta_{ep-10} = 107.6\%\Delta_{is} \tag{11.62}$$

displacement in the SE system Δ_{se-10}:

$$\Delta_{se-10} = 97.4\%\Delta_{is} \tag{11.63}$$

shear force in the EP system V_{ep-10}:

$$V_{ep-10} = 104.7\%V_d/2 \tag{11.64}$$

shear force in the SE system V_{se-10}:

$$V_{se-10} = 97.6\%V_d/2 \tag{11.65}$$

Therefore the influence on the mean values of the most severe ground motion is more relevant than the influence of the less severe record and reducing the record set the mean values are reduced as well. Considering only the 10 record ground motion set, the design targets results verified for the SE system and only slightly exceeded in the EP system.

As a general conclusion on the isolation system response in near fault events, it can be noted how the SE system demand is in general less severe both in terms of displacement and shear force with respect to the EP system. This is probably due to the initial high stiffness which is particularly effective in limiting the pulse effects of near fault ground motion.

A significative influence is played in this context also by the elastic damping. Even if the damping coefficient is very small in the model, almost negligible in the overall response of the structure, its effectiveness in reducing impulse effects in SE system is more important than in the EP system, again due to the larger initial stiffness in the SE system.

(b)   Superstructure Response

The superstructure assessment is reported in the present section. All the results shown in this context are relative to the total (12 records) ground motion set.

(a) EP system   (b) SE system
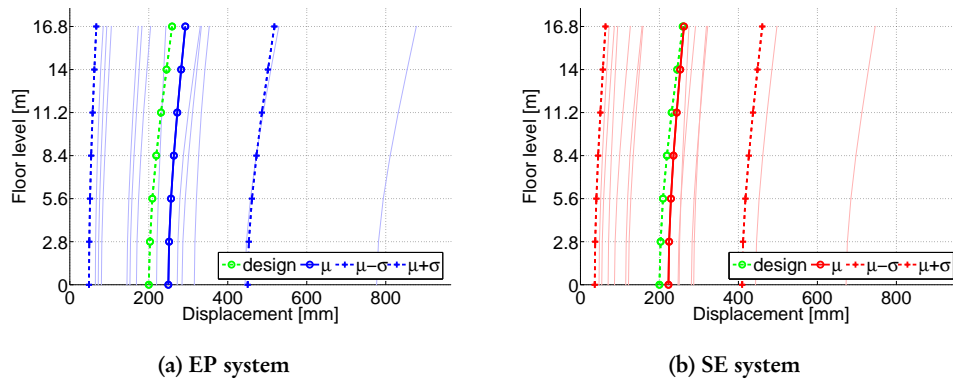
Figure 11.47. Storey displacement envelope

The displacement envelopes for all the ground motion set are reported in Figure 11.47. The superstructure deformed shape can be appreciated as almost linear. The most severe ground motion displacement demand is easy to identify being about three times larger than the mean value. Because of this, the standard deviation is quite high as well. The mean envelope exceeds the design displacement profile, but this is due to the larger displacement demand at the isolation system, as already noted in the previous section. In fact, the base

(a) EP system   (b) SE system
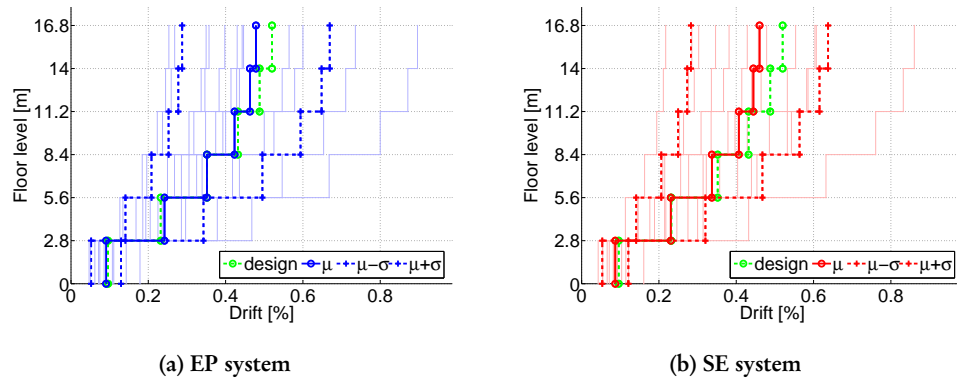
Figure 11.48. Interstorey drift demand

(a) EP system   (b) SE system
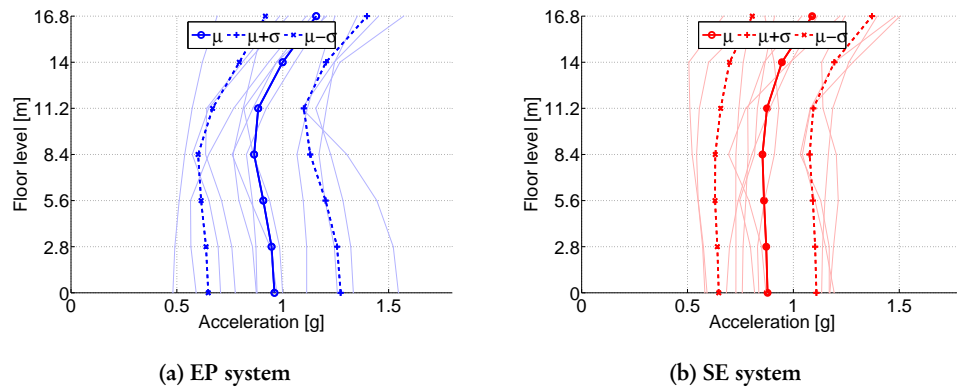
Figure 11.49. Storey acceleration demand

displacement mean value reported in Figure 11.47 is computed considering all the ground motion set, like in Figure 11.45a and Figure 11.46a.

Referring on the other side to the interstorey drift profile, as reported in Figure 11.48, it can be seen that the mean demand value is lower than the maximum design drift in both the isolation systems. For the most severe record the maximum drift value is of the order of 0.85%. The EP system seems more demanding, especially at the lower floors, with respect to the SE system and its standard deviation is higher. Nevertheless differences between the two isolation systems are small, as reported in Figure 11.50a.

Concerning the floor acceleration, the near fault condition leads to floor acceleration
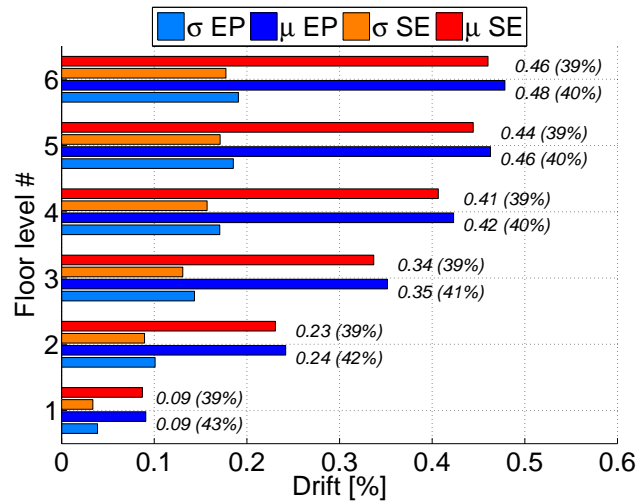
(a) interstorey drift demand comparison
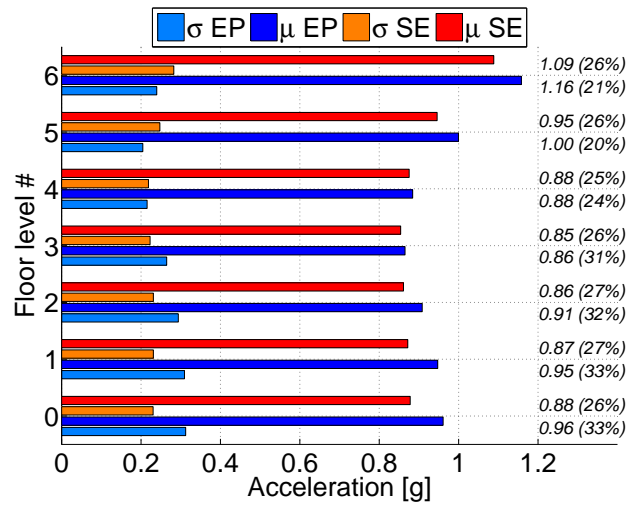
(b) floor acceleration demand comparison

Figure 11.50. Superstructure response comparison: mean values and standard deviation of interstorey drift and floor acceleration

generally higher than the previous case, and the maximum demand is recorded at the top of the wall, as shown in Figure 11.49. The EP system is in mean more demanding and characterized by a larger standard deviation, as reported in the comparison of Figure 11.50b.

(a) EP system   (b) SE system
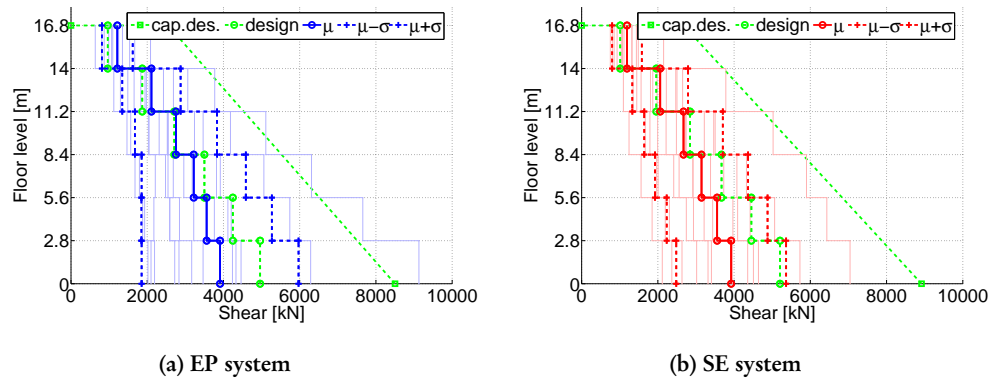
Figure 11.51. Wall shear envelope

(a) EP system   (b) SE system
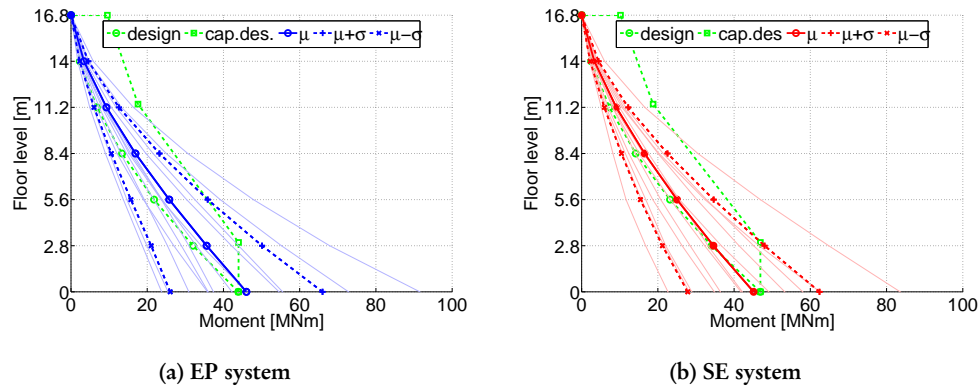
Figure 11.52. Wall moment envelope

Regarding the superstructure shear force distribution, as reported in Figure 11.51, it can be noted again that the design shear profile is larger than the mean shear profile for both the EP and the SE system, with exceptions at the top floors. The mean plus standard deviation profile is anyway exceeding the design value in the two systems. Nevertheless the capacity design profile is able to envelope all the shear distributions in the SE system design but it is exceeded in a single response of the EP system configuration.

Again, the floor shear distribution in the two systems is about the same, as shown in Figure 11.53a, but the design base shear is larger in the SE system than in the EP system. Consequently, the design condition is respected in the SE system but not in the EP system.
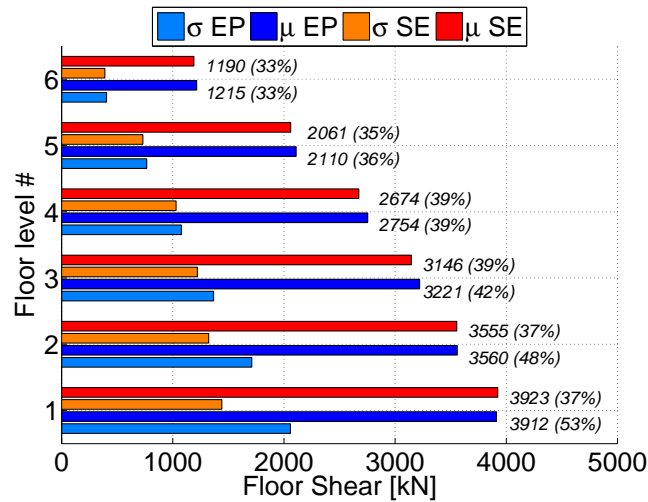
(a) shear force
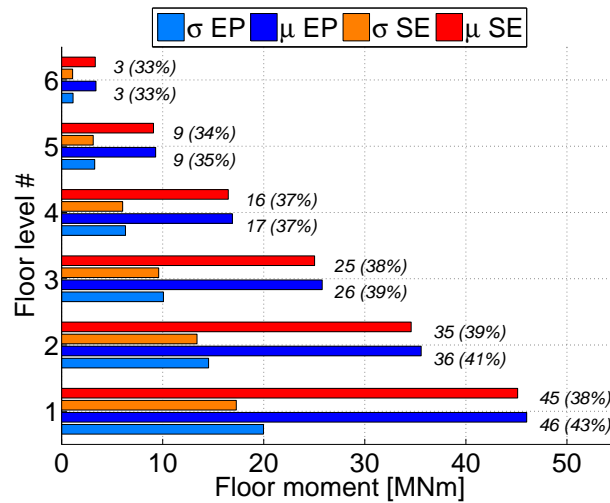
(b) bending moment

Figure 11.53. Wall bending moment and shear force comparison

The same conclusion is valid also for the bending moment distribution in the cantilever wall, in which the floor demand of the two systems is about the same as reported in Figure 11.53b, but in which the design condition is respected considering the mean demand of the SE system (as reported in Figure 11.52b) and it is slightly exceeded in the EP system
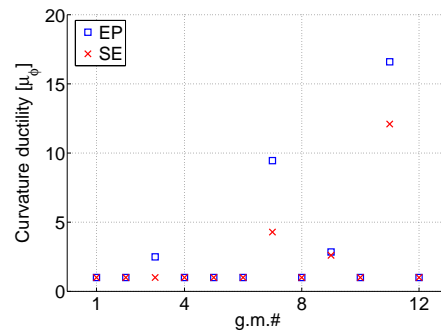
Figure 11.54. Maximum curvature ductility demand at the wall plastic hinge

design (as reported in Figure 11.52a).

Finally, the maximum curvature ductility in the wall plastic hinge is reported in Figure 11.54. The EP system results more demanding both in terms of plastic hinge occurrences and in terms of curvature ductility demand. Nevertheless the wall maximum curvature ductility capacity is not reached.

11.6 CONCLUSIONS

In the present chapter, the displacement based design for base isolated structures using superelastic devices is presented.
The superelastic isolation bearing is composed by two component, a superelastic restraining system made of SMA manufactures springs, and a slider to transmit the vertical load and provide a design shear force. A design procedure has been proposed to design the different component shear force contributions in order to guarantee the device recentering. The eventual residual displacement is very small and it is independent from the maximum displacement reached by the device.

A suitable expression to compute the equivalent viscous damping for the innovative device has been proposed as well. The relative hysteretic contributions of the two components have been considered and the expressions to compute the relative weight have been formalized.

A design example has then been proposed considering a six-storey building lay-out which was already presented in literature. The design has been performed considering a superelastic (SE) system and an actual LRB (EP) system for far field and near fault conditions and it was targeted to reach a design displacement profile. The process ended out providing very similar results for the SE and EP system. The design shear force of the base isolation system differs only for about the 10% of the maximum value. Differences in the superstructure lateral resisting system actions are of the same order of magnitude.

The structure design has been assessed using time history analyses considering spectrum compatible ground motions. The mean response of the isolation system is compatible with the design targets in the far field condition. In the near fault condition, on the contrary, the isolation system design targets are exceeded by the mean demands. This is ascribed in particular to a very severe ground motion, whose response affects the mean values significantly. Considering a reduced statistical response distribution eliminating the maximum and the minimum demand values, the design target is not exceeded in the SE system design check while it is still exceeded in the EP system. In general anyway, concerning the isolation system response, the EP system turned out to be in mean more demanding than the SE system.

Regarding the superstructure response, the mean design drift level is compatible with the target drift both for the EP and SE systems. Even if the superstructure was supposed to respond elastically, some inelastic demands are recorded in few record responses, being the EP demand more critical than the SE system one. The floor acceleration are about the same in the two systems, so no acceleration related non structural damage is supposed to be given changing between different isolation technology. Shear force and bending moment demand in lateral resisting superstructure in the SE and EP systems turn out to be very close.

Therefore, the present work provides the direct displacement based design procedure for the base isolation system using superelastic devices. The procedure has been validated considering an example in different design conditions. In general, the superelastic isolation technology is attractive for its capability in reducing the residual displacements. Nevertheless, from the present outcomes, its results are very interesting also in terms of maximum design demands. If the design is accomplished properly, the structure has been demonstrated to respond at the same or a better level than if designed considering actual high dissipative isolation systems.

This page intentionally left blank.

12. Conclusions

In the present study, an innovative superelastic system for base isolation is proposed. The potentials of a remarkable class of advanced materials (the shape memory alloys) are reported and the implementation of a new device concept based on a superelastic (i.e. flag-shaped) lateral displacement-shear force hysteresis is investigated.

Firstly, the feasibility of shape memory alloy technology application to seismic isolation devices has been evaluated.
The behavior of a model representing a conventional lead rubber bearing device and the behavior of a hypothetical shape memory alloy device were compared. Displacement and force demand of a shape memory alloy device resulted close to the demands for a lead rubber bearing system and the energy dissipation was almost the same, regardless the big differences in hysteretic area. Moreover, shape memory alloy based technology system was characterized by zero residual displacement. A sensitivity analysis on SDOF system was conducted to examine the effect of variability of fundamental hysteresis parameters on the effectiveness of SMA isolation bearing.
It was recognized that the SMA application in seismic isolation is possible and can lead to several advantages, since the SMA device provides re-centering properties together with good energy dissipation capability.

Secondly, an isolation system configuration based on superelastic SMA elements has been proposed. The design result is a flexible innovative device which composed by an independent element for the transmission of the vertical load and by another system working as a lateral restrainer.
The first element is a flat sliding bearing, a traditional device well known for civil engineering applications. The lateral restrainer is a superelastic device system composed by SMA coil springs. The restraining system is demanded to carry the design shear force and to accommodate the design displacement.
SMA springs mechanical properties and behavior have been numerically and experimentally investigated and the numerical model turned out to predict very well the experimental results. It has been demonstrated that superelastic material coil spring response consists of a flag-shaped force-displacement relation, thus superelastic spring is a recentering-theoretical zero residual displacement device suitable as a lateral restraining system component.
A simplified design procedure has then been proposed for the innovative SMA springs and

it has been demonstrated that it is an effective tool to find a device configuration suitable to reach the design targets.

A superelastic isolation device design example has been performed assuming to design a superelastic device characterized by the same response in terms of period elongation with respect to an actual lead rubber bearing. The aims of the design were reached and the final device results to be very attractive. The proposed isolation device is theoretically able to satisfy all the design requirements, which are carrying the vertical load, accommodating the design displacement, avoiding residuals, limiting the transmittable base shear to the superstructure, providing suitable initial and lateral stiffness, and making possible to replace components which need to be substituted. It is believed that the proposed device is more suitable for base isolation applications than the others previously presented and based on shape memory alloy devices.

The response of a structural system isolated using innovative bearings has then been compared with respect to the one isolated using traditional equivalent isolation devices (LRB system).

Investigations on single degree of freedom systems, on stiff and on flexible superstructure multi degree of freedom systems have been performed. Two bearing configurations have been considered, in one the flat slider is characterized by negligible friction coefficient (SL system) and in another the friction is significant (FR system).

It resulted that the maximum displacement and shear force recorded in the isolation layer are very close between the three considered systems. This is despite the fact that the theoretical hysteretic damping and therefore the response envelopes are supposed to be significantly different, given the differences in force-displacement relations. The isolated system configuration computed considering the largest dissipation capability, which is the one provided by the LRB, are generally met even considering the flag-shaped FR system. The SL system demand is more severe but differences are very much smaller than what would be expect based on a equivalent hysteretic damping approach. Regarding the superstructure response, LRB system and FR system responses resulted very close in all the cases. The isolation turns out to be very effective in terms of reduction of interstorey drift, floor shear and floor acceleration, both when the superstructure is damaged and when it responds elastically. The SL technology response on the contrary turned out to be more demanding.

Based on the performed analysis, it has been recognized that the actual LRB system and the innovative flag-shaped with friction (FR system) are almost equivalent in terms of the device and the superstructure response. The main parameter envelopes, which are the values we accounted the most because they are at the base of the design procedure, are almost the same at both the isolation and superstructure level.

Therefore, based on the structural response results, the FR system configuration, in which the flat slider is supposed to contribute with some friction force to the total device shear force capability, has been chosen as the most suitable superelastic isolation system

configuration.

Finally, the displacement based design for base isolated structures using superelastic devices has been presented. The FR system configuration was considered. A design procedure has been proposed to design the different component shear force contributions in order to guarantee the device recentering. The eventual residual displacement is very small and it is independent from the maximum displacement reached by the device. A suitable expression to compute the equivalent viscous damping for the innovative device has been proposed as well. The relative hysteretic contributions of the two components have been considered and the expressions to compute the relative weight have been formalized.

A design example has then been performed considering a six storey building lay out already presented in literature. The design has been finalized independently considering superelastic (SE) system and actual LRB system for far field and near fault conditions and it was targeted to reach a design displacement profile. The process ended out providing structural design results very similar for the SE and LRB system. Differences in term of design base shear force are of the order of the 10% of the maximum value. Differences in the superstructure lateral resisting system actions are of the same order of magnitude. The structure design has been assessed using time history analyses considering spectrum compatible ground motions. Concerning the isolation system response, the LRB system turned out to be in mean more demanding than the SE system. The SE system designed superstructure has been demonstrated to respond at the same level, or better, than if designed considering actual high dissipative isolation systems.

At the end of this investigation, the main conclusion that a superelastic isolation system configuration is suitable for reaching the structural goals is drawn. It is suggested that main efforts in the future work have to be targeted to build a real prototype and experimentally validate its global response in quasi static and dynamic tests.

This page intentionally left blank.

Bibliography

ABAQUS [2003] *Analysis User's Manual Version 6.4*. Hibbitt, Karlsson & Sorensen Inc., USA. [78, 82, 99, 136, 141, 171, 278, 279]

AISC [1997] "Seismic provisions for structural steel buildings.", American Institute of Steel Construction, Chicago, IL, USA. [223]

Akkar, S.D. and Miranda, E. [2005] "Statistical evaluation of approximate methods for estimating maximum deformation demands on existing structures." *Journal of Structural Engineering*, Vol. 131, No. 1 pp. 160 – 172. [169]

Andrawes, B. and DesRoches, R. [2007] "Effect of hysteretic properties of superelastic shape memory alloys on the seismic performance of structures." *Structural Control and Health Monitoring*, Vol. 14, No. 2 pp. 301 – 320. [30, 60]

Ates, S., Dumanoglub, A.A., and Bayraktara, A. [2005] "Stochastic response of seismically isolated highway bridges with friction pendulum systems to spatially varying earthquake ground motions." *Engineering Structures*, Vol. 27 pp. 1843–1858. [13]

Attanasi, G. [2008] "Feasibility assessment of innovative isolation bearing system with shape memory alloys." Master's dissertation, European School for Advanced Studies in Reduction of Seismic Risk (ROSE School), Italy. [50]

Attanasi, G., Auricchio, F., and Fenves, G.L. [2009a] "Feasibility investigation of superelastic effect devices for seismic isolation applications." *Journal of Materials Engineering and Performance*, Vol. 18, No. 5 pp. 729 – 737. [47, 269]

Attanasi, G., Auricchio, F., and Fenves, G.L. [2009b] "Feasibility assessment of an innovative isolation bearing system with shape memory alloys." *Journal of Earthquake Engineering*, Vol. 13, No. 1 (supp 1) pp. 18 – 39. [12, 42, 46, 50, 152, 269, 270]

Auricchio, F., Fugazza, D., and DesRoches, R. [2006a] "Earthquake performance of steel frames with nitinol braces." *Journal of Earthquake Engineering*, Vol. 10, No. 1 (supp 1) pp. 45 – 66. [33]

Auricchio, F., Fugazza, D., and DesRoches, R. [2006b] "Numerical and experimental evaluation of the damping properties of Shape-Memory alloys." *Journal of Engineering Materials and Technology*, Vol. 128, No. 3 pp. 312 – 319. [33]

Bondonet, G. and Filiatrault, A. [1996] "Shape-memory alloys for seismic isolation of bridges." In *11th World Conference on Earthquake Engineering*, Vol. 1443. 11WCEE, Acapulco, Mexico. [35]

Bondonet, G. and Filiatrault, A. [1997] "Elabotation d'un isolateur parasismique a la base pour les ponts et viaducs au canada." *Research Report 11*, Ecole Polytechnique de Montreal. [35, 108, 113, 137]

Borzi, B., Calvi, G.M., Elnashai, A.S., Faccioli, E., and Bommer, J.J. [2001] "Inelastic spectra for displacement-based seismic design." *Soil Dynamics and Earthquake Engineering*, Vol. 21, No. 1 pp. 47 – 61. [169]

Borzi, B. and Elnashai, A.S. [2000] "Refined force reduction factors for seismic design." *Engineering Structures*, Vol. 22, No. 10 pp. 1244 – 1260. [169]

Bruno, S. and Valente, C. [2002] "Comparative response analysis of conventional and innovative seismic protection strategies." *Earthquake Engineering & Structural Dynamics*, Vol. 31, No. 5 pp. 1067 – 1092. [37]

BSSC [1997] "NEHRP guidelines for the seismic rehabilitation of buildings." *FEMA 273 (Guidelines) and FEMA 274 (Commentary)*, Building Seismic Safety Council, Washington, D.C., USA. [148]

Cardone, D., Canio, G.D., Dolce, M., Marnetto, R., Moroni, C., Nicoletti, M., Nigro, D., Pizzari, A., Ponzo, F., Renzi, E., and Santarsiero, G. [2003] "Comparison of different passive control techniques through shaking table tests." In *8th World Seminar on Seismic Isolation, Energy Dissipation and Active Vibration Control of Structure*. Yerevan, Armenia. [38, 39, 109]

Cardone, D., Dolce, M., and Palermo, G. [2009] "Evaluation of simplified methods for the design of bridges with seismic isolation systems." *Earthquake Spectra*, Vol. 25, No. 2 pp. 221 – 238. [39]

Carr, A.J. [2001] *SIMQKE – A Program Artificial Motion Generation*. Department of Civil Engineering, University of Canterbury, ChristChurch, New Zealand. [50]

Carr, A.J. [2007] *Ruaumoko Manual Volume 2: User Manual for the 2-Dimensional Version, Ruaumoko2D*. Departement of Civil Engineering, University of Canterbury, ChristChurch, New Zealand. [143, 173, 185, 203, 204, 223, 290]

Casciati, F., Faravelli, L., and Hamdaoui, K. [2007] "Performance of a base isolator with shape memory alloy bars." *Earthquake Engineering and Engineering Vibration*, Vol. 6, No. 4 pp. 401 – 408. [39, 40, 137]

Casciati, F. and Hamdaoui, K. [2008] "Modelling the uncertainty in the response of a base isolator." *Probabilistic Engineering Mechanics*, Vol. 23, No. 4 pp. 427 – 437. [39]

Castellano, M.G., Indirli, M., Martelli, A., and Liu, S. [2001] "Progress of application, research and development, and design guidelines for shape memory alloy devices for cultural heritage structures in italy." In *Smart Structures and Materials 2001: Smart Systems for Bridges, Structures, and Highways*, Vol. 4330. SPIE, Newport Beach, CA, USA, pp. 250 – 261. [30, 31]

CEN [2004] "Eurocode 8: Design of structures for earthquake resistance —Part 1: General rules, seismic actions and rules for buildings." *EN 1998-1:2004*, Comité Européen de Normalisation, Brussels, Belgium. [43, 140, 148, 149, 152, 172, 198, 199, 208, 209, 229, 235, 236, 268, 279]

Choi, E., Nam, T., Oh, J., and Cho, B. [2006] "An isolation bearing for highway bridges using shape memory alloys." *Materials Science and Engineering: A*, Vol. 438-440 pp. 1081 – 1084. [38, 39, 137]

Chopra, A.K. [2006] *Dynamics of Structures. Theory and Applications to Earthquake Engineering, Third Edition.* Prentice-Hall, Upper Saddle River, New Jersey. [6, 22, 43, 46, 170]

Christopoulos, C. and Filiatrault, A. [2006] *Principles of Passive Supplemental Damping and Seismic Isolation.* IUSS Press, Pavia. [13]

Christopoulos, C., Filiatrault, A., and Folz, B. [2002] "Seismic response of self-centring hysteretic SDOF systems." *Earthquake Engineering & Structural Dynamics*, Vol. 31, No. 5 pp. 1131 – 1150. [48]

Clark, P.W., Aiken, I.D., Kelly, J.M., Higashino, M., Krumme, R., and Johnson, C.D. [1995] "Experimental and analytical studies of shape-memory alloy dampers for structural control." In *Smart Structures and Materials 1995: Passive Damping*, Vol. 2445. SPIE, San Diego, CA, USA, pp. 241 – 251. [21, 23, 24, 29]

Constantinou, M.C., Mokha, A.S., and Reinhorn, A.M. [1991] "Study of sliding bearing and Helical-Steel-Spring isolation system." *Journal of Structural Engineering*, Vol. 117, No. 4 pp. 1257 – 1275. [108, 112, 113]

Constantinou, M., Mokha, A., and Reinhorn, A. [1990] "Teflon bearings in base isolation II: modeling." *Journal of Structural Engineering*, Vol. 116, No. 2 pp. 455 – 474. [108]

Corbi, O. [2003] "Shape memory alloys and their application in structural oscillations attenuation."

Simulation Modelling Practice and Theory, Vol. 11, No. 5-6 pp. 387 – 402. [32]

Crede, C.E. [1951] *Vibration and shock isolation.* John Wiley & Sons, (New York). [77, 78]

DesRoches, R. and Andrawes, B. [2002] "Seismic retrofit of bridges using shape memory alloy restrainers." In *3rd National Seismic Conferences for Bridges and Highways.* Portland, OR, USA, pp. 43 – 55. [30]

DesRoches, R. and Delemont, M. [2002] "Seismic retrofit of simply supported bridges using shape memory alloys." *Engineering Structures*, Vol. 24, No. 3 pp. 325 – 332. [30]

DesRoches, R. and Liu, S. [1999] "Seismic mitigation of bridges using smart restrainers." In *Smart Structures and Materials 1999: Smart Systems for Bridges, Structures, and Highways*, Vol. 3671. SPIE, Newport Beach, CA, USA, pp. 11 – 20. [30]

DesRoches, R., McCormick, J., and Delemont, M. [2004] "Cyclic properties of superelastic shape memory alloy wires and bars." *Journal of Structural Engineering*, Vol. 130, No. 1 pp. 38 – 46. [19, 21, 23]

Dolce, M., Cardone, D., and Croatto, F. [2005] "Frictional behavior of Steel-PTFE interfaces for seismic isolation." *Bulletin of Earthquake Engineering*, Vol. 3, No. 1 pp. 75 – 99. [38, 107, 108, 109, 110, 111, 133]

Dolce, M. and Cardone, D. [2001a] "Mechanical behaviour of shape memory alloys for seismic applications 1. martensite and austenite NiTi bars subjected to torsion." *International Journal of Mechanical Sciences*, Vol. 43, No. 11 pp. 2631 – 2656. [20, 25, 104, 138]

Dolce, M. and Cardone, D. [2001b] "Mechanical behaviour of shape memory alloys for seismic applications 2. austenite NiTi wires subjected to tension." *International Journal of Mechanical Sciences*, Vol. 43, No. 11 pp. 2657 – 2677. [20, 22, 23, 24, 25, 26]

Dolce, M., Cardone, D., and Marnetto, R. [2000] "Implementation and testing of passive control devices based on shape memory alloys." *Earthquake Engineering & Structural Dynamics*, Vol. 29, No. 7 pp. 945 – 968. [20, 23, 26, 27, 28, 33, 35, 36, 137]

Dolce, M., Cardone, D., Marnetto, R., and Liu, S. [2001] "SMA recentering devices for seismic isolation of civil structures." In *Smart Structures and Materials 2001: Smart Systems for Bridges, Structures, and Highways*, Vol. 4330. SPIE, Newport Beach, CA, USA, pp. 238 – 249. [20]

Dolce, M., Cardone, D., and Palermo, G. [2007a] "Seismic isolation of bridges using isolation systems based on flat sliding bearings." *Bulletin of Earthquake Engineering*, Vol. 5, No. 4 pp. 491 – 509. [10, 11, 38, 109]

Dolce, M., Cardone, D., and Ponzo, F.C. [2007b] "Shaking-table tests on reinforced concrete frames with different isolation systems." *Earthquake Engineering & Structural Dynamics*, Vol. 36, No. 5 pp. 573 – 596. [38, 109]

Duerig, T.W., Melton, K.N., Stöckel, D., and Wayman, C.M. [1990] *Engineering Aspects of Shape Memory Alloys*. Butterworth-Heinemann. [24]

Dwairi, H.M., Kowalsky, M.J., and Nau, J.M. [2007] "Equivalent damping in support of direct displacement-based design." *Journal of Earthquake Engineering*, Vol. 11 pp. 512 – 530. [46]

Filiatrault, A., Tremblay, R., and Wanitkorkul, A. [2001] "Performance evaluation of passive damping systems for the seismic retrofit of steel Moment-Resisting frames subjected to Near-Field ground motions." *Earthquake Spectra*, Vol. 17, No. 3 pp. 427 – 456. [223]

Forni, M., Martelli, A., Indirli, M., Spadoni, B., Venturi, G., Cavina, L., Sobrero, E., and Rinaldis, D. [1996a] "Progress of the development of innovative antiseismic techniques in italy: Systems formed by shape memory alloy devices." In *ASME Pressure Vessels and Piping Conference*, Vol. 357. Orlando, FL, USA, pp. 31 – 46. [30]

Forni, M., Martelli, A., Simoncini, M., La Grotteria, M., Dusi, A., Bettinali, F., Bonacina, G., and Bergamo, G. [1996b] "Progress of the development of innovative antiseismic techniques in italy: Systems formed by shape memory alloy devices." In *1998 AMSE/JSME Joint Pressure Vessels and Piping Conference*, Vol. 379. San Diego, CA, USA, pp. 19 – 41. [30]

Graesser, E.J. and Cozzarelli, F.A. [1991] "Shape-Memory alloys as new materials for aseismic isolation." *Journal of Engineering Mechanics*, Vol. 117, No. 11 pp. 2590 – 2608. [17, 22, 35]

Grant, D.N., Blandon, C.A., and Priestley, M.J.N. [2005] *Modelling Inelastic Response in Direct Displacement Based Design*. IUSS Press, Pavia. [46, 48, 173, 185, 267, 270, 271]

Hall, J.F. [1994] "Parameter study of the response of moment-resisting steel frame buildings to near-source ground motions." *DB95-05*, Woodward-Clyde Federal Services, SAC Steel Project. [223]

Han, Y., Li, Q.S., Li, A., Leung, A.Y.T., and Lin, P. [2003] "Structural vibration control by shape memory alloy damper." *Earthquake Engineering & Structural Dynamics*, Vol. 32, No. 3 pp. 483 – 494. [32]

Haringx, J.A. [1949] "On highly compressible helical springs and rubber rods, and their application for vibration-free mountings." *Research Report 4*, Philips. [77]

Higashino, M., Aizawa, S., Clark, P.W., Whittaker, A.S., Aiken, I.D., and Kelly, J.M. [1996] "Experimental and analytical studies of structural control system using shape memory alloy."

In *2nd International Workshop on Structural Control*. Hong Kong, pp. 221 – 232. [29]

Higashino, M., Hamaguchi, H., Minewaki, S., and Aizawa, S. [2003] "Basic characteristics and durability of low-friction sliding bearing for base isolation." *Earthquake Engineering and Engineering Seismology*, Vol. 4, No. 1 pp. 95 – 105. [108]

ICBO [1994] "Uniform building code." , International Conference of Building Officials, Whittier, CA, USA. [223]

Inaudi, J.A. and Kelly, J.M. [1994] "Experiments on tuned mass dampers using viscoelastic, frictional and shape-memory alloy materials." In *1st World Conference on Structural Control*, Vol. 2. Los Angeles, CA, USA, pp. 127 – 136. [34]

Indirli, M., Castellano, M.G., Clemente, P., Martelli, A., and Liu, S. [2001] "Demo-application of shape memory alloy devices: the rehabilitation of the S. Giorgio church bell tower." In *Smart Structures and Materials 2001: Smart Systems for Bridges, Structures, and Highways*, Vol. 4330. SPIE, Newport Beach, CA, USA, pp. 262 – 272. [30, 31]

Jackson, C.M., Wagner, H.J., and Wasilewsky, R.J. [1972] "Nitinol-the alloy with a memory: Its physical metallurgy, properties, and applications." *SP-5110*, NASA Report, Washington, D.C. [15]

Jacobsen, L.S. [1930] "Steady forced vibrations as influenced by damping." *ASME Transactione*, Vol. 52 pp. 169 – 181". [45]

Jacobsen, L.S. [1960] "Damping on composite structures." In *Proceedings of the II World Conference of Earthquake Engineering*, Vol. 2. Tokyo and Kyoto, Japan, pp. 1029 – 1044. [45, 267]

Jain, S.K. and Thakkar, S.K. [2005] "Experimental investigations on laminated rubber bearings." *Bulletin of Earthquake Engineering*, Vol. 3 pp. 129 – 136. [11]

Jangid, R.S. [2000] "Optimum frictional elements in sliding isolation systems." *Computers & Structures*, Vol. 76, No. 5 pp. 651 – 661. [108]

Jennings, P.C. [1968] "Equivalent viscous damping for yielding structures." *Journal of Earthquake Engineering*, Vol. 94 pp. 103 – 116. [45]

Kelly, J.M. [1986] "Aseismic base isolation: review and bibliography." *Soil Dynamics and Earthquake Engineering*, Vol. 5, No. 4 pp. 202 – 216. [106]

Khan, M.M., Lagoudas, D.C., Mayes, J.J., and Henderson, B.K. [2004] "Pseudoelastic SMA spring elements for passive vibration isolation: Part i - modeling." *Journal of Intelligent Material Systems and Structures*, Vol. 15, No. 6 pp. 415 – 441. [37, 38]

Krumme, R., Hayes, J., Sweeney, S., and Johnson, C.D. [1995] "Structural damping with shape-memory alloys: one class of devices." In *Smart Structures and Materials 1995: Passive Damping*, Vol. 2445. SPIE, San Diego, CA, USA, pp. 225 – 240. [21, 23, 27, 34]

Lagoudas, D.C., Khan, M.M., Mayes, J.J., and Henderson, B.K. [2004] "Pseudoelastic SMA spring elements for passive vibration isolation: Part II - simulations and experimental correlations." *Journal of Intelligent Material Systems and Structures*, Vol. 15, No. 6 pp. 443 – 470. [37, 38]

Leon, R.T., DesRoches, R., Ocel, J., Hess, G., and Liu, S. [2001] "Innovative beam column connections using shape memory alloys." In *Smart Structures and Materials 2001: Smart Systems for Bridges, Structures, and Highways*, Vol. 4330. SPIE, Newport Beach, CA, USA, pp. 227 – 237. [31, 32]

Liang, C. and Rogers, C.A. [1997] "Design of shape memory alloy springs with applications in vibration control." *Journal of Intelligent Material Systems and Structures*, Vol. 8, No. 4 pp. 314 – 322. [37, 113]

Liu, H., Cui, Y., Ou, J., and Wang, X. [2008a] "Damping effect analysis of mega-frame structure based on SMA compound bearing." *Engineering and Engineering Vibration*, Vol. 28, No. 6 pp. 239 – 244. [39]

Liu, H., Wang, X., and Liu, J. [2008b] "The shaking table test of an SMA strands-composite bearing." *Engineering and Engineering Vibration*, Vol. 28, No. 3 pp. 152 – 156. [39, 137]

Liu, H., Wang, X., Sun, F., and Ou, J. [2008c] "Shaketable test of seismic isolation structure based on sma wire-laminated rubber combined bearings." In *14th World Conference on Earthquake Engineering*. 14WCEE, Beijing, China. [39]

Liu, Y., Xie, Z., Humbeeck, J.V., and Delaey, L. [1998] "Asymmetry of stress strain curves under tension and compression for NiTi shape memory alloys." *Acta Materialia*, Vol. 46, No. 12 pp. 4325 – 4338. [22]

Liu, Y., Xie, Z., and Humbeeck, J.V. [1999] "Cyclic deformation of NiTi shape memory alloys." *Materials Science and Engineering A*, Vol. 273-275 pp. 673 – 678. [22]

Ma, H. and Cho, C. [2008] "Feasibility study on a superelastic SMA damper with re-centring capability." *Materials Science and Engineering: A*, Vol. 473, No. 1-2 pp. 290 – 296. [33, 34, 114]

Makris, N. and Chang, S. [2000] "Effect of viscous, viscoplastic and friction damping on the response of seismic isolated structures." *Earthquake Engineering & Structural Dynamics*, Vol. 29, No. 1 pp. 85 – 107. [108, 110]

Mazzolani, F.M. and Mandara, A. [2002] "Modern trends in the use of special metals for the improvement of historical and monumental structures." *Engineering Structures*, Vol. 24, No. 7 pp. 843 – 856. [31]

McCormick, J., DesRoches, R., Fugazza, D., and Auricchio, F. [2006] "Seismic vibration control using superelastic shape memory alloys." *Journal of Engineering Materials and Technology*, Vol. 128, No. 3 pp. 294 – 301. [33]

Miranda, E. and Bertero, V.V. [1994] "Evaluation of strength reduction factors for Earthquake-Resistant design." *Earthquake Spectra*, Vol. 10, No. 2 pp. 357 – 379. [169]

Miranda, E. and Ruiz-Garcia, J. [2002] "Evaluation of approximate methods to estimate maximum inelastic displacement demands." *Earthquake Engineering & Structural Dynamics*, Vol. 31, No. 3 pp. 539 – 560. [169]

Mokha, A., Constantinou, M., and Reinhorn, A. [1990] "Teflon bearings in base isolation i: Testing." *Journal of Structural Engineering*, Vol. 116, No. 2 pp. 438 – 454. [107]

Montejo, L.A. [2007] *Cumbia, Section and Member Response of RC Members.* Departement of Civil, Construction and Enviromental Engineering, North Carolina University, USA. [200, 201, 202]

Naeim, F. and Kelly, J.M. [1999] *Desing of Seismic Isolated Structures. From Theory to Practice.* John Wiley and Sons, New York. [5, 7]

Nagarajaiah, S., Feng, M.Q., and Shinozuka, M. [1993] "Control of structures with friction controllable sliding isolation bearings." *Soil Dynamics and Earthquake Engineering*, Vol. 12, No. 2 pp. 103 – 112. [108]

Ocel, J., DesRoches, R., Leon, R.T., Hess, W.G., Krumme, R., Hayes, J.R., and Sweeney, S. [2004] "Steel Beam-Column connections using shape memory alloys." *Journal of Structural Engineering*, Vol. 130, No. 5 pp. 732 – 740. [17, 18]

Olander, A. [1932] "An electrochemical investigation of solid cadmium-gold alloys." *Journal of American Chemistry Society*, Vol. 54 pp. 3819 – 3833. [15]

Paulay, T. and Priestley, M.J.N. [1992] *Seismic Design of Reinforced Concrete and Masonry Buildings.* Wiley-Interscience, New York. [231, 282, 289]

Petrini, L., Maggi, C., Priestley, M.J.N., and Calvi, G.M. [2008] "Experimental verification of viscous damping modeling for inelastic time history analyzes." *Journal of Earthquake Engineering*, Vol. 12, No. 1 pp. 125 – 145. [49, 173, 185]

Piedboeuf, M.C., Gauvin, R., and Thomas, M. [1998] "Damping Behaviour of Shape Memory Alloys: Strain Aplitude, Frequency and Temperature Effects." *Journal of Sound and Vibration*, Vol. 214, No. 5 pp. 885 – 901. [21, 23, 24]

Plietsch, R. and Ehrlich, K. [1997] "Strength differential effect in pseudoelastic NiTi shape memory alloys." *Acta Materialia*, Vol. 45, No. 6 pp. 2417 – 2424. [21, 22]

Priestley, M.J.N. and Grant, D.N. [2005] "Viscous damping in seismic design and analysis." *Journal of Earthquake Engineering*, Vol. 9, No. (supp 2) pp. 229 – 255. [48]

Priestley, M.J.N. and Tao, J.R.T. [1993] "Seismic response of precast-prestressed concrete frames with partially debonded tendons." *PCI Journal*, Vol. 38 pp. 58 – 69. [49]

Priestley, M., Calvi, G., and Kowalsky, M. [2007] *Displacement Based Seismic Design of Structures*. IUSS Press, Pavia, Italy, 1st edition. [5, 10, 11, 12, 13, 14, 42, 44, 47, 48, 56, 111, 173, 184, 196, 198, 222, 227, 229, 230, 231, 240, 261, 265, 268, 274, 275, 276, 279, 280, 281, 282]

Riddell, R. [2008] "Inelastic response spectrum: Early history." *Earthquake Engineering & Structural Dynamics*, Vol. 37, No. 8 pp. 1175 – 1183. [168]

Rosenblueth, E. and Herrera, I. [1964] "On a kind of hysteretic damping." *Journal of the Engineering Mechanical Division, ASCE*, Vol. 90 pp. 37 – 48. [45]

SAC [1997] "Suites of earthquake ground motion for analysis of steel moment frame structures." *BD97-03*, Woodward-Clyde Federal Services, SAC Steel Project. [50, 146, 148, 150, 171, 173, 174, 185, 189, 208, 235, 291, 292, 293, 294, 295]

Shibata, A. and Sozen, M. [1976] "Substitute structure method for seismic design in rc." *Journal of the Structural Division, ASCE*, Vol. 102 pp. 1 – 18. [45]

Shook, D.A., Roschke, P.N., and Ozbulut, O.E. [2008] "Superelastic semi-active damping of a base-isolated structure." *Structural Control and Health Monitoring*, Vol. 15, No. 5 pp. 746 – 768. [40]

Skinner, R.I., Robinson, W.H., and McVerry, G.H. [1993] *An Introduction to Seismic Isolation*. John Wiley and Sons, Chichester. [5]

Song, G., Ma, N., and Li, H. [2006] "Applications of shape memory alloys in civil structures." *Engineering Structures*, Vol. 28, No. 9 pp. 1266 – 1274. [15, 33, 38]

Sweeney, S. and Hayes, J. [1995] "Shape memory alloy dampers for seismic rehabilitation of existing buildings." In *27th Joint Meeting of the US-Japan Cooperative Program in Natural Resources, Panel on Wind and Seismic Effects*. SPIE, Tsukuba Japan, pp. 317 – 332. [34]

Tamai, H. and Kitagawa, Y. [2002] "Pseudoelastic behavior of shape memory alloy wire and its application to seismic resistance member for building." *Computational Materials Science*, Vol. 25, No. 1-2 pp. 218 – 227. [32, 33]

Tamai, H., Miura, K., Kitagawa, Y., Fukuta, T., and Liu, S. [2003] "Application of SMA rod to exposed-type column base in smart structural system." In *Smart Structures and Materials 2003: Smart Systems and Nondestructive Evaluation for Civil Infrastructures*, Vol. 5057. SPIE, San Diego, CA, USA, pp. 169 – 177. [32]

Tirelli, D. and Mascelloni, S. [2000] "Characterization and optimization of shape memory alloys for seismic applications." *Journal de Physique*, Vol. 10, No. IV pp. 665 – 670. [30]

Torra, V., Isalgue, A., Martorell, F., Terriault, P., and Lovey, F. [2007] "Built in dampers for family homes via SMA: an ANSYS computation scheme based on mesoscopic and microscopic experimental analyses." *Engineering Structures*, Vol. 29, No. 8 pp. 1889 – 1902. [33]

Tsai, C., Lu, P., Chen, W., Chiang, T., Yang, C., and Lin, Y. [2008] "Finite element formulation and shaking table tests of direction-optimized-friction-pendulum system." *Engineering Structures*, Vol. 30, No. 9 pp. 2321 – 2329. [13]

Tsai, K.C. and Popov, E.P. [1994] "Steel beam column joints in seismic moment resisting frames." *UCB/EERC-88/19*, Earthquake Research Center, University of California, Berkeley. [223]

Wahl, A.M. [1963] *Mechanical Springs*. McGraw-Hill, New York, 2nd edition edition. [71, 75, 77, 78, 81, 112]

Wanitkorkul, A. and Filiatrault, A. [2008] "Influence of passive supplemental damping systems on structural and nonstructural seismic fragilities of a steel building." *Engineering Structures*, Vol. 30, No. 3 pp. 675 – 682. [223]

Wilde, K., Zheng, Y., Gardoni, P., Fujino, Y., and Liu, S. [1998] "Experimental and analytical study on a shape memory alloy damper." In *Smart Structures and Materials 1998: Smart Systems for Bridges, Structures, and Highways*, Vol. 3325. SPIE, San Diego, CA, USA, pp. 182 – 191. [22]

Wilde, K., Gardoni, P., and Fujino, Y. [2000] "Base isolation system with shape memory alloy device for elevated highway bridges." *Engineering Structures*, Vol. 22, No. 3 pp. 222 – 229. [35]

Wilson, J.C. and Wesolowsky, M.J. [2005] "Shape memory alloys for seismic response modification: A State-of-the-Art review." *Earthquake Spectra*, Vol. 21, No. 2 pp. 569 – 601. [15, 16, 17, 18, 19, 20, 24, 25, 27, 29, 34]

Wolons, D., Gandhi, F., and Malovrh, B. [1998] "Experimental investigation of the pseudoelastic

hysteresis damping characteristics of shape memory alloy wires." *Journal Of Intelligent Material Systems And Structures*, Vol. 9, No. 2 pp. 116 – 126. [24]

Zhai, C. and Xie, L. [2005] "Constant-ductility strength demand spectra for seismic design of structures." *Earthquake Engineering and Engineering Vibration*, Vol. 4, No. 2 pp. 243 – 250. [169, 171]